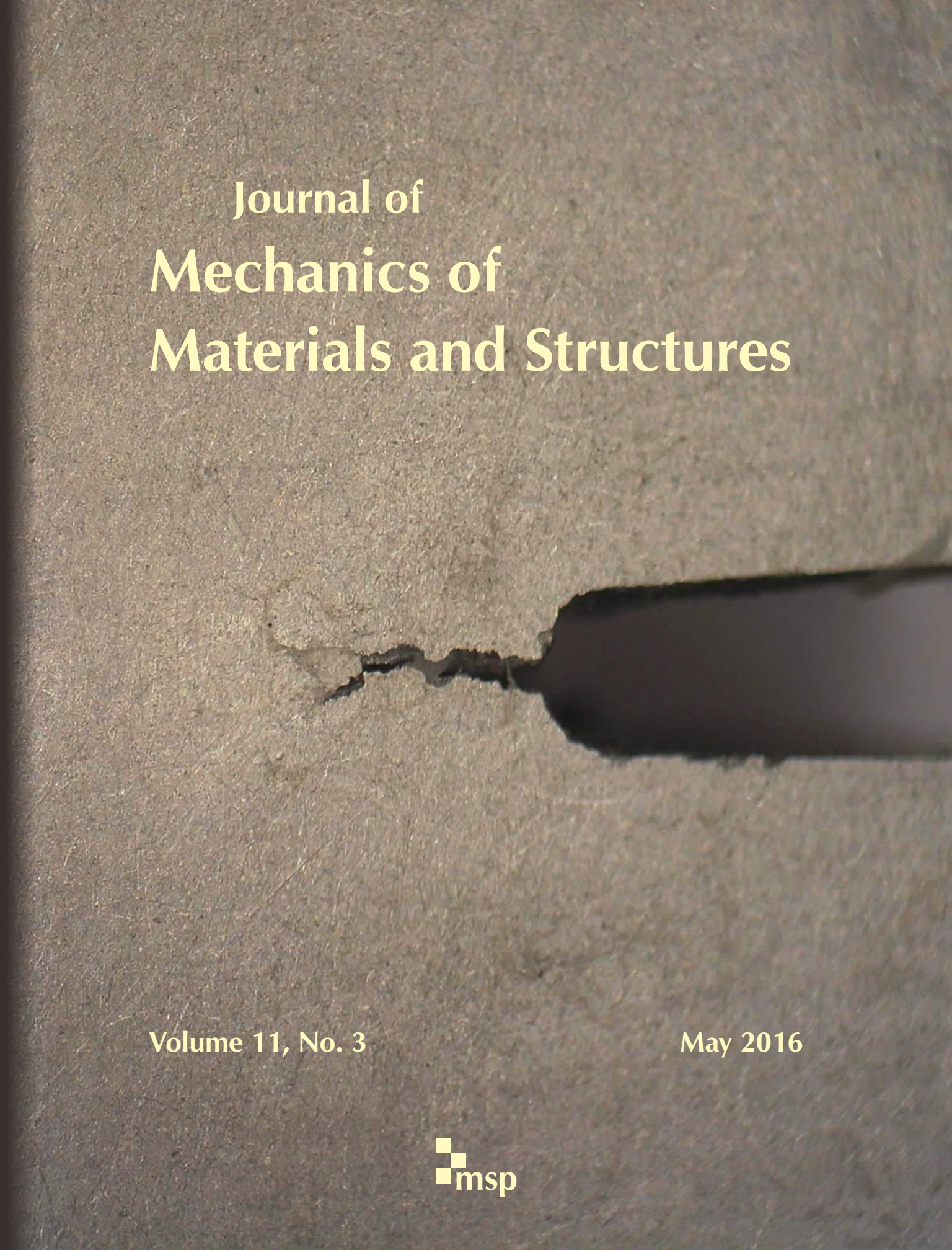

Volume 11, No. 3 May 2016

msp

JOURNAL OF MECHANICS OF MATERIALS AND STRUCTURES

msp.org/jomms

Founded by Charles R. Steele and Marie-Louise Steele

See msp.org/jomms for submission guidelines.

JoMMS (ISSN 1559-3959) at Mathematical Sciences Publishers, 798 Evans Hall #6840, c/o University of California, Berkeley, CA 94720-3840, is published in 10 issues a year. The subscription price for 2016 is US $575/year for the electronic version, and $735/year (+$60, if shipping outside the US) for print and electronic. Subscriptions, requests for back issues, and changes of address should be sent to MSP.

JoMMS peer-review and production is managed by EditFLOW® from Mathematical Sciences Publishers.

PUBLISHED BY

mathematical sciences publishers

nonprofit scientific publishing

http://msp.org/

JOURNAL OF MECHANICS OF MATERIALS AND STRUCTURES
Vol. 11, No. 3, 2016
dx.doi.org/10.2140/jomms.2016.11.197

msp

AN EULERIAN FORMULATION FOR LARGE DEFORMATIONS OF ELASTICALLY ISOTROPIC ELASTIC-VISCOPLASTIC MEMBRANES

M. B. RUBIN AND BEN NADLER

Typical models of membrane-like structures use a Lagrangian formulation of a hyperelastic membrane with a specified reference configuration. Here, an Eulerian formulation is proposed for modeling elastically isotropic, elastic-viscoplastic membranes. The membrane is modeled as a composite of an elastic and an inelastic component with evolution equations for elastic deformation tensors for each component. The model includes hyperelastic response as a special case and has a smooth elastic-inelastic transition capable of modeling both rate-independent and rate-dependent inelastic response. Strongly objective numerical algorithms are developed for integrating the proposed evolution equations. Also, an example of an initially flat circular membrane loaded by a follower pressure is considered to examine: rate-independent elastic and elastic-plastic responses, as well as rate-dependent inelastic relaxation effects.

1. Introduction

The Cosserat surface model of an elastic membrane can be developed as a restricted theory of a shell with no bending stiffness [Naghdi 1972, Section 14]. In this formulation the membrane is modeled as a deformable two-dimensional surface in three-dimensional space that can change area and distort. More specifically, the membrane is modeled as a hyperelastic solid using a Lagrangian formulation with director vectors that depend on convected coordinates related to a reference configuration.

Standard formulations of plasticity theory [Hill 1950; Green and Naghdi 1965; Cristescu 1967; Lee 1969; Lubliner 1990; Bertram 2005] are Lagrangian, with constitutive equations that depend on: a total deformation measure from a reference configuration, an inelastic deformation measure from the reference configuration and an elastic deformation measure from an intermediate configuration. In particular, for finite deformations it is common to use a multiplicative form relating total, elastic and plastic deformations [Bilby 1960; Kröner 1960; Lee 1969]. Moreover, overstress models of viscoplasticity for rate-dependent plasticity were introduced by Malvern [1951] and Perzyna [1963].

Eckart [1948] seems to be the first to emphasize that the stress tensor is determined by a constitutive equation that depends on an elastic deformation tensor which is determined by integrating an evolution equation. This evolution equation for elastic deformation is Eulerian in nature since it depends only on quantities that characterize the present state of the material, which can be measured in principle. More specifically, this evolution equation does not depend on tensor quantities, like total and plastic deformation, that depend on arbitrariness of reference and intermediate configurations. Eckart's formulation [1948] is limited to elastically isotropic material response and is essentially the same as the one proposed later by Leonov [1976] for polymeric media. Rubin [1994] generalized this approach

This research was partially supported by M. B. Rubin's Gerard Swope Chair in Mechanics.
Keywords: Eulerian formulation, elastic-viscoplastic, membranes, large deformations, smooth elastic-inelastic transition.

for elastically anisotropy materials. An important feature of this formulation [Rubin 1994] is that it removes unphysical arbitrariness of the specification of a reference configuration and an intermediate configuration from which elastic deformation is measured [Rubin 2012].

The main objective of this paper is to present a new formulation of an isotropic elastic-viscoplastic membrane for large deformations based on recent developments in viscoplasticity modeling of three-dimensional continua. One novel feature of this new formulation is that it is Eulerian and does not depend on convected Lagrangian coordinates from a fixed reference configuration for both elastic and inelastic responses.

The membrane is modeled as a composite of an elastic component and an elastic-inelastic dissipative component. Specifically, the elastic response of each component is taken to be isotropic. Evolution equations are proposed for elastic deformations of both the elastic and dissipative components. In particular, the relaxation effect of inelasticity in the evolution equation for the elastic deformation of the dissipative component is introduced through a rate of relaxation term. Using the recent developments in [Hollenstein et al. 2013] the rate of relaxation term exhibits a smooth elastic-inelastic transition and models both rate-independent and rate-dependent inelasticity. Simple functional forms are proposed for this inelastic model with only five material constants. Two constants control rate-independent inelastic response, two constants control rate-dependent inelastic response and an additional constant controls the yield strain. Moreover, these simple functional forms yield robust, strongly objective [Papes 2012; Rubin and Papes 2011] closed form (i.e., noniterative) numerical integration algorithms for the evolution equations. Also, an evolution equation for an isotropic hardening variable could be proposed which includes both hardening and softening without difficulty [Hollenstein et al. 2013], but is not included here.

One challenge in developing an Eulerian formulation of deformation of a membrane is the removal of dependence on a reference configuration in the formulation of the balance laws and constitutive equations for the membrane. Membrane theory is typically formulated using the same convected (i.e., Lagrangian) coordinates θ^α $(\alpha = 1, 2)$ for all time. This means that the director vectors $\boldsymbol{a}_\alpha$, determined by differentiating the position vector $\boldsymbol{x}$ of material points on the surface of the membrane with respect to θ^α, identify the same material line elements for all time. In order to develop the Eulerian formulation presented here, use is made of the fact that the convected coordinates are arbitrary and thus can be changed with time. In this formulation, at each instant of time, the director vectors can be chosen to be any two linearly independent vectors in the tangent plane of the membrane's surface. These director vectors characterize different material line elements at each instant of time and can be used to define coordinates that are instantaneously convected.

The example of an initially flat circular membrane subjected to a follower pressure normal on its surface is considered to examine: rate-independent elastic and elastic-plastic responses, as well as rate-dependent inelastic relaxation effects. This problem has important applications to the bursting disks of safety valves and the "bulge test" used to obtain the mechanical properties of thin films and ductile materials. The response to small deformations was analyzed in [Hill and Storåkers 1980]. Large deformations of a thin shell with explicit modeling of changes in thickness of the shell have been considered in [Storåkers 1966; Chater and Neale 1983a; 1983b; Ilahi and Paul 1985]. Cristescu [1967] discusses wave propagation problems for thin elastic-plastic plates that are deformed by dynamic loads.

More recently, Atai and Steigmann [2014] have developed a model for finite deformations of an elastic-viscoplastic thin sheet directly from the three-dimensional theory. This model uses a Lagrangian formulation with multiplicative relations between total, elastic and plastic tensorial deformation measures connecting the reference, intermediate and present configurations. Also, the model characterizes a generalized membrane since it introduces a director vector through the thickness of the sheet that is determined by conditions based on the assumption of generalized plane stress in the sheet. In contrast, here the membrane is modeled as a two-dimensional surface with no thickness and the formulation is Eulerian. The deformation tensor of the membrane's surface has only two invariants: one characterizing area change and the other characterizing surface distortion. Although the thickness of the membrane is not modeled explicitly, the constitutive equations are appropriate for generalized plane-stress response in the surface of the membrane.

An outline of the paper is as follows. Section 2 discusses mathematical aspects of a two-dimensional surface embedded in three-dimensional space with associated tensor analysis. The balance laws of a membrane are presented in Section 3, and Section 4 develops constitutive equations for an elastic-viscoplastic membrane. Invariance under superposed rigid body motions (SRBM) is discussed in Section 5 and numerical integration algorithms are detailed in Section 6. Section 7 discusses an example of axisymmetric deformation and conclusions are presented in Section 8. Also, details of invariance under SRBM are presented in the Appendix.

2. Tensor preliminaries

This paper is concerned with a membrane that is a surface $\mathcal{P}$ with a closed boundary $\partial\mathcal{P}$, which at time t is embedded in three-dimensional Euclidean space. The usual summation convention is used for repeated indices with Greek letters having the range $(\alpha = 1, 2)$ and Latin indices having the range $(i = 1, 2, 3)$. Moreover, use is made of a triad $\boldsymbol{a}_i$ of linearly independent vectors, with $\boldsymbol{a}_\alpha$ being tangent to the membrane's surface and $\boldsymbol{a}_3$ being a unit vector normal to $\mathcal{P}$, such that

$$a^{1/2} = \boldsymbol{a}_1 \times \boldsymbol{a}_2 \cdot \boldsymbol{a}_3 > 0, \quad \boldsymbol{a}_3 = \frac{\boldsymbol{a}_1 \times \boldsymbol{a}_2}{|\boldsymbol{a}_1 \times \boldsymbol{a}_2|}, \tag{2-1}$$

where it is noted that $\boldsymbol{a}_3$ is determined by the tangent vectors $\boldsymbol{a}_\alpha$. The associated reciprocal vectors $\boldsymbol{a}^i$ are defined by

$$\boldsymbol{a}^1 = a^{-1/2}\boldsymbol{a}_2 \times \boldsymbol{a}_3, \quad \boldsymbol{a}^2 = a^{-1/2}\boldsymbol{a}_3 \times \boldsymbol{a}_1, \quad \boldsymbol{a}^3 = \boldsymbol{a}_3. \tag{2-2}$$

Let $\boldsymbol{a} \otimes \boldsymbol{b}$ denote the tensor product between two vectors $\{\boldsymbol{a}, \boldsymbol{b}\}$ and $\boldsymbol{A} \cdot \boldsymbol{B} = \mathrm{tr}(\boldsymbol{A}\boldsymbol{B}^T)$ denote the inner product between two second order tensors $\{\boldsymbol{A}, \boldsymbol{B}\}$. The second order three-dimensional unit tensor $\boldsymbol{I}^*$ has the properties that for an arbitrary vector $\boldsymbol{c}$

$$\boldsymbol{c}\boldsymbol{I}^* = \boldsymbol{I}^*\boldsymbol{c} = \boldsymbol{c}, \quad \boldsymbol{I}^* \cdot \boldsymbol{I}^* = 3. \tag{2-3}$$

The second order tensor $\boldsymbol{A}$ is denoted as a surface tensor if it has the properties

$$\boldsymbol{a}_3\boldsymbol{A} = \boldsymbol{A}\boldsymbol{a}_3 = 0. \tag{2-4}$$

Then, the associated second order surface unit tensor $\boldsymbol{I}$ is defined by

$$\boldsymbol{I} = \boldsymbol{a}_\alpha \otimes \boldsymbol{a}^\alpha = \boldsymbol{a}^\alpha \otimes \boldsymbol{a}_\alpha = \boldsymbol{I}^* - \boldsymbol{a}_3 \otimes \boldsymbol{a}_3, \tag{2-5}$$

and has the properties

$$\boldsymbol{cI} = \boldsymbol{Ic} = (\boldsymbol{c}\cdot\boldsymbol{a}_\alpha)\boldsymbol{a}^\alpha = (\boldsymbol{c}\cdot\boldsymbol{a}^\alpha)\boldsymbol{a}_\alpha, \quad \boldsymbol{a}_3\boldsymbol{I} = \boldsymbol{I}\boldsymbol{a}_3 = 0, \quad \boldsymbol{I}\cdot\boldsymbol{I} = 2. \tag{2-6}$$

In this paper, tensors will be considered to be three-dimensional unless specifically stated otherwise.

The surface deviatoric operator generates the deviatoric part $\mathrm{dev}(\boldsymbol{A})$ of a second order surface tensor $\boldsymbol{A}$ and is defined by

$$\mathrm{dev}(\boldsymbol{A}) = \boldsymbol{A} - \tfrac{1}{2}(\boldsymbol{A}\cdot\boldsymbol{I})\boldsymbol{I}, \quad \mathrm{dev}(\boldsymbol{A})\cdot\boldsymbol{I} = 0. \tag{2-7}$$

Also, the surface determinant $\det(\boldsymbol{A})$ of the surface tensor $\boldsymbol{A}$ is defined by

$$\det(\boldsymbol{A}) = \frac{\boldsymbol{A}\boldsymbol{a}_1 \times \boldsymbol{A}\boldsymbol{a}_2 \cdot \boldsymbol{a}_3}{\boldsymbol{a}_1 \times \boldsymbol{a}_2 \cdot \boldsymbol{a}_3}. \tag{2-8}$$

If the surface determinant of the surface tensor $\boldsymbol{A}$ is nonzero, then $\boldsymbol{A}$ has a surface inverse $\mathrm{inv}(\boldsymbol{A})$ defined by

$$\boldsymbol{A}\,\mathrm{inv}(\boldsymbol{A}) = \mathrm{inv}(\boldsymbol{A})\boldsymbol{A} = \boldsymbol{I}, \quad \boldsymbol{A}\cdot\mathrm{inv}(\boldsymbol{A}) = 2. \tag{2-9}$$

In addition, the three-dimensional determinant of a general three-dimensional second order tensor $\boldsymbol{B}$ is defined by

$$\det^*(\boldsymbol{B}) = \frac{\boldsymbol{B}\boldsymbol{a} \times \boldsymbol{B}\boldsymbol{b} \cdot \boldsymbol{B}\boldsymbol{c}}{\boldsymbol{a} \times \boldsymbol{b} \cdot \boldsymbol{c}} \quad \text{for } \boldsymbol{a} \times \boldsymbol{b} \cdot \boldsymbol{c} \neq 0, \tag{2-10}$$

where $\{\boldsymbol{a}, \boldsymbol{b}, \boldsymbol{c}\}$ are arbitrary linearly independent vectors.

3. Basic equations

Let $\boldsymbol{x}$ locate an arbitrary material point on the surface $\mathcal{P}$ of a membrane. Also, let θ^α be arbitrary convected coordinates at time t that map θ^α to the material point $\boldsymbol{x}$ on the surface $\mathcal{P}$

$$\boldsymbol{x} = \boldsymbol{x}(\theta^\alpha, t). \tag{3-1}$$

The velocity $\boldsymbol{v}$ of this material point is given by

$$\boldsymbol{v} = \dot{\boldsymbol{x}}, \tag{3-2}$$

where $(\,\dot{}\,)$ denotes material time differentiation following the material point, which corresponds to partial differentiation of $\boldsymbol{x}$ in (3-1) with respect to time holding θ^α fixed. The director vectors $\boldsymbol{a}_\alpha$, which are tangent to the surface $\mathcal{P}$, are defined by

$$\boldsymbol{a}_\alpha = \boldsymbol{x}_{,\alpha}, \tag{3-3}$$

where a comma denotes partial differentiation with respect to θ^α. Then, the director $\boldsymbol{a}_3$, which is the unit normal to the surface $\mathcal{P}$, and the reciprocal vectors $\boldsymbol{a}^i$ are defined by (2-1) and (2-2), respectively.

Next, the rate tensor $\boldsymbol{L}$, its symmetric part $\boldsymbol{D}$ and its skew-symmetric part $\boldsymbol{W}$ are defined by

$$\boldsymbol{L} = \boldsymbol{v}_{,\alpha} \otimes \boldsymbol{a}^\alpha = \boldsymbol{D} + \boldsymbol{W}, \quad \boldsymbol{D} = \tfrac{1}{2}(\boldsymbol{L} + \boldsymbol{L}^T), \quad \boldsymbol{W} = \tfrac{1}{2}(\boldsymbol{L} - \boldsymbol{L}^T). \tag{3-4}$$

It follows that the material derivative of an arbitrary material line element $d\boldsymbol{x}$ in the membrane's surface $\mathcal{P}$ can be determined by the expression

$$\dot{d\boldsymbol{x}} = \boldsymbol{L}\,d\boldsymbol{x}. \tag{3-5}$$

The formulation is Lagrangian when the tensors are expressed in terms of the same convected coordinates for all time. For an Eulerian formulation it is necessary to be able to change the choice of the convected coordinates with time. In particular, let $\boldsymbol{b}_\beta$ be two linearly independent vectors defined in the surface $\mathscr{P}$ satisfying the conditions

$$\boldsymbol{b}_\beta \cdot \boldsymbol{a}_3 = 0, \quad \boldsymbol{b}_1 \times \boldsymbol{b}_2 \cdot \boldsymbol{a}_3 > 0. \tag{3-6}$$

Then, another set of convected coordinate y^α can be defined so that

$$\theta^\alpha = \theta^\alpha(y^\beta), \quad y^\beta = y^\beta(\theta^\alpha), \quad \boldsymbol{x} = \boldsymbol{x}(\theta^\alpha, t) = \tilde{\boldsymbol{x}}(y^\beta, t), \quad \boldsymbol{v} = \boldsymbol{v}(\theta^\alpha, t) = \tilde{\boldsymbol{v}}(y^\beta, t),$$
$$\frac{\partial \tilde{\boldsymbol{x}}}{\partial y^\beta} = (\partial\theta^\alpha/\partial y^\beta)\boldsymbol{a}_\alpha = \boldsymbol{b}_\beta. \tag{3-7}$$

Next, taking the material derivative of this expression yields

$$\dot{\boldsymbol{b}}_\beta = \frac{\partial \tilde{\boldsymbol{v}}}{\partial y^\beta} = (\partial\theta^\alpha/\partial y^\beta)\boldsymbol{v}_{,\alpha} = \boldsymbol{L}\boldsymbol{b}_\beta. \tag{3-8}$$

Thus, $\boldsymbol{b}_\beta$ can be identified with material line elements in $\mathscr{P}$ at each instant of time. In this sense, y^β can be thought of as coordinates that are instantaneously convected.

For later reference, it is noted that the current element of area $d\sigma$ of the surface $\mathscr{P}$, the current element of arc length ds of the boundary $\partial\mathscr{P}$ and the unit outward normal vector $\boldsymbol{n}$ to $\partial\mathscr{P}$ tangent to the surface $\mathscr{P}$ are defined by

$$d\sigma = a^{1/2} d\theta^1 d\theta^2, \quad \boldsymbol{n} ds = \boldsymbol{a}_\alpha d\theta^\alpha \times \boldsymbol{a}_3, \quad \boldsymbol{n} \cdot \boldsymbol{n} = 1, \tag{3-9}$$

so that $a^{1/2}$ is the element of area per unit $d\theta^1 d\theta^2$.

From [Rubin 2000], the conservation of mass for the membrane can be expressed in the form

$$m = \rho a^{1/2}, \quad \dot{m} = 0, \tag{3-10}$$

where ρ is the mass per unit present element of area $d\sigma$. Using the fact that $\boldsymbol{a}_3$ is a unit vector, the director velocity $\boldsymbol{w}_3$ satisfies the conditions

$$\boldsymbol{w}_3 = \dot{\boldsymbol{a}}_3, \quad \boldsymbol{w}_3 \cdot \boldsymbol{a}_3 = 0, \quad \boldsymbol{w}_3 = -(\boldsymbol{w}_\alpha \cdot \boldsymbol{a}_3)\boldsymbol{a}^\alpha = -\boldsymbol{L}^T \boldsymbol{a}_3 = -\boldsymbol{a}_3 \boldsymbol{L}. \tag{3-11}$$

Then, taking the material derivative of the expression (2-1) for $a^{1/2}$ yields

$$\frac{d}{dt}(a^{1/2}) = a^{1/2} \boldsymbol{D} \cdot \boldsymbol{I}, \tag{3-12}$$

which allows the conservation of mass equation (3-10) to be rewritten in the form

$$\dot{\rho} + \rho \boldsymbol{D} \cdot \boldsymbol{I} = 0. \tag{3-13}$$

To develop constitutive equations for the response to area changes it is convenient to define the area dilatation J by

$$\rho J = \rho_0, \tag{3-14}$$

where ρ_0 is the constant density of the membrane in its zero stress state ($J = 1$). Then, using (3-13), J satisfies the evolution equation

$$\dot{J} = J \boldsymbol{D} \cdot \boldsymbol{I}. \tag{3-15}$$

Next, using the work in [Rubin 2000], the balance of linear momentum for a membrane can be expressed in the form

$$\rho \dot{\boldsymbol{v}} = \rho \boldsymbol{b} + \operatorname{div}(\boldsymbol{T}), \tag{3-16}$$

where $\boldsymbol{b}$ is the external assigned force per unit mass due to body force and surface tractions on the membrane's surface $\mathcal{P}$ and $\boldsymbol{T}$ is a second order tensor, which has the units of force per unit current length in $\mathcal{P}$, to be determined by constitutive equations. Moreover, the surface divergence $\operatorname{div}(\boldsymbol{T})$ of the $\boldsymbol{T}$ can be defined by [Rubin 2000, Section 4.4]

$$a^{1/2} \operatorname{div}(\boldsymbol{T}) = \boldsymbol{t}^{\alpha}_{,\alpha}, \quad \boldsymbol{t}^{\alpha} = a^{1/2} \boldsymbol{T} \boldsymbol{a}^{\alpha}, \quad \boldsymbol{T} = a^{-1/2} \boldsymbol{t}^{\alpha} \otimes \boldsymbol{a}_{\alpha}, \tag{3-17}$$

so that (3-16) can be multiplied by $a^{1/2}$ to obtain the alternative form

$$m \dot{\boldsymbol{v}} = m \boldsymbol{b} + \boldsymbol{t}^{\alpha}_{,\alpha}. \tag{3-18}$$

Also, the force $\boldsymbol{t}$ and rate of work $\mathcal{W}_s$ done on the membrane, per unit current arc length ds, applied to the boundary $\partial\mathcal{P}$ can be expressed in the forms

$$\boldsymbol{t} = \boldsymbol{T} \boldsymbol{n}, \quad \mathcal{W}_s = \boldsymbol{t} \cdot \boldsymbol{v} \quad \text{on } \partial\mathcal{P}. \tag{3-19}$$

In addition, the balance of angular momentum requires the second order tensor $\boldsymbol{T}$ to be symmetric

$$\boldsymbol{T} = \boldsymbol{T}^{T}. \tag{3-20}$$

Then, the rate of material dissipation $\mathcal{D}$ is given by

$$a^{1/2} \mathcal{D} = a^{1/2} \boldsymbol{T} \cdot \boldsymbol{D} - m \dot{\Sigma} \geq 0, \tag{3-21}$$

where Σ is the strain energy function per unit mass.

4. Constitutive equations

Consider a membrane which is a composite of an elastic component and a dissipative component. Specifically, the elastic component resists both total area changes and total distortional deformations. The total area changes are characterized by the area dilatation J, which satisfies the evolution equation (3-15). Motivated by the work of Flory [1961], the total distortional deformations of $\mathcal{P}$ are characterized by the symmetric, unimodular, positive definite surface tensor $\boldsymbol{B}'$. This tensor satisfies the restrictions

$$\boldsymbol{a}_3 \boldsymbol{B}' = \boldsymbol{B}' \boldsymbol{a}_3 = 0, \quad \boldsymbol{B}' \cdot \boldsymbol{I} > 0, \quad \det(\boldsymbol{B}') = 1, \tag{4-1}$$

where $\boldsymbol{B}'$ and its invariant β, satisfy the equations

$$\dot{\boldsymbol{B}}' = \boldsymbol{L} \boldsymbol{B}' + \boldsymbol{B}' \boldsymbol{L}^{T} - (\boldsymbol{D} \cdot \boldsymbol{I}) \boldsymbol{B}', \quad \beta = \boldsymbol{B}' \cdot \boldsymbol{I}, \quad \dot{\beta} = 2 \operatorname{dev}(\boldsymbol{B}') \cdot \boldsymbol{D}. \tag{4-2}$$

In addition, the elastic area changes and the elastic distortional deformations of $\mathcal{P}$ of the dissipative component are characterized by the elastic area dilatation J_d and the symmetric, unimodular, positive definite surface tensor $\boldsymbol{B}'_d$, which satisfies the restrictions

$$\boldsymbol{a}_3 \boldsymbol{B}'_d = \boldsymbol{B}'_d \boldsymbol{a}_3 = 0, \quad \boldsymbol{B}'_d \cdot \boldsymbol{I} > 0, \quad \det(\boldsymbol{B}'_d) = 1, \tag{4-3}$$

where J_d, $\boldsymbol{B}'_d$ and its invariant α satisfy the evolution equations

$$\dot{J}_d = J_d[\boldsymbol{D}\cdot\boldsymbol{I} - \Gamma_d \ln(J_d)], \quad \dot{\boldsymbol{B}}'_d = \boldsymbol{L}\boldsymbol{B}'_d + \boldsymbol{B}'_d\boldsymbol{L}^T - (\boldsymbol{D}\cdot\boldsymbol{I})\boldsymbol{B}'_d - \Gamma\boldsymbol{A}_d,$$

$$\boldsymbol{A}_d = \boldsymbol{B}'_d - \left[\frac{2}{\mathrm{inv}(\boldsymbol{B}'_d)\cdot\boldsymbol{I}}\right]\boldsymbol{I}, \tag{4-4}$$

$$\alpha = \boldsymbol{B}'_d\cdot\boldsymbol{I}, \quad \dot{\alpha} = 2\,\mathrm{dev}(\boldsymbol{B}'_d)\cdot\boldsymbol{D} - \Gamma\boldsymbol{A}_d\cdot\boldsymbol{I}.$$

In these equations, Γ_d determines the magnitude of the rate of inelastic area changes and $\boldsymbol{A}_d$ determines the direction and Γ determines the magnitude of the rate of inelastic distortional deformations. When Γ_d vanishes, the evolution equation (4-4) for J_d reduces to the same form as (3-15) for the total area dilation J. Also, when Γ vanishes, the evolution equation (4-4) for $\boldsymbol{B}'_d$ reduces to the same form as (4-2) for $\boldsymbol{B}'$. Thus, when $\{\Gamma_d, \Gamma\}$ both vanish, the instantaneous response of the dissipative component becomes elastic with zero rate of dissipation. Moreover, the scalars $\{\Gamma_d, \Gamma\}$ need to be specified by constitutive equations which will be discussed later in this section. In addition, the term $\ln(J_d)$ used for the inelastic area change in (4-4) is similar to the term used in [Rubin 2015] for the inelastic contribution of the active stretch in cardiac muscle and is introduced for simplification of the numerical integration algorithm discussed in Section 6. The inelastic response due to area dilatation can be used to model inelastic distortional deformations due to area and thickness changes of a thin three-dimensional structure within the context of a pure two-dimensional membrane model.

To analyze the rate of material dissipation of the dissipative component use is made of (3-11), (4-2) and (4-4) to deduce the results

$$\frac{d}{dt}(\boldsymbol{B}'\boldsymbol{a}_3) = 0, \quad \frac{d}{dt}(\boldsymbol{a}_3\boldsymbol{B}') = 0, \quad \frac{d}{dt}(\boldsymbol{B}'_d\boldsymbol{a}_3) = 0, \quad \frac{d}{dt}(\boldsymbol{a}_3\boldsymbol{B}'_d) = 0, \tag{4-5}$$

which show that the evolution equations (4-2) and (4-4) are consistent with $\{\boldsymbol{B}', \boldsymbol{B}'_d\}$ remaining surface tensors that satisfy (4-1) and (4-3). These evolution equations for $\{\boldsymbol{B}', \boldsymbol{B}'_d\}$ also satisfy the conditions

$$\dot{\boldsymbol{B}}'\cdot\mathrm{inv}(\boldsymbol{B}') = 0, \quad \dot{\boldsymbol{B}}'_d\cdot\mathrm{inv}(\boldsymbol{B}'_d) = 0, \tag{4-6}$$

which ensure that $\{\boldsymbol{B}', \boldsymbol{B}'_d\}$ remain unimodular $\{\det(\boldsymbol{B}') = \det(\boldsymbol{B}'_d) = 1\}$. In deriving the evolution equations for $\{\beta, \alpha\}$ use has been made of (2-5), (3-11), the restrictions (4-1), (4-3) and the results that

$$\dot{\boldsymbol{I}} = -(\boldsymbol{w}_3\otimes\boldsymbol{a}_3 + \boldsymbol{a}_3\otimes\boldsymbol{w}_3), \quad \boldsymbol{B}'\cdot\dot{\boldsymbol{I}} = 0, \quad \boldsymbol{B}'_d\cdot\dot{\boldsymbol{I}} = 0. \tag{4-7}$$

For the class of membranes under consideration here, the strain energy Σ is additively separated into an elastic part Σ_e and a dissipative part Σ_d, with

$$\Sigma = \Sigma_e(J, \beta) + \Sigma_d(J_d, \alpha). \tag{4-8}$$

This considers the membrane to be modeled like an elastic component in parallel with a dissipative component that is composed of an elastic element in series with a dissipative element (see Figure 1). Here, the dissipative component is introduced to model dissipation, which includes rate-independent or rate-dependent hysteresis in cyclic loadings. Also, the kinetic quantity $\boldsymbol{T}$ separates additively into its elastic part $\boldsymbol{T}_e$ and its dissipative part $\boldsymbol{T}_d$

$$\boldsymbol{T} = \boldsymbol{T}_e + \boldsymbol{T}_d. \tag{4-9}$$

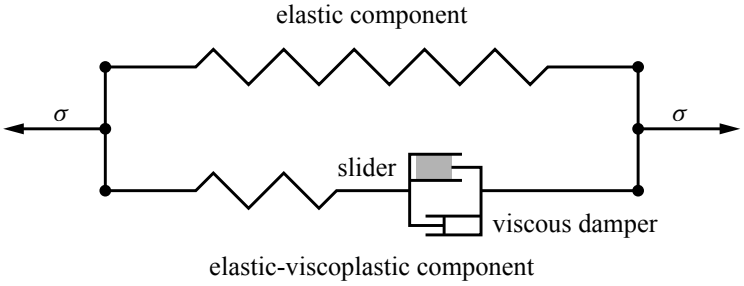

Figure 1. Sketch of an elastic-viscoplastic model with an elastic component and an elastic-viscoplastic dissipative component in parallel.

Now, taking the constitutive equations for $\{\boldsymbol{T}_e, \boldsymbol{T}_d\}$ in the forms

$$\begin{aligned} &\boldsymbol{T}_e = T_e\boldsymbol{I} + \operatorname{dev}(\boldsymbol{T}_e), \quad T_e = \rho_0 \frac{\partial \Sigma_e}{\partial J}, \qquad \operatorname{dev}(\boldsymbol{T}_e) = 2J^{-1}\rho_0 \frac{\partial \Sigma_e}{\partial \beta} \operatorname{dev}(\boldsymbol{B}'), \\ &\boldsymbol{T}_d = T_d\boldsymbol{I} + \operatorname{dev}(\boldsymbol{T}_d), \quad T_d = \left(\frac{J_d}{J}\right)\rho_0 \frac{\partial \Sigma_d}{\partial J_d}, \quad \operatorname{dev}(\boldsymbol{T}_d) = 2J^{-1}\rho_0 \frac{\partial \Sigma_d}{\partial \alpha} \operatorname{dev}(\boldsymbol{B}'_d), \end{aligned} \tag{4-10}$$

and using (3-15), (4-2) and (4-4), it can be shown that the rate of material dissipation (3-21) requires

$$\mathcal{D} = \Gamma_d \left(\frac{J_d}{J}\right)\rho_0 \frac{\partial \Sigma_d}{\partial J_d} \ln(J_d) + \Gamma J^{-1}\rho_0 \frac{\partial \Sigma_d}{\partial \alpha} \boldsymbol{A}_d \cdot \boldsymbol{I} \geq 0. \tag{4-11}$$

Furthermore, with the help of (2-6) and (4-4) it follows that

$$\boldsymbol{A}_d \cdot \boldsymbol{I} = \boldsymbol{B}'_d \cdot \boldsymbol{I} - \frac{4}{\operatorname{inv}(\boldsymbol{B}'_d) \cdot \boldsymbol{I}}. \tag{4-12}$$

However, by expressing $\boldsymbol{B}'_d$ in its spectral form and using (4-3), the fact that $\boldsymbol{B}'_d$ is a positive definite, symmetric, unimodular surface tensor with eigenvalues $\{\lambda^2, 1/\lambda^2\}$ it follows that

$$\boldsymbol{B}'_d \cdot \boldsymbol{I} = \operatorname{inv}(\boldsymbol{B}'_d) \cdot \boldsymbol{I} = \lambda^2 + \frac{1}{\lambda^2}, \tag{4-13}$$

which can be used to deduce the result

$$\boldsymbol{A}_d \cdot \boldsymbol{I} \geq 0. \tag{4-14}$$

Then, using (3-14) and the expression for $\boldsymbol{T}_d$ in (4-10), it is assumed that the strain energy of the dissipative component satisfies the restrictions

$$\frac{\partial \Sigma_d}{\partial J_d} = 0 \text{ for } J_d = 1, \quad \rho_0 \frac{\partial \Sigma_d}{\partial J_d} \ln(J_d) > 0 \text{ for } J_d \neq 1, \quad \rho_0 \frac{\partial \Sigma_d}{\partial \alpha} > 0. \tag{4-15}$$

It then follows that sufficient, but not necessary, conditions for inelasticity to be dissipative and the restriction (4-11) to be satisfied are

$$\Gamma_d \geq 0, \quad \Gamma \geq 0. \tag{4-16}$$

Moreover, in the absence of deformation rate $\boldsymbol{L}$, the evolution equations (4-4) cause J_d to relax towards 1 and $\boldsymbol{B}'_d$ to relax towards $\boldsymbol{I}$, which cause $\boldsymbol{T}_d$ to relax towards zero.

For the examples considered later in the text, the strain energy functions are specified by

$$\begin{aligned}\rho_0\Sigma_e(J,\beta) &= \tfrac{1}{4}K_e[J^2-1-2\ln(J)]+\tfrac{1}{2}\mu_e(\beta-2),\\ \rho_0\Sigma_d(\alpha) &= \tfrac{1}{4}K_d[J_d^2-1-2\ln(J_d)]+\tfrac{1}{2}\mu_d(\alpha-2),\end{aligned} \tag{4-17}$$

where the constants $\{K_e, \mu_e\}$ are the zero stress bulk and shear moduli of the elastic component and the constants $\{K_d, \mu_d\}$ are the zero stress bulk and shear moduli of the dissipative component. These constants $\{K_e, \mu_e, K_d, \mu_d\}$ have the units of force per unit length [N/m]. Then, with the help of (4-10) the kinetic quantities are given by

$$\begin{aligned}&\boldsymbol{T}_e = T_e\boldsymbol{I}+\operatorname{dev}(\boldsymbol{T}_e), \quad T_e=\frac{1}{2}K_e\left(J-\frac{1}{J}\right), && \operatorname{dev}(\boldsymbol{T}_e)=J^{-1}\mu_e\operatorname{dev}(\boldsymbol{B}'),\\ &\boldsymbol{T}_d = T_d\boldsymbol{I}+\operatorname{dev}(\boldsymbol{T}_d), \quad T_d=\frac{1}{2}K_d\left(\frac{J_d}{J}\right)\left(J_d-\frac{1}{J_d}\right), && \operatorname{dev}(\boldsymbol{T}_d)=J^{-1}\mu_d\operatorname{dev}(\boldsymbol{B}_d').\end{aligned} \tag{4-18}$$

These constitutive equations are similar to those of a compressible neo-Hookean material except that $\{\boldsymbol{T}_e, \boldsymbol{T}_d\}$ are surface tensors instead of three-dimensional tensors. Also, the constants $\{K_e, \mu_e, K_d, \mu_d\}$ are taken to be nonnegative so the restrictions (4-15) are satisfied.

Moreover, following [Hollenstein et al. 2013], the constitutive equation for the function Γ in (4-4), which controls the rate of inelastic response, is proposed in the form

$$\Gamma=\Gamma_0+\Gamma_1\langle g\rangle, \quad \Gamma_i=a_i+b_i\dot{\epsilon}\ (i=0,1), \quad g=1-\frac{\kappa}{\gamma_d}, \quad a_i\ge 0, \quad b_i\ge 0, \tag{4-19}$$

where $\{a_i, b_i\}$ are nonnegative material constants, g is the yield function with κ being a constant yield strain and the equivalent elastic strain γ_d of the dissipative component being defined by

$$\gamma_d=\sqrt{\tfrac{3}{2}\boldsymbol{g}_d\cdot\boldsymbol{g}_d}, \quad \boldsymbol{g}_d=\tfrac{1}{2}\operatorname{dev}(\boldsymbol{B}_d'). \tag{4-20}$$

Also, the equivalent rate $\dot{\epsilon}$ of total distortional strain is defined by

$$\dot{\epsilon}=\sqrt{\tfrac{2}{3}\operatorname{dev}(\boldsymbol{D})\cdot\operatorname{dev}(\boldsymbol{D})}, \tag{4-21}$$

and the Macaulay brackets $\langle g\rangle$ are defined by

$$\langle g\rangle=\max(g,0). \tag{4-22}$$

This constitutive equation produces a smooth elastic-inelastic transition, which is rate-independent when a_i vanish. The constants a_i control relaxation effects for vanishing $\dot{\epsilon}$ and the constants b_i control the magnitude of overstrain when $\dot{\epsilon}$ is nonzero and g is positive. In particular, large values of b_i cause g to be limited by a small positive value since the relaxation effects of inelasticity tend to cause g to decrease. Similar constitutive equations for Γ_d and a yield function g_d for inelasticity of the elastic area dilatation J_d could be proposed, but are not considered here since the example problems considered in Section 7 do not depend on J_d.

For the analysis of plasticity it is common to analyze a measure of accumulated plastic strain. Since the rate of inelastic area dilatation and the rate of inelastic distortional deformation in the evolution

equations (4-4) model different physical mechanisms it is natural to introduce two measures of accumulated plastic strain. The formulation of inelastic response in this paper is based on a rate of inelastic deformation and not on an inelastic deformation tensor. In this regard, it is noted from (4-4) and (4-20) that for small elastic strains

$$\boldsymbol{A}_d \approx 2\boldsymbol{g}_d. \tag{4-23}$$

Therefore, the accumulated distortional plastic strain ϵ_p, defined in [Rubin and Attia 1996], is determined by integrating the evolution equation

$$\dot{\epsilon}_p = \Gamma\sqrt{\tfrac{2}{3}\boldsymbol{g}_d\cdot\boldsymbol{g}_d} = \tfrac{2}{3}\Gamma\gamma_d, \tag{4-24}$$

subject to the initial condition that ϵ_p vanishes. Since $\dot{\epsilon}_p$ is nonnegative, a positive value of ϵ_p denotes regions which have experienced some inelastic deformations even though they may be responding elastically in the present state. An additional measure of inelastic area dilatation ϵ_d can be defined by integrating the evolution equation

$$\dot{\epsilon}_d = \Gamma_d|\ln(J_d)|. \tag{4-25}$$

It can be seen from (4-4) that this corresponds to a logarithmic rate of inelastic area dilatation.

5. Superposed rigid body motions (SRBM)

Under SRBM the position vector $\boldsymbol{x}$, time t and the directors $\boldsymbol{a}_i$, transform to their superposed values $\{\boldsymbol{x}^+, t^+, \boldsymbol{a}_i^+\}$, such that

$$\boldsymbol{x}^+ = \boldsymbol{c}(t) + \boldsymbol{Q}(t)\boldsymbol{x}, \quad t^+ = t + c, \quad \boldsymbol{a}_i^+ = \boldsymbol{Q}\boldsymbol{a}_i, \tag{5-1}$$

where $\boldsymbol{c}(t)$ is an arbitrary translation vector, c is an arbitrary constant time shift and $\boldsymbol{Q}(t)$ is an arbitrary proper orthogonal tensor

$$\boldsymbol{Q}\boldsymbol{Q}^T = \boldsymbol{I}^*, \quad \det^*(\boldsymbol{Q}) = +1, \quad \boldsymbol{\Omega} = \dot{\boldsymbol{Q}}\boldsymbol{Q}^T = -\boldsymbol{\Omega}^T, \tag{5-2}$$

with $\boldsymbol{\Omega}$ being a skew symmetric tensor. It can be shown that the velocity $\boldsymbol{v}$, the reciprocal vectors $\boldsymbol{a}^\alpha$ and the director velocities $\boldsymbol{w}_\alpha$ transform under SRBM to $\{\boldsymbol{v}^+, \boldsymbol{a}^{\alpha+}, \boldsymbol{w}_\alpha^+\}$, such that

$$\boldsymbol{v}^+ = \dot{\boldsymbol{c}} + \boldsymbol{Q}\boldsymbol{v} + \boldsymbol{\Omega}(\boldsymbol{x}^+ - \boldsymbol{c}), \quad \boldsymbol{a}^{\alpha+} = \boldsymbol{Q}\boldsymbol{a}^\alpha, \quad \boldsymbol{w}_\alpha^+ = \boldsymbol{Q}\boldsymbol{w}_\alpha + \boldsymbol{\Omega}\boldsymbol{a}_\alpha^+. \tag{5-3}$$

Here, and throughout the text, a superposed $(^+)$ is added to a symbol to denote the value of a quantity in the superposed configuration. Moreover, in the Appendix it is shown that

$$\boldsymbol{L}^+ = \boldsymbol{Q}\boldsymbol{L}\boldsymbol{Q}^T + \boldsymbol{\Omega}\boldsymbol{Q}\boldsymbol{I}\boldsymbol{Q}^T, \quad \boldsymbol{D}^+ = \boldsymbol{Q}\boldsymbol{D}\boldsymbol{Q}^T + \tfrac{1}{2}(\boldsymbol{\Omega}\boldsymbol{Q}\boldsymbol{I}\boldsymbol{Q}^T - \boldsymbol{Q}\boldsymbol{I}\boldsymbol{Q}^T\boldsymbol{\Omega}). \tag{5-4}$$

Additional transformations under SRBM are given by

$$\begin{gathered} a^{1/2+} = a^{1/2}, \quad \rho^+ = \rho, \quad J^+ = J, \quad \boldsymbol{B}'^+ = \boldsymbol{Q}\boldsymbol{B}'\boldsymbol{Q}^T, \quad J_d^+ = J_d, \quad \boldsymbol{B}_d'^+ = \boldsymbol{Q}\boldsymbol{B}_d'\boldsymbol{Q}^T, \\ \boldsymbol{b}^+ = \dot{\boldsymbol{v}}^+ + \boldsymbol{Q}(\boldsymbol{b} - \dot{\boldsymbol{v}}), \quad \boldsymbol{T}^+ = \boldsymbol{Q}\boldsymbol{T}\boldsymbol{Q}^T, \quad \boldsymbol{n}^+ = \boldsymbol{Q}\boldsymbol{n}, \quad \boldsymbol{t}^+ = \boldsymbol{Q}\boldsymbol{t}, \\ \Gamma_d^+ = \Gamma_d, \quad \Gamma^+ = \Gamma, \quad \epsilon_p^+ = \epsilon_p, \quad \epsilon_d^+ = \epsilon_d. \end{gathered} \tag{5-5}$$

Then, using these expressions and other results recorded in the Appendix, it can be shown that the entire theory discussed in the previous sections is properly invariant under SRBM.

6. Robust, strongly objective numerical integration algorithms

The objective of this section is to develop robust, strongly objective numerical algorithms for integrating the evolution equations (3-15) for J, (4-2) for $\boldsymbol{B}'$ and (4-4) for J_d and $\boldsymbol{B}'_d$ over a time step which begins at $t = t_1$, ends at $t = t_2$, with time increment $\Delta t = t_2 - t_1$. Specifically, given the values

$$\{J(t_1),\, \boldsymbol{B}'(t_1),\, J_d(t_1),\, \boldsymbol{B}'_d(t_1)\} \tag{6-1}$$

at the beginning of the time step, the numerical algorithm predicts the values

$$\{J(t_2),\, \boldsymbol{B}'(t_2),\, J_d(t_2),\, \boldsymbol{B}'_d(t_2)\} \tag{6-2}$$

at the end of the time step.

Motivated by the work in [Simo 1992; Simo and Hughes 1998, p. 315; Rubin and Papes 2011; Papes 2012; Hollenstein et al. 2013], robust, strongly object numerical algorithms are based on the relative deformation gradient $\boldsymbol{F}_r$, which satisfies the evolution equation and initial conditions

$$\dot{\boldsymbol{F}}_r = \boldsymbol{L}\boldsymbol{F}_r, \quad \boldsymbol{F}_r(t_1) = \boldsymbol{I}. \tag{6-3}$$

In particular, the solution of this equation can be expressed in the form

$$\boldsymbol{F}_r(t) = \boldsymbol{a}_\alpha(t) \otimes \boldsymbol{a}^\alpha(t_1), \tag{6-4}$$

and the relative dilatation J_r satisfies the equations

$$J_r(t) = \det(\boldsymbol{F}_r), \quad \dot{J}_r = J_r \boldsymbol{D} \cdot \boldsymbol{I}, \quad J_r(t_1) = 1, \tag{6-5}$$

Moreover, the unimodular part $\boldsymbol{F}'_r$ of $\boldsymbol{F}_r$ satisfies the equations

$$\boldsymbol{F}'_r = J_r^{-1/2}\boldsymbol{F}_r, \quad \dot{\boldsymbol{F}}'_r = [\boldsymbol{L} - \tfrac{1}{2}(\boldsymbol{D}\cdot\boldsymbol{I})\boldsymbol{I}]\boldsymbol{F}'_r, \quad \boldsymbol{F}'_r(t_1) = \boldsymbol{I}. \tag{6-6}$$

Using (6-5) and (6-6), the exact solutions of (3-15) and (4-2), which satisfy the initial conditions (6-1), are given by

$$J(t_2) = J_r(t_2)J(t_1), \quad \boldsymbol{B}'(t_2) = \boldsymbol{F}'_r(t_2)\boldsymbol{B}'(t_1)\boldsymbol{F}'^T_r(t_2). \tag{6-7}$$

Also, the elastic trial values J_d^* of J_d and $\boldsymbol{B}'^*_d(t)$ of $\boldsymbol{B}'_d$, defined by

$$J_d^*(t) = J_r(t)J_d(t_1), \quad \boldsymbol{B}'^*_d(t) = \boldsymbol{F}'_r(t)\boldsymbol{B}'_d(t_1)\boldsymbol{F}'^T_r(t), \tag{6-8}$$

satisfy the evolution equations and initial conditions

$$\begin{aligned} \dot{J}_d^* &= J_d^*(\boldsymbol{D}\cdot\boldsymbol{I}), & J_d^*(t_1) &= J_d(t_1), \\ \dot{\boldsymbol{B}}'^*_d &= \boldsymbol{L}\boldsymbol{B}'^*_d + \boldsymbol{B}'^*_d\boldsymbol{L}^T - (\boldsymbol{D}\cdot\boldsymbol{I})\boldsymbol{B}'^*_d, & \boldsymbol{B}'^*_d(t_1) &= \boldsymbol{B}'_d(t_1), \end{aligned} \tag{6-9}$$

where $\boldsymbol{B}'^*_d$ in these equations is a surface tensor. Next, it is convenient to use an implicit backward Euler approximation of the evolution equation (4-4) for J_d of the form

$$\ln\{J_d(t_2)\} = \ln\{J_d^*(t_2)\} - \Delta t\,\Gamma_d(t_2)\ln[J_d(t_2)], \tag{6-10}$$

where $\Gamma_d(t_2)$ denotes the value of Γ_d at the end of the time step. Then, the value $J_d(t_2)$ at the end of the time step is given by

$$J_d(t_2) = [J_d^*(t_2)]^{1/\{1+\Delta t\Gamma_d(t_2)\}}. \tag{6-11}$$

This value of $J_d(t_2)$ represents the exact solution of (4-4) when Γ_d vanishes and it represents an approximate solution of (4-4) if the rate of inelastic area dilatation is nonzero. A discussion similar to the one below for determining $\Gamma_d(t_2)$ could be presented but is not pursued further here since the constitutive response for the example considered in the Section 7 does not depend on J_d.

Similarly, it is convenient to use an implicit backward Euler approximation of the evolution equation (4-4) for $\boldsymbol{B}'_d$ by introducing the auxiliary tensor $\bar{\boldsymbol{B}}'_d$ defined by

$$\bar{\boldsymbol{B}}'_d(t_2) = \boldsymbol{B}'^*_d(t_2) - \Delta t\Gamma(t_2)\left[\bar{\boldsymbol{B}}'_d(t_2) - \left(\frac{2}{\text{inv}[\bar{\boldsymbol{B}}'_d(t_2)]\cdot\boldsymbol{I}}\right)\boldsymbol{I}\right], \tag{6-12}$$

where $\Gamma(t_2)$ denotes the value of Γ at the end of the time step. The tensor $\bar{\boldsymbol{B}}'_d(t_2)$ represents the exact solution of (4-4) if Γ vanishes and it represents an approximate solution of (4-4) if the rate of inelastic distortional deformation is nonzero. Moreover, $\bar{\boldsymbol{B}}'_d(t_2)$ is introduced as an auxiliary tensor since it is not necessarily unimodular and therefore is only an approximation of $\boldsymbol{B}'_d(t_2)$. Now, using the surface deviatoric operator (2-7), the deviatoric part of $\boldsymbol{B}'_d(t_2)$ is set equal to the deviatoric part of $\bar{\boldsymbol{B}}'_d(t_2)$ to obtain

$$\text{dev}\{\boldsymbol{B}'_d(t_2)\} = \text{dev}\{\bar{\boldsymbol{B}}'_d(t_2)\} = \text{dev}\{\boldsymbol{B}'^*_d(t_2)\} - \Delta t\Gamma(t_2)\,\text{dev}\{\boldsymbol{B}'_d(t_2)\}. \tag{6-13}$$

This equation can be solved to obtain

$$\begin{aligned} \text{dev}\{\boldsymbol{B}'_d(t_2)\} &= \frac{\text{dev}\{\boldsymbol{B}'^*_d(t_2)\}}{1+\Delta t\Gamma(t_2)}, \quad \gamma_d(t_2) = \frac{\gamma_d^*(t_2)}{1+\Delta t\Gamma(t_2)}, \\ \gamma_d^*(t_2) &= \sqrt{\tfrac{3}{2}\boldsymbol{g}_d^*\cdot\boldsymbol{g}_d^*}, \qquad \boldsymbol{g}_d^* = \tfrac{1}{2}\,\text{dev}\{\boldsymbol{B}'^*_d(t_2)\}, \\ \gamma_d(t_2) &= \sqrt{\tfrac{3}{2}\boldsymbol{g}_d\cdot\boldsymbol{g}_d}, \qquad \boldsymbol{g}_d = \tfrac{1}{2}\,\text{dev}\{\boldsymbol{B}'_d(t_2)\}, \end{aligned} \tag{6-14}$$

where use has been made of (4-20). Once the value $\Gamma(t_2)$ is known, the value $\boldsymbol{B}'_d(t_2)$ can be determined using $\text{dev}\{\boldsymbol{B}'_d(t_2)\}$ and the expression

$$\boldsymbol{B}'_d(t_2) = \tfrac{1}{2}\alpha(t_2)\boldsymbol{I} + \text{dev}\{\bar{\boldsymbol{B}}'_d(t_2)\}, \tag{6-15}$$

together with the condition that $\boldsymbol{B}'_d(t_2)$ is unimodular, which requires

$$\alpha(t_2) = 2\sqrt{1 - \det[\text{dev}\{\boldsymbol{B}'_d(t_2)\}]}, \tag{6-16}$$

where it is noted that $\det[\text{dev}\{\boldsymbol{B}'_d(t_2)\}]$ is nonpositive so that $\alpha(t_2)$ is real and positive.

More specifically, introducing the relative total distortional deformation measures $\{\boldsymbol{C}'_r, \boldsymbol{B}'_r\}$

$$\boldsymbol{C}'_r = \boldsymbol{F}'^T_r\boldsymbol{F}'_r, \quad \boldsymbol{B}'_r = \boldsymbol{F}'_r\boldsymbol{F}'^T_r, \tag{6-17}$$

and using (2-7), (3-4) and (6-6) it can be shown that

$$\dot{\boldsymbol{C}}'_r = 2\boldsymbol{F}'^T_r\,\text{dev}(\boldsymbol{D})\boldsymbol{F}'_r, \quad \text{dev}(\boldsymbol{D}) = \tfrac{1}{2}\boldsymbol{F}'^{-T}_r\dot{\boldsymbol{C}}'_r\boldsymbol{F}'^{-1}_r. \tag{6-18}$$

Then, the value of $\mathrm{dev}(\boldsymbol{D})$ can be approximated by

$$\mathrm{dev}(\boldsymbol{D}) \approx \mathrm{dev}(\bar{\boldsymbol{D}}) = \frac{1}{2\Delta t}[\boldsymbol{F}_r'^{-T}(t_2)\{\boldsymbol{C}_r'(t_2) - \boldsymbol{I}\}\boldsymbol{F}_r'^{-1}(t_2)] = \frac{1}{2\Delta t}[\boldsymbol{I} - \boldsymbol{B}_r'^{-1}(t_2)], \tag{6-19}$$

so the equivalent rate $\dot{\epsilon}$ in (4-21) can be approximated by

$$\dot{\epsilon}(t_2) \approx \dot{\bar{\epsilon}} = \sqrt{\tfrac{2}{3}\,\mathrm{dev}(\bar{\boldsymbol{D}}) \cdot \mathrm{dev}(\bar{\boldsymbol{D}})}, \quad \Delta\bar{\epsilon} = \Delta t\dot{\bar{\epsilon}}. \tag{6-20}$$

Also, with the help of (4-19) and (6-14), the value of the yield function g at the end of the time step is given by

$$g(t_2) = 1 - \frac{\kappa[1 + \Delta t\Gamma(t_2)]}{\gamma_d^*(t_2)}. \tag{6-21}$$

Moreover, using (4-19) and (6-20), the value of Γ at the end of the time step is given by

$$\Delta t\Gamma(t_2) = \Delta\Gamma_0 + \Delta\Gamma_1\langle g(t_2)\rangle, \quad \Delta\Gamma_i = \Delta t a_i + b_i\Delta\bar{\epsilon} \qquad (i = 0, 1). \tag{6-22}$$

In order to solve these equations for $\Delta t\Gamma(t_2)$ it is convenient to introduce the auxiliary variable $\bar{g}$ defined by

$$\bar{g} = 1 - \frac{\kappa(1 + \Delta\Gamma_0)}{\gamma_d^*(t_2)}, \tag{6-23}$$

to obtain

$$g(t_2) = \frac{\langle\bar{g}\rangle}{1 + \dfrac{\kappa\Delta\Gamma_1}{\gamma_d^*(t_2)}}, \quad \Delta t\Gamma(t_2) = \Delta\Gamma_0 + \frac{\Delta\Gamma_1\langle\bar{g}\rangle}{1 + \dfrac{\kappa\Delta\Gamma_1}{\gamma_d^*(t_2)}}. \tag{6-24}$$

Furthermore, the evolution equations (4-24) and (4-25) are integrated by taking

$$\epsilon_p(t_2) = \epsilon_p(t_1) + \tfrac{2}{3}\Delta t\Gamma(t_2)\gamma_d(t_2), \quad \epsilon_d(t_2) = \epsilon_d(t_1) + \Delta t\Gamma_d(t_2)|\ln(J_d(t_2)|, \tag{6-25}$$

with $\gamma_d(t_2)$ given by (6-14) and $\Delta t\Gamma(t_2)$ given by (6-22). Next, introducing the relative director displacements $\boldsymbol{\delta}_\alpha$ and the relative displacement gradient $\boldsymbol{H}_r$ by the expressions

$$\boldsymbol{a}_\alpha(t_2) = \boldsymbol{a}_\alpha(t_1) + \boldsymbol{\delta}_\alpha, \quad \boldsymbol{H}_r = \boldsymbol{\delta}_\alpha \otimes \boldsymbol{a}^\alpha(t_1), \tag{6-26}$$

it follows that the relative deformation gradient at the end of the time step is given by

$$\boldsymbol{F}_r(t_2) = \boldsymbol{I} + \boldsymbol{H}_r. \tag{6-27}$$

Thus, within the context of standard finite element procedures, the value of $\boldsymbol{F}_r(t_2)$ can be expressed in terms of nodal displacements which are determined at each iteration step.

In summary, given the displacements $\boldsymbol{\delta}_\alpha$: the relative deformation gradient $\boldsymbol{F}_r$ during the time step is determined by (6-26) and (6-27); the exact values $\{J(t_2), \boldsymbol{B}'(t_2)\}$ are determined by (6-7); the elastic trial values $\{J_d^*(t_2), \boldsymbol{B}_d'^*(t_2), \gamma_d'^*(t_2)\}$ are determined by (6-8) and (6-14); the final value $J_d(t_2)$ is determined by (6-11); $\{\Delta\Gamma_i, \Delta t\Gamma(t_2)\}$ are determined by (6-20)–(6-24); and the final value $\boldsymbol{B}_d'(t_2)$ is determined by (6-14)–(6-16). Finally, using these values, the kinetic quantities are determined by the constitutive equations (4-18), which are then used to check that the balance laws are satisfied to the desired accuracy and to update the estimates of the displacements if additional corrections are needed.

The expressions in this section are strongly objective with the numerical estimates of tensor quantities having the same invariance properties under SRBM as the exact values of the tensors (see [Rubin and Papes 2011]).

7. An example of axisymmetric deformation

As an example, the finite deformation of an initially flat circular membrane subjected to pressure normal to its surface, which was analyzed in [Chater and Neale 1983a; 1983b], is used here to illustrate the inelastic response of the proposed model. Figure 2 shows a sketch of a deformed membrane which in its initial unstressed reference configuration at $t = 0$ is a flat circular disk of radius B. Its edges are simply supported by a rigid ring of radius B. The position vector $\boldsymbol{x}$ for this axisymmetric problem is expressed in terms of the cylindrical polar base vectors $\{\boldsymbol{e}_r(\theta), \boldsymbol{e}_\theta(\theta), \boldsymbol{e}_3\}$ in the form

$$\boldsymbol{x} = r(R,t)\boldsymbol{e}_r + z(R,t)\boldsymbol{e}_3, \quad 0 \le R \le \frac{B}{1+b}, \qquad b = 0.01, \tag{7-1}$$

where R is the convected (i.e., Lagrangian) radial coordinate, θ is the circumferential angle, $r(R,t)$ is the current radial position and $z(R,t)$ is the current axial position. In order to avoid numerical problems associated with zero stiffness to normal displacements of a flat membrane, the membrane is slightly stretched in the radial direction in its initial configuration at $t = 0$ with

$$r(R,0) = (1+b)R, \quad z(R,0) = 0. \tag{7-2}$$

A uniform follower force pressure p is applied normal to the surface of the membrane which inflates it to its deformed configuration. For this example, the external assigned force is given by

$$\rho\boldsymbol{b} = p\boldsymbol{a}_3. \tag{7-3}$$

Also, the constitutive equations are specified by (4-17)–(4-19) with K_d set equal to zero.

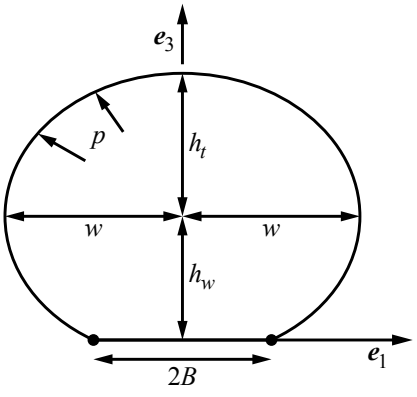

Figure 2. Sketch of inflation of an initially flat circular membrane of radius B which is loaded by an internal pressure p. The maximum width is denoted by $2w$, the height of this maximum width is denoted by h_w and the height of the top of the membrane is denoted by $h_w + h_t$.

In order to emphasize the influence of inelasticity, the elastic component is taken to have no resistance to distortional deformations and the rate of inelasticity is simplified by taking

$$\mu_e = 0, \quad b_0 = 0, \quad a_1 = 0. \tag{7-4}$$

The remaining constants are specified by

$$\mu_d = 100K_e, \quad b_1 = 0 \text{ or } 10^6, \quad \kappa = 0.001. \tag{7-5}$$

Also, the positive value of B is used to normalize the length measures $\{r, z\}$. A positive value of a_0 causes rate-dependent inelasticity which tends to cause the stress $\boldsymbol{T}_d$ in the dissipative component to relax towards zero. When a_0 vanishes and b_1 is positive, then the dissipative component has a finite elastic range and rate-independent plasticity only occurs when the yield function g becomes positive. Moreover, when b_1 attains the large value in (7-5) it causes the yield function g in (4-19) to remain very close to zero during inelastic loading. Also, the applied pressure p is increased to the maximum value $p_{\max}$ given by

$$p_{\max} = 100\frac{K_e}{B}, \tag{7-6}$$

and then is held constant. Here, the rate of loading need not be specified since attention is limited to elastic response and elastic-plastic response, which are both rate-independent, and to fully relaxed viscoplastic response with zero elastic distortional deformation.

The equations of equilibrium [(3-18) with $\dot{\boldsymbol{v}} = 0$] were formulated in terms of $\{R, t\}$ and were solved numerically using finite differences for the spatial dependence at each time. The equilibrium equations for the axisymmetric problem considered here simplify into a system of two second order nonlinear ordinary differential equations in the spatial domain, which can be expressed as a system of four nonlinear first order ordinary differential equations. The system of nonlinear first order ordinary differential equations can be efficiently solved numerically using the shooting method for the spatial dependence at each time. The solution procedure is iterative with the elastic distortional deformation (6-12) of the dissipative component being based on the same initial value $\boldsymbol{B}'_d(t_1)$ in (6-8) until an equilibrium configuration has been obtained and the next time step is analyzed.

7.1. ***Elastic response (E).*** When, b_1 vanishes and the loading is rapid (i.e., $\dot{\epsilon} \gg a_0$), the influence of viscoplasticity is negligible and the solution is purely elastic. This solution is denoted by (E).

7.2. ***Rate-independent elastic-plastic response (P).*** When, b_1 is positive and the loading is rapid (i.e., $b_1\dot{\epsilon} \gg a_0$), the influence of viscoplasticity is negligible and the solution exhibits rate-independent elastic-plastic response. This solution is denoted by (P).

7.3. ***Rate-dependent viscoplastic relaxation (R).*** When the pressure is held constant, the viscoplastic response, controlled by a_0, causes the elastic distortional deformation γ_d to asymptotically approach zero with time. This causes $\boldsymbol{T}_d$ to vanish so the final state is controlled only by the elastic area changes associated with T_e in (4-18). This asymptotic relaxed solution is denoted by (R). Since only the fully relaxed asymptotic solution for viscoplasticity is presented, it is sufficient to solve the elastic problem with vanishing μ_d.

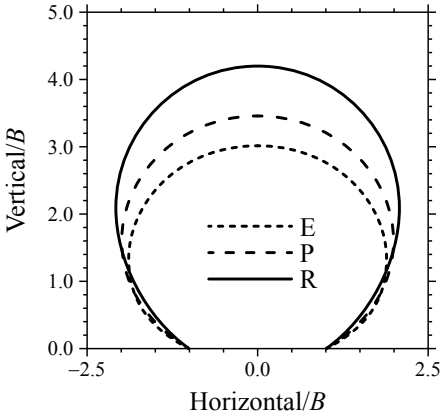

Figure 3. Deformed shapes of the membrane loaded by the constant uniform internal pressure $p = 10K_e/B$ for the elastic solution (E), the plastic solution (P) and the fully relaxed viscoplastic solution (R).

Figure 3 plots the shapes of the membrane normalized by the radius B of the ring for the elastic solution (E), the plastic solution (P) and the viscoplastic relaxed solution (R) with $p = p_{\max}$. From this figure it can be seen that the deformations of the solution (E) are smaller than those of (P) and (R) because the resistance to distortional deformations in the solution (P) is reduced relative to that in the solution (E) due to plasticity. Also, the solution (R) is fully relaxed with zero resistance to distortional deformations. Figure 4 plots the geometric parameters $\{h_t/w, h_w/w\}$ (see Figure 2) as functions of the pressure for the three solutions (E, P, R). From Figure 4 (left) it can be seen that the normalized heights h_t/w of each of the solutions (E, P) are very close to each other and the top part of the fully relaxed membrane attains a near circular shape (i.e., $h_t/w = 1$). Figure 4 (right) shows that the ring controls the maximum width w of the membrane until the pressure attains a critical value when the normalized height h_w/w becomes nonzero. This figure also shows that the effect of distortional strength of the membrane near the constraining ring significantly changes the shape of the lower part of the membrane, with only the solution (R) approaching that of a spherical membrane (i.e., $h_w/w = 1$).

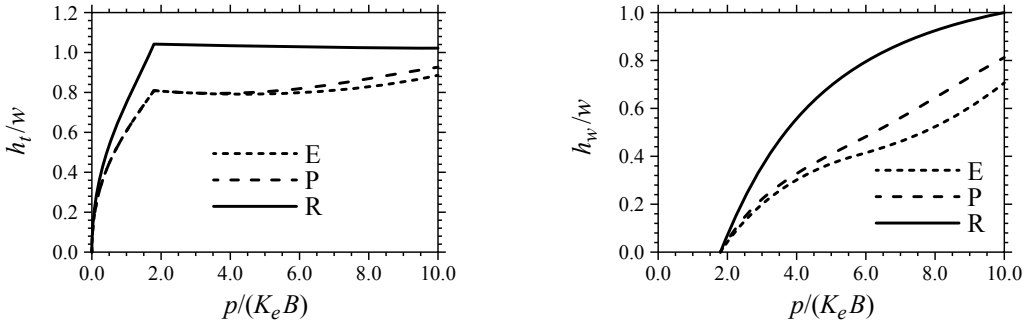

Figure 4. Geometric properties of the membrane as functions of the internal pressure p for the elastic solution (E), the plastic solution (P) and the fully relaxed viscoplastic solution (R).

8. Conclusions

The balance laws and constitutive equations for large deformations of an elastically isotropic elastic-viscoplastic membrane have been developed based on an Eulerian formulation. Specifically, the membrane is considered to be a composite of an elastic component and a dissipative elastic-viscoplastic component. The constitutive equations (4-10) are hyperelastic in the sense that the kinetic quantities $\{\boldsymbol{T}_e, \boldsymbol{T}_d\}$ are determined by derivatives of the strain energy functions $\{\Sigma_e, \Sigma_d\}$, respectively. The response of the elastic component depends on the area dilatation J and on the total elastic distortional deformation $\boldsymbol{B}'_e$, which are determined by the evolution equations (3-15) and (4-2). In addition, the response of the dissipative component depends on the elastic area dilatation J_d and the elastic distortional deformation $\boldsymbol{B}'_d$ of the dissipative component, which are determined by the evolution equations (4-4).

The rate of inelastic deformation in (4-4) is based on the work in [Hollenstein et al. 2013] which models a smooth elastic-inelastic transition, with rate-independent plasticity and rate-dependent viscoplasticity included as special cases. Specifically, this rate of inelasticity depends on five material constants: two $\{a_0, a_1\}$ which control rate-dependent response; two $\{b_0, b_1\}$ which control rate-independent response; and one $\{\kappa\}$ which controls the yield strain.

Numerical algorithms have been developed which are robust and strongly objective. Also, these algorithms produce exact solutions for purely elastic response. Finally, the example of large axisymmetric deformations of an initially flat circular membrane subjected to a follower pressure normal to its surface is considered to examine: the elastic and elastic-plastic responses and the fully relaxed viscoplastic response of the membrane.

This model can be implemented into a general purpose computer program. Then, the influence of dissipation and hysteresis during cyclic loading due to the dissipative component can be examined. Moreover, since the model uses an Eulerian formulation, it would be interesting to use it to model some features of lipid membranes with dissipation to the distortional motion of lipid reorganization in the surface of the membrane.

Appendix: Details of invariance properties under SRBM

With the help of (2-5), (5-1) and (5-3) it follows that

$$\boldsymbol{I}^+ = \boldsymbol{a}^+_\alpha \otimes \boldsymbol{a}^{\alpha+} = \boldsymbol{a}^{\alpha+} \otimes \boldsymbol{a}^+_\alpha = \boldsymbol{Q}\boldsymbol{I}\boldsymbol{Q}^T. \tag{A.1}$$

Then, from (3-4) and (5-3) it can be shown that

$$\boldsymbol{L}^+ = \boldsymbol{v}^+_{,\alpha} \otimes \boldsymbol{a}^{\alpha+} = (\boldsymbol{Q}\boldsymbol{w}_\alpha + \boldsymbol{\Omega}\boldsymbol{a}^+_\alpha) \otimes \boldsymbol{a}^{\alpha+} = \boldsymbol{Q}\boldsymbol{L}\boldsymbol{Q}^T + \boldsymbol{\Omega}\boldsymbol{Q}\boldsymbol{I}\boldsymbol{Q}^T. \tag{A.2}$$

Also, using (5-2) it follows that

$$(\boldsymbol{\Omega}\boldsymbol{Q}\boldsymbol{I}\boldsymbol{Q}^T - \boldsymbol{Q}\boldsymbol{I}\boldsymbol{Q}^T\boldsymbol{\Omega})^T = (\boldsymbol{\Omega}\boldsymbol{Q}\boldsymbol{I}\boldsymbol{Q}^T - \boldsymbol{Q}\boldsymbol{I}\boldsymbol{Q}^T\boldsymbol{\Omega}), \tag{A.3}$$

which verifies (5-4).

Next, using (5-4) and (A.1) it can be shown that

$$\begin{aligned}
\boldsymbol{D}^+ \cdot \boldsymbol{I}^+ &= [\boldsymbol{Q}\boldsymbol{D}\boldsymbol{Q}^T + \tfrac{1}{2}(\boldsymbol{\Omega}\boldsymbol{Q}\boldsymbol{I}\boldsymbol{Q}^T - \boldsymbol{Q}\boldsymbol{I}\boldsymbol{Q}^T\boldsymbol{\Omega})] \cdot \boldsymbol{Q}\boldsymbol{I}\boldsymbol{Q}^T, \\
\boldsymbol{D}^+ \cdot \boldsymbol{I}^+ &= \boldsymbol{D} \cdot \boldsymbol{I} + \tfrac{1}{2}\boldsymbol{\Omega} \cdot \boldsymbol{Q}\boldsymbol{I}\boldsymbol{Q}^T(\boldsymbol{Q}\boldsymbol{I}\boldsymbol{Q}^T)^T - \tfrac{1}{2}\boldsymbol{\Omega} \cdot (\boldsymbol{Q}\boldsymbol{I}\boldsymbol{Q}^T)^T\boldsymbol{Q}\boldsymbol{I}\boldsymbol{Q}^T, \\
\boldsymbol{D}^+ \cdot \boldsymbol{I}^+ &= \boldsymbol{D} \cdot \boldsymbol{I} + \tfrac{1}{2}(\boldsymbol{\Omega} - \boldsymbol{\Omega}) \cdot \boldsymbol{Q}\boldsymbol{I}\boldsymbol{Q}^T = \boldsymbol{D} \cdot \boldsymbol{I}.
\end{aligned} \tag{A.4}$$

It then follows that the invariance properties (5-5) for $\{\rho, J\}$ are consistent with proper invariance under SRBM of the evolution equation (3-15) and the conservation of mass equation (3-16). Moreover, using (5-1) and (5-5) it can be shown that

$$\begin{aligned}
\operatorname{inv}(\boldsymbol{B}_d'^+) &= \boldsymbol{Q}\operatorname{inv}(\boldsymbol{B}_d')\boldsymbol{Q}^T, \\
\operatorname{inv}(\boldsymbol{B}_d'^+) \cdot \boldsymbol{I}^+ &= \boldsymbol{Q}\operatorname{inv}(\boldsymbol{B}_d')\boldsymbol{Q}^T \cdot (\boldsymbol{Q}\boldsymbol{I}\boldsymbol{Q}^T) = \operatorname{inv}(\boldsymbol{B}_d') \cdot \boldsymbol{I},
\end{aligned} \tag{A.5}$$

so with the help of (4-4) it follows that

$$\boldsymbol{A}_d^+ = \boldsymbol{B}_d'^+ - \left[\frac{2}{\operatorname{inv}(\boldsymbol{B}_d'^+) \cdot \boldsymbol{I}^+}\right]\boldsymbol{I}^+ = \boldsymbol{Q}\boldsymbol{A}_d\boldsymbol{Q}^T. \tag{A.6}$$

Next, use is made of (5-4) and (5-5) to deduce that

$$\begin{aligned}
\boldsymbol{L}^+\boldsymbol{B}'^+ + \boldsymbol{B}'^+\boldsymbol{L}^{+T} - (\boldsymbol{D}^+ \cdot \boldsymbol{I}^+)\boldsymbol{B}'^+ &= \boldsymbol{Q}[\boldsymbol{L}\boldsymbol{B}' + \boldsymbol{B}'\boldsymbol{L}^T - (\boldsymbol{D} \cdot \boldsymbol{I})\boldsymbol{B}']\boldsymbol{Q}^T + \boldsymbol{\Omega}\boldsymbol{B}'^+ - \boldsymbol{B}'^+\boldsymbol{\Omega}, \\
\boldsymbol{L}^+\boldsymbol{B}_d'^+ + \boldsymbol{B}_d'^+\boldsymbol{L}^{+T} - (\boldsymbol{D}^+ \cdot \boldsymbol{I}^+)\boldsymbol{B}_d'^+ &= \boldsymbol{Q}[\boldsymbol{L}\boldsymbol{B}_d' + \boldsymbol{B}_d'\boldsymbol{L}^T - (\boldsymbol{D} \cdot \boldsymbol{I})\boldsymbol{B}_d']\boldsymbol{Q}^T + \boldsymbol{\Omega}\boldsymbol{B}_d'^+ - \boldsymbol{B}_d'^+\boldsymbol{\Omega}.
\end{aligned} \tag{A.7}$$

Then, with the help of (5-2) and (5-5) it can be shown that

$$\frac{d}{dt}(\boldsymbol{B}'^+) = \boldsymbol{Q}\dot{\boldsymbol{B}}'\boldsymbol{Q}^T + \boldsymbol{\Omega}\boldsymbol{B}'^+ - \boldsymbol{B}'^+\boldsymbol{\Omega}, \quad \frac{d}{dt}(\boldsymbol{B}_d'^+) = \boldsymbol{Q}\dot{\boldsymbol{B}}_d'\boldsymbol{Q}^T + \boldsymbol{\Omega}\boldsymbol{B}_d'^+ - \boldsymbol{B}_d'^+\boldsymbol{\Omega}, \tag{A.8}$$

which can be used together with (A.4) to deduce that the evolution equations (4-2) for $\boldsymbol{B}'$ and (4-5) for $\boldsymbol{B}_d'$ are properly invariant under SRBM.

The invariance properties (5-5) for $\boldsymbol{T}$ follow directly from the constitutive equations (4-10). Next, using (3-17), (5-3) and (5-5) it follows that

$$\operatorname{div}^+(\boldsymbol{T}^+) = a^{-1/2}(a^{1/2}\boldsymbol{T}^+\boldsymbol{a}^{\alpha+})_{,\alpha} = \boldsymbol{Q}\operatorname{div}(\boldsymbol{T}), \tag{A.9}$$

which with the help of (5-5) can be used to show that the balance of linear momentum (3-16) is properly invariant under SRBM.

References

[Atai and Steigmann 2014] A. A. Atai and D. J. Steigmann, "Transient elastic-viscoplastic dynamics of thin sheets", *J. Mech. Mater. Struct.* **9**:5 (2014), 557–574.

[Bertram 2005] A. Bertram, *Elasticity and plasticity of large deformations: An introduction*, Springer, Heidelberg, 2005.

[Bilby 1960] B. A. Bilby, "Continuous distributions of dislocations", pp. 329–398 in *Progress in solid mechanics, I*, edited by I. N. Sneddon and R. Hill, North-Holland, Amsterdam, 1960.

[Chater and Neale 1983a] E. Chater and K. W. Neale, "Finite plastic deformation of a circular membrane under hydrostatic pressure, I: Rate-independent behaviour", *Int. J. Mech. Sci.* **25**:4 (1983), 219–233.

[Chater and Neale 1983b] E. Chater and K. W. Neale, "Finite plastic deformation of a circular membrane under hydrostatic pressure, II: Strain-rate effects", *Int. J. Mech. Sci.* **25**:4 (1983), 235–244.

[Cristescu 1967] N. Cristescu, *Dynamic plasticity*, Applied Mathematics and Mechanics **4**, North-Holland, Amsterdam, 1967.

[Eckart 1948] C. Eckart, "The thermodynamics of irreversible processes, IV: The theory of elasticity and anelasticity", *Phys. Rev.* **73** (1948), 373–382.

[Flory 1961] P. J. Flory, "Thermodynamic relations for high elastic materials", *Trans. Faraday Soc.* **57** (1961), 829–838.

[Green and Naghdi 1965] A. E. Green and P. M. Naghdi, "A general theory of an elastic-plastic continuum", *Arch. Ration. Mech. Anal.* **18**:4 (1965), 251–281.

[Hill 1950] R. Hill, *The mathematical theory of plasticity*, Oxford Univ. Press, 1950.

[Hill and Storåkers 1980] R. Hill and B. Storåkers, "Plasticity and creep of pressurized membranes: A new look at the small-deflection theory", *J. Mech. Phys. Solids* **28**:1 (1980), 27–48.

[Hollenstein et al. 2013] M. Hollenstein, M. Jabareen, and M. B. Rubin, "Modeling a smooth elastic-inelastic transition with a strongly objective numerical integrator needing no iteration", *Comput. Mech.* **52**:3 (2013), 649–667. Erratum in **55** (2015), p. 453.

[Ilahi and Paul 1985] M. F. Ilahi and T. K. Paul, "Hydrostatic bulging of a circular soft brass diaphragm", *Int. J. Mech. Sci.* **27**:5 (1985), 275–280.

[Kröner 1960] E. Kröner, "Allgemeine kontinuumstheorie der versetzungen und eigenspannungen", *Arch. Ration. Mech. Anal.* **4**:1 (1960), 273–334.

[Lee 1969] E. H. Lee, "Elastic-plastic deformation at finite strains", *J. Appl. Mech.* (*ASME*) **36**:1 (1969), 1–6.

[Leonov 1976] A. I. Leonov, "Nonequilibrium thermodynamics and rheology of viscoelastic polymer media", *Rheol. Acta* **15**:2 (1976), 85–98.

[Lubliner 1990] J. Lubliner, *Plasticity theory*, Macmillan, New York, 1990.

[Malvern 1951] L. E. Malvern, "The propagation of longitudinal waves of plastic deformation in a bar of material exhibiting a strain-rate effect", *J. Appl. Mech.* (*ASME*) **18** (1951), 203–208.

[Naghdi 1972] P. M. Naghdi, "The theory of shells and plates", pp. x+745 in *Handbuch der Physik, VIa/2: Festkörpermechanik II*, edited by C. Truesdell, Springer, Berlin, 1972.

[Papes 2012] O. Papes, *Nonlinear continuum mechanics in modern engineering applications*, Ph.D. thesis, ETH Zurich, 2012. DISS ETH NO 19956.

[Perzyna 1963] P. Perzyna, "The constitutive equations for rate sensitive plastic materials", *Quart. Appl. Math.* **20** (1963), 321–332.

[Rubin 1994] M. B. Rubin, "Plasticity theory formulated in terms of physically based microstructural variables, I: Theory", *Int. J. Solids Struct.* **31**:19 (1994), 2615–2634.

[Rubin 2000] M. B. Rubin, *Cosserat theories: Shells, rods and points*, Solid Mechanics and its Applications **79**, Kluwer, The Netherlands, 2000.

[Rubin 2012] M. B. Rubin, "Removal of unphysical arbitrariness in constitutive equations for elastically anisotropic nonlinear elastic-viscoplastic solids", *Int. J. Eng. Sci.* **53** (2012), 38–45.

[Rubin 2015] M. B. Rubin, "A viscoplastic model for the active component in cardiac muscle", *Biomech. Model. Mechanobiol.* (online publication October 2015).

[Rubin and Attia 1996] M. B. Rubin and A. Attia, "Calculation of hyperelastic response of finitely deformed elastic-viscoplastic materials", *Int. J. Numer. Methods Eng.* **39**:2 (1996), 309–320.

[Rubin and Papes 2011] M. B. Rubin and O. Papes, "Advantages of formulating evolution equations for elastic-viscoplastic materials in terms of the velocity gradient instead of the spin tensor", *J. Mech. Mater. Struct.* **6**:1–4 (2011), 529–543.

[Simo 1992] J. C. Simo, "Algorithms for static and dynamic multiplicative plasticity that preserve the classical return mapping schemes of the infinitesimal theory", *Comput. Methods Appl. Mech. Eng.* **99**:1 (1992), 61–112.

[Simo and Hughes 1998] J. C. Simo and T. J. R. Hughes, *Computational inelasticity*, Interdisciplinary Applied Mathematics **7**, Springer, New York, 1998.

[Storåkers 1966] B. Storåkers, "Finite plastic deformation of a circular membrane under hydrostatic pressure", *Int. J. Mech. Sci.* **8**:10 (1966), 619–628.

Received 8 Jul 2015. Revised 29 Nov 2015. Accepted 4 Dec 2015.

M. B. RUBIN: mbrubin@tx.technion.ac.il
Faculty of Mechanical Engineering, Technion – Israel Institute of Technology, 32000 Haifa, Israel

BEN NADLER: bnadler@me.uvic.ca
Department of Mechanical Engineering, University of Victoria, Victoria, BC V8W 3P6, Canada

JOURNAL OF MECHANICS OF MATERIALS AND STRUCTURES
Vol. 11, No. 3, 2016
dx.doi.org/10.2140/jomms.2016.11.217

msp

PHYSICAL MEANING OF ELASTIC CONSTANTS IN COSSERAT, VOID, AND MICROSTRETCH ELASTICITY

RODERIC S. LAKES

The physical meaning of Cosserat, void, and microstretch elastic constants is analyzed and interpreted. Various torsion experiment designs provide a clear path to extract Cosserat elastic constants independently of any dilatation gradient sensitivity the material may have. For void elasticity (with sensitivity to dilatation gradients) there is no known quasistatic modality to demonstrate phenomena or extract elastic constants independently of any sensitivity to rotation gradients. Wave methods may be appropriate if there is minimal viscoelastic dispersion. Microstretch elasticity, which includes sensitivity to gradients of rotation and of dilatation could account for bending effects larger than those of Cosserat elasticity.

1. Introduction

The amount of freedom embodied in a theory of elasticity is not imposed by the requirement of mathematical consistency. For example, the early uniconstant elasticity theory of Navier [Timoshenko 1983] has only one elastic constant and Poisson's ratio must be $\frac{1}{4}$ for all materials. This theory is based upon the assumption that forces act along the lines joining pairs of atoms and are proportional to changes in distance between them. This theory was abandoned based on *experiment* that showed materials exhibit various values of Poisson's ratio. Classical elasticity has two independent elastic constants for isotropic materials; the Poisson's ratio can have values between -1 and 0.5. Cosserat elasticity [Cosserat and Cosserat 1909; Mindlin 1965] (micropolar [Eringen 1968] if one incorporates an inertia term) has more freedom than classical: points can rotate as well as translate; an isotropic material has six elastic constants. The microstructure elasticity theory of Mindlin [1964], also called micromorphic elasticity, has even more freedom; it allows points in the continuum to translate, rotate, and deform. This adds considerable complexity; for an isotropic micromorphic solid, there are 18 elastic constants. One can also incorporate a local dilatation variable [Cowin and Nunziato 1983] as done in void elasticity (five elastic constants) or combine a dilatation variable with Cosserat elasticity as in microstretch elasticity [Eringen 1990] (nine elastic constants). In nonlocal elasticity, stress at a point depends explicitly on strain in a region around that point [Kröner 1967]. Nonlocal integrals have been approximated as a differential form [Eringen 1983] that entails a simple sensitivity to strain gradients; such gradient approximations have been used and called nonlocal.

The rationale for using a generalized continuum theory with complexity greater than that in classical elasticity is to enable one to interpret phenomena associated with nonzero size of material microstructure and to correctly make predictions of stress and strain fields when gradients of stress or strain are present. There is no length scale in classical elasticity. Length scales do occur in the definition of fracture

We gratefully acknowledge support of this research by the National Science Foundation via Grant CMMI-1361832.
Keywords: Cosserat, microstretch, void theory, generalized continuum.

toughness. Also, toughness of foams is related to the size scale of the cells in the foam [Gibson and Ashby 1997]. Stress concentrations such as holes and cracks entail large gradients of strain. Generalized continuum theories predict stress concentration factors that differ from those of classical elasticity. Understanding the robustness of heterogeneous materials can benefit from a generalized continuum approach. In composite materials and in biological materials, structural length scales may be nonnegligible in comparison with length scales associated with heterogeneity of stress around stress concentrations or in experiments in torsion or bending or indentation. In any material at the nanoscale, length scales in the material's fine structure are likely to be nonnegligible in comparison with specimen size. In such cases, classical elasticity is unlikely to suffice for adequate predictions.

In a review of experimental methods for Cosserat solids [Lakes 1995a]; Cosserat elasticity was compared with other generalized continuum theories, especially nonlocal elasticity; microstretch elasticity was not considered. More recently, microstretch elasticity has become a topic of interest. Also, our laboratory has recently observed evidence of strong Cosserat effects in reticulated foam [Rueger and Lakes 2016a] and in negative Poisson's ratio foam [Rueger and Lakes 2016b]. In this article, elastic constants in several generalized continuum theories are analyzed and elucidated. First the theories are presented, compared and discussed. Predictions of behavior are presented with interpretation of elastic constants. Prior experiments are reviewed and guide for future experiments is provided.

2. Cosserat elasticity

Of the generalized continuum theories, Cosserat elasticity has been the most thoroughly studied. The Cosserat theory of elasticity [Cosserat and Cosserat 1909; Mindlin 1965] incorporates a local rotation of points as well as the translation of points in classical elasticity. In addition to the stress (force per unit area) in classical elasticity, Cosserat elasticity incorporates a couple stress (a torque per unit area). Eringen [1968] added a local inertia term called microinertia and renamed Cosserat elasticity micropolar elasticity. At frequencies low enough that local resonances are not approached, Cosserat and micropolar are used interchangeably.

The physical origin of the Cosserat couple stress is the summation of bending and twisting moments transmitted by structural elements in materials. The local rotation corresponds to the rotation of structural elements.

The Cosserat theory of elasticity is a *continuum* theory that entails a type of nonlocal interaction. The stress σ_{ij} (force per unit area) can be asymmetric. The distributed moment from this asymmetry is balanced by a couple stress m_{ij} (a torque per unit area). Cosserat elasticity incorporates a microrotation vector ϕ_i that is kinematically distinct from the macrorotation vector $r_i = (e_{ijk}u_{k,j})/2$. ϕ_i refers to the rotation of points, while r_i refers to the rotation associated with translation motion of nearby points; e_{ijk} is the permutation symbol; $\epsilon_{ij} = (u_{i,j} + u_{j,i})/2$ is the small strain tensor. The antisymmetric part of the stress is related to rotations. $\sigma_{ij}^{\text{antisym}} = \kappa e_{ijm}(r_m - \phi_m)$ in which κ is an elastic constant. The constitutive equations [Eringen 1968] for linear isotropic Cosserat elasticity are

$$\sigma_{ij} = 2G\epsilon_{ij} + \lambda\epsilon_{kk}\delta_{ij} + \kappa e_{ijk}(r_k - \phi_k), \tag{1}$$

$$m_{ij} = \alpha\phi_{k,k}\delta_{ij} + \beta\phi_{i,j} + \gamma\phi_{j,i}, \tag{2}$$

where λ and G are classical elastic moduli. The physical meaning of G is clear; it is the shear modulus

used in engineering and represents a material stiffness for shear deformation. The physical meaning of λ is $\lambda = C_{12}$, the elastic modulus component [Sokolnikoff 1983] which couples strain in one direction with stress in an orthogonal direction, with all other strains held constant. Further, $\lambda = B - \frac{2}{3}G$, with B as the bulk modulus. The remaining four of the six isotropic Cosserat elastic constants are α, β, γ which provide sensitivity to rotation gradient; κ is a modulus that quantifies the degree of coupling between macro and micro rotation fields. The following technical elastic constants [Gauthier and Jahsman 1975] facilitate physical interpretation:

$$\text{Young's modulus} \qquad E = \frac{G(3\lambda + 2G)}{\lambda + G}, \tag{3}$$

$$\text{Shear modulus} \qquad G, \tag{4}$$

$$\text{Poisson's ratio} \qquad \nu = \frac{\lambda}{2(\lambda + G)}, \tag{5}$$

$$\text{Characteristic length, torsion} \qquad \ell_t = \sqrt{\frac{\beta + \gamma}{2G}}, \tag{6}$$

$$\text{Characteristic length, bending} \qquad \ell_b = \sqrt{\frac{\gamma}{4G}}, \tag{7}$$

$$\text{Coupling number} \qquad N = \sqrt{\frac{\kappa}{2G + \kappa}}, \tag{8}$$

$$\text{Polar ratio} \qquad \Psi = \frac{\beta + \gamma}{\alpha + \beta + \gamma}. \tag{9}$$

The Young's modulus, shear modulus, and Poisson's ratio are the values observable in experiments that impose uniform stress without any gradient [Gauthier and Jahsman 1975]. The characteristic lengths appear in analyses of torsion and bending [loc.cit.]; structural rigidity increases as the thickness of a rod or plate assume a sufficiently small multiple of the characteristic length. The coupling number N is a dimensionless measure of the degree of coupling between the rotation and displacement fields. The limit $N = 1$ corresponds to "couple stress elasticity". The dimensionless polar ratio (of rotation sensitivity moduli) is analogous to Poisson's ratio in classical elasticity. We remark that a parameter $\delta = N/\ell_b$ was used in an analysis of bending of a circular cylinder [Krishna Reddy and Venkatasubramanian 1978] of a Cosserat solid. Further, Eringen [1968] used $\mu + \kappa/2$ to represent the shear modulus G observed in the absence of gradients. Because that causes μ to differ from the observed shear modulus contrary to the usual interpretation, we do not use that notation.

Limits on elastic constants imposed by energy considerations [Gauthier and Jahsman 1975] are $G > 0$, $B > 0$, $\ell_b > 0$, $\ell_t > 0$, $0 < N < 1$, $0 < \Psi < 3/2$, $-1 < \beta/\gamma < 1$.

3. Microstretch elasticity

The microstructure elasticity theory of Mindlin [1964] allows points to deform as well as to translate as in classical elasticity and to rotate as in Cosserat elasticity. The theory allows a continuum interpretation of wave dispersion observed in crystal lattices. The points in the continuum may be envisaged as local unit cells of the physical microstructure. A relative deformation, the difference between gradient of

macroscopic displacement and microdeformation is defined. Strain energy arguments couple relative deformation to relative stress. The gradient of microdeformation is coupled to double stress which is a ratio of pairs of forces per area. Double stress includes the Cosserat couple stress. Microstructure elasticity requires 18 elastic constants for an isotropic material. The complexity of this theory presents challenges for interpretation.

Microstretch elasticity [Eringen 1990] is a subset of Mindlin microstructure [1964] / micromorphic elasticity. Microstretch elasticity is a generalized continuum representation that includes the rotation sensitivity of Cosserat elasticity and the sensitivity to dilatation gradient associated with void theory (Section 4). Microstretch elasticity was stated to be simpler than microstructure elasticity; indeed, it entails nine static isotropic elastic constants rather than 18. The constitutive equations for isotropic material at constant temperature are

$$\sigma_{ij} = 2G\epsilon_{ij} + (\lambda u_{k,k} + \lambda_0 \phi)\delta_{ij} + \kappa e_{ijk}(r_k - \phi_k), \tag{10}$$

$$m_{ij} = \alpha \phi_{k,k}\delta_{ij} + \beta \phi_{i,j} + \gamma \phi_{j,i}, \tag{11}$$

$$3s = \lambda_1 \phi + \lambda_0 u_{k,k}, \tag{12}$$

$$\lambda_k = a_0 \phi_{,k}. \tag{13}$$

Here λ_k is called an internal traction that causes local dilatation [Eringen 1990]; it is also called an equilibrated stress vector [Cowin and Nunziato 1983]; λ_k is the dilatational component of double stress [Mindlin 1964] which Eringen calls first stress moments. Double stress refers to pairs of force per unit area; if the pair of forces generates a moment, then it is a couple stress. Variable s is the difference between the trace of a local stress and the trace of the true stress; it is also called intrinsic equilibrated body force [Cowin and Nunziato 1983]; u is displacement and ϕ represents a local dilatation variable, a change in volume fraction [Cowin and Nunziato 1983]. Observe that ϕ as a scalar has no relation to the local rotation vector ϕ_k in Cosserat elasticity.

Nonclassical contributions to the stress σ_{ij} include (i) an asymmetric contribution due to Cosserat rotation difference coupled via Cosserat κ and (ii) a hydrostatic contribution due to local dilatation ϕ coupled via the microstretch constant λ_0.

As for elastic constants, λ and G are classical elastic moduli, α, β, γ are Cosserat elastic constants that provide sensitivity to rotation gradient, and κ is a Cosserat elastic constant that quantifies the coupling between macro and micro rotation fields. New microstretch elastic constants include a_0, λ_0, and λ_1. Constant a_0 provides sensitivity to gradient of local dilatation, λ_0 is a microstretch modulus that couples dilatation variable change to stress and dilatation to equilibrated body force s, and λ_1 is a modulus that couples local dilatation variable ϕ to s.

As with Cosserat elasticity, characteristic lengths may be defined for microstretch elasticity. The most natural definition is in terms of a ratio of a nonclassical elastic constant to a classical one. So, we define a characteristic length in terms of the ratio of the gradient sensitivity constant to a classical modulus; C_{1111} is the constrained modulus tensor element.

$$\ell_m = \sqrt{\frac{3a_0}{C_{1111}}}. \tag{14}$$

In some analyses, more complex length parameters arise. For example in a study of bending [Ieşan and Nappa 1995] a variable ζ was defined with dimensions of inverse length.

$$\zeta = \sqrt{\frac{1}{3a_0}\left(\lambda_1 - \frac{\lambda_0^2}{\lambda + 2G}\right)}. \tag{15}$$

But $\lambda + 2G = C_{1111}$, the constrained modulus. So by analogy to Cosserat elasticity we define a coupling coefficient in terms of a ratio of generalized continuum moduli to a classical modulus.

$$N_m = \sqrt{\frac{\lambda_1 - \dfrac{\lambda_0^2}{\lambda + 2G}}{C_{1111}}} = \sqrt{\frac{\lambda_1}{C_{1111}} - \frac{\lambda_0^2}{C_{1111}^2}}. \tag{16}$$

So $\zeta = N_m/\ell_m$. So size effects in bending are influenced by the coupling parameter; this is analogous to a parameter $\delta = N/\ell_b$ that was used in an analysis of bending of a circular Cosserat cylinder [Krishna Reddy and Venkatasubramanian 1978]. In contrast to Cosserat elasticity, the observed value of C_{1111} even under uniform strain will be influenced by the dilatational degrees of freedom [Ieşan and Nappa 1995; Cowin and Nunziato 1983].

It is also expedient for simplification of bending size effect analysis to define

$$N_{m0} = \frac{\lambda_0}{C_{1111}}, \tag{17}$$

$$N_{m1} = \frac{\lambda_1}{C_{1111}}. \tag{18}$$

So $N_m = \sqrt{N_{m1} - N_{m0}^2}$.

Energy based limits on the elastic constants [Eringen 1990; Ieşan and Nappa 1995] include those for classical and Cosserat elasticity as well as $a_0 > 0$, $\lambda_1 > 0$, and

$$3\lambda + 2G - 3\frac{\lambda_0^2}{\lambda_1} > 0 \tag{19}$$

Equation (19) may be rewritten as

$$\frac{1}{3}\,\frac{1+\nu}{1-\nu} > \frac{N_{m0}^2}{N_{m1}} \quad \text{or} \quad N_{m1} > 3\,\frac{1-\nu}{1+\nu}\,N_{m0}^2.$$

For Poisson's ratio 0.3, the energy based limit implies $N_{m1} > 1.62N_{m0}^2$. Because $\lambda = B - \frac{2}{3}G$, (19) may also be written in terms of the bulk modulus B:

$$B - \frac{\lambda_0^2}{\lambda_1} > 0.$$

4. Void elasticity

Cosserat elasticity incorporates sensitivity to gradients of rotation by virtue of the coupling between rotations and stresses. It is also possible to supplement classical elasticity with sensitivity to gradients of dilatation alone via a generalized continuum theory containing a local dilatation variable suggested

Parameter	[Eringen 1990]	[Cowin and Nunziato 1983]	[Ieşan and Nappa 1995]
Dilatation gradient sensitivity	a_0	$\alpha_v/3$	σ
Microstretch modulus	λ_0	β_v	η
Internal modulus	λ_1	ξ	b
Microinertia	j	$\frac{2}{3}k$	–

Table 1. Symbols used by various authors.

to be associated with void volume change [Cowin and Nunziato 1983]. In contrast to Cosserat and microstretch elasticity there is no local rotation variable and no sensitivity to rotation gradient. This theory incorporates three elastic constants in addition to the usual two of classical isotropic elasticity. There is also a rate parameter that is omitted here because viscoelastic behavior can be incorporated in any generalized elasticity theory using the elastic viscoelastic correspondence principle which allows solutions to viscoelasticity problems to be obtained from known solutions of elasticity problems via Laplace or Fourier transforms [Alfrey 1944; Read 1950]. The constitutive equations for an isotropic material at constant temperature are

$$\sigma_{ij} = 2G\epsilon_{ij} + (\lambda\epsilon_{kk} + \beta_v\phi)\delta_{ij}, \tag{20}$$

$$h_i = \alpha_v\phi_{,i}, \tag{21}$$

$$g = -\xi\phi - \beta_v\epsilon_{kk}. \tag{22}$$

Cowin and Nunziato [1983] use α as a void elastic constant but that symbol is already used as a Cosserat constant (Equation (2)), so here it is called α_v. Similarly β_v is used for void theory to distinguish it from the Cosserat constant β. Comparing (20) and (10), via $u_{k,k} = \epsilon_{kk}$, the classical constant λ is seen in both; also, $\lambda_0 = \beta_v$. Cosserat type constants are present in microstretch elasticity and absent in void elasticity. Comparing (22) and (12), there is a factor -3 difference on the left side. We already have $\lambda_0 = \beta_v$ so the factor -3 cannot be in λ_1; it must be in g. One may presume that microstretch internal traction λ_k is the same as void equilibrated stress vector h_i; similarly it appears that microstretch equilibrated body force s in (12) corresponds to void intrinsic equilibrated body force g in (22). If that were the case, factors of 3 would appear in λ_0 and λ_1 compared with β_v and ξ. That would contradict the correspondence for the elastic constants from (20) and (10). So to avoid contradictions in elastic constants, we make the correspondences $3s = -g$ and $\alpha_v = 3a_0$.

An alternate coupling coefficient [Puri and Cowin 1985] which may be expressed

$$N_c = \frac{\beta_v^2}{\xi}\frac{1}{C_{1111}}$$

obeys $0 < N_c < 1$; it may also be written

$$N_c = \frac{N_{m0}^2}{N_{m1}}.$$

Aside from the difference in symbols (Table 1), the void theory is equivalent to microstretch elasticity with the Cosserat type constants α, β, γ, κ set to zero. A comparison of symbols for Cosserat elasticity was given in [Cowin 1970].

5. Predictions and experiments

5.1. ***Cosserat elasticity.*** The Cosserat theory has been explored the most extensively. For example, a size effect is predicted in the torsion [Gauthier and Jahsman 1975] and bending [Krishna Reddy and Venkatasubramanian 1978] of circular cylinders of Cosserat elastic solids. Thin cylinders are more structurally rigid than expected classically. A stiffening-type size effect is also predicted in the bending of plates [Gauthier and Jahsman 1975]. No size effect is predicted in tension. By contrast, in classical elastic solids, there is no size effect in torsion or bending; structural rigidity is proportional to the fourth power of the radius. Detailed plots of size effects are available [Gauthier and Jahsman 1975; Krishna Reddy and Venkatasubramanian 1978] so they are omitted here. Size effects of large magnitude are possible in torsion if $N \to 1$ or if Ψ is well below its upper limit of 1.5.

The stress concentration factor for a circular hole in a thin Cosserat plate is smaller than the classical value, and small holes exhibit less stress concentration than larger ones [Mindlin 1963]. By contrast, the classical stress concentration around a hole is independent of hole size. Strain is redistributed in other situations as well. For example, warp in torsion of a bar of rectangular cross section is less in a Cosserat elastic solid than in a classical elastic solid [Park and Lakes 1987]. The deformation in bending is also altered in Cosserat solids: sigmoid curvature of the lateral surfaces of square cross section bars of Cosserat solids is predicted [Lakes and Drugan 2015]. As for plane waves in a Cosserat solid, shear waves travel faster at higher frequency; longitudinal waves propagate without frequency dependence. There is no prediction of a cut-off frequency for any waves in Cosserat elasticity.

5.2. ***Void and microstretch elasticity.*** We consider these theories together because microstretch elasticity is a superposition of void elasticity and Cosserat elasticity. Some predictions are available for void and microstretch theories.

As for tension/compression, analysis of a uniform stress field reveals that the effective constrained modulus is reduced by the presence of the void degree of freedom [Cowin and Nunziato 1983]; specifically,

$$C_{1111}^{\text{effective}} = C_{1111} - \left(\frac{\lambda_0^2}{\lambda_1}\right) = C_{1111}\left(1 - \frac{N_{m0}^2}{N_{m1}}\right). \tag{23}$$

The modulus that would be observed in an experiment is $C_{1111}^{\text{effective}}$. It is claimed [Cowin and Nunziato 1983] that one can measure some of the additional elastic constants if the experimenter has an independent method to measure the volume change associated with voids. The difficulty with such an approach is that one cannot necessarily assume that the void / local dilatation degree of freedom in the continuum theory corresponds directly to the concentration of physical voids in a laboratory specimen. Indeed, these generalized continuum degrees of freedom were explored in a homogenization analysis [Eringen 1990; 1998] of a mass-spring system in the study of waves; there are no voids in a mass-spring system. Tension was also studied analytically in microstretch elasticity [Ieşan and Nappa 1995]. As is the case with Cosserat elasticity, size effects are predicted not to occur in tension. The predicted effective Young's modulus in tension is reduced by the microstretch variables [loc. cit.] so the classical moduli no longer have the same meaning as in classical or Cosserat elasticity. Similarly the Poisson's ratio is changed by the microstretch variables [Ieşan and Nappa 1995]. This situation is analogous to the use [Eringen 1968] in Cosserat elasticity of $\mu + \kappa/2$ to represent the shear modulus G observed in the absence of gradients.

The difficulty with such notation is that μ is used in elasticity theory to represent the observed shear modulus and it no longer represents the shear modulus when used as above. We avoid the potential for confusion by using G to represent the shear modulus in Cosserat elasticity.

Size effects arise due to sensitivity to dilatation gradient [Cowin and Nunziato 1983]. Size effects are predicted in bending but not in torsion. This bending analysis [loc. cit.] allowed surface tractions on the lateral surfaces, so it does not represent an exact solution for bending. It is not obvious whether the size effect represents stiffening or softening. Stress concentration around a small hole is predicted to be larger than for a large hole [Cowin 1984] and the stress concentration factor is larger than the value predicted by classical elasticity. This is the opposite effect of Cosserat elasticity. Too, the velocity of longitudinal waves increases with frequency but shear waves are not affected. The generalized continuum theory of voids is in contrast to the classic Biot theory [Biot 1941] which analyzes the stress-induced pressure and flow of fluids between communicating pores in the solid. Void theory does not contain such physics, but it does allow sensitivity to gradients.

Void theory predicts bending size effects [Cowin and Nunziato 1983] for a bar of width h; the result of the approximate analysis is here considerably simplified in terms of a dimensionless ratio J. A length parameter $\ell_0 = \ell_m/N_m$ with $N_m = \sqrt{N_{m1} - N_{m0}^2}$ as above was used in the analysis [loc. cit.].

$$J = \left(\frac{N_{m0}^2}{N_{m1} - N_{m0}^2}\right)\left(\frac{1-2\nu}{1+\nu}\right)\left(1 - 3\left(\frac{\ell_0}{h}\right)^3\left(\frac{h}{\ell_0} - \tanh\left(\frac{h}{\ell_0}\right)\right)\right). \tag{24}$$

The rigidity ratio Ω is the ratio of bend rigidity in void elasticity to bend rigidity in classical elasticity.

$$\Omega = \frac{1-J}{1-\frac{1}{2}J(1+\nu)}. \tag{25}$$

Stiffening size effects in bending are possible as shown in Figure 1. Curves are for $\nu = 0.3$, $N_{m0} = 1$; $N_{m1} = 1.65, 2, 3$.

Size effects are not of large magnitude in this series, even for elastic constants approaching the stability limit of (19). This is in contrast with Cosserat elasticity in which large size effects are possible and are observed.

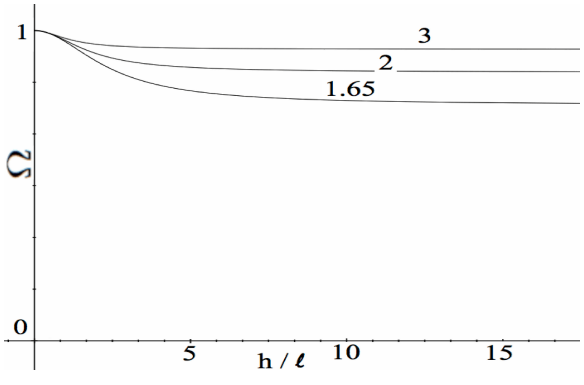

Figure 1. Bending size effect for void theory; normalized rigidity Ω versus normalized specimen thickness h/ℓ_m, for $\nu = 0.3$, $N_{m0} = 1$; $N_{m1} = 1.65, 2, 3$.

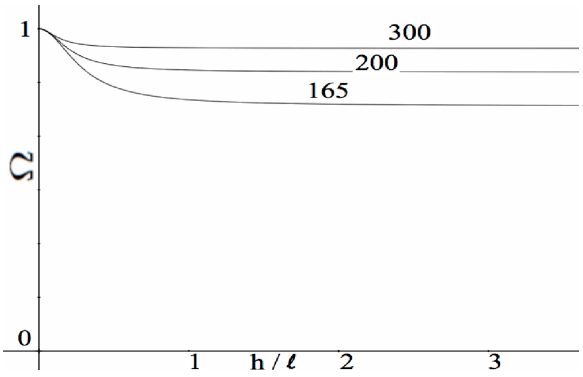

Figure 2. Bending size effect for void theory; normalized rigidity Ω vs. normalized specimen thickness h/ℓ_m, for $\nu = 0.3$, $N_{m0} = 10$; $N_{m1} = 165, 200, 300$.

If larger N values are assumed, $N_{m0} = 10$; $N_{m1} = 165, 200, 300$, corresponding to λ_0 larger than C_{1111}, size effects are shown in Figure 2. Again, size effects are not of large magnitude, in contrast with Cosserat elasticity. All size effects explored within this solution entail increasing apparent modulus as thickness is reduced.

The lowest of the size effect curves corresponds to ratios of elastic constants approaching the stability limit, (19), but the stiffness does not tend to zero anywhere. The limit from the denominator in (24) to be positive and nonzero is $N_{m1} > N_{m0}^2$. This is less stringent than the energy limit (19) for Poisson's ratio 0.3; for Poisson's ratio 0.5 they are equivalent.

The nature of the instability mode must be found elsewhere. The void theory stability limit of Cowin and Nunziato [1983] $3\lambda + 2G - 12\beta_v^2/\xi > 0$ differs from that of [Eringen 1990], (19), by a factor of four in the last term. The origin of the disparity is unknown.

As for microstretch elasticity, a complicated exact solution for tension and for bending of a circular cylinder was presented [Ieşan and Nappa 1995]; this is much more complicated than the corresponding exact solution [Krishna Reddy and Venkatasubramanian 1978] for bending in Cosserat elasticity. It is not obvious whether this microstretch size effect represents stiffening or softening.

5.3. ***Determination of Cosserat elastic constants by experiment.*** Measurements of torsional size effects is sufficient to demonstrate the presence of Cosserat effects because there is no dilatation or dilatation gradient; void elasticity predicts no size effects in torsion. If the material is a Cosserat solid or a microstretch solid, torsional size effect measurements, if done over a sufficient range in specimen diameter, allow extraction of four of the elastic constants, specifically the shear modulus G, characteristic length in torsion ℓ_t, coupling number N and polar ratio Ψ. One obtains G via a pure shear test without gradient or a torsion test on a sufficiently large specimen or from an asymptote at large diameter in torsion size effect curve. The characteristic length ℓ_t is obtained via size effects in torsion of rods of different radius r for relatively large specimens via the approximate solution for the rigidity ratio

$$\Omega \approx 1 + 6(\ell_t/r)^2. \tag{26}$$

The full Bessel function solution [Gauthier and Jahsman 1975] is required to obtain N from size effects on smaller specimens and also Ψ from yet smaller specimens. Such inference is valid for a Cosserat solid

or a microstretch solid; there is no dilatation in torsion, hence no effect of dilatation gradients. If the material is a Cosserat solid, Young's modulus E can be obtained from simple tension or compression experiments or from or from an asymptote at large size in a bending size effect curve. Bending of a plate to a cylindrical shape via controlled moments on all edges reveals ℓ_b independently of other constants provided one bends plates of various thickness [loc. cit.]. Bending of the same circular rod used for torsion can also be used to obtain ℓ_b with confirmation of N via a somewhat more complex procedure using a solution [Krishna Reddy and Venkatasubramanian 1978] containing Bessel functions. So, for Cosserat solids, measurement of size effects in both bending and torsion suffice to determine all six elastic constants. If the material is a microstretch solid, then bending size effects will contain a Cosserat (rotation gradient) and a dilatation gradient contribution; there are then too many elastic constants to extract them from a single curve.

Cosserat elastic effects have been observed experimentally. Torsion and bending studies on closed cell foams [Lakes 1986; Anderson and Lakes 1994] and of compact bone [Lakes 1995b] reveal size effects consistent with Cosserat elasticity. The apparent modulus increases substantially as the specimen diameter becomes smaller. This is in contrast to the predictions of classical elasticity. For dense (340 kg/m^3) closed cell polyurethane foam [Lakes 1986], $E = 300$ MPa, $G = 104$ MPa, $\nu = 0.4$, $\ell_t = 0.62$ mm, $\ell_b = 0.33$ mm, $N^2 = 0.04$, $\Psi = 1.5$. The cell size is from 0.05 mm to 0.15 mm. For dense (380 kg/m^3) polymethacrylamide closed cell foam (Rohacell WF300) [Anderson and Lakes 1994], $E = 637$ MPa, $G = 285$ MPa, $\ell_t = 0.8$ mm, $\ell_b = 0.77$ mm, $N^2 \approx 0.04$, $\Psi = 1.5$. The cell size is about 0.65 mm. The Cosserat characteristic length was also determined in a (two dimensional) polymer honeycomb [Mora and Waas 2000].

Full field measurements of deformation of square section bars in torsion have been conducted to ascertain the predictive ability of Cosserat elasticity. Warp of a bar of rectangular cross section in torsion is predicted to be reduced in a Cosserat elastic solid [Park and Lakes 1987]. The corresponding strain field was observed in compact bone [Park and Lakes 1986]; the nonclassical effects observed were in agreement with predictions based on Cosserat constants obtained from size effects observed in separate experiments on circular cylinders. Deformation spills over into the corner of the square section where it would be zero in classical elasticity [Lakes et al. 1985] as revealed by holography. Such strain redistribution ameliorates concentration of strain. Strain at the corner of the section entails asymmetry of the stress as is predicted by Cosserat elasticity. The corresponding reduction of warp deformation of square section bars of dense foam has been observed via holography [Anderson et al. 1995]. The strain field in bending is also altered in Cosserat solids. Sigmoid curvature of the lateral surfaces of bent square cross section bars of open cell foam was observed experimentally and predicted theoretically via Cosserat elasticity [Lakes and Drugan 2015].

Wave methods could be used for Cosserat solids provided the material has minimal viscoelastic damping. In viscoelastic materials, the dispersion (frequency dependence of velocity) increases with damping. Cosserat elasticity predicts increase of shear wave velocity with frequency [Eringen 1968]; dispersion due to viscoelasticity would be a confounding variable.

5.4. ***Determination of microstretch elastic constants by experiment.*** No known experimental results are available for void or microstretch elasticity. However homogenization analysis of a one dimensional mass-spring system was used to calculate the dilatation elastic constants [Eringen 1998] and

homogenization analyses of lattices of ribs are available for Cosserat elasticity. In this section the prospects for such experiments are explored. Void elasticity predicts size effects in bending but not in torsion. At first sight such an observation would appear as a clear signature of a void elastic solid, i.e., a microstretch solid with dilatational degrees of freedom but not rotational degrees of freedom. However such an effect could also occur in a Cosserat solid (Equation (2)) if β/γ = -1, the lower limit allowed by energy considerations. If there is reason to infer a larger β/γ, either from the shape of the bending size effect curves or from comparison with other experiments or from homogenization analysis, then a microstretch dilatation gradient contribution is to be suspected. Such size effects do not suffice for the calculation of all the elastic constants of a microstretch solid; there are too many constants to extract from one curve.

Configurations sensitive only to dilatation gradient, not to rotation gradient, are available. For example static pressurization of a hollow cylinder or sphere will generate a gradient in strain without the rotations that would drive Cosserat effects. Solutions are available for the cylindrical and spherical thick wall pressure vessel problems for a material obeying void elasticity [Cowin 1983]. The stress field is not affected by the void degrees of freedom but the displacements are altered giving rise to a larger structural compliance. Curiously the gradient sensitivity parameter α_v hence the characteristic length, does not enter the final solution for the displacements. So the reduction in structural rigidity is similar to that predicted (Equation (23)) for uniform compression, in that there is a change in effective stiffness but no gradient sensitivity parameter α_v. The classical displacement field for the hollow sphere contains r and $1/r^2$ terms with the latter coupled via the shear modulus. The void contribution to displacement contains only an r term; similarly the dilatation variable ϕ is independent of r. This is not promising for experiments based on size effects. In any case, experiments of this or related type are likely to be more difficult than bending or torsion, particularly if the specimen is porous and permeable as with open cell foams.

The presence of dilatation sensitive elastic effects may be studied with waves. As with void theory, microstretch elasticity admits two kinds of longitudinal waves [Eringen 1998]. A cut off frequency phenomenon is predicted: at sufficiently high frequency, the wave speed drops to zero. Viscoelasticity cannot account for such an effect; the effect of viscoelasticity is an increase of wave speed with frequency. Beyond the cut off frequency, no waves propagate. The cut-off angular frequency is

$$\omega_{cr} = \sqrt{\frac{2\lambda_1}{\rho j}},$$

with j as microinertia and ρ as density [Eringen 1998]. While it is suggested that measurement of this frequency enables extraction of the elastic constant λ_1, the microinertia is not known a priori. It has dimensions of length squared. The constant λ_0 is also needed to interpret size effect studies; the wave cut off frequency has λ_1 but does not reveal λ_0 or a_0 which provides sensitivity to gradient of local dilatation. Experimental results are available for dispersion and cut off frequencies in open cell foam [Chen and Lakes 1989]. These experiments were interpreted in the context of structural vibration of cell ribs and also via [Mindlin 1964] microstructure elasticity. Cut off frequencies were not sufficient to determine generalized continuum elastic constants. The shape of the longitudinal speed vs. frequency curve might be studied as a way to obtain several constants; the curve depends on four constants, the three

dilatational elastic constants and the microinertia. Mindlin [1964] and Puri and Cowin [1985] present further detail regarding waves. There are two kinds of longitudinal waves corresponding to acoustic and optical branches observed in crystals. If it is possible to observe both waves, then it might be possible to extract elastic constants. Biot theory [Biot 1941] also allows two kinds of longitudinal waves. Biot type slow waves have been observed in synthetic [Plona 1980] and in natural [Lakes et al. 1983] liquid filled permeable materials. Biot slow waves depend on fluid-solid interactions in permeable materials. Waves predicted in void elasticity, by contrast, will occur in a solid material with no fluid in any pores. By removing any fluid from the pores, one may distinguish the origin of the waves. Even so, thus far no experiments with a microstretch interpretation to determine elastic constants are known on physical materials.

6. Conclusions

Cosserat elasticity may be demonstrated and four of the six elastic constants extracted via torsion modalities independently of any dilatation gradient sensitivity the material may have. No comparable quasistatic modality for void elasticity has emerged. In Cosserat solids, methods are known and have been applied to obtain all six elastic constants via quasistatic experiments. Wave methods may be appropriate for both Cosserat and microstretch solids provided viscoelastic dispersion is not too large. Microstretch elasticity, which includes sensitivity to gradients of rotation and of dilatation could account for bending effects larger than those of Cosserat elasticity.

References

[Alfrey 1944] T. Alfrey, "Non-homogeneous stresses in visco-elastic media", *Quart. Appl. Math.* **2** (1944), 113–119.

[Anderson and Lakes 1994] W. B. Anderson and R. S. Lakes, "Size effects due to Cosserat elasticity and surface damage in closed-cell polymethacrylimide foam", *J. Mater. Sci.* **29**:24 (1994), 6413–6419.

[Anderson et al. 1995] W. B. Anderson, R. S. Lakes, and M. C. Smith, "Holographic evaluation of warp in the torsion of a bar of cellular solid", *Cell. Polymers* **14** (1995), 1–13.

[Biot 1941] M. A. Biot, "General theory of three-dimensional consolidation", *J. Appl. Phys.* **12**:2 (1941), 155–164.

[Chen and Lakes 1989] C. P. Chen and R. S. Lakes, "Dynamic wave dispersion and loss properties of conventional and negative Poisson's ratio polymeric cellular materials", *Cell. Polymers* **8**:5 (1989), 343–359.

[Cosserat and Cosserat 1909] E. Cosserat and F. Cosserat, *Théorie des corps déformables*, Hermann, Paris, 1909.

[Cowin 1970] S. C. Cowin, "Stress functions for a Cosserat elasticity", *Int. J. Solids Struct.* **6**:4 (1970), 389–398.

[Cowin 1983] S. C. Cowin, "The classical pressure vessel problems for linear elastic materials with voids", *J. Elasticity* **13**:2 (1983), 157–163.

[Cowin 1984] S. C. Cowin, "The stresses around a hole in a linear elastic material with voids", *Quart. J. Mech. Appl. Math.* **37**:3 (1984), 441–465.

[Cowin and Nunziato 1983] S. C. Cowin and J. W. Nunziato, "Linear elastic materials with voids", *J. Elasticity* **13**:2 (1983), 125–147.

[Eringen 1968] A. C. Eringen, "Theory of micropolar elasticity", pp. 621–729 in *Fracture, 2: Mathematical fundamentals*, edited by H. Liebowitz, Academic Press, New York, 1968.

[Eringen 1983] A. C. Eringen, "On differential equations of nonlocal elasticity and solutions of screw dislocations and surface waves", *J. Appl. Phys.* **54**:9 (1983), 4703–4710.

[Eringen 1990] A. C. Eringen, "Theory of thermomicrostretch elastic solids", *Int. J. Eng. Sci.* **28**:12 (1990), 1291–1301.

[Eringen 1998] A. C. Eringen, *Plane harmonic microstretch waves*, Section 6.3, Springer, New York, 1998.

[Gauthier and Jahsman 1975] R. D. Gauthier and W. E. Jahsman, "A quest for micropolar elastic constants", *J. Appl. Mech.* (*ASME*) **42**:2 (1975), 369–374.

[Gibson and Ashby 1997] L. J. Gibson and M. F. Ashby, *Cellular solids: structure and properties*, 2nd ed., Cambridge University Press, 1997.

[Ieşan and Nappa 1995] D. Ieşan and L. Nappa, "Extension and bending of microstretch elastic circular cylinders", *Int. J. Eng. Sci.* **33**:8 (1995), 1139–1151.

[Krishna Reddy and Venkatasubramanian 1978] G. V. Krishna Reddy and N. K. Venkatasubramanian, "On the flexural rigidity of a micropolar elastic circular cylinder", *J. Appl. Mech.* (*ASME*) **45**:2 (1978), 429–431.

[Kröner 1967] E. Kröner, "Elasticity theory of materials with long range cohesive forces", *Int. J. Solids Struct.* **3**:5 (1967), 731–742.

[Lakes 1986] R. S. Lakes, "Experimental microelasticity of two porous solids", *Int. J. Solids Struct.* **22** (1986), 55–63.

[Lakes 1995a] R. S. Lakes, "Experimental methods for study of Cosserat elastic solids and other generalized continua", Chapter 1, pp. 1–22 in *Continuum models for materials with micro-structure*, edited by H.-B. Mühlhaus, Wiley, Chichester, 1995.

[Lakes 1995b] R. S. Lakes, "On the torsional properties of single osteons", *J. Biomech.* **28**:11 (1995), 1409–1410.

[Lakes and Drugan 2015] R. S. Lakes and W. J. Drugan, "Bending of a Cosserat elastic bar of square cross section: theory and experiment", *J. Appl. Mech.* (*ASME*) **82**:9 (2015), Article ID #091002.

[Lakes et al. 1983] R. S. Lakes, H. S. Yoon, and J. L. Katz, "Slow compressional wave propagation in wet human and bovine cortical bone", *Science* **220**:4596 (1983), 513–515.

[Lakes et al. 1985] R. S. Lakes, D. Gorman, and W. Bonfield, "Holographic screening method for microelastic solids", *J. Mater. Sci.* **20**:8 (1985), 2882–2888.

[Mindlin 1963] R. D. Mindlin, "Effect of couple stresses on stress concentrations", *Exp. Mech.* **3**:1 (1963), 1–7.

[Mindlin 1964] R. D. Mindlin, "Micro-structure in linear elasticity", *Arch. Ration. Mech. Anal.* **16** (1964), 51–78.

[Mindlin 1965] R. D. Mindlin, "Stress functions for a Cosserat continuum", *Int. J. Solids Struct.* **1**:3 (1965), 265–271.

[Mora and Waas 2000] R. Mora and A. M. Waas, "Measurement of the Cosserat constant of circular cell polycarbonate honeycomb", *Philos. Mag. A* **80**:7 (2000), 1699–1713.

[Park and Lakes 1986] H. C. Park and R. S. Lakes, "Cosserat micromechanics of human bone: strain redistribution by a hydration-sensitive constituent", *J. Biomech.* **19**:5 (1986), 385–397.

[Park and Lakes 1987] H. C. Park and R. S. Lakes, "Torsion of a micropolar elastic prism of square cross section", *Int. J. Solids Struct.* **23** (1987), 485–503.

[Plona 1980] T. J. Plona, "Observation of a second bulk compressional wave in a porous medium at ultrasonic frequencies", *Appl. Phys. Lett.* **36**:4 (1980), 259–261.

[Puri and Cowin 1985] P. Puri and S. C. Cowin, "Plane waves in linear elastic materials with voids", *J. Elasticity* **15**:2 (1985), 167–183.

[Read 1950] W. T. Read, Jr., "Stress analysis for compressible visco-elastic materials", *J. Appl. Phys.* **21** (1950), 671–674.

[Rueger and Lakes 2016a] Z. Rueger and R. S. Lakes, "Experimental Cosserat elasticity in open-cell polymer foam", *Philos. Mag.* **96**:2 (2016), 93–111.

[Rueger and Lakes 2016b] Z. Rueger and R. S. Lakes, "Cosserat elasticity of negative Poisson's ratio foam: experiment", *Smart Mater. Struct.* (2016). To appear.

[Sokolnikoff 1983] I. S. Sokolnikoff, *Theory of elasticity*, Krieger, Malabar, FL, 1983.

[Timoshenko 1983] S. P. Timoshenko, *History of strength of materials*, Dover, New York, 1983.

Received 12 Oct 2015. Revised 7 Jan 2016. Accepted 16 Jan 2016.

RODERIC S. LAKES: lakes@engr.wisc.edu
Department of Engineering Physics, University of Wisconsin – Madison, 147 Engineering Research Building, 1500 Engineering Drive, Madison, WI 53706-1687, United States

JOURNAL OF MECHANICS OF MATERIALS AND STRUCTURES
Vol. 11, No. 3, 2016
dx.doi.org/10.2140/jomms.2016.11.231

ON LOW-FREQUENCY VIBRATIONS OF A COMPOSITE STRING WITH CONTRAST PROPERTIES FOR ENERGY SCAVENGING FABRIC DEVICES

ASKAR KUDAIBERGENOV, ANDREA NOBILI AND LUDMILLA PRIKAZCHIKOVA

Free vibrations of a two-component string with high-contrast material parameters are considered at different boundary conditions to illustrate the very low-frequency energy harvesting capability of fabric devices. It is revealed that, only for the case of mixed boundary conditions, low-frequency (locally) almost rigid-body vibrations are admissible, provided that material parameter ratios lie in some well defined interval. A low-frequency perturbation procedure is carried out to determine the eigenfrequencies as well as the eigenforms. The analysis is extended to a piecewise inhomogeneous string and to a string supported on an elastic foundation. It is shown that both situations may still admit low-frequency vibrations, under certain restrictions on the material properties. This is particularly remarkable given that the situation of elastic support normally possesses two nonzero cutoff frequencies. The results may be especially relevant for energy scavenging fabric devices, where very low-frequency (< 10 Hz) mechanical vibrations of textile fibers are harvested through friction.

1. Introduction

Low-frequency mechanical vibrations of composite structures have been the object of extensive studies; see the classic textbooks [Graff 1975; Le 1999] and, for a modern account, [Wang and Wang 2013]. In recent years, a revival of interest in the subject has been taking place owing to the appearance of new applications connected to the development of multiphase or multilayered structures with high contrast in the geometrical and mechanical properties. Alongside multilayered composite structures with high-contrast material parameters, which are currently widely used in various fields of civil and mechanical engineering [Horgan and Chan 1999; Elishakoff 2005], another promising application area is related to the rapidly developing field of metamaterials. Metamaterials are engineered materials endowed with unique properties, often stemming from the interplay of periodically arranged phases exhibiting extremely high contrast [Martin et al. 2012]. The same principle of phase periodicity is adopted to design and construct waveguides with tailored filtering properties [Gei et al. 2009; Piccolroaz and Movchan 2014; Kaplunov and Nobili 2016].

Mechanical vibrations arise naturally in a variety of environments and they can be harvested to power self-sustaining micro- and especially nanodevices. Despite high-frequency vibrations being very attractive in light of their high energy content, much greater interest lies in the exploitation of low-frequency vibrations for their ubiquitous character (body movements such as footsteps or heartbeat, wind or thermal generated vibrations, air flow and noise) [Song et al. 2006].

Nobili acknowledges financial support from the National Group of Mathematical Physics (GNFM-INdAM) through the "Progetto Giovani Ricercatori 2015" scheme, grant U2015/000125.

Keywords: low-frequency vibration, energy scavenging, contrast properties, strings.

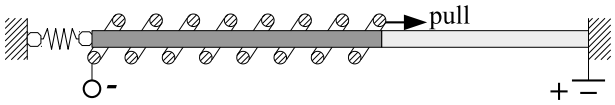

Figure 1. Schematics of a textile energy harvester; compare [Qin et al. 2008, Figure 2a]. A microwire is wound around the vibrating string and frictional energy is harvested through pulling or vibrating. Note that friction causes (mechanical) tension to vary along the string.

Recently, textile fabric devices have been proposed as a mean of scavenging very low-frequency ($< 10\,\mathrm{Hz}$) mechanical energy through the coupling of a vibrating string wound around by electrically coupled microwires [Qin et al. 2008; Nobili and Lanzoni 2010]. A device schematics is given in Figure 1, although other arrangements are equally possible. In this paper, we focus attention on low-frequency vibrations of a two-component piecewise-constant finite string, in an attempt to better elucidate the energy harvesting capability of the passive element in an energy scavenging device. For the best performance, the string is endowed with high contrast in the material and/or in the geometrical properties. Continuity conditions are assumed between the components.

The analysis is carried out for three types of boundary conditions, namely free-free, fixed-fixed and fixed-free (mixed) end conditions. It is shown that the low-frequency behavior is possible only for the case of mixed boundary conditions, which appears especially attractive for energy harvesting purposes.

A low-frequency perturbation approach is adopted to obtain the lowest eigenfrequency and the corresponding eigenform, whose character appears almost rigid-body like.

The analysis of the case of variable material parameters confirms that the low-frequency regime is accessible only in a fixed-free setup, although the almost rigid-body behavior is now restricted to the strong component. Finally, vibrations of a high-contrast two-component piecewise homogeneous string supported on a Winkler elastic foundation are considered [Nobili 2012]. In this case, the asymptotic approximation is carried out for frequencies standing in the vicinity of the cut-off frequency of the stronger component, which still can be made very small under some conditions on the ratios of the geometrical and mechanical properties.

It is worth mentioning that the eigenfrequencies of a composite string correspond to the lowest cutoff frequencies for a plate (or a shell) from the standpoint of 3D elasticity [Kaplunov 1995]. The same analogy can be extended to incorporate the effects of prestress [Kaplunov et al. 2002] and anisotropy [Kaplunov et al. 2000].

The paper is organized as follows. In Section 2, three types of boundary conditions for the ends of the string are considered and it is revealed that the low-frequency regime is possible only in the case of free-fixed boundary conditions. A restriction on the material parameters entailing such behavior is also obtained. In Section 3, a perturbative approach is first conducted on piecewise homogeneous string and then extended to the case of variable material properties. It is shown that, although the almost rigid-body eigenbehavior retrieved in the former case is lost in the latter, low-frequency vibrations are still admissible under suitable conditions. The effect of an elastic support is considered in Section 4 and it brings a cutoff frequency which may be greatly decreased. Finally, conclusions are drawn in Section 5.

2. Frequency equation for a two-component string

Let us consider a finite linear string made of two-components, named 1 and 2, with high material and geometric contrast parameters. The length of the components is h_1 and h_2. Let the x axis be taken to lie along the string with the origin coinciding with the interface between the two components (see Figure 2).

The governing equation of the string in harmonic motion is

$$\frac{\mathrm{d}^2 u_i}{\mathrm{d}x^2} + \frac{\omega^2}{c_i^2} u_i = 0, \quad i = 1, 2, \tag{2-1}$$

where u_i is the transverse displacement in the relevant component of the string, T_i and $c_i = \sqrt{T_i/\rho_i}$ the corresponding string tension and wave speed, ρ_i the linear mass density and $\omega > 0$ the vibration frequency [Wang and Wang 2013, Chapter 2]. The conditions enforcing displacement and traction continuity at the interface between the components are given by

$$u_1(0) = u_2(0), \quad T_1 \frac{\mathrm{d}u_1}{\mathrm{d}x}(0) = T_2 \frac{\mathrm{d}u_2}{\mathrm{d}x}(0). \tag{2-2}$$

Let introduce the following notation for the ratios of the material parameters in the two components of the string:

$$T = \frac{T_1}{T_2}, \quad h = \frac{h_1}{h_2}, \quad \rho = \frac{\rho_1}{\rho_2}, \quad c = \frac{c_1}{c_2}, \tag{2-3}$$

together with the nondimensional frequency parameters

$$\lambda_i = \frac{\omega}{c_i} h_i > 0, \quad i = 1, 2. \tag{2-4}$$

It is observed that the parameters λ_1 and λ_2 are related through the connection

$$\lambda_2 = \frac{1}{h}\sqrt{\frac{T}{\rho}}\lambda_1. \tag{2-5}$$

The general solution of the constant coefficient linear ODEs (2-1) is given by

$$\begin{aligned} u_1(x) &= A\cos\left(\lambda_1 \frac{x}{h_1}\right) + B\sin\left(\lambda_1 \frac{x}{h_1}\right), \qquad 0 \le x \le h_1, \\ u_2(x) &= C\cos\left(\lambda_2 \frac{x}{h_2}\right) + D\sin\left(\lambda_2 \frac{x}{h_2}\right), \quad -h_2 \le x \le 0, \end{aligned} \tag{2-6}$$

where A, B, C, D are arbitrary constants.

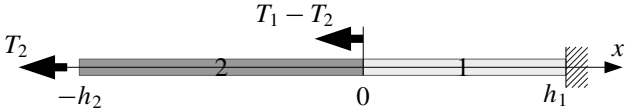

Figure 2. A two-component fixed-free string. The tension jump $T_1 - T_2$ approximate the effect of friction with the microwire (see Figure 1); a more refined model considering continuous variation of the tension is discussed in Section 3B.

For a one-parameter asymptotic analysis, the small positive quantity ε is introduced as follows:

$$\varepsilon = \frac{T}{h} \ll 1. \tag{2-7}$$

Besides, let

$$\eta = \frac{T}{c} = \sqrt{T\rho}, \tag{2-8}$$

whence (2-5) gives the connection

$$\lambda_2 = \frac{\varepsilon}{\eta}\lambda_1. \tag{2-9}$$

We shall consider three types of end conditions for the string and, in each case, investigate the possibility for low-frequency vibrations.

2A. ***Traction free end conditions.*** The boundary conditions for a string with traction free ends can be written in the form

$$\frac{\mathrm{d}u_1}{\mathrm{d}x}(h_1) = 0 \quad \text{and} \quad \frac{\mathrm{d}u_2}{\mathrm{d}x}(-h_2) = 0. \tag{2-10}$$

Substituting the general solution (2-6) into the boundary conditions (2-10) and into the continuity relations (2-2) we arrive at a homogeneous system of algebraic equations which is linear in the integration constants. As well known, such system possesses nontrivial solution provided that the determinant of the associated coefficient matrix is equal to zero, namely

$$\begin{vmatrix} -\sin\lambda_1 & \cos\lambda_1 & 0 & 0 \\ 0 & 0 & \sin\lambda_2 & \cos\lambda_2 \\ 1 & 0 & -1 & 0 \\ 0 & \eta & 0 & -1 \end{vmatrix} = 0. \tag{2-11}$$

Such requirement leads to the frequency equation

$$\eta\tan\lambda_1 + \tan\lambda_2 = 0, \tag{2-12}$$

which, clearly, cannot sustain low-frequency vibrations (i.e., vibrations at $\lambda_1, \lambda_2 \ll 1$) unless materials with exotic properties, like negative density, are considered (see, for example, [Martin et al. 2012] and references therein).

2B. ***Fixed end conditions.*** The situation of a string with fixed ends is now considered. In this case, the boundary conditions (2-10) are replaced by

$$u_1(h_1) = 0 \quad \text{and} \quad u_2(-h_2) = 0. \tag{2-13}$$

Following the usual procedure, we arrive at the frequency equation

$$\tan\lambda_1 + \eta\tan\lambda_2 = 0, \tag{2-14}$$

which closely resembles (2-12). Hence, low-frequency vibrations in a string with fixed ends cannot be achieved. However, an interesting remark appears in [Wang and Wang 2013], where it is observed that, in the case of a fixed-fixed two-segment string, the eigenfrequency is a decreasing function of the density ratio ρ.

2C. ***Fixed-free ends.*** Let us consider yet another type of boundary conditions, namely the fixed-free end conditions, wherein

$$u_1(h_1) = 0 \quad \text{and} \quad \frac{\mathrm{d}u_2}{\mathrm{d}x}(-h_2) = 0. \tag{2-15}$$

The frequency equation may be written as

$$\tan\lambda_1 \tan\lambda_2 = \eta.$$

In the low-frequency regime, characterized by $\lambda_1 \ll 1$ and $\lambda_2 \ll 1$, the frequency equation is approximated by

$$\lambda_1\lambda_2 = \eta,$$

or, employing the connection (2-9), by the following condition on λ_1:

$$\lambda_1 = \frac{\eta}{\sqrt{\varepsilon}} \ll 1. \tag{2-16}$$

Clearly, (2-9) demands

$$\lambda_2 = \sqrt{\varepsilon} \ll 1. \tag{2-17}$$

According to the definitions (2-7) and (2-8), the (order) inequalities (2-16) and (2-17) amount to

$$\rho h \ll 1 \quad \text{and} \quad \frac{T}{h} \ll 1, \tag{2-18}$$

respectively. In particular, the first inequality may be rewritten in term of masses as

$$m_1 = \rho_1 h_1 \ll \rho_2 h_2 = m_2;$$

that is, the mass of one string component must be much smaller than the other's (note that 1 and 2 are interchangeable). Together, the inequalities (2-18) require

$$\eta^2 \ll \varepsilon \ll 1,$$

which, by the definitions (2-7) and (2-8), gives a single condition on the geometric/mechanical parameters allowing for low-frequency vibrations, namely

$$T \ll h \ll \frac{1}{\rho}. \tag{2-19}$$

Low-frequency vibrations may arise, for example, in a string with soft and light part 1, while part 2 is stiff and heavy, i.e., $T_1 \ll T_2$ and $\rho_1 \ll \rho_2$. Besides, the corresponding string component lengths, h_1 and h_2, need be chosen of the same order of magnitude, i.e., $h_1/h_2 \sim 1$.

3. Asymptotic analysis of low-frequency vibrations in a composite string with free-fixed ends

The study of the frequency equation carried out in Section 2 leads to the conclusion that low-frequency vibrations are only possible for a string with free-fixed end conditions, provided some restriction on the material parameter ratios is met. For a more refined analysis, a low-frequency asymptotic approximation is now employed. A constant coefficient boundary-value problem is considered first and then results are generalized to the variable coefficients situation.

3A. ***Piecewise homogeneous string.*** For a two-component string with homogeneous material parameters, the equations of motion (2-1) hold together with the boundary conditions (2-10) and the continuity relations (2-2) at the interface. We restrict our attention to low-frequency vibrations at $\eta \sim \varepsilon$, whence $\lambda_1 \sim \lambda_2 \sim \sqrt{\varepsilon}$. To this aim, let

$$\eta = \alpha\varepsilon, \quad \text{where } \alpha = O(1). \tag{3-1}$$

Hence, the connection (2-9) between λ_1 and λ_2 now reads

$$\lambda_2 = \alpha^{-1}\lambda_1. \tag{3-2}$$

Let us introduce nondimensional spatial variables in each component of the string

$$\xi_1 = \frac{x}{h_1} \in [0, 1] \quad \text{and} \quad \xi_2 = \frac{x}{h_2} \in [-1, 0].$$

Then, our boundary-value problem may be rewritten in terms of the dimensionless variables

$$\frac{\mathrm{d}^2 u_i^*}{\mathrm{d}\xi_i^2} + \lambda_i^2 u_i^* = 0, \quad i = 1, 2, \tag{3-3}$$

together with the fixed-free end conditions

$$u_1^*(1) = 0, \quad \frac{\mathrm{d}u_2^*}{\mathrm{d}\xi_2}(-1) = 0$$

and the continuity conditions

$$u_1^*(0) = u_2^*(0), \quad \varepsilon\frac{\mathrm{d}u_1^*}{\mathrm{d}\xi_1}(0) = \frac{\mathrm{d}u_2^*}{\mathrm{d}\xi_2}(0)$$

at the interface $\xi_1 = \xi_2 = 0$. Here, it is let $u_i^*(\xi_i) = u_i(x/h_i)$, $i = 1, 2$. Assuming for u_i^* a regular asymptotic expansion in the small parameter ε, we write

$$u_i^* = u_i^{(0)} + \varepsilon u_i^{(1)} + \varepsilon^2 u_i^{(2)} + O(\varepsilon^3), \quad i = 1, 2, \tag{3-4}$$

while, in the low-frequency regime, it is

$$\lambda_1^2 = \varepsilon(\Lambda_0 + \varepsilon\Lambda_1 + \varepsilon^2\Lambda_2 + O(\varepsilon^3)). \tag{3-5}$$

Clearly, λ_2 follows from the connection (3-2).

3A.1. *Leading order problem.* At the leading order, the equations of motion (3-3) give

$$u_1^{(0)} = A_0\xi_1 + B_0,$$
$$u_2^{(0)} = C_0\xi_2 + D_0,$$

where A_0, B_0, C_0 and D_0 are integration constants. Using the boundary and continuity conditions, we arrive at

$$u_1^{(0)} = D_0(1 - \xi_1), \tag{3-6a}$$
$$u_2^{(0)} = D_0, \tag{3-6b}$$

which shows a local rigid-body behavior (rotation for 1 and translation for 2). Given that frequency cannot be derived at this stage, we need proceed to the next order.

3A.2. *First-order problem.* At the first order, compatibility gives the leading-order frequency term

$$\Lambda_0 = \alpha^2,$$

whereupon

$$\lambda_1^2 = \alpha^2\varepsilon(1 + O(\varepsilon)), \quad \lambda_2^2 = \varepsilon(1 + O(\varepsilon)).$$

Expressions for first-order correction to displacements, $u_1^{(1)}$ and $u_2^{(1)}$, take up the form:

$$u_1^{(1)} = \tfrac{1}{6}\alpha^2 D_0(1-\xi_1)(2-\xi_1)\xi_1 + D_1(1-\xi_1),$$
$$u_2^{(1)} = -D_0\xi_2\left(\frac{\xi_2}{2} + 1\right) + D_1,$$

where D_1 is yet another integration constant.

3A.3. *Second order.* At the second order, compatibility yields the first-order correction to the frequency

$$\Lambda_1 = -\frac{\alpha^2(1+\alpha^2)}{3},$$

and we arrive at the expansion

$$\lambda_1^2 = \varepsilon\alpha^2\left(1 - \frac{1+\alpha^2}{3}\varepsilon + O(\varepsilon^2)\right).$$

3B. ***Piecewise inhomogeneous string.*** It is now assumed that the material properties of each component of the string are no longer constant along the length, namely $T_i = T_i(x) > 0$, $\rho_i = \rho_i(x) > 0$, $i = 1, 2$. The equation for harmonic transverse vibrations [Wang and Wang 2013] are

$$\frac{\mathrm{d}}{\mathrm{d}x}\left(T_i(x)\frac{\mathrm{d}u_i}{\mathrm{d}x}\right) + \rho_i(x)\omega^2 u_i = 0, \quad i = 1, 2, \tag{3-7}$$

while the fixed-free boundary conditions (2-15), together with the continuity relations (2-2), hold. It is expedient to introduce the nondimensional quantities

$$T_i^*(\xi_i) = \frac{T_i(x)}{T_i(0)}, \quad \rho_i^*(\xi_i) = \frac{\rho_i(x)}{\rho_i(0)}, \qquad i = 1, 2, \tag{3-8}$$

as well as the ratios

$$T = \frac{T_1(0)}{T_2(0)}, \quad \rho = \frac{\rho_1(0)}{\rho_2(0)}. \tag{3-9}$$

In terms of the dimensionless coordinates ξ_i, (3-7) becomes

$$\frac{\mathrm{d}}{\mathrm{d}\xi_i}\left(T_i^*(\xi_i)\frac{\mathrm{d}u_i^*}{\mathrm{d}\xi_i}\right) + \lambda_i^2\rho_i^*(\xi_i)u_i^* = 0, \tag{3-10}$$

where

$$\lambda_i^2 = \frac{\omega^2 h_i^2 \rho_i(0)}{T_i(0)}, \quad i = 1, 2, \tag{3-11}$$

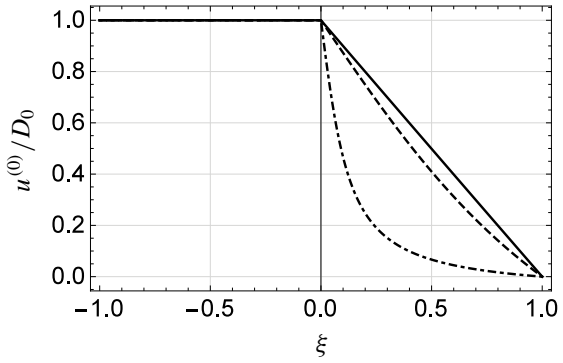

Figure 3. Leading order eigenforms for $T_1^*(\xi_1) = 1 + A^2\xi_1^2$ and $T_2^*(\xi_2) = 1$ at $A = 0.1$ (solid), $A = 1$ (dashed) and $A = 10$ (dot-dashed).

and the connection (3-2) still holds. The boundary conditions give

$$u_1^*(1) = 0, \quad \frac{\mathrm{d}u_2^*}{\mathrm{d}\xi_2}(-1) = 0,$$

while continuity at the interface reads

$$u_1^*(0) = u_2^*(0), \quad \varepsilon\frac{\mathrm{d}u_1^*}{\mathrm{d}\xi_1}(0) = \frac{\mathrm{d}u_2^*}{\mathrm{d}\xi_2}(0),$$

where the small parameter ε is introduced as at (2-7). Solution of this boundary value problem is taken in the form of the asymptotic expansions (3-4) and (3-5) for u_i^* and λ_1, respectively.

At the leading order we obtain

$$u_1^{(0)}(\xi_1) = D_0\left(1 - \frac{\phi_1(\xi_1)}{\phi_1(1)}\right), \tag{3-12a}$$

$$u_2^{(0)}(\xi_2) = D_0, \tag{3-12b}$$

where D_0 is an integration constant and we have let

$$\phi_i(\xi_i) = \int_0^{\xi_i} \frac{\mathrm{d}t}{T_i^*(t)}, \quad i = 1, 2. \tag{3-13}$$

In order to better illustrate the leading-order expressions for the first eigenform (3-12), a string with quadratic and constant behavior for the dimensionless tensions T_1^* and T_2^* is considered, i.e.,

$$T_1^*(\xi_1) = 1 + A^2\xi_1^2 \quad \text{and} \quad T_2^*(\xi_2) = 1.$$

Then, it is

$$\phi_1(\xi_1) = \frac{1}{|A|}\arctan(|A|\xi_1) \quad \text{and} \quad \phi_2(\xi_2) = \xi_2.$$

In Figure 3, the leading-order expressions for the first eigenform, given by Equations (3-12), are plotted at three values of the parameter A. As expected, the locally rigid-body behavior is retrieved for small

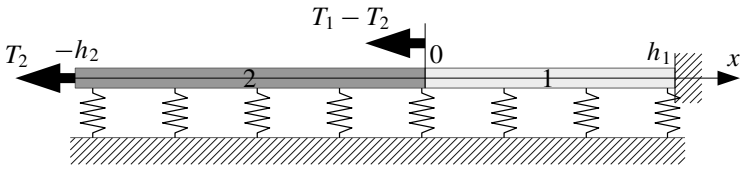

Figure 4. A two-component free-fixed string supported by a Winkler elastic foundation. The foundation is introduced to account for an embedding elastic matrix

values of A. However, it is perhaps less obvious that large values of A lead to a step function. Besides, we further observe that the transformation $u_i^*(\xi_i) = U_i^*(z_i)$, with the mapping

$$\xi_i \mapsto z_i \mid z_i(\xi_i) = \frac{\phi_i(\xi_i)}{\phi_i((-1)^{i+1})},$$

can be used to turn the variable coefficient problem (3-10) into Lioville's normal form [Horgan and Chan 1999; Wang and Wang 2013].

Bringing the analysis one step further, we obtain the displacement first-order correction

$$u_1^{(1)}(\xi_1) = D_0\Lambda_0\left(\frac{1}{\phi_1(1)}\int_0^{\xi_1}\frac{\int_0^{\sigma_2}\rho_1^*(\sigma_1)\phi_1(\sigma_1)\,\mathrm{d}\sigma_1}{T_1^*(\sigma_2)}\,\mathrm{d}\sigma_2 - \Phi_1(\xi_1)\right) + A_1^{(1)}\phi_1(\xi_1) + B_1^{(1)},$$
$$u_2^{(1)}(\xi_2) = -D_0\Lambda_0\frac{1}{\alpha^2}\Phi_2(\xi_2) + C_1^{(1)}\phi_2(\xi_2) + D_1^{(1)},$$

being

$$\Phi_i(\xi) = \int_0^{\xi}\frac{\int_0^{\sigma_2}\rho_i^*(\sigma_1)\,\mathrm{d}\sigma_1}{T_i^*(\sigma_2)}\,\mathrm{d}\sigma_2, \quad i = 1, 2.$$

Here, compatibility gives the leading-order term in the frequency expansion

$$\Lambda_0 = \frac{\alpha^2}{\phi_1(1)m_2^*},$$

having set the dimensionless mass of the 2-component

$$m_2^* = \int_{-1}^{0}\rho_2^*(\sigma_1)\mathrm{d}\sigma_1.$$

Clearly, the expression for λ_2 may be readily obtained from (3-2).

4. Piecewise homogeneous string on a Winkler foundation

In this section, near-zero frequency vibrations of a two-component piecewise homogeneous string on a Winkler foundation are considered (Figure 4).

The equations of motion for a string on a Winkler foundation [Graff 1975] are

$$\frac{\mathrm{d}^2u_i}{\mathrm{d}x^2} + \left(\frac{\omega^2}{c_i^2} - \frac{\kappa}{T_i}\right)u_i = 0, \quad i = 1, 2, \tag{4-1}$$

where κ is the Winkler foundation modulus (whose physical dimensions are force over length squared).

These equations clearly show that local cutoff frequencies exist [Kaplunov and Nobili 2015], namely

$$\omega_{\text{cutoff}\,i}^2 = \frac{\kappa}{\rho_i},$$

such that harmonic vibrations are possible only whenever $\omega > \max(\omega_{\text{cutoff}\,1}, \omega_{\text{cutoff}\,2})$. Equations (4-1) are most conveniently put in dimensionless form

$$\frac{\mathrm{d}^2 u_i}{\mathrm{d}\xi_i^2} + \gamma_i^2 u_i = 0, \quad i = 1, 2, \tag{4-2}$$

where it is let

$$\gamma_i^2 = \lambda_i^2 - \beta_i^2 \quad \text{and} \quad \beta_i^2 = \frac{h_i^2}{T_i}\kappa, \quad i = 1, 2. \tag{4-3}$$

It is remarked that the λ_i are defined according to (2-4) and therefore the connection (2-9) still holds. Obviously, we demand $\lambda_i > \beta_i$ for global vibrations to take place, which shows that β_i are the dimensionless local cutoff frequencies. Furthermore, the connection

$$\beta_2^2 = \frac{\varepsilon}{h}\beta_1^2 \tag{4-4}$$

stands between β_1 and β_2. The general solution of the ODEs (4-2) is given by

$$u_1(\xi_1) = A\cos(\gamma_1\xi_1) + B\sin(\gamma_1\xi_1), \qquad 0 \le \xi_1 \le 1, \tag{4-5a}$$

$$u_2(\xi_2) = C\cos(\gamma_2\xi_2) + D\sin(\gamma_2\xi_2), \quad -1 \le \xi_2 \le 0, \tag{4-5b}$$

where A, B, C, D are arbitrary constants. As in the case of a string with homogeneous parameters, we shall consider three types of boundary conditions, namely free-free, fixed-fixed and fixed-free end conditions. The frequency equation for harmonic vibrations of a string is, for the case of fixed ends,

$$\varepsilon\frac{\gamma_1}{\gamma_2}\tan\gamma_1 + \tan\gamma_2 = 0,$$

while, for the case of free ends, it is

$$\varepsilon\frac{\gamma_1}{\gamma_2}\tan\gamma_2 + \tan\gamma_1 = 0.$$

Clearly, both equations do not allow for low-frequency vibrations. Conversely, the frequency equation for the fixed-free case reads

$$\varepsilon\frac{\gamma_1}{\gamma_2} = \tan\gamma_1\tan\gamma_2, \tag{4-6}$$

which may admit low-frequency vibrations. Indeed, assuming γ_1 and γ_2 small — which amounts to considering near-cutoff vibrations (see also [Craster et al. 2010]) — we get

$$\gamma_2^2 = \varepsilon + O(\varepsilon^3),$$

whence the condition for γ_2 to be small is given by

$$\varepsilon = T/h \ll 1. \tag{4-7}$$

The (squared) scaled frequency λ_2^2 is readily obtained from (4-3) through shifting by the local cutoff frequency β_2^2, i.e.,

$$\lambda_2^2 = \beta_2^2 + \varepsilon + O(\varepsilon^3),$$

which, in light of (4-4), is enough for low-frequency vibrations of the 2-component (assuming that β_1 is of order unity or smaller and h of order unity or larger). In order to achieve global low-frequency vibrations, we demand λ_1 to be small as well and, using the connections (2-9), this requires

$$\lambda_1^2 = \frac{\eta^2}{\varepsilon}\left(\frac{\beta_1^2}{h} + 1 + O(\varepsilon^2)\right) \ll 1, \tag{4-8}$$

which amounts to the condition

$$(\beta_1^2 + h)\rho \ll 1. \tag{4-9}$$

Similarly to what was chosen in Section 3, this condition may be fulfilled taking, for instance,

$$\eta = \eta_0 \varepsilon. \tag{4-10}$$

It remains to be seen whether γ_1 is also small as it was initially assumed. To this aim, using the definition (4-3), we further demand that

$$0 < \beta_1^2(\rho - 1) + \rho h \ll 1. \tag{4-11}$$

Together, Equations (4-9) and (4-11) imply

$$\beta_1^2 < (\beta_1^2 + h)\rho \ll 1,$$

whereupon β_1 needs also be a small quantity. For instance, we could set

$$\beta_1 = \varepsilon \beta_0. \tag{4-12}$$

Leading order asymptotic expansions for the displacement may be equally well derived. To this end, we first write the eigenforms u_1 and u_2 through introducing the general solution (4-5) into the fixed-free boundary conditions (2-15) and into the continuity relations (2-2)

$$u_1(\xi_1) = D\big(\sin(\gamma_1\xi_1) - \tan(\gamma_1)\cos(\gamma_1\xi_1)\big),$$
$$u_2(\xi_2) = D\left(\varepsilon\frac{\gamma_1}{\gamma_2}\sin(\gamma_2\xi_2) - \tan(\gamma_1)\cos(\gamma_2\xi_2)\right),$$

where it is understood that γ_1 and γ_2 are related through the frequency Equation (4-6). Then, we introduce the smallness assumptions (4-10) and (4-12) together with the expansion (4-8) for λ_1 and proceed to expand in the small parameter ε. Thus, the asymptotic expansion for the eigenform is obtained:

$$u_1 = D(1 - \xi_1) + O(\varepsilon),$$
$$u_2 = D + O(\varepsilon).$$

It is perhaps surprising to observe that, under the smallness assumptions, the presence of the Winkler foundation does not alter the leading-order shape of the eigenforms (see Equations (3-6)), and a local rigid body-motion is again retrieved.

5. Conclusions

Very low-frequency vibrations in a two-component high-contrast string have been investigated for the case of fixed-fixed, free-free and free-fixed boundary conditions, in an attempt to enhance the energy scavenging capability of the soft element in a fabric device. It is shown that low-frequency vibrations are achievable only for the case of fixed-free end conditions, which seems especially apt at harvesting low-power energy sources. Besides, conditions on the material and geometrical property ratios were given in order to sustain near-zero frequency vibrations. Piecewise constant as well as variable material parameters are considered. In the former case, the exact solution is obtainable and an almost rigid-body motion is found. The almost rigid-body behavior is especially welcome as it warrants little wear in the system. Conversely, the latter situation can only be addressed in an approximate way, through a two-scale approach, and it is shown that, although the almost rigid body behavior is generally lost, low-frequency vibrations can still be sustained, provided that suitable conditions on the material parameters hold. The question whether low-frequency vibrations may be still admitted in a soft element supported by a Winkler foundation was then addressed, because energy harvesters may be embedded in an elastic matrix. In this case, the soft string is assumed piecewise constant and an exact solution is obtained. As expected, two cutoff frequencies appear which, however, may be brought close to zero under suitable smallness assumptions on the material parameter ratios. A somewhat surprising result is obtained, for the local rigid-body character of the leading-order expressions for the eigenforms, already met in the unsupported case, is again retrieved. It is finally observed that our results apply equally well to the analysis of low-frequency vibrations in composite plates and shells treated within the framework of 3D elasticity. For example, in case of a two-layered elastic plate, the eigenfrequencies λ_1, λ_2 would be associated with the lowest cutoff frequencies; see, for instance, [Kaplunov et al. 1998; Le 1999].

6. Acknowledgements

Fruitful discussions with Dr. D. A. Prikazchikov are also gratefully acknowledged.

References

[Craster et al. 2010] R. V. Craster, J. Kaplunov, and A. V. Pichugin, "High-frequency homogenization for periodic media", *Proc. R. Soc. Lond. A* **466**:2120 (2010), 2341–2362.

[Elishakoff 2005] I. Elishakoff, *Eigenvalues of inhomogeneous structures: unusual closed-form solutions*, CRC Press, Boca Raton, FL, 2005.

[Gei et al. 2009] M. Gei, A. B. Movchan, and D. Bigoni, "Band-gap shift and defect-induced annihilation in prestressed elastic structures", *J. Appl. Phys.* **105**:6 (2009), 063507.

[Graff 1975] K. F. Graff, *Wave motion in elastic solids*, reprinted 1991, Dover, Mineola, NY ed., Clarendon Press, Oxford, 1975.

[Horgan and Chan 1999] C. O. Horgan and A. M. Chan, "Vibration of inhomogeneous strings, rods and membranes", *J. Sound Vib.* **225**:3 (1999), 503 – 513.

[Kaplunov 1995] J. D. Kaplunov, "Long-wave vibrations of a thin-walled body with fixed faces", *Quart. J. Mech. Appl. Math.* **48**:3 (1995), 311–327.

[Kaplunov and Nobili 2015] J. D. Kaplunov and A. Nobili, "The edge waves on a Kirchhoff plate bilaterally supported by a two-parameter elastic foundation", *J. Vib. Control* (2015), 1–9.

[Kaplunov and Nobili 2016] J. D. Kaplunov and A. Nobili, "Multi-parametric analysis of strongly inhomogeneous periodic waveguides with internal cutoff frequencies", *Math. Methods Appl. Sci.* (2016). To appear.

[Kaplunov et al. 1998] J. D. Kaplunov, L. Y. Kossovich, and E. V. Nolde, *Dynamics of thin walled elastic bodies*, Academic Press, San Diego, CA, 1998.

[Kaplunov et al. 2000] J. D. Kaplunov, L. Y. Kossovich, and G. A. Rogerson, "Direct asymptotic integration of the equations of transversely isotropic elasticity for a plate near cut-off frequencies", *Quart. J. Mech. Appl. Math.* **53**:2 (2000), 323–341.

[Kaplunov et al. 2002] J. D. Kaplunov, E. V. Nolde, and G. A. Rogerson, "An asymptotically consistent model for long-wave high-frequency motion in a pre-stressed elastic plate", *Math. Mech. Solids* **7**:6 (2002), 581–606.

[Le 1999] K. C. Le, *Vibrations of shells and rods*, Springer, Berlin, 1999.

[Martin et al. 2012] T. P. Martin, C. N. Layman, K. M. Moore, and G. J. Orris, "Elastic shells with high-contrast material properties as acoustic metamaterial components", *Phys. Rev. B* **85** (2012), 161103.

[Nobili 2012] A. Nobili, "Superposition principle for the tensionless contact of a beam resting on a Winkler or a Pasternak foundation", *J. Eng. Mech.* (*ASCE*) **139**:10 (2012), 1470–1478.

[Nobili and Lanzoni 2010] A. Nobili and L. Lanzoni, "Electromechanical instability in layered materials", *Mech. Mater.* **42**:5 (2010), 581 – 591.

[Piccolroaz and Movchan 2014] A. Piccolroaz and A. B. Movchan, "Dispersion and localisation in structured Rayleigh beams", *Int. J. Solids Struct.* **51**:25–26 (2014), 4452–4461.

[Qin et al. 2008] Y. Qin, X. Wang, and Z. L. Wang, "Microfibre–nanowire hybrid structure for energy scavenging", *Nature* **451**:7180 (2008), 809–813.

[Song et al. 2006] J. Song, J. Zhou, and Z. L. Wang, "Piezoelectric and semiconducting coupled power generating process of a single ZnO belt/wire: a technology for harvesting electricity from the environment", *Nano Lett.* **6**:8 (2006), 1656–1662.

[Wang and Wang 2013] C. Y. Wang and C. M. Wang, *Structural vibration: exact solutions for strings, membranes, beams, and plates*, CRC Press, Boca Raton, FL, 2013.

Received 20 Nov 2015. Revised 29 Jan 2016. Accepted 7 Feb 2016.

ASKAR KUDAIBERGENOV: as5kar@mail.ru
Department of Mathematical and Computer Modelling, al-Farabi Kazakh National University, 71 al-Farabi Avenue, Almaty, 480078, Kazakhstan

ANDREA NOBILI: andrea.nobili@unimore.it
DIEF - Dipartimento di Ingegneria "Enzo Ferrari", Università di Modena e Reggio Emilia, Via Vignolese 905, I-41125 Modena, Italy

LUDMILLA PRIKAZCHIKOVA: l.prikazchikova@keele.ac.uk
School of Computing and Mathematics, Keele University, Keele, Staffordshire, ST5 5BG, United Kingdom

JOURNAL OF MECHANICS OF MATERIALS AND STRUCTURES
Vol. 11, No. 3, 2016
dx.doi.org/10.2140/jomms.2016.11.245

WAVE PROPAGATION IN LAYERED PIEZOELECTRIC RINGS WITH RECTANGULAR CROSS SECTIONS

JIANGONG YU, XIAODONG YANG AND JEAN-ETIENNE LEFEBVRE

Wave propagation in multilayered piezoelectric structures has received much attention in past forty years. But the research objects of previous research works are almost only for semi-infinite structures and one-dimensional structures, i.e., structures with a finite dimension in only one direction, such as horizontally infinite flat plates and axially infinite hollow cylinders. This paper proposes a double orthogonal polynomial series approach to solve the wave propagation in a two-dimensional (2-D) layered piezoelectric structure, namely, a multilayered piezoelectric ring with a rectangular cross-section. Through numerical comparison with the available reference results for a purely elastic multilayered rectangular straight bar, the validity of the double polynomial series approach is illustrated. The dispersion curves and electric potential distributions of various layered piezoelectric rectangular rings with different material stacking directions, different polarization directions, different radius to thickness ratios, and different width to thickness ratios are calculated to reveal their wave propagation characteristics.

1. Introduction

Because of the applications in ultrasonic nondestructive evaluation and transducer design and optimization, wave propagation in multilayered piezoelectric structures has received considerable attention from engineering and scientific communities. Many solution methods have been used to investigate the wave propagation phenomena in multilayered piezoelectric structures. The mostly used method is the transfer matrix method (TMM) [Nayfeh 1995; Adler 2000; Cai et al. 2001] and the finite element method (FEM) [Ballandras et al. 2004]. Because the TMM and FEM suffer from numerical instability in some particular cases, some improvements have been developed, such as the recursive asymptotic stiffness matrix method [Wang and Rokhlin 2002; 2004], the surface impedance matrix method [Collet 2004; Zhang et al. 2001], the scattering-matrix method [Pastureaud et al. 2002] and the reverberation-ray matrix method [Guo et al. 2009].

The series expansion technique has been used for the problem of vibrations and waves. As early as 1960, Mindlin and McNiven [1960] used the Jacobi polynomial series to investigate the axially symmetric waves in elastic rods. Wu et al. [2014] also used the Jacobi polynomial series for the axially symmetric waves in piezoelectric ceramic rods. Dökmeci [1974] developed a double power series method to investigate the high frequency vibrations of piezoelectric crystal bars. Chou et al. [1991] used the double power series method for the dynamic analysis of a vibratory piezoelectric beam gyroscope. In 1972, an orthogonal polynomial approach has been developed to analyze linear acoustic waves in homogeneous semi-infinite wedges [Maradudin et al. 1972]. This approach has a special feature: it incorporates

Keywords: wave propagation, rectangular ring, piezoelectric materials, multilayered structures, double orthogonal polynomials.

the boundary conditions into the equations of motion. So the boundary conditions are automatically accounted for by assuming position-dependent material parameters. The equations of motion are then converted into a matrix eigenvalue problem through the expansion of the independent mechanical variables into appropriate series of orthonormal functions which makes the semivariational determination of the frequencies and the 8 associated modes possible. After that, this approach has been used to solve various wave propagation and vibration problems, including surface acoustic waves in layered semi-infinite piezoelectric structures [Datta and Hunsinger 1978; Kim and Hunt 1990], Lamb-like waves in multilayered piezoelectric plates [Lefebvre et al. 1999] and multilayered piezoelectric curved structures [Yu et al. 2013; 2012].

So far, investigations on wave propagation in multilayered piezoelectric structures are almost only for semi-infinite structures and one-dimensional structures, i.e., structures having a finite dimension in only one direction, such as horizontally infinite flat plates and axially infinite hollow cylinders. But in practical applications, many piezoelectric elements have finite dimensions in two directions, such as rings with rectangular cross sections. One-dimensional models are thus not suitable for these structures. This paper proposes a double orthogonal polynomial series approach to solve wave propagation in a 2-D piezoelectric structure, namely, a multilayered piezoelectric ring with rectangular cross-section. To the authors' knowledge, few references concerned on guided waves in multilayered piezoelectric rings. Two material stacking directions (radial direction and axial direction) and two polarization directions (also radial direction and axial direction) are respectively considered. The dispersion curves and the electric potential profiles of various layered piezoelectric rectangular rings are presented and discussed. In this paper, traction-free and open-circuit boundary conditions are assumed.

2. Problem formulation and solution method

We consider a multilayered piezoelectric ring with rectangular cross-section. In the cylindrical coordinate system (θ, z, r), a, b are the inner and outer radii. Figure 1 shows the schematic diagram of a multilayered ring with its stacking direction being in the axial direction. Its width is d, and the total height is $h = h_N$. The radius to thickness ratio is defined as $\eta = b/(b-a)$.

For the wave propagation problem considered in this paper, the body forces and electric charges are assumed to be zero. The dynamic wave equations are

$$\begin{aligned}
\frac{\partial T_{rr}}{\partial r} + \frac{1}{r}\frac{\partial T_{r\theta}}{\partial \theta} + \frac{\partial T_{rz}}{\partial z} + \frac{T_{rr} - T_{\theta\theta}}{r} &= \rho \frac{\partial^2 u_r}{\partial t^2} \\
\frac{\partial T_{r\theta}}{\partial r} + \frac{1}{r}\frac{\partial T_{\theta\theta}}{\partial \theta} + \frac{\partial T_{\theta z}}{\partial z} + \frac{2T_{r\theta}}{r} &= \rho \frac{\partial^2 u_\theta}{\partial t^2} \\
\frac{\partial T_{rz}}{\partial r} + \frac{1}{r}\frac{\partial T_{\theta z}}{\partial \theta} + \frac{\partial T_{zz}}{\partial z} + \frac{T_{rz}}{r} &= \rho \frac{\partial^2 u_z}{\partial t^2} \\
\frac{\partial D_r}{\partial r} + \frac{1}{r}\frac{\partial D_\theta}{\partial \theta} + \frac{\partial D_z}{\partial z} + \frac{D_r}{r} &= 0
\end{aligned} \tag{1}$$

where T_{ij}, u_i, and D_i are the stress, elastic displacement, and electric displacement components, respectively, and ρ is the density of the material.

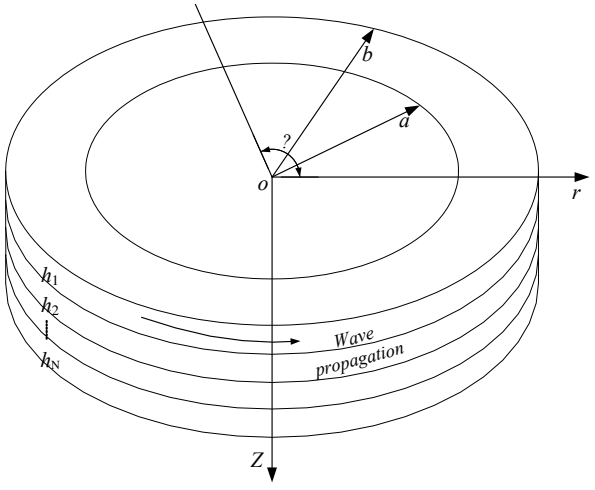

Figure 1. Schematic diagram of a z-direction multilayered rectangular ring.

The relationships between the generalized strain and generalized displacement components can be expressed as

$$\begin{aligned}
&\epsilon_{rr} = \frac{\partial u_r}{\partial r}, && \epsilon_{\theta\theta} = \frac{1}{r}\frac{\partial u_\theta}{\partial \theta} + \frac{u_r}{r}, && \epsilon_{zz} = \frac{\partial u_z}{\partial z},\\
&\epsilon_{\theta z} = \frac{1}{2}\left(\frac{\partial u_\theta}{\partial z} + \frac{\partial u_z}{r\partial \theta}\right), && \epsilon_{rz} = \frac{1}{2}\left(\frac{\partial u_r}{\partial z} + \frac{\partial u_z}{\partial r}\right), && \epsilon_{r\theta} = \frac{1}{2}\left(\frac{1}{r}\frac{\partial u_r}{\partial \theta} + \frac{\partial u_\theta}{\partial r} - \frac{u_\theta}{r}\right)\\
&E_r = -\frac{\partial \phi}{\partial r}, && E_\theta = -\frac{1}{r}\frac{\partial \phi}{\partial \theta}, && E_z = -\frac{\partial \phi}{\partial z},
\end{aligned} \tag{2}$$

where ϵ_{ij}, E_i, and ϕ are the strain components, electric field, and electric potential, respectively.

In this paper, we consider two kinds of layered piezoelectric rings, namely the material stacking direction being respectively in the radial direction and in the axial direction. For a ring with a material stacking direction being in the axial direction, we denote it as a-directional layered ring. Its elastic parameters are expressed as

$$\begin{aligned}
C_{ij} &= \sum_{n=1}^{N} C_{ij}^n \pi_{h_{n-1},h_n}(z), \quad e_{ij} = \sum_{n=1}^{N} e_{ij}^n \pi_{h_{n-1},h_n}(z),\\
\in_{ij} &= \sum_{n=1}^{N} \in_{ij}^n \pi_{h_{n-1},h_n}(z), \qquad \rho = \sum_{n=1}^{N} \rho^n \pi_{h_{n-1},h_n}(z)
\end{aligned} \tag{3}$$

where

$$\pi_{h_{n-1},h_n}(z) = \begin{cases} 1, & h_{n-1} \le z \le h_n,\\ 0, & \text{elsewhere;} \end{cases}$$

N is the number of the layers and C_{ij}^n, e_{ij}^n, $\in_{ij}^n$ are the elastic, piezoelectric and dielectric constants of the n-th layer.

For a layered ring with a stacking direction being in the radial direction, we denote it as r-directional layered ring. Its material constants are expressed as

$$\begin{aligned} C_{ij} &= \sum_{n=1}^{N} C_{ij}^{n}\pi_{d_{n-1},d_n}(r), \quad e_{ij} = \sum_{n=1}^{N} e_{ij}^{n}\pi_{d_{n-1},d_n}(r), \\ \in_{ij} &= \sum_{n=1}^{N} \in_{ij}^{n}\pi_{d_{n-1},d_n}(r), \qquad \rho = \sum_{n=1}^{N} \rho^{n}\pi_{d_{n-1},d_n}(r) \end{aligned} \tag{4}$$

where

$$\pi_{d_{n-1},d_n}(z) = \begin{cases} 1, & d_{n-1} \le r \le d_n, \\ 0, & \text{elsewhere.} \end{cases}$$

Simultaneously, two different polarization directions, i.e., radially polarized direction and axially polarized direction, will be considered. We use "Pr" and "Pa" to represent the two different polarization directions.

We introduce the function $I(r, z)$

$$I(r, z) = \pi(r)\pi(z) = \begin{cases} 1, & a \le r \le b \text{ and } 0 \le z \le h, \\ 0, & \text{elsewhere,} \end{cases} \tag{5}$$

where $\pi(r)$ and $\pi(z)$ are rectangular window functions (the subtraction of two Heaviside function)

$$\pi(r) = \begin{cases} 1, & a \le r \le b, \\ 0, & \text{elsewhere,} \end{cases} \quad \text{and} \quad \pi(z) = \begin{cases} 1, & 0 \le z \le h, \\ 0, & \text{elsewhere.} \end{cases}$$

The derivatives along r and z of $I(r, z)$ are

$$\frac{\partial I(r, z)}{\partial r} = \delta(r - a) - \delta(r - b) \quad \text{and} \quad \frac{\partial I(r, z)}{\partial z} = \delta(z) - \delta(z - h).$$

By introducing the function $I(r, z)$, the traction-free and open-circuit boundary conditions — that is, $T_{rr} = T_{r\theta} = T_{rz} = T_{\theta z} = T_{zz} = D_r = D_z = 0$ at the four boundaries — are automatically incorporated in the constitutive relations of the ring [Ludwig and Lengeler 1964]:

$$\begin{Bmatrix} T_{\theta\theta} \\ T_{zz} \\ T_{rr} \\ T_{rz} \\ T_{r\theta} \\ T_{\theta z} \end{Bmatrix} = \begin{bmatrix} C_{11} & C_{12} & C_{13} & C_{14} & C_{15} & C_{16} \\ & C_{22} & C_{23} & C_{24} & C_{25} & C_{26} \\ & & C_{33} & C_{34} & C_{35} & C_{36} \\ & & & C_{44} & C_{45} & C_{46} \\ & \text{symmetry} & & & C_{55} & C_{56} \\ & & & & & C_{66} \end{bmatrix} \begin{Bmatrix} \epsilon_{\theta\theta} I(r, z) \\ \epsilon_{zz} I(r, z) \\ \epsilon_{rr} I(r, z) \\ 2\epsilon_{rz} I(r, z) \\ 2\epsilon_{r\theta} I(r, z) \\ 2\epsilon_{\theta z} I(r, z) \end{Bmatrix} - \begin{bmatrix} e_{11} & e_{21} & e_{31} \\ e_{12} & e_{22} & e_{32} \\ e_{13} & e_{23} & e_{33} \\ e_{14} & e_{24} & e_{34} \\ e_{15} & e_{25} & e_{35} \\ e_{16} & e_{26} & e_{36} \end{bmatrix} \begin{Bmatrix} E_\theta I(r, z) \\ E_z I(r, z) \\ E_r I(r, z) \end{Bmatrix} \tag{6a}$$

$$\begin{Bmatrix} D_\theta \\ D_z \\ D_r \end{Bmatrix} = \begin{bmatrix} e_{11} & e_{12} & e_{13} & e_{14} & e_{15} & e_{16} \\ e_{21} & e_{22} & e_{23} & e_{24} & e_{25} & e_{26} \\ e_{31} & e_{32} & e_{33} & e_{34} & e_{35} & e_{36} \end{bmatrix} \begin{Bmatrix} \epsilon_{\theta\theta} I(r, z) \\ \epsilon_{zz} I(r, z) \\ \epsilon_{rr} I(r, z) \\ 2\epsilon_{rz} I(r, z) \\ 2\epsilon_{r\theta} I(r, z) \\ 2\epsilon_{\theta z} I(r, z) \end{Bmatrix} + \begin{bmatrix} \in_{11} & \in_{12} & \in_{13} \\ & \in_{22} & \in_{23} \\ \text{symmetry} & & \in_{33} \end{bmatrix} \begin{Bmatrix} E_\theta I(r, z) \\ E_z I(r, z) \\ E_r I(r, z) \end{Bmatrix}. \tag{6b}$$

For a time-harmonic wave propagating in the circumferential direction of a ring, we assume the displacement components to be of the form

$$\begin{aligned} u_r(r,\theta,z,t) &= \exp(ikb\theta - i\omega t)\,U(r,z), \quad u_\theta(r,\theta,z,t) = \exp(ikb\theta - i\omega t)\,V(r,z), \\ u_z(r,\theta,z,t) &= \exp(ikb\theta - i\omega t)\,W(r,z), \quad \psi(r,\theta,z,t) = \exp(ikb\theta - i\omega t)\,X(r,z), \end{aligned} \tag{7}$$

where $U(r,z)$, $V(r,z)$, and $W(r,z)$ represent the amplitude of vibration in the r, θ, z directions, respectively, and $X(r,z)$ represents the amplitude of electric potential. Also, k is the magnitude of the wave vector in the propagation direction, and ω is the angular frequency.

Substituting (2), (6), and (7) into (1), the governing differential equations in terms of the displacement and the electric potential components can be obtained. In the case of Pr r-directional layered orthotropic ring, they are given by

$$\begin{aligned} \sum_{n=1}^{N}\big\{&[C_{33}^n(r^2U_{,rr}+rU_{,r}) - (C_{11}^n+(kb)^2C_{55}^n)U + C_{44}^n r^2U_{,zz} + ikb(C_{13}^n+C_{55}^n)rV_{,r} \\ &- ikb(C_{11}^n+C_{55}^n)V + (C_{23}^n+C_{44}^n)r^2W_{,rz} + (C_{23}^n-C_{12}^n)rW_{,z} + e_{33}^n(r^2X_{,rr}+rX_{,r}) + e_{24}^n r^2X_{,zz} \\ &- (kb)^2e_{15}^nX - e_{31}^nrX_{,r}]\pi_{d_{n-1},d_n}(r)\cdot\pi(z) + [C_{44}^nr^2(U_{,z}+W_{,r}) + e_{24}^nr^2X_{,z}]\pi_{d_{n-1},d_n}(r)\cdot\pi(z)_{,z} \\ &+ [C_{33}^nr^2U_{,r} + C_{13}^nr(ikbV+U) + C_{23}^nr^2W_{,z} + e_{33}^nr^2X_{,r}]\pi_{d_{n-1},d_n}(r)_{,r}\cdot\pi(z)\big\} \\ &= -\sum_{n=1}^{N}\rho^n\pi_{d_{n-1},d_n}(r)r^2\omega^2U\cdot\pi(z), \end{aligned} \tag{8a}$$

$$\begin{aligned} \sum_{n=1}^{N}\big\{&[C_{55}^n(r^2V_{,rr}+rV_{,r}) - (C_{55}^n+(kb)^2C_{11}^n)V + ikb(C_{13}^n+C_{55}^n)rU_{,r} + ikb(C_{11}^n+C_{66}^n)U \\ &+ C_{66}^nr^2V_{,zz} + ikb(C_{12}^n+C_{66}^n)rW_{,z} + (e_{31}^n+e_{15}^n)rX_{,r} + 2e_{15}^nX]\pi_{d_{n-1},d_n}(r)\cdot\pi(z) \\ &+ C_{66}^n(r^2V_{,z} + ikbrW)\pi_{d_{n-1},d_n}(r)\cdot\pi(z)_{,z} \\ &+ [C_{55}^n(r^2V_{,r}+rV+ikbrU) + e_{15}^nrX]\pi_{d_{n-1},d_n}(r)_{,r}\cdot\pi(z)\big\} \\ &= -\sum_{n=1}^{N}\rho^n\pi_{d_{n-1},d_n}(r)\cdot\pi(z)r^2\omega^2V, \end{aligned} \tag{8b}$$

$$\begin{aligned} \sum_{n=1}^{N}\big\{&[C_{44}^n(r^2W_{,rr}+rW_{,r}) - (kb)^2C_{66}^nW + C_{22}^nr^2W_{,zz} + (C_{23}^n+C_{44}^n)r^2U_{,rz} + (C_{12}^n+C_{44}^n)rU_{,z} \\ &+ ikb(C_{12}^n+C_{66}^n)rV_{,z} + (e_{24}^n+e_{32}^n)r^2X_{,rz} + e_{24}^nrX_{,z}]\pi_{d_{n-1},d_n}(r)\cdot\pi(z) \\ &+ [C_{12}^nr(ikbV+U)C_{23}^nr^2U_{,r} + C_{22}^nr^2W_{,z} + e_{32}^nr^2X_{,r}]\pi_{d_{n-1},d_n}(r)\cdot\pi(z)_{,z} \\ &+ [C_{44}^nr^2(W_{,r}+U_{,z}) + e_{24}^nr^2X_{,z}]\pi_{d_{n-1},d_n}(r)_{,r}\cdot\pi(z)\big\} \\ &= -\sum_{n=1}^{N}\rho^nr^2\omega^2V\pi_{d_{n-1},d_n}(r)\cdot\pi(z), \end{aligned} \tag{8c}$$

$$\sum_{n=1}^{N}\Big\{[e_{33}^n(r^2U_{,rr}+rU_{,r})+e_{31}^n rU_{,r}-(kb)^2e_{15}^nU+e_{24}^nr^2U_{,zz}-e_{15}^nV+(e_{31}^n+e_{15}^n)rV_{,r}+e_{24}^nrW_{,z}$$
$$+(e_{24}^n+e_{32}^n)r^2W_{,rz}+(kb)^2\in_{11}^nX-\in_{33}^n(r^2X_{,rr}+rX_{,r})-\in_{22}^nr^2X_{,zz}]\pi_{d_{n-1},d_n}(r)\cdot\pi(z)$$
$$+[e_{33}^nr^2U_{,r}+e_{31}^nrU+e_{31}^nrV+e_{32}^nr^2W_{,z}-\in_{33}^nr^2X_{,r}]\pi_{d_{n-1},d_n}(r)_{,r}\cdot\pi(z)$$
$$+[e_{24}^nr^2U_{,z}+e_{24}^nr^2W_{,r}-\in_{22}^nr^2X_{,z}]\pi_{d_{n-1},d_n}(r)\cdot\pi(z)_{,z}\Big\}$$
$$=0. \tag{8d}$$

where a subscript comma indicates partial derivative.

To solve the coupled wave equation, $U(r,z)$, $V(r,z)$, $W(r,z)$, and $X(r,z)$ are expanded into products of two Legendre orthogonal polynomial series as

$$\begin{aligned} U(r,z)&=\sum_{m,j=0}^{\infty}p_{m,j}^1Q_m(r)Q_j(z), & V(r,z)&=\sum_{m,j=0}^{\infty}p_{m,j}^2Q_m(r)Q_j(z),\\ W(r,z)&=\sum_{m,j=0}^{\infty}p_{m,j}^3Q_m(r)Q_j(z), & X(r,z)&=\sum_{m,j=0}^{\infty}p_{m,j}^4Q_m(r)Q_j(z), \end{aligned} \tag{9}$$

where $p_{m,j}^i$ $(i=1,2,3,4)$ are the expansion coefficients and

$$Q_m(r)=\sqrt{\frac{2m+1}{b-a}}P_m\left(\frac{2r-b-a}{b-a}\right),\qquad Q_j(z)=\sqrt{\frac{2j+1}{h}}P_j\left(\frac{2z-h}{h}\right) \tag{10}$$

with P_m and P_j being the m-th and the j-th Legendre polynomial. Theoretically, m and j run from 0 to ∞. However, in practice the summation over the polynomials in (9) can be truncated at some finite values $m=M$ and $j=J$, when the effects of higher order terms become negligible.

Equations (8) are multiplied by $Q_n(r)$ with n running from 0 to M, and by $Q_p(z)$ with p from 0 to J, respectively. Then integrating over z from 0 to h and over r from a to b gives the following system of linear algebraic equations:

$${}^lA_{11}^{n,p,m,j}p_{m,j}^1+{}^lA_{12}^{n,p,m,j}p_{m,j}^2+{}^lA_{13}^{n,p,m,j}p_{m,j}^3+{}^lA_{14}^{n,p,m,j}p_{m,j}^4=-\omega^2\cdot{}^lM_{n,p,m,j}p_{m,j}^1, \tag{11a}$$
$${}^lA_{21}^{n,p,m,j}p_{m,j}^1+{}^lA_{22}^{n,p,m,j}p_{m,j}^2+{}^lA_{23}^{n,p,m,j}p_{m,j}^3+{}^lA_{24}^{n,p,m,j}p_{m,j}^4=-\omega^2\cdot{}^lM_{n,p,m,j}p_{m,j}^2, \tag{11b}$$
$${}^lA_{31}^{n,p,m,j}p_{m,j}^1+{}^lA_{32}^{n,p,m,j}p_{m,j}^2+{}^lA_{33}^{n,p,m,j}p_{m,j}^3+{}^lA_{34}^{n,p,m,j}p_{m,j}^4=-\omega^2\cdot{}^lM_{n,p,m,j}p_{m,j}^3, \tag{11c}$$
$${}^lA_{41}^{n,p,m,j}p_{m,j}^1+{}^lA_{42}^{n,p,m,j}p_{m,j}^2+{}^lA_{43}^{n,p,m,j}p_{m,j}^3+{}^lA_{44}^{n,p,m,j}p_{m,j}^4=0, \tag{11d}$$

where ${}^lA_{\alpha\beta}^{n,p,m,j}$ $(\alpha,\beta=1,2,3,4)$ and ${}^lM_{n,p,m,j}$ are the elements of the nonsymmetric matrices $\boldsymbol{A}$ and $\boldsymbol{M}$, which can be obtained by using (8).

Equation (11d) can be written as

$$p_{m,j}^4=-\left({}^lA_{44}^{n,p,m,j}\right)^{-1}\left({}^lA_{41}^{n,p,m,j}p_{m,j}^1+{}^lA_{42}^{n,p,m,j}p_{m,j}^2+{}^lA_{43}^{n,p,m,j}p_{m,j}^3\right). \tag{12}$$

Substituting (12) into (11a)–(11c) gives

$$\begin{aligned}
&\left[{}^{l}A_{11}^{n,p,m,j} - {}^{l}A_{14}^{n,p,m,j}\left({}^{l}A_{44}^{n,p,m,j}\right)^{-1}\cdot {}^{l}A_{41}^{n,p,m,j}\right]p_{m,j}^{1}\\
&+\left[{}^{l}A_{12}^{n,p,m,j} - {}^{l}A_{14}^{n,p,m,j}\left({}^{l}A_{44}^{n,p,m,j}\right)^{-1}\cdot {}^{l}A_{42}^{n,p,m,j}\right]p_{m,j}^{2}\\
&+\left[{}^{l}A_{13}^{n,p,m,j} - {}^{l}A_{14}^{n,p,m,j}\left({}^{l}A_{44}^{n,p,m,j}\right)^{-1}\cdot {}^{l}A_{43}^{n,p,m,j}\right]p_{m,j}^{3} = -\omega^{2l}M_{n,p,m,j}\,p_{m,j}^{1}, \qquad (13a)\\
&\left[{}^{l}A_{21}^{n,p,m,j} - {}^{l}A_{24}^{n,p,m,j}\left({}^{l}A_{44}^{n,p,m,j}\right)^{-1}\cdot {}^{l}A_{41}^{n,p,m,j}\right]p_{m,j}^{1}\\
&+\left[{}^{l}A_{22}^{n,p,m,j} - {}^{l}A_{24}^{n,p,m,j}\left({}^{l}A_{44}^{n,p,m,j}\right)^{-1}\cdot {}^{l}A_{42}^{n,p,m,j}\right]p_{m,j}^{2}\\
&+\left[{}^{l}A_{23}^{n,p,m,j} - {}^{l}A_{24}^{n,p,m,j}\left({}^{l}A_{44}^{n,p,m,j}\right)^{-1}\cdot {}^{l}A_{43}^{n,p,m,j}\right]p_{m,j}^{3} = -\omega^{2l}M_{n,p,m,j}\,p_{m,j}^{2}, \qquad (13b)\\
&\left[{}^{l}A_{31}^{n,p,m,j} - {}^{l}A_{34}^{n,p,m,j}\left({}^{l}A_{44}^{n,p,m,j}\right)^{-1}\cdot {}^{l}A_{41}^{n,p,m,j}\right]p_{m,j}^{1}\\
&+\left[{}^{l}A_{32}^{n,p,m,j} - {}^{l}A_{34}^{n,p,m,j}\left({}^{l}A_{44}^{n,p,m,j}\right)^{-1}\cdot {}^{l}A_{42}^{n,p,m,j}\right]p_{m,j}^{2}\\
&+\left[{}^{l}A_{33}^{n,p,m,j} - {}^{l}A_{34}^{n,p,m,j}\left({}^{l}A_{44}^{n,p,m,j}\right)^{-1}\cdot {}^{l}A_{43}^{n,p,m,j}\right]p_{m,j}^{3} = -\omega^{2l}M_{n,p,m,j}\,p_{m,j}^{3}. \qquad (13c)
\end{aligned}$$

Then, (11) can be rewritten as

$$\begin{bmatrix} {}^{l}\bar{A}_{11}^{n,p,m,j} & {}^{l}\bar{A}_{12}^{n,p,m,j} & {}^{l}\bar{A}_{13}^{n,p,m,j} \\ {}^{l}\bar{A}_{21}^{n,p,m,j} & {}^{l}\bar{A}_{22}^{n,p,m,j} & {}^{l}\bar{A}_{22}^{n,p,m,j} \\ {}^{l}\bar{A}_{31}^{n,p,m,j} & {}^{l}\bar{A}_{32}^{n,p,m,j} & {}^{l}\bar{A}_{33}^{n,p,m,j} \end{bmatrix} \begin{Bmatrix} p_{m,j}^{1} \\ p_{m,j}^{2} \\ p_{m,j}^{3} \end{Bmatrix} = -\omega^{2l}M_{n,p,m,j} \begin{bmatrix} 1 & 0 & 0 \\ 0 & 1 & 0 \\ 0 & 0 & 1 \end{bmatrix} \begin{Bmatrix} p_{m,j}^{1} \\ p_{m,j}^{2} \\ p_{m,j}^{3} \end{Bmatrix}. \qquad (14)$$

So, (14) forms the eigenvalue problem to be solved. The eigenvalues ω^2 give the angular frequency of the guided wave modes, and the eigenvectors $p_{m,j}^{i}$ $(i = 1, 2, 3)$ allow the mechanical displacement components to be calculated, and $p_{m,j}^{4}$, which can be obtained from (12), determines the electric potential distribution. By using the relation $Vph = \omega/k$, the phase wave velocity Vph can be obtained. In the computing progress, the obtained eigenvalues are complex, but their imaginary parts are all very small compared to their corresponding real parts. For one eigenvalue, its imaginary part is less than one millionth of its real part. So, we just think the real parts are solutions of the system.

3. Numerical results and discussions

Based on the solution procedure as described in Section 2, a computer program in terms of the extended polynomial approach has been written using Mathematica to calculate the wave dispersion curves, the displacement and the electric potential distributions for the layered piezoelectric rectangular rings.

3.1. ***Comparison with the available solution from the transfer matrix method.*** Since no reference results for the wave dispersion curves in layered piezoelectric rectangular rings can be found in literature, we consider an a-direction layered purely elastic rectangular ring with a very large radius to thickness ratio ($\eta = 1000$) to make a comparison with known results of a straightly layered bar from the semi-analytical finite element method [Taweel et al. 2000]. It is a three layer $+30°/-30°/+30°$ (with respect to the θ-axis) fiber composite rectangular ring with equal layer-thickness. The bar's width-to-height ratio is $d/h = 2$ and the material properties are given by (15) [loc. cit.]. Figure 2 shows the corresponding dispersion curves, in which the solid lines are from [loc. cit.], and the dotted lines are obtained from the

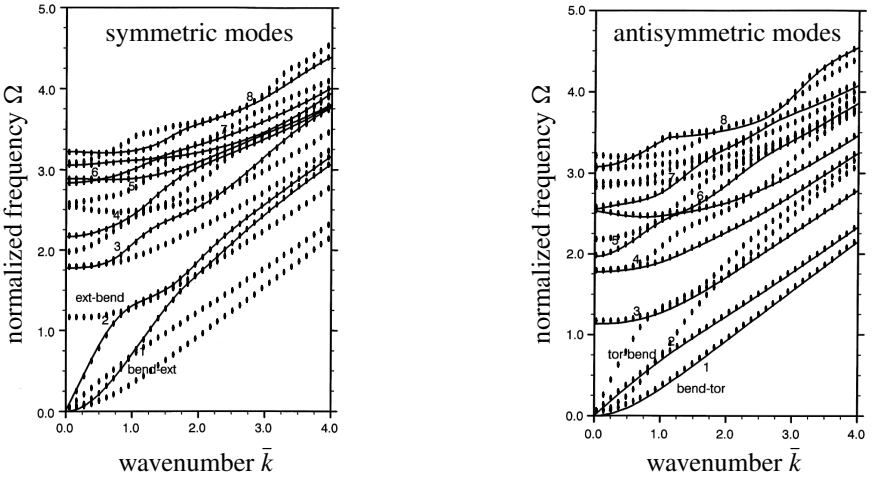

Figure 2. Dispersion curves for the three-layer $[+30°/-30°/+30°]$, equal thickness fiber composite rectangular structures. Solid lines: the results from the semi-analytical FEM [Taweel et al. 2000] for the straightly layered bar; dotted lines: the results of the presented method for the layered ring with a very large radius to thickness ratio ($\eta = 1000$).

proposed polynomial approach. The normalized frequency is defined by $\omega/\sqrt{15.167\,\text{GPa}/\rho h^2}$, and the dimensionless wave number kh is introduced. In [Taweel et al. 2000], all wave modes are assorted into two classes and shown in two separate figures. But the proposed method in this paper can only calculate all wave modes together. So, we put the dispersion curves of all wave modes in each figure to make the comparison. As can be seen, the results from the proposed polynomial approach agree very well with the available reference data.

$$[C]_{\pm 30^\circ} = \begin{bmatrix} 86.231 & 27.5875 & 3.9233 & 0 & 0 & \mp 40.6352 \\ & 23.73 & 3.6078 & 0 & 0 & \mp 13.4923 \\ & & 15.986 & 0 & 0 & \mp 0.2732 \\ & & & 6.1663 & 0 & 0 \\ & \text{symmetry} & & & 5.9628 & 0 \\ & & & & & 29.3675 \end{bmatrix} \text{GPa}. \tag{15}$$

3.2. ***Dispersion curves in multilayered piezoelectric rectangular rings.*** In this section, layered piezoelectric rectangular rings composed of BSN (B) and PZT-4 (P) are studied. The corresponding material parameters can be seen in [Guo et al. 2009]. Here, the elastic constants of r-polarization and a-polarization are taken as the same in order to make appropriate comparisons.

Firstly, four square rings with $\eta = 10$ are considered. Their stacking sequences, thickness ratio are the same, P/B/P-1/1/1. Their stacking directions and polarization directions are different: (a) is a Pr r-directional layered ring; (b) is a Pr a-directional layered ring; (c) is a Pa r-directional layered ring; (d) is a Pa a-directional layered ring. Their phase velocity dispersion curves are shown in Figure 3. It can be seen that both the stacking direction and the polarization direction have influences on the dispersion curves.

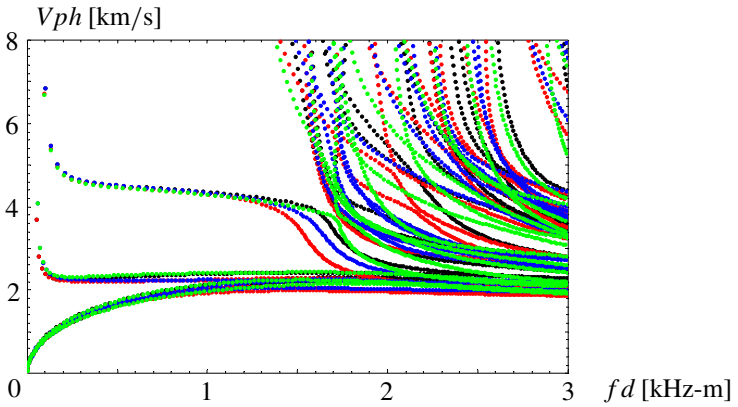

Figure 3. Phase velocity dispersion curves for the P/B/P-1/1/1 square rings with $\eta = 10$. Layered rings: Pa a-directional (red), Pa r-directional (green), Pr a-directional (black), and Pr r-directional (blue).

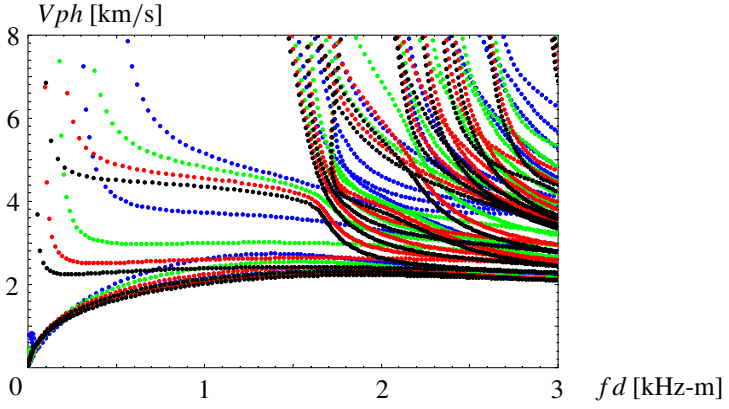

Figure 4. Phase velocity dispersion curves for r-polarized and a-directional P/B/P-1/1/1 square rings: $\eta = 2$ (blue), $\eta = 3$ (green), $\eta = 5$ (red), and $\eta = 10$ (black).

Then, Figure 4 shows the dispersion curves for r-polarized and a-directional P/B/P-1/1/1 square rings with different radius to thickness ratios, $\eta = 2, 3, 5$, and 10, respectively. Obviously, the radius to thickness ratio has significant influences on the dispersion curves.

Next, the different stacking sequences are discussed. Phase velocity dispersion curves for three r-polarized and r-directional thickness-equal rectangular rings with $\eta = 2$ and $d/h = 0.5$ are shown in Figure 5. Their stacking sequences are B/P/P, P/B/P, and P/P/B. On the whole, the phase velocity of B/P/P ring is the lowest and that of P/P/B ring is the highest. In fact, the wave velocity of BSN is higher than that of PZT-4. Moreover, the volume fraction of BSN in B/P/P ring is the lowest in the three r-directional layered rings because of its BSN being located at the innermost layer. When the radius to thickness ratio becomes smaller, the difference among the volume factions of the three r-directional

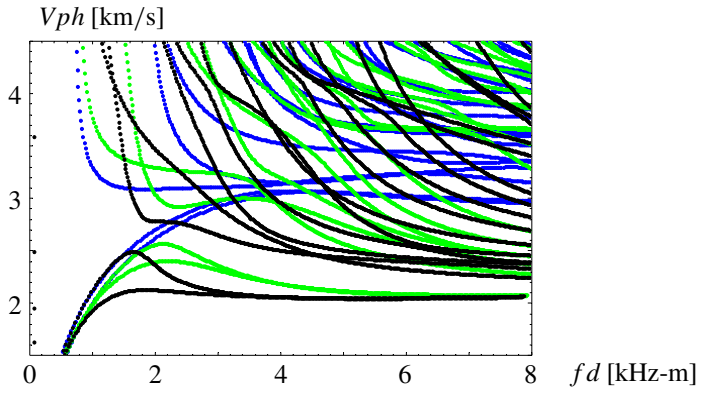

Figure 5. Phase velocity dispersion curves for r-polarized and r-directional thickness equal rectangular rings with $\eta = 2$ and $d/h = 0.5$: B/P/P (black), P/B/P (green), and P/P/B (blue).

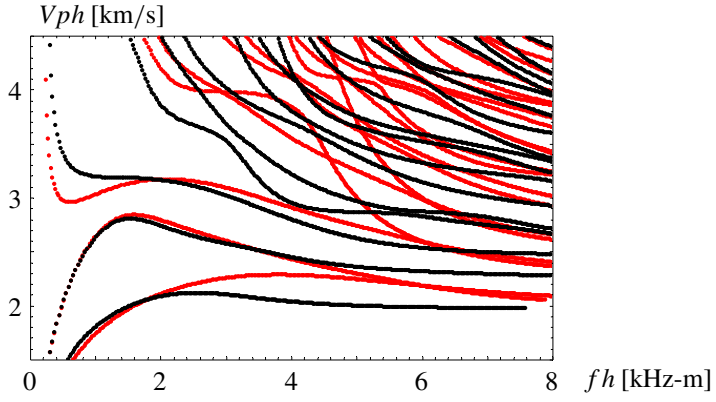

Figure 6. Phase velocity dispersion curves for r-polarized and a-directional thickness equal rectangular rings with $\eta = 2$ and $d/h = 2$: P/B/P (red) and P/P/B (black).

layered rings becomes larger. For a-directional layered rings, the volume fractions of P/B/P-1/1/1 and P/P/B-1/1/1 rings are the same, but different stacking sequence still results in different dispersion curves, as shown in Figure 6.

3.3. ***Displacement and electric potential shapes.*** This section discusses the wave characteristics of layered square rings through the displacement and the electric potential shapes. The displacement in wave propagating direction and the electric potential shapes at $kd = 30.3$ of the fourth and seventh modes for Pr a-directional layered square ring are illustrated in Figure 7. It can be seen that the displacement and the electric potential are always concentrated near the four boundaries. Furthermore, they are mostly localized in the layers of PZT-4, which has a lower wave speed than BSN. In order to confirm this phenomenon, the top of Figure 8 shows the seventh mode of the Pr a-directional B/P/B-1/1/1 square ring with $\eta = 10$ at $kd = 30.3$. The displacement and the electric potential are mostly localized in the middle layer, the layer of PZT-4. Finally, the bottom of Figure 8 shows, for the case of small radius

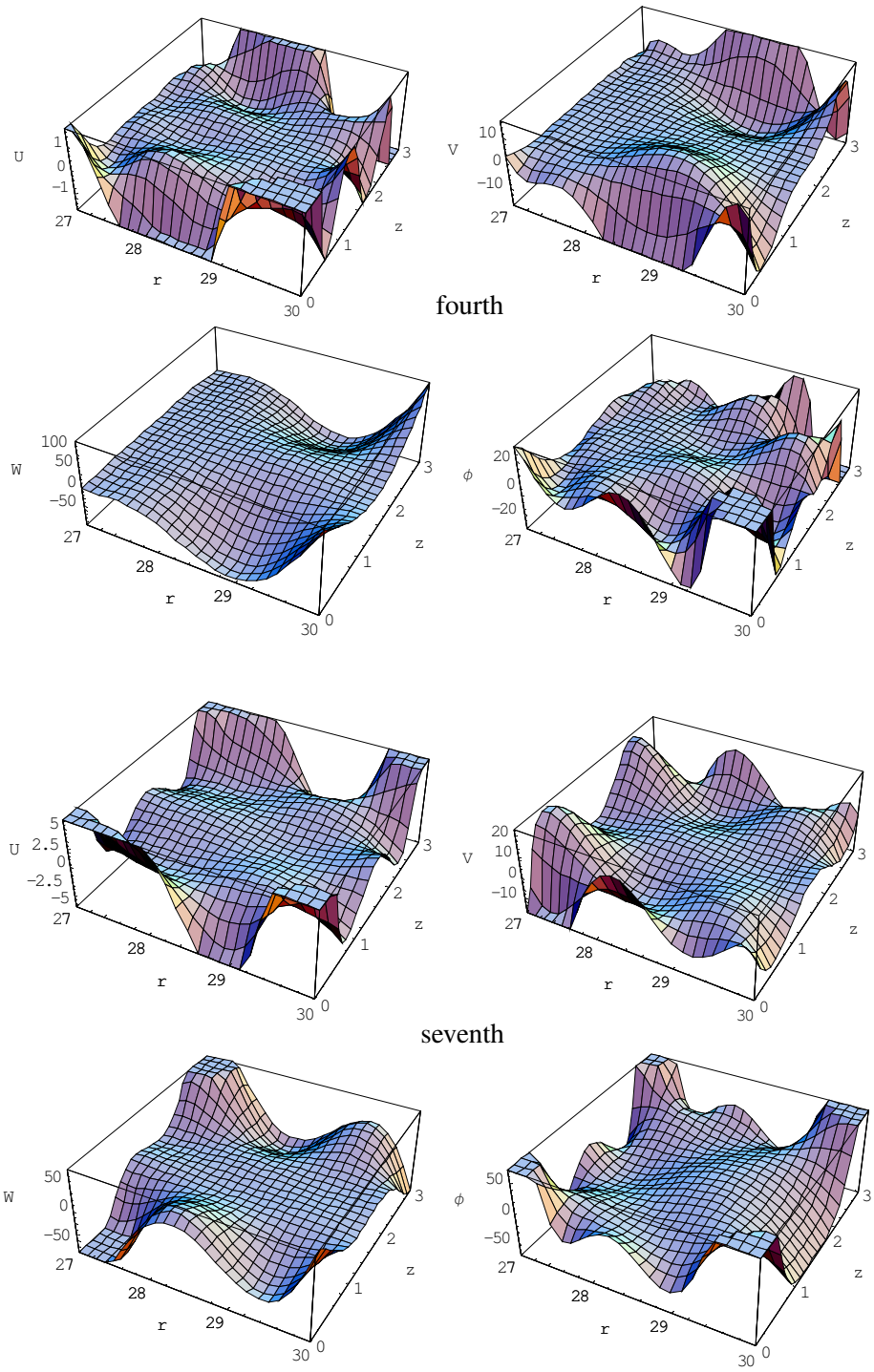

Figure 7. Displacement and electric potential profiles of the fourth mode (top) and seventh mode (bottom) for the Pr a-directional P/B/P-1/1/1 square ring with $\eta = 10$ at $kd = 30.3$.

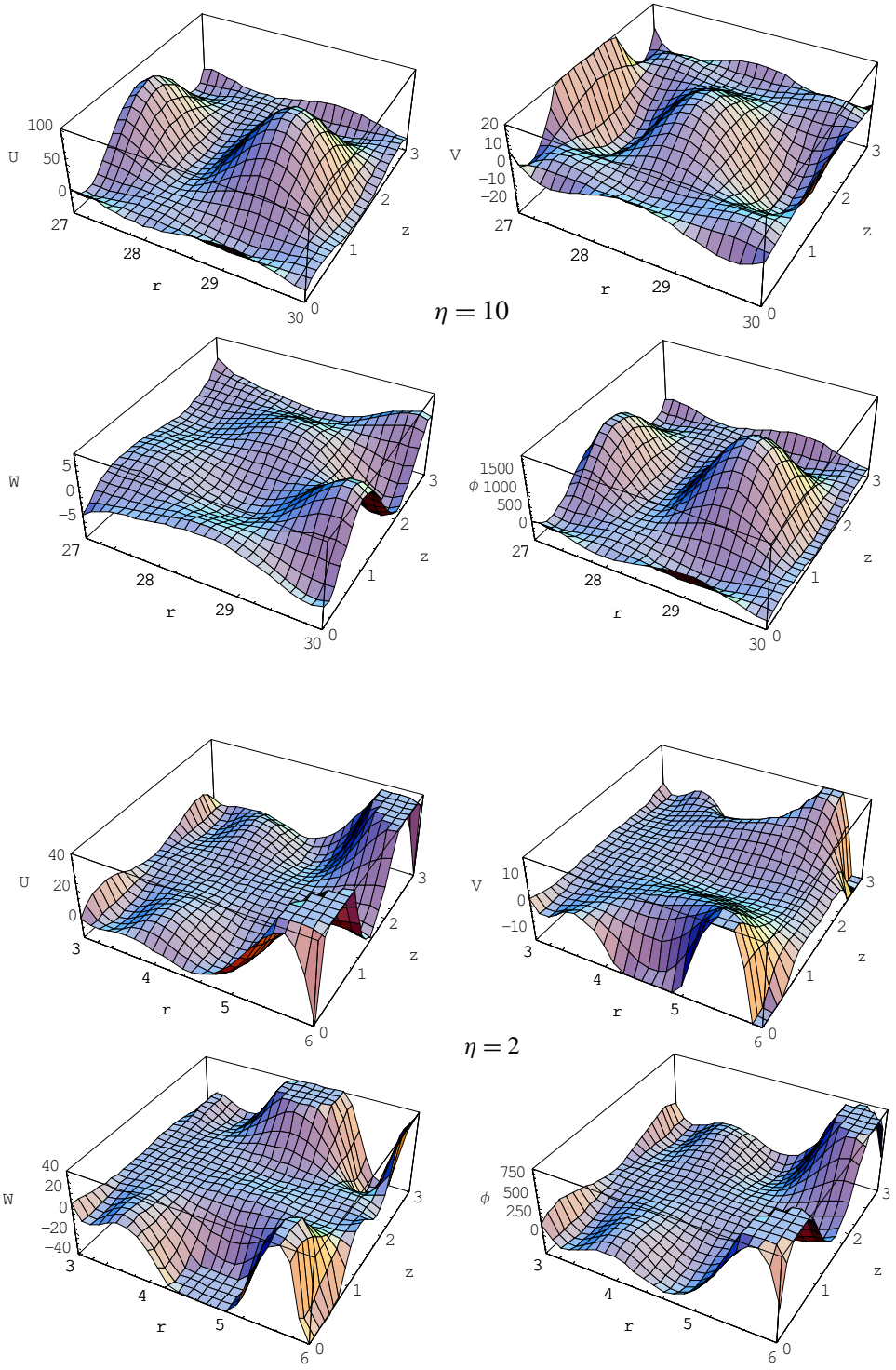

Figure 8. Displacement and electric potential profiles of the seventh mode for the Pr a-directional B/P/B-1/1/1 square ring at $kd = 30.3$. with $\eta = 10$ (top) and $\eta = 2$ (bottom).

to thickness ratio, the displacement and the electric potential of the Pr a-directional P/B/P-1/1/1 square ring with $\eta = 2$. The displacement and the electric potential are still mostly localized in the layers of PZT-4, but they become closer to the outer surface. In order to save space, above figures only show the displacement profile in the x direction. The displacement profiles in the other two directions show the same phenomena as the x direction displacement.

4. Conclusions

This paper proposed a double orthogonal polynomial series approach to solve wave propagation problems in 2-D multilayered piezoelectric rectangular rings. The dispersion curves, the displacement, and the electric potential shapes of various layered rectangular rings are obtained. According to the present numerical results, we can draw the following conclusions:

(a) Numerical comparison of the wave dispersion curves show that the double orthogonal polynomial method can accurately and efficiently solve the guided wave propagation problems in multilayered rectangular ring.

(b) The polarization direction and stacking sequence have weak influences on the dispersion curves, but radius to thickness ratio, volume fraction, and width to height ratio have significant influences on the dispersion curves. So, we can change the wave speed of the piezoelectric ring transducer through adjusting its thickness ratio, volume fraction and width to height ratio.

(b) The high frequency wave displacements and electric potential are mainly concentrated in the layer with a lower wave speed and they approach the outer surface of the ring with a little radius to thickness. Through changing the stacking sequence of the layered piezoelectric ring transducer, we can position the maximum displacement and electric potential where we want.

Acknowledgments

This work was supported by the National Natural Science Foundation of China (No. 11272115) and the Outstanding Youth Science Foundation of Henan Polytechnic University (No. J2013-08) and Science and Technology Agency of Henan Province (No. 144100510016), China.

References

[Adler 2000] E. L. Adler, "Bulk and surface acoustic waves in anisotropic solids", *Int. J. High Speed Electron. Syst.* **10**:03 (2000), 653–684.

[Ballandras et al. 2004] S. Ballandras, A. Reinhardt, V. Laude, A. Soufyane, S. Camou, W. Daniau, T. Pastureaud, W. Steichen, R. Lardat, M. Solal, and P. Ventura, "Simulations of surface acoustic wave devices built on stratified media using a mixed finite element/boundary integral formulation", *J. Appl. Phys.* **96**:12 (2004), 7731–7741.

[Cai et al. 2001] C. Cai, G. R. Liu, and K. Y. Lam, "A technique for modelling multiple piezoelectric layers", *Smart Mater. Struct.* **10**:4 (2001), 689–694.

[Chou et al. 1991] C. S. Chou, J. W. Yang, Y. C. Hwang, and H. J. Yang, "Analysis on vibrating piezoelectric beam gyroscope", *Int. J. Appl. Electrom. Mater.* **2**:3 (1991), 227–241.

[Collet 2004] B. Collet, "Recursive surface impedance matrix methods for ultrasonic wave propagation in piezoelectric multilayers", *Ultrasonics* **42**:1–9 (2004), 189–197.

[Datta and Hunsinger 1978] S. Datta and B. J. Hunsinger, "Analysis of surface waves using orthogonal functions", *J. Appl. Phys.* **49**:2 (1978), 475–479.

[Dökmeci 1974] M. C. Dökmeci, "A theory of high frequency vibrations of piezoelectric cyrstal bars", *Int. J. Solids Struct.* **10**:4 (1974), 401–409.

[Guo et al. 2009] Y. Q. Guo, W. Q. Chen, and Y. L. Zhang, "Guided wave propagation in multilayered piezoelectric structures", *Sci. China G Phys. Mech. Astronom.* **52**:7 (2009), 1094–1104.

[Kim and Hunt 1990] Y. Kim and W. D. Hunt, "Acoustic fields and velocities for surface-acoustic-wave propagation in multilayered structures: An extension of the Laguerre polynomial approach", *J. Appl. Phys.* **68**:10 (1990), 4993–4997.

[Lefebvre et al. 1999] J.-E. Lefebvre, V. Zhang, J. Gazalet, and T. Gryba, "Legendre polynomial approach for modeling free-ultrasonic waves in multilayered plates", *J. Appl. Phys.* **85**:7 (1999), 3419–3427.

[Ludwig and Lengeler 1964] W. Ludwig and B. Lengeler, "Surface waves and rotational invariance in lattice theory", *Solid State Comm.* **2**:3 (1964), 83–86.

[Maradudin et al. 1972] A. A. Maradudin, R. F. Wallis, D. L. Mills, and R. L. Ballard, "Vibrational edge modes in finite crystals", *Phys. Rev. B* **6**:4 (1972), 1106–1111.

[Mindlin and McNiven 1960] R. D. Mindlin and H. D. McNiven, "Axially symmetric waves in elastic rods", *J. Appl. Mech.* (*ASME*) **27**:1 (1960), 145–151.

[Nayfeh 1995] A. H. Nayfeh, *Wave propagation in layered anisotropic media: With applications to composites*, North-Holland Ser. Appl. Math. Mech. **39**, North-Holland, Amsterdam, 1995.

[Pastureaud et al. 2002] T. Pastureaud, V. Laude, and S. Ballandras, "Stable scattering-matrix method for surface acoustic waves in piezoelectric multilayers", *Appl. Phys. Lett.* **80**:14 (2002), 2544–2546.

[Taweel et al. 2000] H. Taweel, S. B. Dong, and M. Kazic, "Wave reflection from the free end of a cylinder with an arbitrary cross-section", *Int. J. Solids Struct.* **37**:12 (2000), 1701–1726.

[Wang and Rokhlin 2002] L. Wang and S. I. Rokhlin, "Recursive asymptotic stiffness matrix method for analysis of surface acoustic wave devices on layered piezoelectric media", *Appl. Phys. Lett.* **81**:21 (2002), 4049–4051.

[Wang and Rokhlin 2004] L. Wang and S. I. Rokhlin, "Modeling of wave propagation in layered piezoelectric media by a recursive asymptotic method", *IEEE Trans. Ultrason. Ferroelectr. Freq. Control* **51**:9 (2004), 1060–1071.

[Wu et al. 2014] B. Wu, W. Q. Chen, and J. Yang, "One-dimensional equations for coupled extensional, radial, and axial-shear motions of circular piezoelectric ceramic rods with axial poling", *Arch. Appl. Mech.* **84**:9-11 (2014), 1677–1689.

[Yu et al. 2012] J. G. Yu, J.-E. Lefebvre, Y. G. Guo, and L. Elmaimouni, "Wave propagation in the circumferential direction of general multilayered piezoelectric cylindrical plates", *IEEE Trans. Ultrason. Ferroelectr. Freq. Control* **59**:11 (2012), 2498–2508.

[Yu et al. 2013] J. G. Yu, J.-E. Lefebvre, and Y. Q. Guo, "Wave propagation in multilayered piezoelectric spherical plates", *Acta Mech.* **224**:7 (2013), 1335–1349.

[Zhang et al. 2001] V. Y. Zhang, J.-E. Lefebvre, C. Bruneel, and T. Gryba, "A unified formalism using effective surface permittivity to study acoustic waves in various anisotropic and piezoelectric multilayers", *IEEE Trans. Ultrason. Ferroelectr. Freq. Control* **48**:5 (2001), 1449–1461.

Received 11 Mar 2014. Revised 31 Jul 2015. Accepted 29 Nov 2015.

JIANGONG YU: yu@emails.bjut.edu.cn
School of Mechanical and Power Engineering, Henan Polytechnic University, Jaiozuo, 454003, China

XIAODONG YANG: 806607231@qq.com
School of Mechanical and Power Engineering, Henan Polytechnic University, Jiaozuo, 454003, China

JEAN-ETIENNE LEFEBVRE: jean-etienne.lefebvre@univ-valenciennes.fr
University of Lille Nord de France, F-59000 Lille, France, and, UVHC, IEMN-DOAE, F-59313 Valenciennes Cedex 9, France, and, CNRS, UMR 8520, F-59650 Villeneuve d'Ascq, France

JOURNAL OF MECHANICS OF MATERIALS AND STRUCTURES
Vol. 11, No. 3, 2016
dx.doi.org/10.2140/jomms.2016.11.259

EFFECTIVE BOUNDARY CONDITION METHOD AND APPROXIMATE SECULAR EQUATIONS OF RAYLEIGH WAVES IN ORTHOTROPIC HALF-SPACES COATED BY A THIN LAYER

PHAM CHI VINH AND VU THI NGOC ANH

In this paper, the effective boundary condition method for deriving approximate secular equations of Rayleigh waves propagating in elastic half-spaces coated by a thin layer is introduced. Then, the method is used to obtain approximate secular equations of Rayleigh waves in compressible (incompressible) orthotropic half-spaces covered by a thin incompressible (compressible) orthotropic layer. Approximate secular equations of third order have been derived and it is shown that they have high accuracies. Some numerical examples are carried out to evaluate the effect of incompressibility on the Rayleigh wave propagation. It is shown that the incompressibility affects considerably on the Rayleigh wave velocity.

1. Introduction

The structures of a thin film attached to solids, modeled as half-spaces coated by a thin layer, are widely applied in modern technology. The measurement of mechanical properties of thin films deposited on half-spaces before and during loading is therefore very significant; for examples, see [Makarov et al. 1995; Every 2002] and references therein. Among various measurement methods, the surface/guided wave method is most widely used [Every 2002], because it is non-destructive and it is connected with reduced cost, less inspection time, and greater coverage [Hess et al. 2013], and for which the guided Rayleigh wave is a versatile and convenient tool [Küchler and Richter 1998; Hess et al. 2013].

For the Rayleigh-wave approach, the explicit dispersion relations of Rayleigh waves supported by thin-film/substrate interactions are employed as theoretical bases for extracting the mechanical properties of the thin films from experimental data. They are therefore the main purpose of any investigation of Rayleigh waves propagating in half-spaces covered by a thin layer.

Since the layer is assumed to be thin, i. e. its dimensionless thickness $\varepsilon = k.h$ (h is the thickness of the layer, k is the wave number) satisfies $0 < \varepsilon \ll 1$, it is reasonable that all researchers want to find approximate secular equations of Rayleigh waves that take the form $F = 0$, where F is a polynomial of n-order ($n \geq 1$) in terms of ε and the coefficients of the polynomial are functions of the material parameters and the Rayleigh wave velocity. Tiersten [1969] and Bövik [1996] assumed that the layer and the half-space are both isotropic and the authors derived approximate secular equations of second order. For this case, Vinh and Anh [2014a] obtained a fourth-order approximate secular equation with very high accuracy. Steigmann and Ogden [2007] considered a transversely isotropic layer with residual stress overlying an isotropic half-space and the authors obtained a second-order approximate dispersion relation. In [Vinh and Linh 2012; Vinh et al. 2014b] the layer and the half-space are both assumed to be orthotropic and approximate secular equations of third-order were obtained. In [Vinh and Linh 2013]

Keywords: Rayleigh waves, thin layer, effective boundary condition method, approximate secular equation.

the layer and the half-space are both subjected to homogeneous prestrains and an approximate secular equation of third-order was established which is valid for any prestrain and for a general strain energy function.

In the mentioned above investigations, the contact between the layer and the half-space is assumed to be perfectly bonded. For the case of sliding contact, Achenbach and Keshava [1967] derived an approximate secular equation of third-order. However, this approximate secular equation includes the shear coefficient, originating from Mindlin's plate theory [1951], whose usage should be avoided as noted by Touratier [1991], Muller and Touratier [1995] and Stephen [1997]. Recently, Vinh, Anh and Thanh [Vinh et al. 2014a] derived a fourth-order approximate secular equation with very high accuracy for the isotropic case. For the orthotropic case, an approximate secular equation of third order was established recently by Vinh and Anh [2014b].

To derive approximate secular equations, all researchers replace approximately the effect of the thin layer on the half-space by the so-called effective boundary conditions on the interface and the Rayleigh wave is then considered as a surface wave propagating in the half-space (without the coating layer) that is subjected to the effective boundary conditions. We call this approach "the effective boundary condition method".

For obtaining the effective boundary conditions, Achenbach and Keshava [1967] and Tiersten [1969] replaced the thin layer by a plate, while Bövik [1996] expanded the stresses at the top surface of the layer into Taylor series of its thickness up to the first-order, and expressed the first-order normal derivative in terms of the tangential and time derivatives by using the basic equations in component form. With this technique Bövik [1996] derived the first-order effective boundary conditions. It should be noted that this first-order effective boundary conditions contain some second-order terms as indicated in Remark 2. In order to obtain higher-order effective boundary conditions we need to get expressions of higher-order normal derivative in terms of the tangential and time derivatives. However, it is not easy to have them if we start from the basic equations in component form. Recently, starting from the basic equations in matrix form, Vinh and Linh [2012; 2013], Vinh and Anh [2014a; 2014b], and Vinh et al. [2014a; 2014b] obtained the effective boundary conditions of third and fourth orders. Nevertheless, in these papers the effective boundary condition method based on the Taylor expansion technique and the basic equations in matrix form has not been presented in detail. Furthermore, in these works (and in all other previous papers) both the layer and the half-space were assumed to be either compressible or incompressible. The case when the half-space is compressible (incompressible) and the layer incompressible (compressible) has never been under investigation.

The main aim of this paper is first to present in detail "the effective boundary condition method" that is based on the Taylor expansion technique and the basic equations in matrix form. Then, the method is employed to derive approximate secular equations of:

(i) Rayleigh waves propagating in a compressible orthotropic half-space covered by a thin incompressible orthotropic layer.

(ii) Rayleigh waves propagating in an incompressible half-space covered by a thin compressible layer.

Approximate secular equations of third order have been derived and it is shown that they have high accuracies. Some numerical examples are carried out to investigate the effect of incompressibility on the

Rayleigh wave propagation. It is shown that the incompressibility affects considerably on the Rayleigh wave velocity.

Note that, for Rayleigh waves propagating in compressible (incompressible) orthotropic half-spaces coated by a thin compressible (incompressible) orthotropic layer, the third-order approximate secular equations have been derived in [Vinh and Linh 2012; Vinh et al. 2014b].

It should be noted that there has been recently progress in studying not only a free surface wave and its speed, but also the case of loading, e.g., in application to moving loads; see, e.g., [Erbaş et al. 2014].

The paper is organized as follows. In Section 2, the effective boundary condition method is presented in detail. In Sections 3 and 4, the propagation of Rayleigh waves in an incompressible (compressible) orthotropic elastic half-space coated by a thin compressible (incompressible) orthotropic elastic layer is considered. The third-order approximate secular equations have been derived using the effective boundary condition method. In Section 5, as an application of the obtained results, the effect of the incompressibility of half-spaces and layers on the Rayleigh wave velocity is evaluated numerically using the obtained approximate secular equations.

2. The effective boundary condition method

Consider an orthotropic elastic homogeneous half-space $x_2 \geq 0$ coated by a thin orthotropic elastic homogeneous layer $-h \leq x_2 \leq 0$. Note that same quantities related to the half-space and the layer have the same symbol but are systematically distinguished by a bar if pertaining to the layer. We are interested in the plane strain so that:

$$\bar{u}_n = \bar{u}_n(x_1, x_2, t), \quad u_n = u_n(x_1, x_2, t), \qquad n = 1, 2,\ \bar{u}_3 \equiv 0,\ u_3 \equiv 0, \tag{1}$$

where $\bar{u}_n$ and u_n are the displacement components, t is the time. The effective boundary condition method based on the Taylor expansion technique and the basic equations in matrix form is carried out as follows.

Step 1. From the basic equations in component form governing the plane motions (1) of the layer including the equations of motions (without body forces):

$$\bar{\sigma}_{11,1} + \bar{\sigma}_{12,2} = \bar{\rho}\ddot{\bar{u}}_1, \quad \bar{\sigma}_{12,1} + \bar{\sigma}_{22,2} = \bar{\rho}\ddot{\bar{u}}_2 \tag{2}$$

(a comma indicates differentiation with respect to x_k, a dot signifies differentiation with respect to t), and the strain-stress relations (Equation (55) with bars for compressible materials, Equation (23) with bars for incompressible ones) we establish a matrix equation that is of the form

$$\begin{bmatrix} \bar{\boldsymbol{u}}' \\ \bar{\boldsymbol{t}}' \end{bmatrix} = \boldsymbol{M} \begin{bmatrix} \bar{\boldsymbol{u}} \\ \bar{\boldsymbol{t}} \end{bmatrix}, \quad -h \leq x_2 \leq 0, \tag{3}$$

where

$$\bar{\boldsymbol{u}} = \begin{bmatrix} \bar{u}_1 \\ \bar{u}_2 \end{bmatrix}, \quad \bar{\boldsymbol{t}} = \begin{bmatrix} \bar{\sigma}_{12} \\ \bar{\sigma}_{22} \end{bmatrix}, \quad \boldsymbol{M} = \begin{bmatrix} \boldsymbol{M}_1 & \boldsymbol{M}_2 \\ \boldsymbol{M}_3 & \boldsymbol{M}_4 \end{bmatrix}, \qquad \boldsymbol{M}_4 = \boldsymbol{M}_1^T, \tag{4}$$

where $\bar{\sigma}_{mn}$ are the components of the stress tensor, $\bar{\rho}$ is the mass density of the layer, the prime signifies differentiation with respect to x_2, $\boldsymbol{M}_k$ are 2×2-matrices whose entries are expressed in terms of the material parameters of the layer, the derivatives with respect to x_1 and t (they do not depend on the

derivatives with respect to x_2), the symbol ^{T} indicates the transpose of a matrix. For the compressible elastic materials, the matrix Equation (3) is derived by using Equations (1), (2) and (55). For the incompressible elastic materials, in addition to Equations (1), (2) and (23), the incompressibility condition is taken into account, and to obtain the matrix Equation (3) we have to eliminate from the basic equations the Lagrange multiplier p (also called the hydrostatic pressure) associated with the incompressibility constraint.

Remark 1. (i) Equation (3) expresses the normal derivative $\partial/\partial x_2$ in terms of the tangential derivative $\partial/\partial x_1$ and the time-derivative $\partial/\partial t$.

(ii) From the matrix (3) we arrive immediately at the Stroh formalism [1962].

From (3) we have:

$$\begin{bmatrix} \bar{\boldsymbol{u}}^{(n)} \\ \bar{\boldsymbol{t}}^{(n)} \end{bmatrix} = \boldsymbol{M}^n \begin{bmatrix} \bar{\boldsymbol{u}} \\ \bar{\boldsymbol{t}} \end{bmatrix} = \begin{bmatrix} \boldsymbol{M}_1^{(n)} & \boldsymbol{M}_2^{(n)} \\ \boldsymbol{M}_3^{(n)} & \boldsymbol{M}_4^{(n)} \end{bmatrix} \begin{bmatrix} \bar{\boldsymbol{u}} \\ \bar{\boldsymbol{t}} \end{bmatrix}, \quad -h \le x_2 \le 0, \tag{5}$$

where $\bar{\boldsymbol{u}}^{(n)}$ and $\bar{\boldsymbol{t}}^{(n)}$ are the derivative of n-order with respect to x_2 of $\bar{\boldsymbol{u}}$ and $\bar{\boldsymbol{t}}$. Taking $x_2 = 0$ in (5) provides

$$\begin{bmatrix} \bar{\boldsymbol{u}}^{(n)}(0) \\ \bar{\boldsymbol{t}}^{(n)}(0) \end{bmatrix} = \begin{bmatrix} \boldsymbol{M}_1^{(n)} & \boldsymbol{M}_2^{(n)} \\ \boldsymbol{M}_3^{(n)} & \boldsymbol{M}_4^{(n)} \end{bmatrix} \begin{bmatrix} \bar{\boldsymbol{u}}(0) \\ \bar{\boldsymbol{t}}(0) \end{bmatrix}, \quad n = 1, 2, \ldots. \tag{6}$$

Here $\bar{\boldsymbol{u}}(0)$ and $\bar{\boldsymbol{t}}(0)$ are the value of $\bar{\boldsymbol{u}}$ and $\bar{\boldsymbol{t}}$ at the bottom plane $x_2 = 0$ of the layer. From (6) it follows that

$$\bar{\boldsymbol{t}}^{(k)}(0) = \boldsymbol{M}_3^{(k)} \bar{\boldsymbol{u}}(0) + \boldsymbol{M}_4^{(k)} \bar{\boldsymbol{t}}(0), \quad k = 1, 2, \ldots. \tag{7}$$

Step 2. To expand the traction vector at the top surface of the layer into Taylor series of its thickness up to n-order:

$$\bar{\boldsymbol{t}}(-h) = \bar{\boldsymbol{t}}(0) + \bar{\boldsymbol{t}}'(0)\frac{(-h)}{1!} + \bar{\boldsymbol{t}}''(0)\frac{(-h)^2}{2!} + \cdots + \bar{\boldsymbol{t}}^{(n)}(0)\frac{(-h)^n}{n!}. \tag{8}$$

Suppose that the top surface of the layer is free from traction, i.e., $\bar{\boldsymbol{t}}(-h) = 0$.

Step 3. To derive the so-called pre-effective boundary condition of n-order in matrix form by substituting the expressions (7) into (8). It is of the form:

$$\bar{\boldsymbol{t}}(0) + \sum_{k=1}^{n} \left[\boldsymbol{M}_3^{(k)} \bar{\boldsymbol{u}}(0) + \boldsymbol{M}_4^{(k)} \bar{\boldsymbol{t}}(0)\right] \frac{(-h)^k}{k!} = \boldsymbol{0}. \tag{9}$$

Step 4. To obtain the effective boundary condition by using the pre-effective boundary condition (9) and the contact conditions between the layer and the half-space.

If the layer and the half-space are in welded contact with each other, then the displacement vector and the traction vector are continuous through the plane $x_2 = 0$, i. e.,

$$\bar{\boldsymbol{u}}(0) = \boldsymbol{u}(0), \quad \bar{\boldsymbol{t}}(0) = \boldsymbol{t}(0). \tag{10}$$

From (10) one can see that the derivative of any order of the displacement and traction vectors with respect to x_1 and t are also continuous through the plane $x_2 = 0$. From these facts it implies:

$$\boldsymbol{M}_3^{(k)}\bar{\boldsymbol{u}}(0) = \boldsymbol{M}_3^{(k)}\boldsymbol{u}(0), \quad \boldsymbol{M}_4^{(k)}\bar{\boldsymbol{t}}(0) = \boldsymbol{M}_4^{(k)}\boldsymbol{t}(0), \qquad k = 1, 2, \ldots. \tag{11}$$

From (9)–(11) we have

$$\boldsymbol{t}(0) + \sum_{k=1}^{n} \left[\boldsymbol{M}_3^{(k)}\boldsymbol{u}(0) + \boldsymbol{M}_4^{(k)}\boldsymbol{t}(0)\right] \frac{(-h)^k}{k!} = \boldsymbol{0}. \tag{12}$$

This is the effective boundary condition of n-order in matrix form for the case of welded contact. Note that this effective boundary condition can be used not only for the plane wave problems but also for any dynamic problem.

For the case of sliding contact, where the normal displacement and stress components are continuous through the plane $x_2 = 0$, the horizontal displacement component is discontinuous through this plane, the tangential stresses vanish at it [Vinh and Anh 2014b; Vinh et al. 2014a], the situation is rather different. The effective boundary condition (in matrix form) can not be obtained directly from the pre-effective boundary condition (9) due to the discontinuity of the horizontal displacement component. In order to derive the effective boundary condition for this case we restrict ourselves to the plane wave motions [Vinh and Anh 2014b; Vinh et al. 2014a] and eliminate the horizontal displacement component from the pre-effective boundary condition (9).

Step 5. To derive the approximate secular equation (of n-order) by considering the Rayleigh wave as a surface wave propagating in the half-space (with wave number k and velocity c), without the coating layer, that is subjected the effective boundary condition. It is of the form

$$D_0(x) + D_1(x)\varepsilon + D_2(x)\frac{\varepsilon^2}{2!} + \cdots + D_n(x)\frac{\varepsilon^n}{n!} + O(\varepsilon^{n+1}) = 0, \tag{13}$$

where x is the dimensionless squared velocity of Rayleigh waves, $\varepsilon = k.h$ (the dimensionless thickness of the layer) is assumed to be much smaller than the unit, $D_n(x)$ are explicit functions of x and the dimensionless material parameters of the layer and the half-space. The error of the approximate secular equation (13) in comparison with the exact secular equation is $O(\varepsilon^{n+1})$.

In the next two sections, we apply the effective boundary condition method to two cases:

(i) An incompressible elastic half-space covered by a thin compressible elastic layer.

(ii) A compressible elastic half-space covered by a thin incompressible elastic layer.

The layer and the half-space are assumed to be in welded contact with each other.

3. Rayleigh waves in incompressible half-spaces coated by a thin compressible layer

3.1. ***Effective boundary conditions.*** Consider an incompressible orthotropic homogeneous half-space $x_2 \geq 0$ coated by a thin compressible orthotropic homogeneous layer $-h \leq x_2 \leq 0$. The layer is assumed to be perfectly bonded to the half-space. The matrix equation for the layer is of the form (3) in which

matrices $\boldsymbol{M}_k$ are given by [Vinh and Linh 2012]

$$\boldsymbol{M}_1 = \begin{bmatrix} 0 & -\partial_1 \\ -\dfrac{\bar{c}_{12}}{\bar{c}_{22}}\partial_1 & 0 \end{bmatrix}, \qquad \boldsymbol{M}_2 = \begin{bmatrix} \dfrac{1}{\bar{c}_{66}} & 0 \\ 0 & \dfrac{1}{\bar{c}_{22}} \end{bmatrix},$$
$$\boldsymbol{M}_3 = \begin{bmatrix} \dfrac{\bar{c}_{12}^2 - \bar{c}_{11}\bar{c}_{22}}{\bar{c}_{22}}\partial_1^2 + \bar{\rho}\partial_t^2 & 0 \\ 0 & \bar{\rho}\partial_t^2 \end{bmatrix}, \quad \boldsymbol{M}_4 = \boldsymbol{M}_1^T. \tag{14}$$

Here we use the notations $\partial_1 = \partial/\partial x_1$, $\partial_1^2 = \partial^2/\partial x_1^2$, $\partial_t^2 = \partial^2/\partial t^2$. The pre-effective boundary condition of n-order in matrix form is (9). Since the layer and the half-space are in welded contact with each other, the effective boundary condition of n-order in matrix form is therefore (12). For $n = 3$, in component form, (12) is written as [Vinh and Linh 2012]

$$\sigma_{12} + h(r_1\sigma_{22,1} - r_3u_{1,11} - \bar{\rho}\ddot{u}_1) + \frac{h^2}{2}\left[r_2\sigma_{12,11} + \frac{\bar{\rho}}{\bar{c}_{66}}\ddot{\sigma}_{12} - r_3u_{2,111} - \bar{\rho}(1+r_1)\ddot{u}_{2,1}\right]$$
$$+\frac{h^3}{6}\left(r_4\sigma_{22,111} + \bar{\rho}r_5\ddot{\sigma}_{22,1} - r_6u_{1,1111} - \bar{\rho}r_7\ddot{u}_{1,11} - \frac{\bar{\rho}^2}{\bar{c}_{66}}\ddot{u}_{1,tt}\right) = 0, \quad \text{at } x_2 = 0, \tag{15}$$

and

$$\sigma_{22} + h(\sigma_{12,1} - \bar{\rho}\ddot{u}_2) + \frac{h^2}{2}\left[r_1\sigma_{22,11} + \frac{\bar{\rho}}{\bar{c}_{22}}\ddot{\sigma}_{22} - r_3u_{1,111} - \bar{\rho}(1+r_1)\ddot{u}_{1,1}\right]$$
$$+\frac{h^3}{6}\left[r_2\sigma_{12,111} + \bar{\rho}r_8\ddot{\sigma}_{12,1} - r_3u_{2,1111} - \bar{\rho}(1+2r_1)\ddot{u}_{2,11} - \frac{\bar{\rho}^2}{\bar{c}_{22}}\ddot{u}_{2,tt}\right] = 0, \quad \text{at } x_2 = 0, \tag{16}$$

where

$$r_1 = \frac{\bar{c}_{12}}{\bar{c}_{22}}, \qquad r_2 = r_1 + \frac{r_3}{\bar{c}_{66}}, \qquad r_3 = \frac{\bar{c}_{12}^2 - \bar{c}_{11}\bar{c}_{22}}{\bar{c}_{22}}, \quad r_4 = r_1r_2 + \frac{r_3}{\bar{c}_{22}},$$
$$r_5 = \frac{1+r_1}{\bar{c}_{22}} + \frac{r_1}{\bar{c}_{66}}, \quad r_6 = (r_1+r_2)r_3, \quad r_7 = r_1^2 + 2r_2, \qquad r_8 = \frac{1+r_1}{\bar{c}_{66}} + \frac{1}{\bar{c}_{22}} \tag{17}$$

Remark 2. (i) From the traction-free boundary condition $\bar{\boldsymbol{t}}(-h) = 0$, by expanding $\bar{\boldsymbol{t}}(0)$ into Taylor series at $x_2 = -h$ one can see that $\bar{\boldsymbol{t}}(0) = O(h)$, consequently $\boldsymbol{t}(0) = O(h)$ due to the continuity of stresses at the interface.

(ii) From Equations (15), (16) and the fact: $hr_1\sigma_{22,1} = O(h^2)$, $h\sigma_{12,1} = O(h^2)$ that is implied from (i), the first-order approximate effective boundary conditions are

$$\sigma_{12} - h(r_3u_{1,11} + \bar{\rho}\ddot{u}_1) = 0, \quad \sigma_{22} - h\bar{\rho}\ddot{u}_2 = 0, \qquad \text{at } x_2 = 0. \tag{18}$$

These first-order approximate effective boundary conditions recover the ones for the isotropic case obtained by Tiersten [1969] and Dai, Kaplunov and Prikazchikov [Dai et al. 2010].

(iii) Also from the fact: $hr_1\sigma_{22,1} = O(h^2)$, $h\sigma_{12,1} = O(h^2)$ one can see that the first-order approximate effective boundary conditions derived by Bövik [1996] include some $O(h^2)$ terms.

(iv) Again from the statement (i) it follows

$$\frac{h^3}{6}(r_4\sigma_{22,111}+\bar{\rho}r_5\ddot{\sigma}_{22,1})=O(h^4),\quad \frac{h^3}{6}(r_2\sigma_{12,111}+\bar{\rho}r_8\ddot{\sigma}_{12,1})=O(h^4). \tag{19}$$

These terms therefore can be excluded from the third-order conditions (15) and (16).

Now we consider a Rayleigh wave with velocity $c\,(>0)$ and the wave number $k\,(>0)$ traveling with the x_1-direction and decaying in the x_2-direction. Then its displacements and the stresses are sought in the form

$$\begin{gathered} u_1=U_1(y)\mathrm{e}^{ik(x_1-ct)},\quad u_2=iU_2(y)\mathrm{e}^{ik(x_1-ct)}\\ \sigma_{12}=-k\Sigma_1(y)\mathrm{e}^{ik(x_1-ct)},\quad \sigma_{22}=ik\Sigma_2(y)\mathrm{e}^{ik(x_1-ct)},\quad y=kx_2 \end{gathered} \tag{20}$$

Introducing (20) into (15) and (16) and taking into account (19) yield

$$\begin{aligned} &\Sigma_1(0)+\varepsilon[r_1\Sigma_2(0)-(r_3+\bar{\rho}c^2)U_1(0)]\\ &\quad+\frac{\varepsilon^2}{2}\left\{[r_3+\bar{\rho}c^2(1+r_1)]U_2(0)-\left(r_2+\frac{\bar{\rho}c^2}{\bar{c}_{66}}\right)\Sigma_1(0)\right\}\\ &\quad+\frac{\varepsilon^3}{6}\left(r_6+r_7\bar{\rho}c^2+\frac{\bar{\rho}^2c^4}{\bar{c}_{66}}\right)U_1(0)=0, \end{aligned} \tag{21}$$

and

$$\begin{aligned} &\Sigma_2(0)+\varepsilon[\bar{\rho}c^2U_2(0)-\Sigma_1(0)]\\ &\quad+\frac{\varepsilon^2}{2}\left\{[r_3+\bar{\rho}c^2(1+r_1)]U_1(0)-\left(r_1+\frac{\bar{\rho}c^2}{\bar{c}_{22}}\right)\Sigma_2(0)\right\}\\ &\quad-\frac{\varepsilon^3}{6}\left[r_3+\bar{\rho}c^2(1+2r_1)+\frac{\bar{\rho}^2c^4}{\bar{c}_{22}}\right]U_2(0)=0. \end{aligned} \tag{22}$$

Since $0<\varepsilon\ll 1$, the relations (21) and (22) are the third-order approximate effective boundary conditions whose error is $O(\varepsilon^4)$.

3.2. ***Approximate secular equation of third-order.*** Now we can ignore the layer and consider the propagation of Rayleigh waves in the half-space, without the coating layer, that is subjected to the effective boundary conditions (21) and (22).

Since the half-space is made of incompressible orthotropic materials, the strain-stress relations are (see [Ogden and Vinh 2004])

$$\sigma_{11}=-p+c_{11}u_{1,1}+c_{12}u_{2,2},\quad \sigma_{22}=-p+c_{12}u_{1,1}+c_{22}u_{2,2},\quad \sigma_{12}=c_{66}(u_{1,2}+u_{2,1}), \tag{23}$$

where σ_{ij} and p are respectively the stress, the hydrostatic pressure associated with the incompressibility constraint. The material constants c_{11}, c_{22}, c_{12}, c_{66} satisfy the inequalities [Ogden and Vinh 2004]

$$c_{kk}>0\quad (k=1,2,6),\qquad c_{11}+c_{22}-2c_{12}>0. \tag{24}$$

In the absent of body forces, the equations of motion are

$$\sigma_{11,1}+\sigma_{12,2}=\rho\ddot{u}_1,\quad \sigma_{12,1}+\sigma_{22,2}=\rho\ddot{u}_2. \tag{25}$$

For an incompressibility material, we have

$$u_{1,1} + u_{2,2} = 0. \tag{26}$$

In addition to Equations (23), (25) and (26) are required the effective boundary conditions (15) and (16) at $x_2 = 0$ and the decay condition at $x_2 = +\infty$, namely

$$u_n = 0, \quad n = 1, 2, \qquad \text{at } x_2 = +\infty. \tag{27}$$

Since the Rayleigh wave propagates in the x_1-direction with velocity c, wave number k and decays in the x_2-direction, according to [Ogden and Vinh 2004], its displacement components satisfying the decay condition (27) are given by $(20)_1$ in which

$$U_1(y) = b_1 B_1 e^{-b_1 y} + b_2 B_2 e^{-b_2 y}, \quad U_2(y) = B_1 e^{-b_1 y} + B_2 e^{-b_2 y}, \tag{28}$$

where B_1 and B_2 are constants to be determined and b_1 and b_2 are the roots of the equation

$$\gamma b^4 - (2\beta - X)b^2 + (\gamma - X) = 0, \tag{29}$$

with positive real parts (for ensuring the decay conditions), $X = \rho c^2$, and

$$\gamma = c_{66}, \quad \beta = (\delta - 2\gamma)/2, \quad \delta = c_{11} + c_{22} - 2c_{12}. \tag{30}$$

From (29) it follows

$$b_1^2 + b_2^2 = \frac{2\beta - X}{\gamma} := S, \quad b_1^2 b_2^2 = \frac{\gamma - X}{\gamma} := P. \tag{31}$$

It is not difficult to verify that if the Rayleigh wave exists (this implies that the real parts of b_1, b_2 must be positive), then

$$0 < X < c_{66}, \tag{32}$$

and

$$b_1 b_2 = \sqrt{P}, \quad b_1 + b_2 = \sqrt{S + 2\sqrt{P}}. \tag{33}$$

Substituting $(20)_1$, (28) into (23) and using (25) lead to that the stresses are given by $(20)_2$ in which

$$\Sigma_1(y) = \beta_1 B_1 e^{-b_1 y} + \beta_2 B_2 e^{-b_2 y}, \quad \Sigma_2(y) = \gamma_1 B_1 e^{-b_1 y} + \gamma_2 B_2 e^{-b_2 y}, \tag{34}$$

where

$$\beta_n = c_{66}(b_n^2 + 1), \quad \gamma_n = (X - \delta + \beta_n) b_n, \qquad n = 1, 2. \tag{35}$$

Introducing Equations (28) and (34) into Equations (21) and (22) provides a homogeneous system linear equations for B_1, B_2, namely,

$$\begin{cases} f(b_1)B_1 + f(b_2)B_2 = 0, \\ F(b_1)B_1 + F(b_2)B_2 = 0, \end{cases} \tag{36}$$

in which

$$f(b_n)=\beta_n+\varepsilon[r_1\gamma_n-(r_3+\overline{X})b_n]+\frac{\varepsilon^2}{2}\left[r_3+\overline{X}(1+r_1)-\left(r_2+\frac{\overline{X}}{\bar{c}_{66}}\right)\beta_n\right]$$
$$+\frac{\varepsilon^3}{6}\left(r_6+r_7\overline{X}+\frac{\overline{X}^2}{\bar{c}_{66}}\right)b_n,$$
$$F(b_n)=\gamma_n+\varepsilon(\overline{X}-\beta_n)+\frac{\varepsilon^2}{2}\left\{[r_3+\overline{X}(1+r_1)]b_n-\left(r_1+\frac{\overline{X}}{\bar{c}_{22}}\right)\gamma_n\right\} \tag{37}$$
$$-\frac{\varepsilon^3}{6}\left[r_3+\overline{X}(1+2r_1)+\frac{\overline{X}^2}{\bar{c}_{22}}\right],\quad n=1,2,\ \overline{X}=\bar{\rho}c^2.$$

For a nontrivial solution, the determinant of the matrix of the system (36) must vanish, i.e,

$$f(b_1)F(b_2)-f(b_2)F(b_1)=0. \tag{38}$$

Using (37) into (38), after algebraically lengthy but straightforward calculations, we arrive at the approximate secular equation of third order of Rayleigh waves, namely

$$A_0+A_1\varepsilon+A_2\frac{\varepsilon^2}{2}+A_3\frac{\varepsilon^3}{6}+O(\varepsilon^4)=0, \tag{39}$$

where

$$A_0=c_{66}[(X-\delta)\sqrt{P}+X],$$
$$A_1=c_{66}[\overline{X}+(r_3+\overline{X})\sqrt{P}]\sqrt{S+2\sqrt{P}},$$
$$A_2=-\left(\frac{r_3}{\bar{c}_{66}}+\frac{\overline{X}}{\bar{c}_{22}}+\frac{\overline{X}}{\bar{c}_{66}}\right)A_0+c_{66}[r_3+\overline{X}(1-r_1)](1-\sqrt{P})$$
$$-[r_3+\overline{X}(1-r_1)][X-\delta+c_{66}(S+\sqrt{P}+1)]-2\overline{X}(r_3+\overline{X}),$$
$$A_3=c_{66}\left\{2r_3-\overline{X}\left[2(r_1-1)+\frac{3r_3}{\bar{c}_{66}}\right]-\overline{X}\left(\frac{\overline{X}}{\bar{c}_{22}}+\frac{3\overline{X}}{\bar{c}_{66}}\right)\right.$$
$$\left.-\left[r_6-\overline{X}\left(3r_1^2-\frac{3r_3}{\bar{c}_{22}}-r_7\right)+\overline{X}\left(\frac{3\overline{X}}{\bar{c}_{22}}+\frac{\overline{X}}{\bar{c}_{66}}\right)\right]\sqrt{P}\right\}\sqrt{S+2\sqrt{P}}. \tag{40}$$

Equation (39) in which A_k given by (40) is the desired approximate secular of third order and it is fully explicit. It is useful to convert the secular equations (39) into a dimensionless equation. For this end we use the following dimensionless parameters

$$x=\frac{X}{c_{66}},\quad \bar{e}_1=\frac{\bar{c}_{11}}{\bar{c}_{66}},\quad \bar{e}_2=\frac{\bar{c}_{66}}{\bar{c}_{22}},\quad \bar{e}_3=\frac{\bar{c}_{12}}{\bar{c}_{66}},$$
$$e_\delta=\frac{\delta}{c_{66}},\quad \bar{e}_d=\bar{e}_1-\bar{e}_2\bar{e}_3^2,\quad r_\mu=\frac{\bar{c}_{66}}{c_{66}},\quad r_v=\frac{c_2}{\bar{c}_2},\quad c_2=\sqrt{\frac{c_{66}}{\rho}},\quad \bar{c}_2=\sqrt{\frac{\bar{c}_{66}}{\bar{\rho}}}. \tag{41}$$

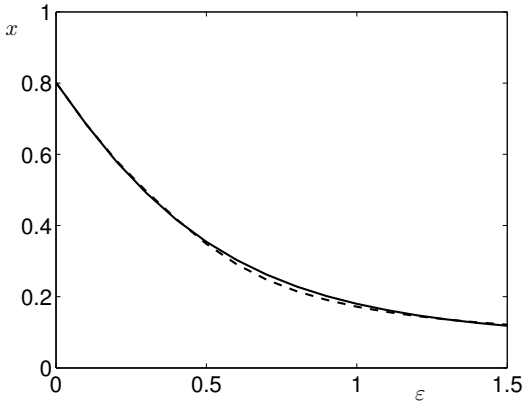

Figure 1. Dimensionless Rayleigh wave velocity $x(\varepsilon)$ in the interval [0 1.5], calculated by the exact secular equation (solid line) and by the approximate secular equation (42) (dashed line). Here we take $e_\delta = 2.6,\ \bar{e}_1 = 2,\ \bar{e}_2 = 1,\ \bar{e}_3 = 0.6,\ r_v = 2.8,\ r_\mu = 0.6$.

By dividing two sides of (39) by $(c_{66})^2$ we have

$$D_0 + D_1\varepsilon + D_2\frac{\varepsilon^2}{2} + D_3\frac{\varepsilon^3}{6} + O(\varepsilon^4) = 0, \tag{42}$$

where

$$\begin{aligned}
D_0 &= (x - e_\delta)\sqrt{P} + x,\\
D_1 &= r_\mu[r_v^2 x + (r_v^2 x - \bar{e}_d)\sqrt{P}]\sqrt{S + 2\sqrt{P}},\\
D_2 &= [\bar{e}_d - r_v^2 x(1 + \bar{e}_2)]D_0 + 2r_\mu[\bar{e}_d - r_v^2 x(1 - \bar{e}_2\bar{e}_3)]\sqrt{P} - 2r_\mu[\bar{e}_d - r_v^2 x(1 - \bar{e}_2\bar{e}_3 + r_\mu\bar{e}_d) + r_\mu r_v^4 x^2],\\
D_3 &= -r_\mu\big\{2\bar{e}_d + r_v^2 x(2\bar{e}_2\bar{e}_3 - 2 - 3\bar{e}_d) + r_v^4 x^2(\bar{e}_2 + 3)\\
&\quad + \big[\bar{e}_d(\bar{e}_d - 2\bar{e}_2\bar{e}_3) - r_v^2 x(2\bar{e}_2^2\bar{e}_3^2 - 2\bar{e}_2\bar{e}_3 + 2\bar{e}_d + 3\bar{e}_2\bar{e}_d) + r_v^4 x^2(1 + 3\bar{e}_2)\big]\sqrt{P}\big\}\sqrt{S + 2\sqrt{P}},\\
&\qquad S = e_\delta - 2 - x,\ P = 1 - x.
\end{aligned} \tag{43}$$

It is clear from (42) and (43) that the squared dimensionless Rayleigh wave velocity $x = c^2/c_2^2$ depends on 7 dimensionless parameters $e_\delta,\ \bar{e}_1,\ \bar{e}_2,\ \bar{e}_3,\ r_\mu,\ r_v$ and ε. Note that $e_\delta > 0,\ \bar{e}_1 > 0,\ \bar{e}_2 > 0$ and $\bar{e}_1 - \bar{e}_2\bar{e}_3^2 > 0$, according to the inequalities (24) and (56).

When $\varepsilon = 0$, from (42) and the first of (43) it implies

$$(x - e_\delta)\sqrt{1 - x} + x = 0. \tag{44}$$

That is the secular equation of Rayleigh waves in an incompressible orthotropic elastic half-space [Ogden and Vinh 2004].

Figure 1 presents the dependence on $\varepsilon = k.h \in [0\ 1.5]$ of the dimensionless Rayleigh wave velocity $x = c^2/c_2^2$ that is calculated by the exact secular equation (solid line) and by the approximate secular (42) (dashed line). The dimensionless parameters are taken as $e_\delta = 2.6,\ \bar{e}_1 = 2,\ \bar{e}_2 = 1,\ \bar{e}_3 = 0.6,\ r_v = 2.8,\ r_\mu = 0.6$. Note that the exact secular equation is of the form of a 6×6 determinant that is established

from the traction-free conditions at the layer surface and the continuity conditions of displacements and stresses at the interface between the layer and the half-space. It is similar to Equation (19) in [Farnell and Adler 1972, p. 48]. As it is rather cumbersome it need not be written down. It is shown from Figure 1 that the exact and approximate curves of Rayleigh wave velocity almost totally coincide with each other for the values of $\varepsilon \in [0\,1.5]$. The maximum absolute error in the interval $[0\,1.5]$ is 0.0141 at $\varepsilon = 0.7$. This says that the approximate secular (42) has high accuracy.

3.3. ***Isotropic case.*** When the layer is isotropic and the half-space is transversely isotropic (with the plane of isotropy being the (x_1x_2)-plane), we have

$$\bar{c}_{11} = \bar{c}_{22} = \bar{\lambda} + 2\bar{\mu}, \quad \bar{c}_{12} = \bar{\lambda}, \quad \bar{c}_{66} = \bar{\mu}, \quad c_{11} = c_{22}, \quad c_{11} - c_{12} = 2c_{66}, \tag{45}$$

consequently

$$\bar{e}_1 = 1/\bar{g}, \quad \bar{e}_2 = \bar{g}, \quad \bar{e}_3 = 1/\bar{g} - 2, \quad \bar{e}_d = 4(1-\bar{g}), \quad e_\delta = 4, \quad S = 2 - x, \tag{46}$$

where $\bar{g} = \bar{\mu}/(\bar{\lambda} + 2\bar{\mu})$. Taking into account (46), the expressions (43) of D_k are simplified to

$$\begin{aligned}
D_0 &= (x-4)\sqrt{1-x} + x,\\
D_1 &= r_\mu[r_v^2 x + (r_v^2 x - 4 + 4\bar{g})\sqrt{1-x}](1+\sqrt{1-x}),\\
D_2 &= [4(1-\bar{g}) - (1+\bar{g})r_v^2 x]D_0 + 4r_\mu[2(1-\bar{g}) - \bar{g}r_v^2 x]\sqrt{1-x}\\
&\qquad -2r_\mu[4(1-\bar{g}) - 2(2r_\mu - 2r_\mu\bar{g} + \bar{g})r_v^2 x + r_\mu r_v^4 x^2],\\
D_3 &= -r_\mu\big\{8(1-\bar{g}) + 4(2\bar{g}-3)r_v^2 x + (3+\bar{g})r_v^4 x^2\\
&\qquad +\big[8(1-\bar{g}) + 4(\bar{g}^2 - 2)r_v^2 x + (1+3\bar{g})r_v^4 x^2\big]\sqrt{P}\big\}(1+\sqrt{1-x}).
\end{aligned} \tag{47}$$

When the layer and the half-space are both isotropic, the expressions (47) are unchanged, but in which: $x = \rho c^2/\mu$, $r_\mu = \bar{\mu}/\mu$, $\bar{\mu}$ and μ are the shear moduli.

4. Rayleigh waves in compressible half-spaces coated by a thin incompressible layer

4.1. ***Effective boundary conditions.*** Consider a compressible orthotropic homogeneous half-space $x_2 \geq 0$ coated by a thin incompressible orthotropic homogeneous layer $-h \leq x_2 \leq 0$. The layer and the half-space are assumed to be in perfectly bonded contact to each other. For this case, the matrix equation for the layer is (3) in which matrices $\boldsymbol{M}_k$ are given by [Vinh et al. 2014b]

$$\boldsymbol{M}_1 = \begin{bmatrix} 0 & -\partial_1 \\ -\partial_1 & 0 \end{bmatrix}, \quad \boldsymbol{M}_2 = \begin{bmatrix} \dfrac{1}{\bar{c}_{66}} & 0 \\ 0 & 0 \end{bmatrix}, \quad \boldsymbol{M}_3 = \begin{bmatrix} -\bar{\delta}\partial_1^2 + \bar{\rho}\partial_t^2 & 0 \\ 0 & \bar{\rho}\,\partial_t^2 \end{bmatrix}, \quad \boldsymbol{M}_4 = \boldsymbol{M}_1, \tag{48}$$

where $\bar{\delta} = \bar{c}_{11} - 2\bar{c}_{12} + \bar{c}_{22}$. The pre-effective boundary condition of n-order in matrix form is (9). Since the layer is perfectly bonded to the half-space, the effective boundary condition of n-order in matrix form

is (12). For $n = 3$, (12) is written in component form as (see [Vinh et al. 2014b])

$$\sigma_{12} + h(\sigma_{22,1} + \bar{\delta}u_{1,11} - \bar{\rho}\ddot{u}_1) + \frac{h^2}{2}\left(r_9\sigma_{12,11} + \frac{\bar{\rho}}{\bar{c}_{66}}\ddot{\sigma}_{12} + \bar{\delta}u_{2,111} - 2\bar{\rho}\ddot{u}_{2,1}\right) + \frac{h^3}{6}\left(r_9\sigma_{22,111} + \frac{\bar{\rho}}{\bar{c}_{66}}\ddot{\sigma}_{22,1} - r_{10}u_{1,1111} - \bar{\rho}r_{11}\ddot{u}_{1,11} - \frac{\bar{\rho}^2}{\bar{c}_{66}}\ddot{u}_{1,tt}\right) = 0, \quad \text{at } x_2 = 0, \tag{49}$$

$$\sigma_{22} + h(\sigma_{12,1} - \bar{\rho}\ddot{u}_2) + \frac{h^2}{2}(\sigma_{22,11} + \bar{\delta}u_{1,111} - 2\bar{\rho}\ddot{u}_{1,1}) + \frac{h^3}{6}\left(r_9\sigma_{12,111} + \frac{2\bar{\rho}}{\bar{c}_{66}}\ddot{\sigma}_{12,1} + \bar{\delta}u_{2,1111} - 3\bar{\rho}\ddot{u}_{2,11}\right) = 0, \quad \text{at } x_2 = 0, \tag{50}$$

where

$$r_9 = 1 - \frac{\bar{\delta}}{\bar{c}_{66}}, \quad r_{10} = \bar{\delta}\left(\frac{\bar{\delta}}{\bar{c}_{66}} - 2\right), \quad r_{11} = 2r_9 + 1. \tag{51}$$

Suppose that the Rayleigh wave travels along surface $x_2 = 0$ with velocity $c\ (> 0)$ and wave number $k\ (> 0)$ in the x_1-direction and decays in the x_2-direction. Then, the displacements and stresses are sought in the form

$$\begin{aligned} u_1 &= U_1(y)\mathrm{e}^{ik(x_1-ct)}, \qquad u_2 = iU_2(y)\mathrm{e}^{ik(x_1-ct)} \\ \sigma_{12} &= k\Sigma_1(y)\mathrm{e}^{ik(x_1-ct)}, \quad \sigma_{22} = ik\Sigma_2(y)\mathrm{e}^{ik(x_1-ct)}, \qquad y = kx_2 \end{aligned} \tag{52}$$

Introducing (52) into (49) and (50) and taking into account Remark 2(i) yield

$$\Sigma_1(0) + \varepsilon[(\bar{\rho}c^2 - \bar{\delta})U_1(0) - \Sigma_2(0)] + \frac{\varepsilon^2}{2}\left[(\bar{\delta} - 2\bar{\rho}c^2)U_2(0) - \left(r_9 + \frac{\bar{\rho}c^2}{\bar{c}_{66}}\right)\Sigma_1(0)\right] - \frac{\varepsilon^3}{6}\left(r_{10} + r_{11}\bar{\rho}c^2 + \frac{\bar{\rho}^2c^4}{\bar{c}_{66}}\right)U_1(0) = 0, \tag{53}$$

$$\Sigma_2(0) + \varepsilon(\bar{\rho}c^2U_2(0) + \Sigma_1(0)) + \frac{\varepsilon^2}{2}[(2\bar{\rho}c^2 - \bar{\delta})U_1(0) - \Sigma_2(0)] + \frac{\varepsilon^3}{6}(\bar{\delta} - 3\bar{\rho}c^2)U_2(0) = 0. \tag{54}$$

Since $0 < \varepsilon \ll 1$, the relations (53) and (54) are the third-order approximate effective boundary conditions with the error being $O(\varepsilon^4)$.

4.2. ***Approximate secular equation of third-order.*** Now we can consider the propagation of Rayleigh waves in the uncoated half-space $x_2 \geq 0$ whose surface is subjected to the effective boundary conditions (53) and (54).

Since the half-space is made of compressible orthotropic materials, the strain-stress relations are (see [Vinh and Ogden 2004])

$$\sigma_{11} = c_{11}u_{1,1} + c_{12}u_{2,2}, \quad \sigma_{22} = c_{12}u_{1,1} + c_{22}u_{2,2}, \quad \sigma_{12} = c_{66}(u_{1,2} + u_{2,1}), \tag{55}$$

where the material constants c_{11}, c_{22}, c_{12}, c_{66} satisfy the inequalities [Vinh and Ogden 2004]

$$c_{kk} > 0, \quad k = 1, 2, 6, \qquad c_{11}c_{22} - c_{12}^2 > 0. \tag{56}$$

In the absence of body forces, the equations of motion is (25). In addition to Equations (55) and (25),

we require the effective boundary conditions (49) and (50) at $x_2 = 0$ and the decay condition

$$u_n = 0, \quad n = 1, 2, \text{ at } x_2 = +\infty. \tag{57}$$

Suppose that the Rayleigh wave travels along surface $x_2 = 0$ with velocity c and wave number k in the x_1-direction and decays in the x_2-direction. According to [Vinh and Ogden 2004], the Rayleigh wave displacement components satisfying the decay condition (57) are given by $(52)_1$ in which

$$U_1(y) = B_1 e^{-b_1 y} + B_2 e^{-b_2 y}, \quad U_2(y) = \beta_1 B_1 e^{-b_1 y} + \beta_2 B_2 e^{-b_2 y}, \tag{58}$$

where B_1 and B_2 are constant to be determined and b_1, b_2 are roots of the equation

$$c_{22}c_{66}b^4 + [(c_{12} + c_{66})^2 + c_{22}(X - c_{11}) + c_{66}(X - c_{66})]b^2 + (c_{11} - X)(c_{66} - X) = 0, \tag{59}$$

whose real parts are positive to ensure to the decay condition, $X = \rho c^2$, and

$$\beta_k = \frac{b_k(c_{12} + c_{66})}{c_{22}b_k^2 - c_{66} + \rho c^2} = \frac{c_{11} - \rho c^2 - c_{66}b_k^2}{(c_{12} + c_{66})b_k}, \quad k = 1, 2. \tag{60}$$

From (59) we have

$$\begin{aligned} b_1^2 + b_2^2 &= -\frac{(c_{12} + c_{66})^2 + c_{22}(X - c_{11}) + c_{66}(X - c_{66})}{c_{22}c_{66}} := S, \\ b_1^2 b_2^2 &= \frac{(c_{11} - X)(c_{66} - X)}{c_{22}c_{66}} := P. \end{aligned} \tag{61}$$

It is not difficult to verify that if the Rayleigh wave exists (this follows that the real parts of b_1, b_2 must be positive), then

$$0 < X < \min\{c_{11}, c_{66}\}, \tag{62}$$

and $b_1 b_2$, $b_1 + b_2$ are given by (33). Introducing $(52)_1$ and (58) into (55) yields that the stresses are given by $(52)_2$ in which

$$\begin{aligned} \Sigma_1(y) &= -c_{66}\big[(b_1 + \beta_1)B_1 e^{-b_1 y} + (b_2 + \beta_2)B_2 e^{-b_2 y}\big], \\ \Sigma_2(y) &= (c_{12} - c_{22}b_1\beta_1)B_1 e^{-b_1 y} + (c_{12} - c_{22}b_2\beta_2)B_2 e^{-b_2 y}. \end{aligned} \tag{63}$$

Using (58), (63) into the effective boundary conditions (53) and (54) leads to the system (36) with

$$\begin{aligned} f(b_n) &= -c_{66}(b_n + \beta_n) + \varepsilon[(\overline{X} - \bar{\delta}) - (c_{12} - c_{22}b_n\beta_n)] \\ &\quad + \frac{\varepsilon^2}{2}\left[c_{66}\left(r_9 + \frac{\overline{X}}{\bar{c}_{66}}\right)(b_n + \beta_n) + (\bar{\delta} - 2\overline{X})\beta_n\right] - \frac{\varepsilon^3}{6}\left(r_{10} + r_{11}\overline{X} + \frac{\overline{X}^2}{\bar{c}_{66}}\right), \\ F(b_n) &= c_{12} - c_{22}b_n\beta_n + \varepsilon[\overline{X}\beta_n - c_{66}(b_n + \beta_n)] \\ &\quad + \frac{\varepsilon^2}{2}[(2\overline{X} - \bar{\delta}) - (c_{12} - c_{22}b_n\beta_n)] + \frac{\varepsilon^3}{6}(\bar{\delta} - 3\overline{X})\beta_n, \quad n = 1, 2, \ \overline{X} = \bar{\rho}c^2. \end{aligned} \tag{64}$$

Setting to zero the determinant of the coefficients of the system (36)–(64) yields the equation

$$A_0 + A_1\varepsilon + \tfrac{1}{2}A_2\varepsilon^2 + \tfrac{1}{6}A_3\varepsilon^3 + O(\varepsilon^4) = 0, \tag{65}$$

where

$$
\begin{aligned}
A_0 &= c_{66}[(c_{12}^2 - c_{11}c_{22} + c_{22}X)b_1b_2 + (c_{11} - X)X],\\
A_1 &= c_{66}[\overline{X}(c_{11} - X) + c_{22}(\overline{X} - \bar{\delta})b_1b_2](b_1 + b_2),\\
A_2 &= \left(\frac{\bar{\delta}}{\bar{c}_{66}} - \frac{\overline{X}}{\bar{c}_{66}}\right)A_0 + 2[c_{66}\bar{\delta} + \overline{X}(\overline{X} - \bar{\delta})](X - c_{11}) + 2c_{66}[c_{12}\bar{\delta} - \overline{X}(\overline{X} - \bar{\delta})]\, b_1b_2,\\
A_3 &= c_{66}\left\{\left[3\overline{X}\left(\frac{\bar{\delta}}{\bar{c}_{66}} - \frac{\overline{X}}{\bar{c}_{66}}\right) - 2\bar{\delta}\right](c_{11} - X) - c_{22}\left[r_2 + \overline{X}\left(\frac{\overline{X}}{\bar{c}_{66}} - \frac{2\bar{\delta}}{\bar{c}_{66}}\right)\right]b_1b_2\right\}(b_1 + b_2),
\end{aligned}
\tag{66}
$$

in which b_1b_2 and $b_1 + b_2$ are given by (33) and (61). Equation (65) is the desired third-order approximate secular equations and it is fully explicit. In dimensionless form (65) takes the form

$$
D_0 + D_1\varepsilon + D_2\frac{\varepsilon^2}{2} + D_3\frac{\varepsilon^3}{6} + O(\varepsilon^4) = 0, \tag{67}
$$

where

$$
\begin{aligned}
D_0 &= (e_2x - e_d)b_1b_2 + (e_1 - x)x,\\
D_1 &= r_\mu[r_v^2x(e_1 - x) + e_2(r_v^2x - \bar{e}_\delta)\, b_1b_2](b_1 + b_2),\\
D_2 &= -(r_v^2x - \bar{e}_\delta)D_0 + 2r_\mu[\bar{e}_\delta + r_\mu r_v^2x(r_v^2x - \bar{e}_\delta)](x - e_1) + 2r_\mu[e_3\bar{e}_\delta - r_\mu r_v^2x(r_v^2x - \bar{e}_\delta)]\, b_1b_2,\\
D_3 &= r_\mu\left\{[3r_v^2x(\bar{e}_\delta - r_v^2x) - 2\bar{e}_\delta](e_1 - x) - e_2[\bar{e}_\delta(\bar{e}_\delta - 2) + r_v^2x(r_v^2x - 2\bar{e}_\delta)]\, b_1b_2\right\}(b_1 + b_2),\\
b_1b_2 &= \sqrt{P}, \quad b_1 + b_2 = \sqrt{S + 2\sqrt{P}}, \quad P = \frac{(1 - x)(e_1 - x)}{e_2},\\
S &= \frac{e_2(e_1 - x) + 1 - x - (1 + e_3)^2}{e_2}.
\end{aligned}
\tag{68}
$$

Here we use the following dimensionless parameters

$$
\begin{aligned}
&x = \frac{X}{c_{66}}, \quad e_1 = \frac{c_{11}}{c_{66}}, \quad e_2 = \frac{c_{22}}{c_{66}}, \quad e_3 = \frac{c_{12}}{c_{66}}, \qquad e_d = e_1e_2 - e_3^2,\\
&\bar{e}_\delta = \frac{\bar{\delta}}{\bar{c}_{66}}, \quad r_\mu = \frac{\bar{c}_{66}}{c_{66}}, \quad r_v = \frac{c_2}{\bar{c}_2}, \quad c_2 = \sqrt{\frac{c_{66}}{\rho}}, \quad \bar{c}_2 = \sqrt{\frac{\bar{c}_{66}}{\bar{\rho}}}.
\end{aligned}
\tag{69}
$$

It is clear from (67) and (68) that the squared dimensionless Rayleigh wave velocity $x = c^2/c_2^2$ depends on 7 dimensionless parameters $e_1,\ e_2,\ e_3,\ \bar{e}_\delta,\ r_\mu,\ r_v$ and ε. Note that $e_1 > 0,\ e_2 > 0,\ e_1e_2 - e_3^2 > 0,\ \bar{e}_\delta > 0$ according to the inequalities (24) and (56).

If $\varepsilon = 0$, from (67) and the first of (68) it follows

$$
(e_2x - e_d)\sqrt{P} + (e_1 - x)x = 0. \tag{70}
$$

Equation (70) is the secular equation of Rayleigh waves propagating in an orthotropic elastic half-space [Chadwick 1976; Vinh and Ogden 2004].

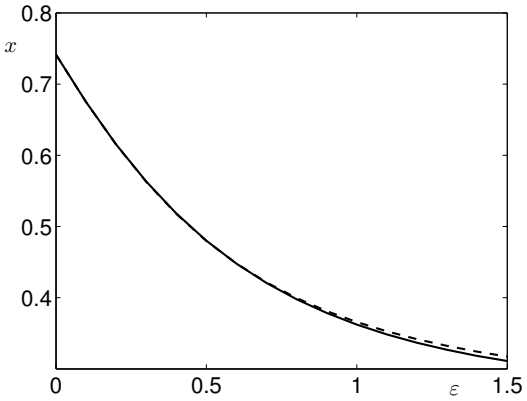

Figure 2. The Rayleigh wave velocity curves drawn by solving the exact dispersion (solid line) and by the approximate secular equation (67) (dashed line) with $r_\mu = 1.2$, $r_v = 1.8$, $e_1 = 2.5$, $e_2 = 2.8$, $e_3 = 1.3$, $\bar{e}_\delta = 3.2$.

Figure 2 presents the dependence on $\varepsilon = k.h \in [0\,1.5]$ of the dimensionless Rayleigh wave velocity $x = c^2/c_2^2$ that is calculated by the exact secular equation (of the form of a 6×6 determinant as noted above, solid line) and by the approximate secular (67) (dashed line) with $r_\mu = 1.2$, $r_v = 1.8$, $e_1 = 2.5$, $e_2 = 2.8$, $e_3 = 1.3$, $\bar{e}_\delta = 3.2$. It is shown from Figure 2 that the exact velocity curve and the third-order approximate velocity curve are very close to each other for the values of $\varepsilon \in [0\,1.5]$. The maximum absolute error in the interval $[0\,1.5]$ is 0.0062 at $\varepsilon = 1.5$. This means that the approximate secular equation (67) have very high accuracy.

4.3. ***Isotropic case.*** When the layer is transversely isotropic (with the plane of isotropy being the (x_1x_2)-plane) and the half-space is isotropic, i.e: $c_{11} = c_{22} = \lambda + 2\mu$, $c_{12} = \lambda$, $c_{66} = \mu$, $\bar{c}_{11} = \bar{c}_{22}$, $\bar{c}_{11} - \bar{c}_{12} = 2\bar{c}_{66}$, from (60), (61) and (69), it is easy to verify that

$$\bar{e}_\delta = 4, \quad b_1 = \sqrt{1 - gx}, \quad b_2 = \sqrt{1 - x}, \quad \beta_1 = b_1, \quad \beta_2 = \frac{1}{b_2}, \tag{71}$$

where $g = \mu/(\lambda + 2\mu)$. With the help of (71), the secular equation (67) is simplified to

$$\overline{D}_0 + \overline{D}_1\varepsilon + \tfrac{1}{2}\overline{D}_2\varepsilon^2 + \tfrac{1}{6}\overline{D}_3\varepsilon^3 = 0, \tag{72}$$

in which

$$\begin{aligned}
&\overline{D}_0 = (x-2)^2 - 4\sqrt{1-x}\sqrt{1-gx},\\
&\overline{D}_1 = r_\mu x[(r_v^2 x - 4)\sqrt{1-x} + r_v^2 x\sqrt{1-gx}],\\
&\overline{D}_2 = -(r_v^2 x - 4)\overline{D}_0 - 2r_\mu[4(2 - x + 2b_1b_2) + r_\mu r_v^2 x(r_v^2 x - 4)(1 - b_1b_2)],\\
&\overline{D}_3 = r_\mu x\big\{b_1[3r_v^2 x(4 - r_v^2 x) - 8] - b_2[8 + r_v^2 x(r_v^2 x - 8)]\big\}.
\end{aligned} \tag{73}$$

Here $r_\mu = \bar{c}_{66}/\mu$. When the layer and the half-space are both isotropic, $\overline{D}_k$, $(k = 0, 1, 2, 3)$ are also calculated by (73), but in which $x = \rho c^2/\mu$, $r_\mu = \bar{\mu}/\mu$, $\bar{\mu}$ and μ are the shear moduli.

5. Numerical examples

In this section, as an example of application of the obtained approximate secular equations, we consider numerically the effect of the incompressibility on the Rayleigh wave velocity. For this aim we consider four examples. In the first example, a compressible half-space is coated either by a compressible layer or by an incompressible layer. Two these layers have the same elastic constants. In the second example, the compressible half-space is replaced by an incompressible. In the third (fourth) example, two different (compressible and incompressible) half-spaces with the same elastic constants are covered with the same compressible (incompressible) layer.

In particular, in the first example, we take $e_1 = 2.8,\ e_2 = 2.6,\ e_3 = 1.2$ for the half-space and $\bar{e}_1 = 4.5$, $\bar{e}_2 = 1,\ \bar{e}_3 = 1$ for the layers and $r_\mu = 0.5,\ r_v = 2.8$.

In the second example, we choose $\bar{e}_1 = 3.5,\ \bar{e}_2 = 1.5,\ \bar{e}_3 = 1$ for the layers and $e_\delta = 3.5$ for the half-space and $r_\mu = 1,\ r_v = 1.6$.

In the third example, the dimensionless parameters are taken as $\bar{e}_1 = 2.2,\ \bar{e}_2 = 1,\ \bar{e}_3 = 0.5$ for the layer and $e_1 = 2.5,\ e_2 = 2.8,\ e_3 = 1$ for the half-spaces and $r_\mu = 0.5,\ r_v = 2.8$.

In the last one, they are $\bar{e}_\delta = 3$ for the layer and $e_1 = 2.8,\ e_2 = 3,\ e_3 = 1.5$ for the half-spaces and $r_\mu = 1,\ r_v = 1.5$.

The numerical results of the first, second, third and fourth examples are presented in Figures 3, 4, 5 and 6, respectively. To establish the wave velocity curves, the approximate secular equations (42), (67) and Equation (29) in [Vinh and Linh 2012], Equation (3.14) in [Vinh et al. 2014b] are employed.

Figures 3–6 show:

(i) The incompressibility affects strongly the Rayleigh wave velocity.

(ii) The effect of incompressible coating layers is considerably stronger than the one of incompressible half-spaces.

(iii) The incompressibility makes the Rayleigh wave velocity increasing.

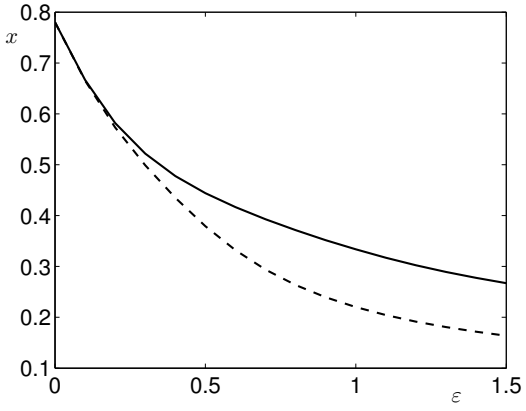

Figure 3. A compressible half-space coated by an incompressible layer (solid line drawn by solving (67)), by an compressible layer (dashed line drawn by solving Eq. (29) in [Vinh and Linh 2012]). Here we take $e_1 = 2.8,\ e_2 = 2.6,\ e_3 = 1.2$ for the half-space and $\bar{e}_1 = 4.5,\ \bar{e}_2 = 1,\ \bar{e}_3 = 1$ for the layers and $r_\mu = 0.5,\ r_v = 2.8$.

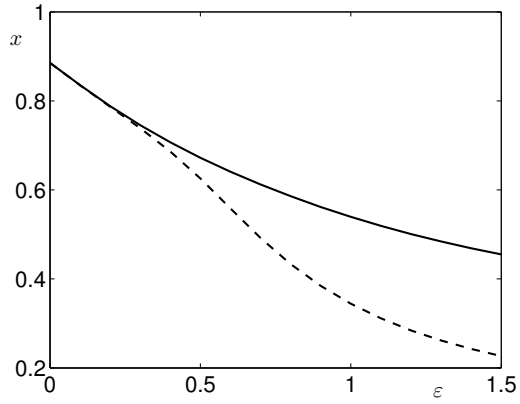

Figure 4. An incompressible half-space coated by an incompressible layer (solid line drawn by solving Equation (3.14) in [Vinh et al. 2014b], by a compressible layer (dashed line drawn by solving (42)). Here we take $\bar{e}_1 = 3.5,\ \bar{e}_2 = 1.5,\ \bar{e}_3 = 1$ for the layers and $e_\delta = 3.5$ for the half-space and $r_\mu = 1,\ r_v = 1.6$.

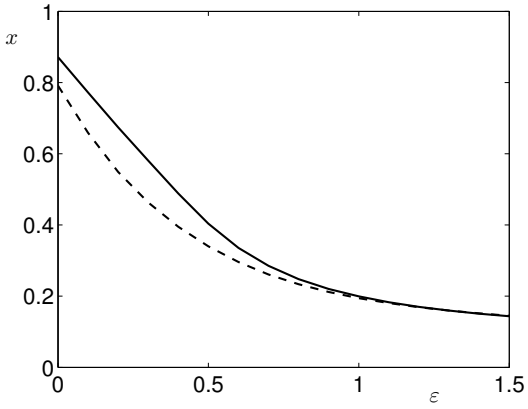

Figure 5. A compressible layer coats a compressible half-space (solid line drawn by solving Equation (29) in [Vinh and Linh 2012], an incompressible half-space (dashed line drawn by solving (42)). Here we take $\bar{e}_1 = 2.2, \bar{e}_2 = 1, \bar{e}_3 = 0.5$ for the layer and $e_1 = 2.5, e_2 = 2.8, e_3 = 1$ for the half-spaces and $r_\mu = 0.5, r_v = 2.8$.

6. Conclusions

In this paper, the effective boundary condition method is presented in detail. This method is then employed to derive the third-order approximate explicit secular equations of Rayleigh waves propagating in compressible (incompressible) half-space covered by a thin incompressible (compressible) layer. It is shown that they have high accuracies. Numerical examples show that the incompressibility affects considerably on the Rayleigh wave velocity. Since the obtained approximate secular equations and formulas for the Rayleigh wave velocity are totally explicit and have high accuracy, they will be significant in practical applications.

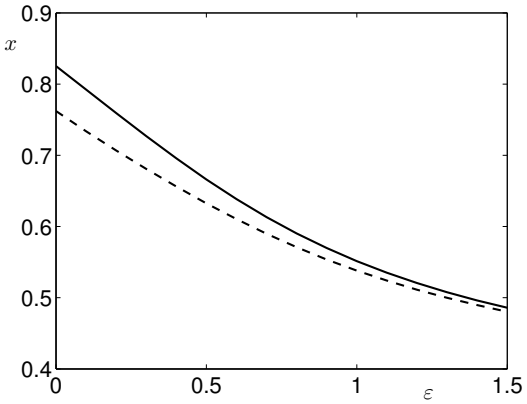

Figure 6. An incompressible layer coats an incompressible half-space (solid line drawn by solving Equation (3.14) in [Vinh et al. 2014b], a compressible half-space (dashed line drawn by solving (67)). Here we take $\bar{e}_\delta = 3$ for the layer and $e_1 = 2.8$, $e_2 = 3$, $e_3 = 1.5$ for the half-spaces and $r_\mu = 1$, $r_\upsilon = 1.5$.

Acknowledgements

The work was supported by the Vietnam National Foundation for Science and Technology Development (NAFOSTED) under grant number 107.02-2014.04.

References

[Achenbach and Keshava 1967] J. D. Achenbach and S. P. Keshava, "Free waves in a plate supported by a semi-infinite continuum", *J. Appl. Mech.* (*ASME*) **34** (1967), 397–404.

[Bövik 1996] P. Bövik, "A comparison between the Tiersten model and O(H) boundary conditions for elastic surface waves guided by thin layers", *J. Appl. Mech.* (*ASME*) **63** (1996), 162–167.

[Chadwick 1976] P. Chadwick, "The existence of pure surface modes in elastic materials with orthorhombic symmetry", *J. Sound Vib.* **47** (1976), 39–52.

[Dai et al. 2010] H.-H. Dai, J. Kaplunov, and D. A. Prikazchikov, "A long-wave model for the surface elastic wave in a coated half-space", *Proc. R. Soc. Lond. A* **466**:2122 (2010), 3097–3116.

[Erbaş et al. 2014] B. Erbaş, J. Kaplunov, and D. A. Prikazchikov, "The near-resonant regimes of a moving load in a three-dimensional problem for a coated elastic half-space", *Math. Mech. Solids* (published online October 2014).

[Every 2002] A. G. Every, "Measurement of the near-surface elastic properties of solids and thin supported films", *Measurement Sci. Tech.* **13**:R21-R39 (2002).

[Farnell and Adler 1972] G. W. Farnell and E. L. Adler, *Elastic wave propagation in thin layers*, Academic Press, New York, New York, 1972.

[Hess et al. 2013] P. Hess, A. M. Lomonosov, and A. P. Mayer, "Laser-based linear and nonlinear guided elastic waves at surfaces (2D) and wedges (1D)", *Ultrasonics* **54** (2013), 39–55.

[Küchler and Richter 1998] K. Küchler and E. Richter, "Ultrasonic surface waves for studying the properties of thin films", *Thin Solid Films* **315** (1998), 29–34.

[Makarov et al. 1995] S. Makarov, E. Chilla, and H. J. Frohlich, "Determination of elastic constants of thin films from phase velocity dispersion of different surface acoustic wave modes", *J. Appl. Phys.* **78** (1995), 5028–5034.

[Mindlin 1951] R. D. Mindlin, "Influence of rotatory inertia and shear on flexural motion isoropic elastic plates", *J. Appl. Mech.* (*ASME*) **18** (1951), 31–38.

[Muller and Touratier 1995] P. Muller and M. Touratier, "On the so-called variational consistency of plate models, I: indefinite plates: evaluation of dispersive behaviour", *J. Sound Vib.* **188**:4 (1995), 515–527.

[Ogden and Vinh 2004] R. W. Ogden and P. C. Vinh, "On Rayleigh waves in incompressible orthotropic elastic solids", *J. Acoust. Soc. Am.* **115** (2004), 530–533.

[Steigmann and Ogden 2007] D. J. Steigmann and R. W. Ogden, "Surface waves supported by thin-film/substrate interactions", *IMA J. Appl. Math.* **72**:6 (2007), 730–747.

[Stephen 1997] N. G. Stephen, "Mindlin plate theory: best shear coefficient and higher spectravalidity", *J. Sound Vib.* **202** (1997), 539–553.

[Stroh 1962] A. N. Stroh, "Steady state problems in anisotropic elasticity", *J. Math. Phys.* (*MIT*) **41** (1962), 77–103.

[Tiersten 1969] H. F. Tiersten, "Elastic surface waves guided by thin films", *J. Appl. Phys.* **40** (1969), 770–789.

[Touratier 1991] M. Touratier, "An efficient standard plate theory", *Int. J. Eng. Sci.* **29** (1991), 901–916.

[Vinh and Anh 2014a] P. C. Vinh and V. T. N. Anh, "An approximate secular equation of Rayleigh waves in an isotropic elastic half-space coated with a thin isotropic elastic layer", *Acta Mech.* **225**:9 (2014), 2539–2547.

[Vinh and Anh 2014b] P. C. Vinh and V. T. N. Anh, "Rayleigh waves in an orthotropic half-space coated by a thin orthotropic layer with sliding contact", *Int. J. Eng. Sci.* **75** (2014), 154–164.

[Vinh and Linh 2012] P. C. Vinh and N. T. K. Linh, "An approximate secular equation of Rayleigh waves propagating in an orthotropic elastic half-space coated by a thin orthotropic elastic layer", *Wave Motion* **49**:7 (2012), 681–689.

[Vinh and Linh 2013] P. C. Vinh and N. T. K. Linh, "An approximate secular equation of generalized Rayleigh waves in pre-stressed compressible elastic solids", *Int. J. Non-Linear Mech.* **50** (2013), 91–96.

[Vinh and Ogden 2004] P. C. Vinh and R. W. Ogden, "Formulas for the Rayleigh wave speed in orthotropic elastic solids", *Arch. Mech. Stos.* **56**:3 (2004), 247–265.

[Vinh et al. 2014a] P. C. Vinh, V. T. N. Anh, and V. P. Thanh, "Rayleigh waves in an isotropic elastic half-space coated by a thin isotropic elastic layer with smooth contact", *Wave Motion* **51**:3 (2014), 496–504.

[Vinh et al. 2014b] P. C. Vinh, N. T. K. Linh, and V. T. N. Anh, "Rayleigh waves in an incompressible orthotropic half-space coated by a thin elastic layer", *Arch. Mech. Stos.* **66**:3 (2014), 173–184.

Received 4 Jun 2015. Revised 10 Dec 2015. Accepted 16 Dec 2015.

PHAM CHI VINH: pcvinh@vnu.edu.vn
Faculty of Mathematics, Mechanics and Informatics, Hanoi University of Science, 334 Nguyen Trai Street, Hanoi 1000, Vietnam

VU THI NGOC ANH: anhvungoc.khtn@gmail.com
Faculty of Mathematics, Mechanics and Informatics, Hanoi University of Science, 334 Nguyen Trai Street, Hanoi 1000, Vietnam

JOURNAL OF MECHANICS OF MATERIALS AND STRUCTURES
Vol. 11, No. 3, 2016
dx.doi.org/10.2140/jomms.2016.11.279

NONLOCAL FORCED VIBRATION OF A DOUBLE SINGLE-WALLED CARBON NANOTUBE SYSTEM UNDER THE INFLUENCE OF AN AXIAL MAGNETIC FIELD

MARIJA B. STAMENKOVIĆ, DANILO KARLIČIĆ, GORAN JANEVSKI AND PREDRAG KOZIĆ

The influence of various physical phenomena on the dynamic behavior of nanostructures has been attracting more and more attention of the scientific community. This paper discusses the effects of the axial magnetic field on the externally excited double single-walled carbon nanotube (DSWCNT) coupled by a Winkler elastic medium. It is assumed that both carbon nanotubes are identical and under the influence of compressive axial load with simply supported ends. Based on the Eringen nonlocal elasticity and Euler–Bernoulli beam theory, the system of two coupled nonhomogeneous partial differential equations of motion is derived, where the effects of the Lorentz magnetic force are obtained via a Maxwell relation. The dynamic responses of the DSWCNT system for four different cases of external transversal load are considered. The closed form solutions for the transversal displacements are obtained by applying the Bernoulli–Fourier method of particular integrals on the system of nonhomogeneous partial differential equations of motion. Also, analytical expressions of the amplitude ratio for forced vibration are derived and then validated with existing results. Moreover, the obtained analytical results for fundamental natural frequency are validated with results obtained by molecular dynamics (MD) simulation and show fine agreements. The effects of compressive axial load, nonlocal parameter, axial magnetic field and stiffness coefficient of the elastic medium on the forced dynamic behavior of DSWCNT are considered through numerical examples. From numerical results we can conclude that the dynamical behavior of DSWCNT is greatly influenced by the magnetic field and nonlocal parameter. Furthermore, by selecting the intensity of the axial magnetic field in a certain range, it is possible to adjust the stiffness of the system without changing the material and geometric parameters. This effect implies a change in the natural frequencies of the system.

1. Introduction

In the last few decades, carbon nanotubes (CNTs) [Iijima 1991; Hata et al. 2004; Iijima et al. 1996] have drawn considerable attention from scientists and engineers in the field of nanotechnology due to their extraordinary physical [Reich et al. 2008], chemical [Hu et al. 1999], and mechanical properties [Lu 1997]. Salvetat et al. [1999] explain the properties of nanotubes in the wider context of materials science, where experimental results confirm the theoretical predictions that carbon nanotubes have high strength, extraordinary flexibility and resilience. Moreover, these superior characteristics provide them with a wide range of applications in nanoscale devices, such as biosensors [Murmu and Adhikari 2012; Adhikari and Chowdhury 2010], mass sensors [Murmu and Adhikari 2011; Li and Chou 2004], nanoactuators [Li et al. 2008; Roth and Baughman 2002], field emitters [Saito 2003], nanoelectronic

Keywords: forced vibration, nonlocal elasticity, axial magnetic field, analytical solution, carbon nanotubes.

devices [Avouris et al. 2007], and fillers for nanocomposite structures [Moniruzzaman and Winey 2006; Ajayan et al. 2006]. Single-walled carbon nanotubes (SWCNT) are cylindrical macromolecules obtained in specific technological processes by rolling the two-dimensional structures such as graphene sheets into a tube. Based on the experimental analyses [Ruoff et al. 2003; Dresselhaus et al. 2005] and atomistic theories [Dubay and Kresse 2003; Liu et al. 2003], it has been shown that the "size-effect" plays an important role in describing the physical and mechanical properties of materials on the nanoscale level of CNTs. However, conducting experiments on the nano level is a very complex and expensive task due to difficulties in the control of all system parameters.

Furthermore, an atomistic theory such as molecular dynamic (MD) simulation [Duan et al. 2007] is suitable only for systems with a small number of particles; such theories can be expensive in view of time or computational resources for larger systems. Due to the disadvantages of these two methods, researchers are increasingly turning to models obtained through continuum mechanics. However, because of the existence of small-scale effects, the classical continuum theories need to be reformulated to take these effects into account.

This can be done by introducing nonlocality in the space domain, modifying the corresponding constitutive equation and introducing the material parameter, which takes into account the effects of length scale and influence of the interatomic forces. One of the first scale-dependent continuum theories proposed by Eringen and coworkers [Eringen 1972; 1983; Eringen and Edelen 1972], which takes nonlocal effects into account is known as the nonlocal elasticity theory. According to Eringen [2002], the nonlocal theory gives great approximation for a large class of problems in nanosystems where the influence of length-scales is very pronounced. Yang et al. [2010] investigated nonlinear free vibration of single-walled carbon nanotubes (SWCNTs), while Ke et al. [2009] investigated nonlinear free vibration of embedded double-walled carbon nanotubes (DWNTs), based on Eringen's nonlocal elasticity theory and von Kármán geometric nonlinearity.

Consideration of magnetic field effects is important to complete the knowledge of the mechanical behavior of nanomaterials such as CNTs [Bellucci et al. 2007; Correa-Duarte et al. 2005] and graphene sheets [Goerbig et al. 2006; Ghorbanpour Arani and Shokravi 2014]. Arani et al. [2013] studied thermononlocal vibration of a double bounded graphene sheet under the influence of two-dimensional magnetic field with biaxial in-plane load. They obtained a numerical solution of the coupled partial differential equation by the differential quadrature method for simply supported boundary conditions and analyzed the influences of the magnetic field on the frequency ratio. Based on the nonlocal elasticity theory, Kiani [2012] reformulated Rayleigh, Timoshenko and higher-order beam theories for modeling wave propagation in embedded SWCNT under the influence of an axial magnetic field. The authors derived phase and group velocity and investigated the influence of small-scale parameters, longitudinal magnetic field stiffness coefficients of the surrounding medium on the flexural and shear waves. Narendar et al. [2012] analyzed the effects of a longitudinal magnetic field on wave dispersion characteristics of SWCNT embedded in a Pasternak elastic medium in the framework of nonlocal elasticity. They found that the nonlocality reduces the wave velocity in the presence of a magnetic field, but without the influence on the higher frequency region. In the paper proposed by Murmu et al. [2012b], authors considered transversal vibration of magnetic influenced double walled carbon nanotubes (DWCNT) according to the Eringen nonlocal continuum theory. Analytical solutions of natural frequency and transversal displacements of DWCNT were obtained for simply supported boundary conditions. Also, the effects of different materials

parameters on the vibration behavior were analyzed and discussed in detail. Consideration of the effects of an axial magnetic field on the dynamical behavior of double single-walled carbon nanotubes using the nonlocal Euler–Bernoulli beam theory is shown in the work of Murmu et al. [2012a]. Applying a method of separation of variables, they solved the system of two coupled partial differential equations and obtained a closed form solution for natural frequency. The effects of a nonlocal parameter and intensity of longitudinal magnetic field on the synchronous and asynchronous vibration phases of a double single walled carbon system were also investigated. Karličić et al. [2014c] investigated the influence of damping and axial magnetic field effects on the vibration behavior of a viscoelasticity system of m coupled carbon nanotubes based on the nonlocal viscoelasticity theory. They obtained an analytical solution for damping natural frequency, damping ratio and their critical values in the case when the mode and number of nanotubes tend to infinity.

The modeling of forced vibration states in nanosystems becomes a more and more important part in the design of MEMS and NEMS devices [Kacem et al. 2011; Lazarus et al. 2012]. Based on the Kirchhoff plate theory and Eringen constitutive relation, governing equations of motion are derived and then solved by using the Galerkin procedures for vibration frequencies and forced response. Aksencer and Aydogdu [2012] investigated forced vibration of nanoplates by using the nonlocal elasticity and Kirchhoff plate theory. The Navier-type solution method was used for simply supported nanoplates where forced vibration response was obtained in the analytical form. Claeyssen et al. [2013] explored the forced response of a single carbon nanotube modeled via the nonlocal Euler–Bernoulli beam theory. Forced responses were determined for different external loads and boundary conditions using the Galerkin method. Recently, researchers have focused their investigations on the particular problem of forced vibration such as the influence of moving nanoparticles on nanostructural elements such as nanotubes and nanoplates [Kiani and Mehri 2010; Şimşek 2010a]. Şimşek [2011] presented an analytical method for the forced vibration of an elastically connected double-carbon nanotube system carrying a moving nanoparticle based on the nonlocal elasticity and Euler–Bernoulli beam theory. The closed-form solutions for the dynamic deflections of the two nanobeams were derived for two sets of critical velocity, and then effects of the nonlocal parameter, aspect ratio, velocity of the moving nanoparticle and the elastic layer between the nanotubes on the dynamic responses were discussed. Zhang et al. [2008] introduced compressive axial load on the external excited double beam system. They obtained analytical solutions of forced vibration responses for two cases of particular excitation loadings. Oniszczuk [2003] analyzed undamped forced transverse vibrations of an elastically connected complex double-beam system, based on the Euler–Bernoulli beam and classical elasticity theory. Several cases of particularly interesting excitation loadings such as of stationary harmonic loads and moving forces were investigated.

In this paper, using the Euler–Bernoulli beam theory we analyze the effects of axial compressive load and magnetic field on the forced transversal vibration of a magnetically sensitive double SWCNT system. The Eringen nonlocal continuum theory is used to introduce small-scale effects via a material parameter. It is assumed that the double coupled SWCNT system is modeled as a system of two slender parallel nanobeams elastically connected by a Winkler elastic medium. The system of two coupled partial differential equations of motion is derived by considering the nonlocal Euler–Bernoulli beam theory and classical Maxwell relation. Analytical solutions for natural frequencies, amplitude ratio and forced response in four cases of external excitation load are determined by applying the Bernoulli–Fourier methods. Numerical simulations show that the nonlocal parameter and intensity of axial magnetic fields

have a significant influence on the natural frequencies and dynamical response of the DSWCNT system. It should be noted that this study is limited only to the armchair SWCNT system, where the influence of rotation of magnetically influenced nanotubes is neglected [Popov et al. 2014; Krstić et al. 2004; Slavcheva and Roussignol 2011]. Then molecular dynamics (MD) simulation is implemented to obtain fundamental frequencies of nanotubes for armchair SWCNT and values of aspect ratio to compare them with the results obtained by the nonlocal beam models, presented by Ansari and Sahmani [2012] and Ansari et al. [2012]. The results presented here are validated with the results found in the literature.

2. Problem formulation

2.1. ***Nonlocal elastic constitutive relation.*** The fundamental equations of the nonlocal elasticity theory are considered in this section. The basic assumption in this continuum theory is that the stress at a point is a function of the strains at all points of the whole body. The constitutive elastic relation for a three-dimensional homogeneous isotropic body in the integral form is given by Eringen and coworkers [Eringen 1972; Eringen and Edelen 1972] as

$$\sigma_{ij}(x) = \int \alpha(|x - x'|, \tau) C_{ijkl} \epsilon_{kl}(x')\, dV(x') \quad \text{for all } x \in V, \tag{1a}$$

$$\sigma_{ij,j} = 0, \tag{1b}$$

$$\epsilon_{ij} = \tfrac{1}{2}(u_{i,j} + u_{j,i}), \tag{1c}$$

where C_{ijkl} is the elastic modulus tensor for classical isotropic elasticity; σ_{ij} and ϵ_{ij} are the stress and the strain tensors, respectively, and u_i is the displacement vector. By $\alpha(|x - x'|, \tau)$ we denote the nonlocal modulus or attenuation function, which incorporates nonlocal effects into the constitutive equation at a reference point x produced by the local strain at a source x'. The above absolute value of the difference $|x - x'|$ denotes the Euclidean metric, and τ is the parameter $\tau = (e_0 a)/l$, where l is the external characteristic length (crack length, wave length), a describes the internal characteristic length (lattice parameter, granular size and distance between C-C bounds) and e_0 is a constant appropriate to each material that can be identified from atomistic simulations or by using the dispersive curve of the Born–Karman model of lattice dynamics.

As Equation (1) is difficult to use in practical examples, simplified constitutive relations in the differential form are developed. According to Eringen [1983], constitutive relations in differential form are given as

$$\sigma_{xx} - \mu \frac{d^2 \sigma_{xx}}{dx^2} = E \epsilon_{xx}, \tag{2}$$

$$\sigma_{xz} - \mu \frac{d^2 \sigma_{xz}}{dx^2} = G \gamma_{xz}, \tag{3}$$

where E and G are the elastic modulus and the shear modulus of the beam, respectively, $\mu = (e_0 a)^2$ is the nonlocal parameter, σ_{xx}, σ_{xz} are the normal and the shear nonlocal stresses, respectively, and $\epsilon_{xx} = \partial u / \partial x$ is the axial deformation. The internal characteristic lengths $(e_0 a)$ are often assumed to be in the range 0–2 [nm] for nanomaterials such as carbon nanotubes, zinc oxide, etc. When $e_0 a = 0$, the nonlocal constitutive relation is reduced to the classical constitutive relation of the elastic body.

2.2. ***Maxwell's relation.*** According to Murmu et al. [2012b; 2012a], the equation which connects the current density $\boldsymbol{J}$, distributing vector of magnetic field $\boldsymbol{h}$, strength vector of the electric fields $\boldsymbol{e}$, and magnetic field permeability $\boldsymbol{\eta}$, is represented by Maxwell's expressions [Kraus 1984] as

$$\boldsymbol{J} = \nabla \times \boldsymbol{h}, \quad \nabla \times \boldsymbol{e} = -\eta \frac{\partial \boldsymbol{h}}{\partial t}, \quad \nabla \cdot \boldsymbol{h} = 0, \tag{4}$$

where the vectors of distributing magnetic field $\boldsymbol{h}$ and the electric field $\boldsymbol{e}$ are defined as

$$\boldsymbol{h} = \nabla \times (\boldsymbol{U} \times \boldsymbol{H}), \quad \boldsymbol{e} = -\eta \left(\frac{\partial \boldsymbol{U}}{\partial t} \times \boldsymbol{H} \right), \tag{5}$$

in which $\nabla = (\partial/\partial x)\boldsymbol{i} + (\partial/\partial y)\boldsymbol{j} + (\partial/\partial z)\boldsymbol{k}$ is the Hamilton operator, $\boldsymbol{U} = (x, y, z)$ is the displacement vector and $\boldsymbol{H} = (H_x, 0, 0)$ is the vector of the axial magnetic field. In the present study, we assume that the axial magnetic field acts on the double SWCNT in the x-direction of the system. Now, we can write the vector of the distributing magnetic field [Murmu et al. 2012b; 2012a] in the form

$$\boldsymbol{h} = -H_x \left(\frac{\partial v}{\partial y} + \frac{\partial w}{\partial z} \right) \boldsymbol{i} + H_x \frac{\partial v}{\partial x} \boldsymbol{j} + H_x \frac{\partial w}{\partial x} \boldsymbol{k}. \tag{6}$$

Then we introduce (6) into the first expression of (4):

$$\boldsymbol{J} = \nabla \times \boldsymbol{h} = H_x \left(-\frac{\partial^2 v}{\partial x \partial z} + \frac{\partial^2 w}{\partial x \partial y} \right) \boldsymbol{i} - H_x \left(\frac{\partial^2 v}{\partial y \partial z} + \frac{\partial^2 w}{\partial x^2} + \frac{\partial^2 w}{\partial z^2} \right) \boldsymbol{j} + H_x \left(\frac{\partial^2 v}{\partial x^2} + \frac{\partial^2 v}{\partial y^2} + \frac{\partial^2 w}{\partial z \partial y} \right) \boldsymbol{k}. \tag{7}$$

Introducing (7) into the expressions for the Lorentz force induced by the axial magnetic field yields

$$\boldsymbol{f} = f_x \boldsymbol{i} + f_y \boldsymbol{j} + f_z \boldsymbol{k} = \eta (\boldsymbol{J} \times \boldsymbol{H}), \tag{8}$$

where f_x, f_y and f_z express the Lorentz force along the x, y and z directions, as follows:

$$f_x = 0, \tag{9a}$$

$$f_y = \eta H_x^2 \left(\frac{\partial^2 v}{\partial x^2} + \frac{\partial^2 v}{\partial y^2} + \frac{\partial^2 w}{\partial z \partial y} \right), \tag{9b}$$

$$f_z = \eta H_x^2 \left(\frac{\partial^2 w}{\partial x^2} + \frac{\partial^2 w}{\partial y^2} + \frac{\partial^2 v}{\partial z \partial y} \right). \tag{9c}$$

We assume that the transversal displacements of the first and second SWCNT in the system are denoted as $w_1(x, t)$ and $w_2(x, t)$, respectively, and the Lorentz force acts only in the z direction, which can be written as

$$f_{z,i} = \eta H_x^2 \frac{\partial^2 w_i}{\partial x^2}, \quad i = 1, 2. \tag{10}$$

Finally, it is possible to obtain force per unit length of both SWCNTs in the system as

$$\tilde{q}_i(x, t) = \int_A f_{z,i} \, dA = \eta A H_x^2 \frac{\partial^2 w_i}{\partial x^2}, \quad i = 1, 2. \tag{11}$$

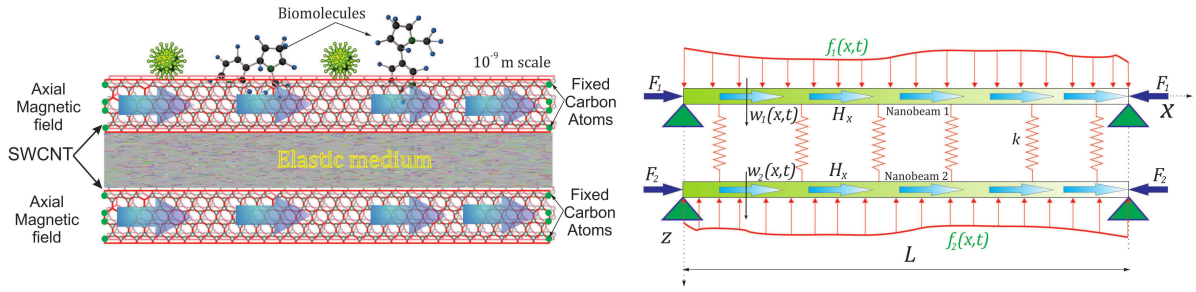

Figure 1. The system of double SWCNT affected by an axial magnetic field. Left: the physical model of external excited DSWCNTS with fixed single layer of carbon atoms [Ansari and Sahmani 2012] coupled by an elastic medium and influenced by an axial magnetic field. Right: the equivalent mechanical model.

2.3. ***Mathematical model.*** Consider a compressive nonlocal double SWCNT system which is under the influence of an axial magnetic field as shown in Figure 1, left. The nonlocal double SWCNT system is assumed to be modeled as a system composed of two parallel nanobeams, which have the same length and are continuously joined by a Winkler elastic layer. It should be noted that the fixed atomic layers on the sides of the carbon nanotubes represent, from the mechanical point of view, simply supported boundary conditions, as shown in [Ansari and Sahmani 2012]. The stiffness modulus of the Winkler elastic layer is denoted with k. The transversal displacement over the two nanobeams is denoted by $w_1(x,t)$ and $w_2(x,t)$, respectively; see Figure 1, right. For the sake of simplicity, we will consider only the case of identical nanobeams, where geometric and physical properties are the same for both nanobeams and defined as follows: A is the cross-sectional area, E is the Young's modulus, ρ is the mass density, I is the moment of inertia and L is the length of the nanobeam. Also, we assume that nanobeams 1 and 2 are subjected to positive axial compressions F_1 and F_2 and arbitrarily distributed transverse continuous loads $f_1(x,t)$ and $f_2(x,t)$, respectively, that are positive when they act downward. The influence of the Lorentz magnetic force on the double nanobeam system is caused by the axial magnetic field which acts in the x direction, as shown in Figure 1.

Using the Euler–Bernoulli beam theory and Eringen nonlocal elasticity following the methodology presented in the work of Kozić et al. [2014], the governing equations of motion of the nonlocal double nanobeam system (NDNBS) can be given as

$$\rho A\frac{\partial^2 w_1}{\partial t^2} - f_1 + k(w_1 - w_2) + F_1\frac{\partial^2 w_1}{\partial x^2} - \eta A H_x^2\frac{\partial^2 w_1}{\partial x^2} + EI\frac{\partial^4 w_1}{\partial x^4} = \mu\frac{\partial^2}{\partial x^2}\left[\rho A\frac{\partial^2 w_1}{\partial t^2} - f_1 + k(w_1 - w_2) + F_1\frac{\partial^2 w_1}{\partial x^2} - \eta A H_x^2\frac{\partial^2 w_1}{\partial x^2}\right], \tag{12}$$

$$\rho A\frac{\partial^2 w_2}{\partial t^2} - f_2 - k(w_1 - w_2) + F_2\frac{\partial^2 w_2}{\partial x^2} - \eta A H_x^2\frac{\partial^2 w_2}{\partial x^2} + EI\frac{\partial^4 w_2}{\partial x^4} = \mu\frac{\partial^2}{\partial x^2}\left[\rho A\frac{\partial^2 w_2}{\partial t^2} - f_2 - k(w_1 - w_2) + F_2\frac{\partial^2 w_2}{\partial x^2} - \eta A H_x^2\frac{\partial^2 w_2}{\partial x^2}\right]. \tag{13}$$

The boundary conditions of the NDNBS are assumed to be simply supported and considered as

$$w_i(0,t) = w_i(L,t) = 0, \tag{14}$$

$$\frac{\partial^2 w_i}{\partial x^2}(0,t) = \frac{\partial^2 w_i}{\partial x^2}(L,t) = 0, \quad i = 1,2, \tag{15}$$

where L is the length of the two nanobeams, and t is the time.

In order to simplify the solving of Equations (12) and (13), we introduce the dimensionless parameters

$$\begin{gathered} \mu = L^2\eta^2, \quad x = L\xi, \quad L = \frac{x}{\xi}, \quad t^2 = \tau^2 L^4 c^2, \quad c^2 = \frac{\rho A}{EI}, \quad \overline{f}_i = \frac{L^3}{EI} f_i, \\ \overline{F}_i = \frac{L^2 F_i}{EI}, \quad K = \frac{kL^4}{EI}, \quad \mathrm{MP} = \frac{L^2}{EI}\eta A H_x^2, \quad w_i = L\overline{w}_i, \quad i = 1,2. \end{gathered} \tag{16}$$

Introducing dimensionless parameters (16) into Equations (12) and (13), we can write the system of partial differential equations as

$$\begin{aligned} &\frac{\partial^2 \overline{w}_1}{\partial \tau^2} + K(\overline{w}_1 - \overline{w}_2) + (\overline{F}_1 - \mathrm{MP})\frac{\partial^2 \overline{w}_1}{\partial \xi^2} + \frac{\partial^4 \overline{w}_1}{\partial \xi^4} \\ &\qquad - \eta^2 \frac{\partial^2}{\partial \xi^2}\left[\frac{\partial^2 \overline{w}_1}{\partial \tau^2} + K(\overline{w}_1 - \overline{w}_2) + (\overline{F}_1 - \mathrm{MP})\frac{\partial^2 \overline{w}_1}{\partial \xi^2}\right] = \overline{f}_1 - \eta^2 \frac{\partial^2 \overline{f}_1}{\partial \xi^2}, \end{aligned} \tag{17}$$

$$\begin{aligned} &\frac{\partial^2 \overline{w}_2}{\partial \tau^2} - K(\overline{w}_1 - \overline{w}_2) + (\overline{F}_2 - \mathrm{MP})\frac{\partial^2 \overline{w}_1}{\partial \xi^2} + \frac{\partial^4 \overline{w}_1}{\partial \xi^4} \\ &\qquad - \eta^2 \frac{\partial^2}{\partial \xi^2}\left[\frac{\partial^2 \overline{w}_1}{\partial \tau^2} - K(\overline{w}_1 - \overline{w}_2) + (\overline{F}_2 - \mathrm{MP})\frac{\partial^2 \overline{w}_1}{\partial \xi^2}\right] = \overline{f}_2 - \eta^2 \frac{\partial^2 \overline{f}_2}{\partial \xi^2}, \end{aligned} \tag{18}$$

where ξ is the dimensionless axial coordinate, and τ is the dimensionless time. Expressions (17) and (18) represent dimensionless governing equations of motion of the NDNBS shown in Figure 1, right.

3. Analytical solution of equations

3.1. ***Free vibrations.*** The homogeneous governing partial differential equations (17) and (18) of the NDNBS with boundary conditions (14) and (15) can be solved by the Bernoulli–Fourier method, assuming the solutions in the forms

$$\overline{w}_1(\xi,\tau) = \sum_{n=1}^{\infty} X_n(\xi) T_{1n}(\tau), \tag{19}$$

$$\overline{w}_2(\xi,\tau) = \sum_{n=1}^{\infty} X_n(\xi) T_{2n}(\tau), \tag{20}$$

where $T_{1n}(\tau)$ and $T_{2n}(\tau)$ denote the unknown dimensionless time functions, and $X_n(\xi)$ is the known mode shape function for the simply supported single nanobeam, which is defined as

$$X_n(\xi) = \sin(k_n \xi), \tag{21}$$

with

$$k_n = n\pi, \quad n = 1, 2, 3, \ldots. \tag{22}$$

The substitution of Equations (19) and (20) into Equations (17) and (18), neglecting the external transversal load $\overline{f}_1$ and $\overline{f}_2$, yields

$$\ddot{T}_{1n} + \left[K - (\overline{F}_1 - \mathrm{MP})k_n^2 + \frac{k_n^4}{1+\eta^2 k_n^2}\right]T_{1n} - KT_{2n} = 0, \tag{23}$$

$$\ddot{T}_{2n} + \left[K - (\overline{F}_2 - \mathrm{MP})k_n^2 + \frac{k_n^4}{1+\eta^2 k_n^2}\right]T_{2n} - KT_{1n} = 0. \tag{24}$$

We assume the solutions of differential equations (23) and (24) in the forms

$$T_{1n} = C_n e^{j\omega_n \tau}, \quad T_{2n} = D_n e^{j\omega_n \tau}, \quad j = \sqrt{-1}, \tag{25}$$

where ω_n denotes the natural frequency of the double-nanobeam system, and C_n and D_n represent the amplitude coefficients of the two nanobeams, respectively. Substituting (25) into (23) and (24) yields

$$\begin{bmatrix} K - (\overline{F}_1 - \mathrm{MP})k_n^2 + \frac{k_n^4}{1+\eta^2 k_n^2} - \omega_n^2 & -K \\ -K & K - (\overline{F}_2 - \mathrm{MP})k_n^2 + \frac{k_n^4}{1+\eta^2 k_n^2} - \omega_n^2 \end{bmatrix} \begin{Bmatrix} C_n \\ D_n \end{Bmatrix} = \begin{Bmatrix} 0 \\ 0 \end{Bmatrix}. \tag{26}$$

Nontrivial solutions for the constants C_n and D_n can be obtained only when the determinant of the coefficients in equations (26) vanishes. This gives the following frequency equation:

$$\omega_n^4 - \omega_n^2\left[2K - \overline{F}_1 k_n^2 - \overline{F}_2 k_n^2 + 2MPk_n^2 + 2\frac{k_n^4}{1+\eta^2 k_n^2}\right] + \left[K - (\overline{F}_1 - \mathrm{MP})k_n^2 + \frac{k_n^4}{1+\eta^2 k_n^2}\right]\left[K - (\overline{F}_2 - \mathrm{MP})k_n^2 + \frac{k_n^4}{1+\eta^2 k_n^2}\right] - K^2 = 0. \tag{27}$$

From (27) we obtain

$$\omega_{n\mathrm{I}}^2 = \tfrac{1}{2}\left[b - \sqrt{b^2 - 4c}\right], \tag{28}$$

$$\omega_{n\mathrm{II}}^2 = \tfrac{1}{2}\left[b + \sqrt{b^2 - 4c}\right], \tag{29}$$

where $\omega_{n\mathrm{I}}$ is the lower natural frequency of the system, and $\omega_{n\mathrm{II}}$ is the higher natural frequency. In the relations (28) and (29) the parameters are given as

$$b = \left[2K - \overline{F}_1 k_n^2 - \overline{F}_2 k_n^2 + 2MPk_n^2 + 2\frac{k_n^4}{1+\eta^2 k_n^2}\right], \tag{30}$$

$$c = \left[K - (\overline{F}_1 - \mathrm{MP})k_n^2 + \frac{k_n^4}{1+\eta^2 k_n^2}\right]\left[K - (\overline{F}_2 - \mathrm{MP})k_n^2 + \frac{k_n^4}{1+\eta^2 k_n^2}\right] - K^2. \tag{31}$$

For each of the natural frequencies, the associated amplitude ratio of vibration modes of the two nanobeams is given by

$$\alpha_{n_i} = \frac{D_{n_i}}{C_{n_i}} = \frac{K - (\overline{F}_1 - \mathrm{MP})k_n^2 + \frac{k_n^4}{1+\eta^2 k_n^2} - \omega_{n_i}^2}{K} = \frac{K}{K - (\overline{F}_2 - \mathrm{MP})k_n^2 + \frac{k_n^4}{1+\eta^2 k_n^2} - \omega_{n_i}^2}, \quad i = \mathrm{I}, \mathrm{II}. \tag{32}$$

By entering $\omega_{n\mathrm{I}}^2$ and $\omega_{n\mathrm{II}}^2$ from (28) and (29) into (32), respectively, we obtain

$$3\alpha_{n\mathrm{I}} = \frac{K - (\overline{F}_1 - \mathrm{MP})k_n^2 + \frac{k_n^4}{1+\eta^2 k_n^2} - \omega_{n\mathrm{I}}^2}{K} = \frac{K}{K - (\overline{F}_2 - \mathrm{MP})k_n^2 + \frac{k_n^4}{1+\eta^2 k_n^2} - \omega_{n\mathrm{I}}^2}, \tag{33}$$

$$\alpha_{n\mathrm{II}} = \frac{K - (\overline{F}_1 - \mathrm{MP})k_n^2 + \frac{k_n^4}{1+\eta^2 k_n^2} - \omega_{n\mathrm{II}}^2}{K} = \frac{K}{K - (\overline{F}_2 - \mathrm{MP})k_n^2 + \frac{k_n^4}{1+\eta^2 k_n^2} - \omega_{n\mathrm{II}}^2}. \tag{34}$$

3.2. ***Forced vibrations.*** The above analysis showed the solution of the homogeneous system of partial differential equations. In the following analysis we will consider the nonhomogeneous differential equations (17) and (18) representing forced vibrations of the (SWCNT) system, assuming solutions in the forms

$$\overline{w}_1(\xi, \tau) = \sum_{n=1}^{\infty} X_n(\xi) \sum_{i=\mathrm{I}}^{\mathrm{II}} S_{ni}(\tau), \tag{35}$$

$$\overline{w}_2(\xi, \tau) = \sum_{n=1}^{\infty} X_n(\xi) \sum_{i=\mathrm{I}}^{\mathrm{II}} \alpha_{ni} S_{ni}(\tau), \tag{36}$$

where $S_{ni}(\tau)$, $i = \mathrm{I}, \mathrm{II}$, denote the unknown dimensionless time functions corresponding to the natural frequencies ω_{ni}, $i = \mathrm{I}, \mathrm{II}$. Introduction (35) and (36) into (17) and (18), we obtain

$$\sum_{n=1}^{\infty} X_n \sum_{i=\mathrm{I}}^{\mathrm{II}} \left[\ddot{S}_{ni} + \left(K - (\overline{F}_1 - \mathrm{MP})k_n^2 + \frac{k_n^4}{1+\eta^2 k_n^2} - K\alpha_{ni} \right) S_{ni} \right] (1+\eta^2 k_n^2) = \overline{f}_1 - \eta^2 \frac{\partial^2 \overline{f}_1}{\partial \xi^2}, \tag{37}$$

$$\sum_{n=1}^{\infty} X_n \sum_{i=\mathrm{I}}^{\mathrm{II}} \left[\ddot{S}_{ni} + \left(K - (\overline{F}_2 - \mathrm{MP})k_n^2 + \frac{k_n^4}{1+\eta^2 k_n^2} - K\alpha_{ni}^{-1} \right) S_{ni} \right] (1+\eta^2 k_n^2)\alpha_{ni} = \overline{f}_2 - \eta^2 \frac{\partial^2 \overline{f}_2}{\partial \xi^2}. \tag{38}$$

By multiplying relations (37) and (38) by the mode shape function $X_m(\xi)$, then integrating with respect to ξ from 0 to 1 and using the orthogonality condition

$$\int_0^1 X_m(\xi) X_n(\xi)\, d\xi = \int_0^1 \sin(m\pi\xi)\sin(n\pi\xi)\, d\xi = \beta\delta_{mn} = \int_0^1 {X_n}^2(\xi)\, d\xi = \tfrac{1}{2}, \tag{39}$$

where δ_{mn} is the Kronecker delta function, we have

$$\sum_{i=\mathrm{I}}^{\mathrm{II}}\left[\ddot{S}_{ni}+\left(K-(\overline{F}_1-\mathrm{MP})k_n^2+\frac{k_n^4}{1+\eta^2k_n^2}-K\alpha_{ni}\right)S_{ni}\right]=2M\int_0^1\left(\overline{f}_1-\eta^2\frac{\partial^2\overline{f}_1}{\partial\xi^2}\right)X_n(\xi)\,d\xi, \quad (40)$$

$$\sum_{i=\mathrm{I}}^{\mathrm{II}}\left[\ddot{S}_{ni}+\left(K-(\overline{F}_2-\mathrm{MP})k_n^2+\frac{k_n^4}{1+\eta^2k_n^2}-K\alpha_{ni}^{-1}\right)S_{ni}\right]\alpha_{ni}=2M\int_0^1\left(\overline{f}_2-\eta^2\frac{\partial^2\overline{f}_2}{\partial\xi^2}\right)X_n(\xi)\,d\xi, \quad (41)$$

with

$$M=\frac{1}{1+\eta^2k_n^2}. \quad (42)$$

By combining equations (33), (34), (40) and (41) we obtain

$$\sum_{i=\mathrm{I}}^{\mathrm{II}}[\ddot{S}_{ni}+\omega_{ni}^2S_{ni}]=2M\int_0^1\left(\overline{f}_1-\eta^2\frac{\partial^2\overline{f}_1}{\partial\xi^2}\right)X_n(\xi)\,d\xi, \quad (43)$$

$$\sum_{i=\mathrm{I}}^{\mathrm{II}}[\ddot{S}_{ni}+\omega_{ni}^2S_{ni}]\alpha_{ni}=2M\int_0^1\left(\overline{f}_2-\eta^2\frac{\partial^2\overline{f}_2}{\partial\xi^2}\right)X_n(\xi)\,d\xi. \quad (44)$$

From equations (43) and (44) we obtain

$$\ddot{S}_{ni}+\omega_{ni}^2S_{ni}=R_{ni}(\tau),\quad i=\mathrm{I},\mathrm{II}, \quad (45)$$

where

$$R_{n\mathrm{I}}=2M\frac{1}{\alpha_{n\mathrm{II}}-\alpha_{n\mathrm{I}}}\int_0^1\left[\alpha_{n\mathrm{II}}\left(\overline{f}_1-\eta^2\frac{\partial^2\overline{f}_1}{\partial\xi^2}\right)-\left(\overline{f}_2-\eta^2\frac{\partial^2\overline{f}_2}{\partial\xi^2}\right)\right]X_n(\xi)\,d\xi, \quad (46)$$

$$R_{n\mathrm{II}}=2M\frac{1}{\alpha_{n\mathrm{I}}-\alpha_{n\mathrm{II}}}\int_0^1\left[\alpha_{n\mathrm{I}}\left(\overline{f}_1-\eta^2\frac{\partial^2\overline{f}_1}{\partial\xi^2}\right)-\left(\overline{f}_2-\eta^2\frac{\partial^2\overline{f}_2}{\partial\xi^2}\right)\right]X_n(\xi)\,d\xi. \quad (47)$$

From the equations (45) we obtain

$$S_{ni}(\tau)=\frac{1}{\omega_{ni}}\int_0^\tau R_{ni}(s)\sin[\omega_{ni}(\tau-s)]\,ds,\quad i=\mathrm{I},\mathrm{II}. \quad (48)$$

By combining (35), (36) and (48), the forced vibrations of the (SWCNT) system can be described by

$$\overline{w}_1(\xi,\tau)=\sum_{n=1}^{\infty}\sin(n\pi\xi)\sum_{i=\mathrm{I}}^{\mathrm{II}}\frac{1}{\omega_{ni}}\int_0^\tau R_{ni}(s)\sin[\omega_{ni}(\tau-s)]\,ds, \quad (49)$$

$$\overline{w}_2(\xi,\tau)=\sum_{n=1}^{\infty}\sin(n\pi\xi)\sum_{i=\mathrm{I}\alpha_{ni}}^{\mathrm{II}}\alpha_{ni}\frac{1}{\omega_{ni}}\int_0^\tau R_{ni}(s)\sin[\omega_{ni}(\tau-s)]\,ds. \quad (50)$$

Solutions (49) and (50) can be used to find the dynamic responses of this system for an arbitrary exciting transversal loading in cases with both stationary and moving loads. For the sake of simplicity

in further consideration, it is assumed that only the first nanobeam is subjected to the exciting load. Introducing $\overline{f}_1(\xi,\tau)\neq 0$ and $\overline{f}_2(\xi,\tau)=0$ into (46) and (47), we obtain

$$R_{n\mathrm{I}}=2M\frac{\alpha_{n\mathrm{II}}}{\alpha_{n\mathrm{II}}-\alpha_{n\mathrm{I}}}\int_0^1\left(\overline{f}_1-\eta^2\frac{\partial^2\overline{f}_1}{\partial\xi^2}\right)\sin(n\pi\xi)\,d\xi, \tag{51}$$

$$R_{n\mathrm{II}}=2M\frac{\alpha_{n\mathrm{I}}}{\alpha_{n\mathrm{I}}-\alpha_{n\mathrm{II}}}\int_0^1\left(\overline{f}_1-\eta^2\frac{\partial^2\overline{f}_1}{\partial\xi^2}\right)\sin(n\pi\xi)\,d\xi. \tag{52}$$

In the following, we conduct an analysis of forced vibrations for four cases of exciting loadings: uniformly distributed harmonic continuous load, concentrated harmonic force, moving constant force F and moving harmonic force.

3.2.1. *Uniformly distributed harmonic load.* The uniformly distributed harmonic load

$$\overline{f}_1(\xi,\tau)=r\sin(\Omega\tau) \tag{53}$$

acts upon the SWCNT system (see Figure 2), where r is the amplitude and Ω is the frequency of the exciting harmonic load. By substituting Equation (53) into (51) and (52), we obtain

$$R_{n\mathrm{I}}=4Mr\frac{\alpha_{n\mathrm{II}}}{n\pi(\alpha_{n\mathrm{II}}-\alpha_{n\mathrm{I}})}\sin(\Omega s),\quad n=1,3,5,\ldots, \tag{54}$$

$$R_{n\mathrm{II}}=4Mr\frac{\alpha_{n\mathrm{I}}}{n\pi(\alpha_{n\mathrm{I}}-\alpha_{n\mathrm{II}})}\sin(\Omega s),\quad n=1,3,5,\ldots. \tag{55}$$

The introduction of equations (54) and (55) into equations (49) and (50) gives

$$\overline{w}_1(\xi,\tau)=\sum_{n=1}^{\infty}\sin(n\pi\xi)\left[A_{n\mathrm{I}}\sin(\Omega\tau)+\sum_{i=\mathrm{I}}^{\mathrm{II}}B_{ni}\sin(\omega_{ni}\tau)\right], \tag{56}$$

$$\overline{w}_2(\xi,\tau)=\sum_{n=1}^{\infty}\sin(n\pi\xi)\left[A_{n\mathrm{II}}\sin(\Omega\tau)+\sum_{i=\mathrm{I}}^{\mathrm{II}}\alpha_{ni}B_{ni}\sin(\omega_{ni}\tau)\right], \tag{57}$$

where

$$A_{n\mathrm{I}}=\lambda_1\left[\frac{\alpha_{n\mathrm{II}}}{(\omega_{n\mathrm{I}}^2-\Omega^2)}-\frac{\alpha_{n\mathrm{I}}}{(\omega_{n\mathrm{II}}^2-\Omega^2)}\right], \tag{58}$$

$$A_{n\mathrm{II}}=\lambda_1\alpha_{n\mathrm{I}}\alpha_{n\mathrm{II}}\left[\frac{1}{(\omega_{n\mathrm{I}}^2-\Omega^2)}-\frac{1}{(\omega_{n\mathrm{II}}^2-\Omega^2)}\right], \tag{59}$$

$$B_{n\mathrm{I}}=-\lambda_1\Omega\alpha_{n\mathrm{II}}\frac{1}{\omega_{n\mathrm{I}}}\cdot\frac{1}{(\omega_{n\mathrm{I}}^2-\Omega^2)}, \tag{60}$$

$$B_{n\mathrm{II}}=\lambda_1\Omega\alpha_{n\mathrm{I}}\frac{1}{\omega_{n\mathrm{II}}}\cdot\frac{1}{(\omega_{n\mathrm{II}}^2-\Omega^2)}, \tag{61}$$

$$\lambda_1=\frac{4Mr}{n\pi(\alpha_{n\mathrm{II}}-\alpha_{n\mathrm{I}})}\quad\text{and}\quad M=\frac{1}{1+\eta^2k_n^2}. \tag{62}$$

It can be noticed that equations (56) and (57) consist of two parts. The first part, containing the term $\sin(\Omega\tau)$, represents the steady-state forced vibrations of the SWCNT system, while the second part,

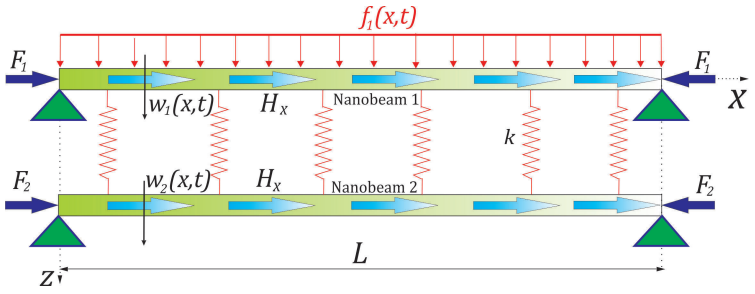

Figure 2. The double nanobeam system coupled by the Winkler elastic medium subjected to the uniformly distributed harmonic load.

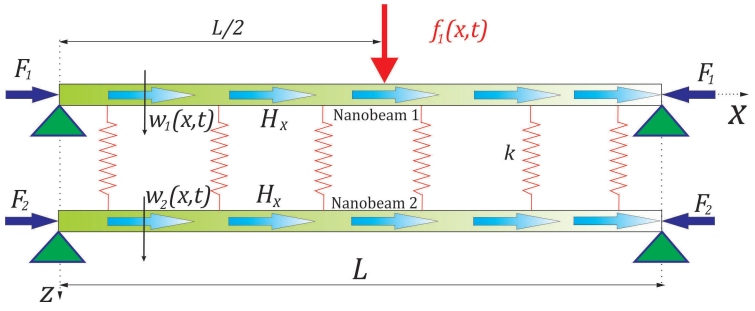

Figure 3. The double nanobeam system coupled by the Winkler elastic medium subjected to the concentrated harmonic force.

involving the terms $\sin(\omega\tau)$, denotes the free vibration of the SWCNT system. Assuming that only the steady-state response has practical significance, and ignoring the free response, the forced vibrations of the SWCNT system can be obtained by

$$\overline{w}_1(\xi,\tau) = \sin(\Omega\tau)\sum_{n=1}^{\infty} A_{n\mathrm{I}}\sin(n\pi\xi), \tag{63}$$

$$\overline{w}_2(\xi,\tau) = \sin(\Omega\tau)\sum_{n=1}^{\infty} A_{n\mathrm{II}}\sin(n\pi\xi), \tag{64}$$

where $A_{n\mathrm{I}}$ and $A_{n\mathrm{II}}$ denote the steady-state vibration amplitudes of the two nanobeams, respectively.

3.2.2. *Concentrated harmonic force.* The concentrated harmonic force

$$\overline{f}_1(\xi,\tau) = r\sin(\Omega\tau)\delta\left(\xi - \tfrac{1}{2}\right) \tag{65}$$

acts at the middle of the SWCNT system (see Figure 3), where r is the amplitude and Ω is the frequency of the exciting harmonic force and $\delta(\xi)$ is the Dirac delta function.

By substituting (65) into equations (51) and (52), we obtain

$$R_{n\mathrm{I}} = 2Mr\frac{\alpha_{n\mathrm{II}}}{\alpha_{n\mathrm{II}} - \alpha_{n\mathrm{I}}}\sin\left(\tfrac{1}{2}n\pi\right)\sin(\Omega\tau)[1+\eta^2 k_n^2], \tag{66}$$

$$R_{n\mathrm{II}} = 2Mr\frac{\alpha_{n\mathrm{I}}}{\alpha_{n\mathrm{I}} - \alpha_{n\mathrm{II}}}\sin\left(\tfrac{1}{2}n\pi\right)\sin(\Omega\tau)[1+\eta^2 k_n^2]. \tag{67}$$

The introduction of (66) and (67) into (49) and (50) gives

$$\overline{w}_1(\xi,\tau) = \sum_{n=1}^{\infty}\sin(n\pi\xi)\left[A_{n\mathrm{I}}\sin(\Omega\tau) + \sum_{i=\mathrm{I}}^{\mathrm{II}} B_{ni}\sin(\omega_{ni}\tau)\right], \tag{68}$$

$$\overline{w}_2(\xi,\tau) = \sum_{n=1}^{\infty}\sin(n\pi\xi)\left[A_{n\mathrm{II}}\sin(\Omega\tau) + \sum_{i=\mathrm{I}}^{\mathrm{II}} \alpha_{ni}B_{ni}\sin(\omega_{ni}\tau)\right], \tag{69}$$

where

$$A_{n\mathrm{I}} = \lambda_2\left[\frac{\alpha_{n\mathrm{II}}}{(\omega_{n\mathrm{I}}^2 - \Omega^2)} - \frac{\alpha_{n\mathrm{I}}}{(\omega_{n\mathrm{II}}^2 - \Omega^2)}\right], \tag{70}$$

$$A_{n\mathrm{II}} = \lambda_2\alpha_{n\mathrm{I}}\alpha_{n\mathrm{II}}\left[\frac{1}{(\omega_{n\mathrm{I}}^2 - \Omega^2)} - \frac{1}{(\omega_{n\mathrm{II}}^2 - \Omega^2)}\right], \tag{71}$$

$$B_{n\mathrm{I}} = -\lambda_2\Omega\alpha_{n\mathrm{II}}\frac{1}{\omega_{n\mathrm{I}}}\cdot\frac{1}{(\omega_{n\mathrm{I}}^2 - \Omega^2)}, \tag{72}$$

$$B_{n\mathrm{II}} = \lambda_2\Omega\alpha_{n\mathrm{I}}\frac{1}{\omega_{n\mathrm{II}}}\cdot\frac{1}{(\omega_{n\mathrm{II}}^2 - \Omega^2)}, \tag{73}$$

$$M = \frac{1}{1+\eta^2 k_n^2} \quad \text{and} \quad \lambda_2 = \frac{2rM(1+n^2\pi^2\eta^2)}{(\alpha_{n\mathrm{II}} - \alpha_{n\mathrm{I}})}\sin\left(\tfrac{1}{2}n\pi\right) = \frac{2r}{(\alpha_{n\mathrm{II}} - \alpha_{n\mathrm{I}})}\sin\left(\tfrac{1}{2}n\pi\right), \tag{74}$$

It can be noticed that equations (68) and (69) consist of two parts described in Section 3.2.1. Assuming that only the steady-state response has practical significance, and ignoring the free response, the forced vibrations of the SWCNT system can be obtained by relations (63) and (64).

3.2.3. *Moving constant force F.* The moving loads with constant force $F(\tau) = F$ and

$$\overline{f}_1(\xi,\tau) = F\delta(\xi - v\tau) \tag{75}$$

act upon the SWCNT system (see Figure 4), where F is the magnitude of a constant force and $\delta(\xi)$ is the Dirac delta function. By substituting (75) into (51) and (52), we obtain

$$R_{n\mathrm{I}} = 2MF\frac{\alpha_{n\mathrm{II}}}{\alpha_{n\mathrm{II}} - \alpha_{n\mathrm{I}}}\sin(n\pi v\tau)[1+\eta^2 k_n^2], \quad n = 1, 3, 5, \ldots, \tag{76}$$

$$R_{n\mathrm{II}} = 2MF\frac{\alpha_{n\mathrm{I}}}{\alpha_{n\mathrm{I}} - \alpha_{n\mathrm{II}}}\sin(n\pi v\tau)[1+\eta^2 k_n^2], \quad n = 1, 3, 5, \ldots. \tag{77}$$

The introduction of (76) and (77) into (49) and (50) gives

$$\overline{w}_1(\xi,\tau)=\sum_{n=1}^{\infty}\sin(n\pi\xi)\left[A_{n\mathrm{I}}\sin(\Omega_n\tau)+\sum_{i=\mathrm{I}}^{\mathrm{II}}B_{ni}\sin(\omega_{ni}\tau)\right], \tag{78}$$

$$\overline{w}_2(\xi,\tau)=\sum_{n=1}^{\infty}\sin(n\pi\xi)\left[A_{n\mathrm{II}}\sin(\Omega_n\tau)+\sum_{i=\mathrm{I}}^{\mathrm{II}}\alpha_{ni}B_{ni}\sin(\omega_{ni}\tau)\right], \tag{79}$$

where

$$A_{n\mathrm{I}}=\lambda_3\left[\frac{\alpha_{n\mathrm{II}}}{\omega_{n\mathrm{I}}^2-\Omega_n^2}-\frac{\alpha_{n\mathrm{I}}}{\omega_{n\mathrm{II}}^2-\Omega_n^2}\right], \tag{80}$$

$$A_{n\mathrm{II}}=\lambda_3\alpha_{n\mathrm{I}}\alpha_{n\mathrm{II}}\left[\frac{1}{\omega_{n\mathrm{I}}^2-\Omega_n^2}-\frac{1}{\omega_{n\mathrm{II}}^2-\Omega_n^2}\right], \tag{81}$$

$$B_{n\mathrm{I}}=-\lambda_3\Omega_n\alpha_{n\mathrm{II}}\frac{1}{\omega_{n\mathrm{I}}}\cdot\frac{1}{(\omega_{n\mathrm{I}}^2-\Omega_n^2)}, \tag{82}$$

$$B_{n\mathrm{II}}=\lambda_3\Omega_n\alpha_{n\mathrm{I}}\frac{1}{\omega_{n\mathrm{II}}}\cdot\frac{1}{(\omega_{n\mathrm{II}}^2-\Omega_n^2)}, \tag{83}$$

$$\lambda_3=\frac{2FM(1+\eta^2k_n^2)}{(\alpha_{n\mathrm{II}}-\alpha_{n\mathrm{I}})}=\frac{2F}{(\alpha_{n\mathrm{II}}-\alpha_{n\mathrm{I}})}, \tag{84}$$

$$\Omega_n=n\pi v=k_n v,\quad n=1,3,5,\ldots. \tag{85}$$

It can be noticed that equations (78) and (79) consist of two parts described in Section 3.2.1. Assuming that only the steady-state response has practical significance, and ignoring the free response, the forced vibrations of the SWCNT system can be obtained by

$$\overline{w}_1(\xi,\tau)=\sin(\Omega_n\tau)\sum_{n=1}^{\infty}A_{n\mathrm{I}}\sin(n\pi\xi), \tag{86}$$

$$\overline{w}_2(\xi,\tau)=\sin(\Omega_n\tau)\sum_{n=1}^{\infty}A_{n\mathrm{II}}\sin(n\pi\xi), \tag{87}$$

where $A_{n\mathrm{I}}$ and $A_{n\mathrm{II}}$ denote the steady-state vibration amplitudes of the two nanobeams, respectively.

3.2.4. *Moving concentrated harmonic force.* The moving loads with harmonic concentrated force $F(\tau)=F\sin(\Omega\tau)$ and

$$\overline{f}_1(\xi,\tau)=F\sin(\Omega\tau)\delta(\xi-v\tau) \tag{88}$$

acts upon the SWCNT system (see Figure 4), where F is the amplitude and Ω is the frequency of the harmonic force. By substituting (88) into (51) and (52), we obtain

$$R_{n\mathrm{I}}=2MF\frac{\alpha_{n\mathrm{II}}}{\alpha_{n\mathrm{II}}-\alpha_{n\mathrm{I}}}\sin(\Omega\tau)\sin(n\pi v\tau)[1+\eta^2k_n^2], \tag{89}$$

$$R_{n\mathrm{II}}=2MF\frac{\alpha_{n\mathrm{I}}}{\alpha_{n\mathrm{I}}-\alpha_{n\mathrm{II}}}\sin(\Omega\tau)\sin(n\pi v\tau)[1+\eta^2k_n^2]. \tag{90}$$

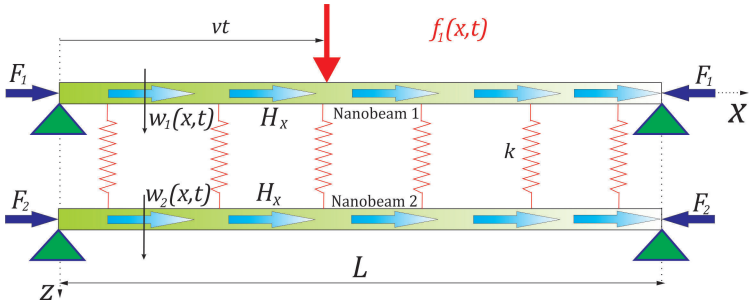

Figure 4. The double nanobeam system coupled by the Winkler elastic medium subjected to the moving concentrated force.

The introduction of (89) and (90) into (49) and (50) gives

$$\overline{w}_1(\xi,\tau)=\sum_{n=1}^{\infty}\sin(n\pi\xi)\left[A_{n\mathrm{I}}\sin(\Omega_n\tau)\sin(\Omega\tau)+B_{n\mathrm{I}}\cos(\Omega_n\tau)\cos(\Omega\tau)+\sum_{i=\mathrm{I}}^{\mathrm{II}}C_{ni}\cos(\omega_{ni}\tau)\right], \tag{91}$$

$$\overline{w}_2(\xi,\tau)=\sum_{n=1}^{\infty}\sin(n\pi\xi)\left[A_{n\mathrm{II}}\sin(\Omega_n\tau)\sin(\Omega\tau)+B_{n\mathrm{II}}\cos(\Omega_n\tau)\cos(\Omega\tau)+\sum_{i=\mathrm{I}}^{\mathrm{II}}\alpha_{ni}C_{ni}\cos(\omega_{ni}\tau)\right], \tag{92}$$

where

$$A_{n\mathrm{I}}=\lambda_4\left[\frac{\alpha_{n\mathrm{II}}u_{n\mathrm{I}}}{n_{n\mathrm{I}}m_{n\mathrm{I}}}-\frac{\alpha_{n\mathrm{I}}u_{n\mathrm{II}}}{n_{n\mathrm{II}}m_{n\mathrm{II}}}\right], \tag{93}$$

$$A_{n\mathrm{II}}=\lambda_4\alpha_{n\mathrm{I}}\alpha_{n\mathrm{II}}\left[\frac{u_{n\mathrm{I}}}{n_{n\mathrm{I}}m_{n\mathrm{I}}}-\frac{u_{n\mathrm{II}}}{n_{n\mathrm{II}}m_{n\mathrm{II}}}\right], \tag{94}$$

$$B_{n\mathrm{I}}=2\lambda_4\Omega_n\Omega\left[\frac{\alpha_{n\mathrm{I}}}{n_{n\mathrm{II}}m_{n\mathrm{II}}}-\frac{\alpha_{n\mathrm{II}}}{n_{n\mathrm{I}}m_{n\mathrm{I}}}\right], \tag{95}$$

$$B_{n\mathrm{II}}=2\lambda_4\Omega_n\Omega\alpha_{n\mathrm{I}}\alpha_{n\mathrm{II}}\left[\frac{1}{n_{n\mathrm{II}}m_{n\mathrm{II}}}-\frac{1}{n_{n\mathrm{I}}m_{n\mathrm{I}}}\right], \tag{96}$$

$$C_{n\mathrm{I}}=\frac{2\lambda_4\Omega_n\Omega\alpha_{n\mathrm{II}}}{n_{n\mathrm{I}}m_{n\mathrm{I}}}, \tag{97}$$

$$C_{n\mathrm{II}}=-\frac{2\lambda_4\Omega_n\Omega\alpha_{n\mathrm{I}}}{n_{n\mathrm{II}}m_{n\mathrm{II}}}, \tag{98}$$

$$\lambda_4=\frac{2FM(1+\eta^2k_n^2)}{(\alpha_{n\mathrm{II}}-\alpha_{n\mathrm{I}})}=\frac{2F}{(\alpha_{n\mathrm{II}}-\alpha_{n\mathrm{I}})}, \tag{99}$$

$$\Omega_n=n\pi v=k_n v, \tag{100}$$

$$m_{ni}=\omega_{ni}^2-(\Omega_n-\Omega)^2, \tag{101}$$

$$n_{ni}=\omega_{ni}^2-(\Omega_n+\Omega)^2, \tag{102}$$

$$u_{ni}=\omega_{ni}^2-\Omega_n^2-\Omega^2,\quad i=\mathrm{I},\mathrm{II}. \tag{103}$$

It can be noticed that equations (91) and (92) consist of three parts. Assuming that only the steady-state response has practical significance, and ignoring the free response, the forced vibrations of the SWCNT system can be obtained by

$$\overline{w}_1(\xi,\tau)=\sum_{n=1}^{\infty}\sin(n\pi\xi)[A_{n\mathrm{I}}\sin(\Omega_n\tau)\sin(\phi\tau)+B_{n\mathrm{I}}\cos(\Omega_n\tau)\cos(\Omega\tau)], \tag{104}$$

$$\overline{w}_2(\xi,\tau)=\sum_{n=1}^{\infty}\sin(n\pi\xi)[A_{n\mathrm{II}}\sin(\Omega_n\tau)\sin(\phi\tau)+B_{n\mathrm{II}}\cos(\Omega_n\tau)\cos(\Omega\tau)], \tag{105}$$

where $A_{n\mathrm{I}}$ and $A_{n\mathrm{II}}$ and $B_{n\mathrm{I}}$ and $B_{n\mathrm{II}}$ denote the steady-state vibration amplitudes of the two nanobeams, respectively. In this paper we will analyze only $A_{n\mathrm{I}}$ and $A_{n\mathrm{II}}$ steady-state vibration amplitudes.

4. Comparative study and numerical results

The presented methodology for the analyzed forced response of the double nanobeam system coupled by the elastic medium based on the nonlocal elasticity theory can be applied for the forced transversal vibration analysis of coupled carbon nanotubes, ZnO nanotubes, boron-nitride nanobeams and other magnetically affected nanomaterials [Barone and Peralta 2008; Kumar and Mohammad 2011]. Also, the Winkler elastic layer may represent some interatomic forces between two nanotubes, such as van der Waals interaction [Ru 2001]. We present a comparative study of the analytical results obtained in this paper and the results found in the literature.

This section is divided into three parts. In the first part, the fundamental frequency of the first nanobeam is compared with [Şimşek 2010b] and implemented via the MD simulation of vibrational response of the SWCNT according to Ansari and Sahmani [2012] and Ansari et al. [2012]. In the second part, the obtained numerical results for the ratio of the steady-state vibration amplitude of the double nanobeam system influenced by the axial magnetic field are compared with the results obtained by the scale-free structural theory proposed by Zhang et al. [2008], who analyzed the forced response of an axially compressed double beam system using the classical elasticity theory where the influence of the magnetic field was neglected. The third part discusses the influence of small scale and the axial magnetic field on the forced response of the double nanobeam system.

4.1. ***Fundamental frequency results.*** In this section, the natural frequency of the first nanobeam is compared with [Şimşek 2010b]. For DSWCNT it is well known that the lowest natural frequency and buckling load of such a system represents the fundamental frequency and critical buckling load and it is independent of the influence of the number of nanobeams in the system and chain coupling conditions; see [Karličić et al. 2014b; 2014a]. Fundamental frequency and critical buckling load are equivalent to the natural frequency and buckling load of a single nanobeam. The following parameters are used in computing the numerical results: $E=1\,\mathrm{TPa}$, $\rho=2300\,\mathrm{kg/m^3}$, $d=1\,\mathrm{nm}$, $t_b=0.35\,\mathrm{nm}$ [Şimşek 2010b]. The length of the nanotube is taken as variable for the various values of the aspect ratio L/d. The parameter e_0 was estimated as $e_0=(\pi^2-4)^{1/2}/2\pi\cong 0.39$ by Eringen [1983]. Therefore, in this study, the nonlocal parameter μ is taken as 0, 1, 2, 3, 4.

Excellent agreement between the present frequencies and those of [Şimşek 2010b] can be observed from Table 1. It is shown that inclusion of the nonlocal parameter μ decreases the frequencies of the

L/d	μ	$\bar{\omega}^0_{n\mathrm{I}}$			
		Şimşek [2010b]	Present study (MP = 0)	Present study (MP = 10)	Present study (MP = 20)
10	0	9.8696	9.8696	11.3501	12.6586
	1	9.4158	9.4158	10.9578	12.3081
	2	9.0194	9.0194	10.6191	12.0076
	3	8.6692	8.6692	10.3233	11.7468
	4	8.3569	8.3569	10.0625	11.5182
20	0	9.8696	9.8696	11.3501	12.6586
	1	9.7501	9.7501	11.2463	12.5656
	2	9.6347	9.6347	11.1464	12.4763
	3	9.5234	9.5234	11.0504	12.3906
	4	9.4158	9.4158	10.9578	12.3081
50	0	9.8696	9.8696	11.3501	12.6586
	1	9.8501	9.8501	11.3332	12.6435
	2	9.8308	9.8308	11.3164	12.6285
	3	9.8116	9.8116	11.2998	12.6135
	4	9.7925	9.7925	11.2832	12.5987

Table 1. Comparison of the nondimensional frequencies from Equation (111) for the simply supported nanobeam.

nanobeam 1. It is seen that the effect of the magnetic field (MP = 10, 20) is to increase frequencies of SWCNT. When the value of L/d is increased, the effect of the nonlocal parameter μ on the frequencies decreases.

Without loss of generality, we assume

$$\overline{F}_2 = \chi \overline{F}_1, \quad 0 \le \chi \le 1. \tag{106}$$

Based on (106), we obtain the same form of natural frequencies for (28) and (29) with different coefficients b_1 and c_1:

$$\bar{\omega}^2_{ni} = \tfrac{1}{2}\left[b \mp \sqrt{b^2 - 4c}\right], \quad i = \mathrm{I}, \mathrm{II}, \tag{107}$$

where

$$b_1 = 2K - (\chi + 1)\overline{F}_1 k_n^2 + 2MPk_n^2 + 2\frac{k_n^4}{1+\eta^2 k_n^2}, \tag{108}$$

$$c_1 = \left[K - (\overline{F}_1 - \mathrm{MP})k_n^2 + \frac{k_n^4}{1+\eta^2 k_n^2}\right]\left[K - (\chi\overline{F}_1 - \mathrm{MP})k_n^2 + \frac{k_n^4}{1+\eta^2 k_n^2}\right] - K^2. \tag{109}$$

By substituting the new expressions (107) for natural frequencies into (33) and (34), we obtain the new expressions for the amplitude as

$$\overline{\alpha}_{ni} = \frac{K - (\overline{F}_1 - \mathrm{MP})k_n^2 + \frac{k_n^4}{1+\eta^2 k_n^2} - \bar{\omega}^2_{ni}}{K}, \quad i = \mathrm{I}, \mathrm{II}. \tag{110}$$

When the axial compression is absent, we obtain

$$(\bar{\omega}_{n\mathrm{I}}^{0})^{2} = \frac{k_n^4}{1+\eta^2 k_n^2} + k_n^2 MP, \tag{111}$$

$$(\bar{\omega}_{n\mathrm{II}}^{0})^{2} = 2K + \frac{k_n^4}{1+\eta^2 k_n^2} + k_n^2 MP, \tag{112}$$

$$\bar{\alpha}_{n\mathrm{I}}^{0} = 1, \quad \bar{\alpha}_{n\mathrm{II}}^{0} = -1. \tag{113}$$

To determine the effect of the axial compressive load and magnetic field on the steady-state vibration amplitudes $A_{n\mathrm{I}}$ and $A_{n\mathrm{II}}$ of the system and also for the comparative study, we define the ratio of the steady-state vibration amplitudes as

$$\psi_1 = \frac{A_{n\mathrm{I}}}{A_{n\mathrm{I}}^{0}}, \quad \psi_2 = \frac{A_{n\mathrm{II}}}{A_{n\mathrm{II}}^{0}}, \tag{114}$$

where $A_{n\mathrm{I}}^{0}$ and $A_{n\mathrm{II}}^{0}$ are the steady-state vibration amplitudes of the two beams without axial compression. We then introduce the ratio of the axial compressive force and critical buckling load as

$$p = \frac{\bar{F}}{P_{\mathrm{cr}}}, \tag{115}$$

with

$$P_{\mathrm{cr}} = \frac{\pi^2}{1+\eta^2\pi^2}, \tag{116}$$

where P_{cr} is the nonlocal critical buckling load, which is the smallest load at which a single nanobeam ceases to be in stable equilibrium under axial compression. From (27) it follows that

$$\bar{F} = \frac{k_n^2}{1+\eta^2 k_n^2}. \tag{117}$$

By substituting the dimensionless $\bar{F}$ from (16) we can write

$$P_{\mathrm{cr}} = \frac{1}{1+\eta^2\pi^2} EI \frac{\pi^2}{L^2}. \tag{118}$$

For $\eta = 0$, namely for an ordinary beam,

$$P_{\mathrm{cr}} = EI \frac{\pi^2}{L^2}, \tag{119}$$

where P_{cr} is known as the Euler load, which is the smallest load at which a single beam ceases to be in stable equilibrium under axial compression [Zhang et al. 2008].

4.1.1. *Molecular dynamics simulation results.* In order to justify the accuracy of this paper, it is necessary to implement the MD simulation of vibrational response of the SWCNT. Molecular dynamics (MD) simulation is an atomistic method for analysis of different nanostructures. Through the fast development of various fields of nanotechnology, MD simulation has been considered as a powerful and accurate implement to study of systems at nanoscale, according to Ansari et al. [2012]. Without introducing the

L/d	MD simulation [Ansari et al. 2012]	Present study ($\eta H_x^2 = 0$)	Present study ($\eta H_x^2 > 0$)
8.3	0.5299	0.5485	0.8284
10.1	0.3618	0.3707	0.6306
13.7	0.1931	0.2016	0.4267
17.3	0.1103	0.1264	0.3236
20.9	0.0724	0.0860	0.2613
24.5	0.0519	0.0630	0.2195
28.1	0.0425	0.0479	0.1895
31.6	0.0358	0.0379	0.1674
35.3	0.0287	0.0303	0.1491
39.1	0.0259	0.0247	0.1341

Table 2. Fundamental frequencies (THz) for (8, 8) armchair SWCNT obtained from MD simulations of Euler–Bernoulli beam models, $R/l = 3$, $l = \mu^{1/2}$, $H_x = 1 \cdot 10^8$ A/m, $\eta = 4\pi \cdot 10^{-7}$.

dimensionless expression (16), the fundamental frequency of the first nanobeam is presented in the form

$$\omega_{n1} = \sqrt{\frac{\eta H_x^2}{\rho}(n\pi/L)^2 + \frac{EI(n\pi/L)^4}{\rho A(1+\mu(n\pi/L)^2)}}. \tag{120}$$

Authors have found MD simulation results for vibration and buckling of a single-layer graphene sheet presented by Ansari and Sahmani [2012] and Ansari et al. [2012]. Thus, our results for the lowest natural frequency of DSWCNT can be used to validate them with the results obtained for the free vibration of a SWCNT via molecular dynamics simulation in [Ansari and Sahmani 2012] and [Ansari et al. 2012].

In the current study, the effective thickness of the SWCNTs is assumed to be equal to the spacing of graphite, $h = 0.34$ nm, radius of the nanotubes is $R = d/2$, where d is diameter of the SWCNT [Ansari et al. 2012]. The Poisson's ratio $\nu = 0.3$, Young's modulus $E = 1.1$ TPa and mass density $\rho = 2300\,\text{kg}/m^3$ are considered in the analysis. To validate the present approach, MD simulations are conducted for a simply supported (8, 8) armchair SWCNT with different aspect ratios ranging from 8.3 to 39.1. Table 2 present the values of fundamental frequency obtained from MD simulations and also the Euler–Bernoulli beam models based on the nonlocal elastic theory. The results predicted by the present models are found to be in excellent agreement with the ones obtained from MD simulation, which indicates the capability of the present approach to accurately predict frequencies of SWCNT. From Table 2, the frequency of SWCNT is decreasing with increasing length-to-diameter ratio.

It can be noticed that the results obtained by using the Bernoulli–Fourier method, when is $\eta H_x^2 = 0$, are in agreement with the results presented by Ansari and Sahmani [2012] and Ansari et al. [2012]. Between these values there is a very little variation because we neglected moment of inertia. Taking into account the value of magnetic field permeability η and axial magnetic field H_x from [Murmu et al. 2012b], as expected, the values of frequency of SWCNT are greater than the values from [Ansari and Sahmani 2012] and [Ansari et al. 2012].

4.2. ***Steady-state amplitudes results of the DSWCNT system.*** In the second part, to validate the results obtained for the steady-state vibration amplitude we adopt the values for material characteristics from [Zhang et al. 2008], where $E = 10^{10}$ [Pa] is the elastic modulus, $I = 4 * 10^{-4}$ [m^4] is the moment of inertia, $L = 10$ [m] is the length of beam, and $K = 2 * 10^5$ [N/m^2] is the stiffness coefficient of the elastic medium. The results obtained by the classical and nonlocal theories are comparable in the case when the results are given in the dimensionless form. Since the steady-state vibration amplitude is expressed in dimensionless form here, it is possible to compare these results with the results obtained in [Zhang et al. 2008]. It should be noted that the validation of the obtained results was conducted for cases of uniform and concentrated harmonic load, and excellent agreement is shown with the results proposed by Zhang et al. [2008].

In order to compare the obtained results for the ratio of the steady-state amplitudes for the case of the uniformly distributed harmonic load, we determine the steady-state vibration amplitudes ($A_{n\mathrm{I}}$ and $A_{n\mathrm{II}}$) and ($A^0_{n\mathrm{I}}$ and $A^0_{n\mathrm{II}}$) by substituting equations (107)–(110) and (111)–(113) into equations (58) and (59), respectively. For the vibration mode number $n = 3$ and the exciting frequency $\Omega = 0.6\omega_{n\mathrm{II}}$, the variation of the steady-state amplitude ratios ψ_1 and ψ_2 with a change in the axial force ratio for different values of axial magnetic fields is shown in Figure 5. It can be observed that the steady-state amplitude ratios ψ_1 and ψ_2 increase with an increase in the axial compressive load, which leads to an increase in the steady-state amplitudes $A_{n\mathrm{I}}$ and $A_{n\mathrm{II}}$ of DNBS. Moreover, it can be noticed that the axial compression ratio χ has negligible effects on the first steady-state amplitude ratio ψ_1, but a significant influence on the second steady-state amplitude ratio ψ_2. Also, decreasing the axial compression ratio χ causes an obvious reduction of the second steady-state amplitude $A_{n\mathrm{II}}$. It is clear from Figure 5 that larger values of the amplitude of the axial magnetic field lead to a reduction in the ratios ψ_1 and ψ_2, which implies that the amplitudes of the steady-state vibrations $A_{n\mathrm{I}}$ and $A_{n\mathrm{II}}$ also decrease. However, from the physical point of view, the axial magnetic field leads to an increase in the overall stiffness and thereby to an increase in the natural frequencies of the system. This effect allows us the practical application of such a system, because it is possible to change the natural frequencies $\omega_{n\mathrm{I}}$ and $\omega_{n\mathrm{II}}$ and the steady-state amplitudes $A_{n\mathrm{I}}$ and $A_{n\mathrm{II}}$ without changing any other material and geometric parameters of the DNBS. It should be noted that when the intensity of the axial magnetic field and nonlocal parameter are equal to zero, the nonlocal double nanobeam system is reduced to the classical double beam system analyzed in [Zhang et al. 2008]. The results for ratios ψ_1 and ψ_2 obtained in the case when $\mathrm{MP} = 0$ and $\eta = 0$ are also shown in Figure 5. The comparative study for the case of the concentrated harmonic force is also carried out in a similar manner. The analysis of the obtained results for the ratios ψ_1 and ψ_2 shows that we get exactly the same results as in the case of the continuous uniformly distributed load. The results obtained in this study are in line with the results obtained in [Zhang et al. 2008].

In the following part of the comparative study we provide an analysis of the steady-state amplitude ratios ψ_1 and ψ_2 for the cases of the uniformly distributed load (Figures 5 and 6), and the moving concentrated harmonic force (Figures 7 and 8). The dimensionless parameters of the coupled DNBS which are used in numerical simulations in Figures 6, 7 and 8 are: $K = 50$, $\chi = 0.5$, $\xi = 0.5$, $\upsilon = 0.3$ and $n = 1$. As already mentioned, the results obtained for the steady-state amplitude ratio in the case of the harmonic concentrated load are identical with the results obtained for the first case of excitation, while the case of the moving constant force represents only a special case of the moving harmonic concentrated force.

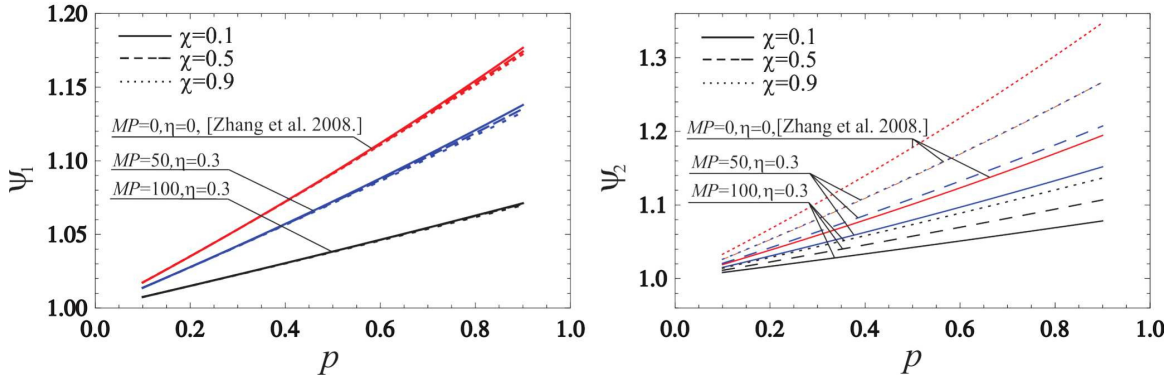

Figure 5. The relationship between the dimensionless parameter $p = \overline{F}/P_{\text{cr}}$ and (left) the ratio $\psi_1 = A_{n\text{I}}/A^0_{n\text{I}}$ and (right) the ratio $\psi_2 = A_{n\text{II}}/A^0_{n\text{II}}$, for different axial compression ratios χ and magnetic fields MP in the case of a uniformly distributed load.

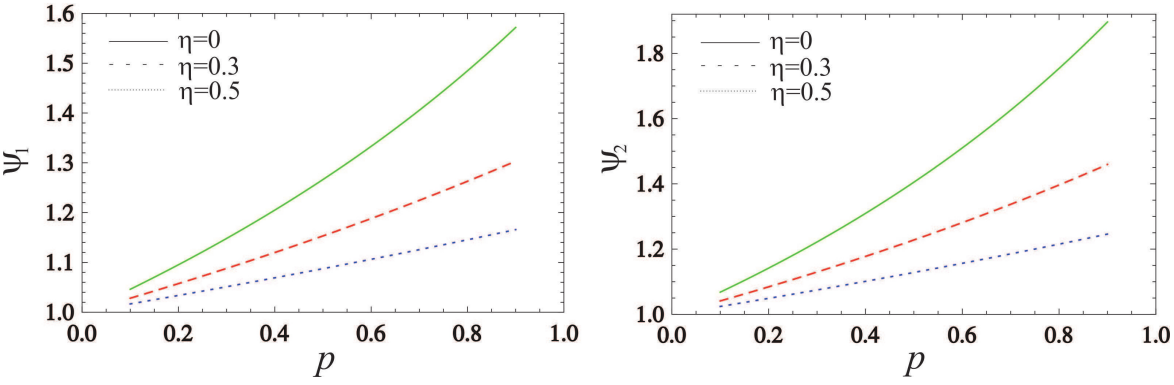

Figure 6. The relationship between the dimensionless parameter $p = \overline{F}/P_{\text{cr}}$ and (left) the ratio $\psi_1 = A_{n\text{I}}/A^0_{n\text{I}}$ and (right) the ratio $\psi_2 = A_{n\text{II}}/A^0_{n\text{II}}$ for different nonlocal parameters η in the case of a uniformly distributed load.

Figure 6 shows the relationship between the ratios ψ_1 and ψ_2 in the case of the uniformly distributed load, and the dimensionless parameter $p = \overline{F}/P_{\text{cr}}$ in the range 0–1 for different nonlocal parameters η. From these figures, the ratios ψ_1 and ψ_2 decrease with an increase in the nonlocal parameter η, which implies that the magnitudes of the steady-state vibration amplitudes $A_{n\text{I}}$ and $A_{n\text{II}}$ get smaller when the nonlocal parameter η becomes larger. Also, it is interesting to note that from the physical point of view the nonlocal parameter has dampening effects on the steady-state vibration amplitudes. In addition, an increase in the ratio p leads to an increase in both steady-state amplitude ratios ψ_1 and ψ_2 in a similar manner. So from the physical point of view, it can be concluded that the overall stiffness of the system decreases with the increase in the ratio p.

Figures 7 and 8 show the influence of the longitudinal magnetic field MP and the nonlocal parameter η on the relationship between the ratios ψ_1 and ψ_2, and ratio $p = \overline{F}/P_{\text{cr}}$ in the range 0–1 in the case of the moving harmonic concentrated force, respectively. From these figures we can see that the steady-state vibration amplitude ratios ψ_1 and ψ_2 decrease with the increase in the parameter of the magnetic field

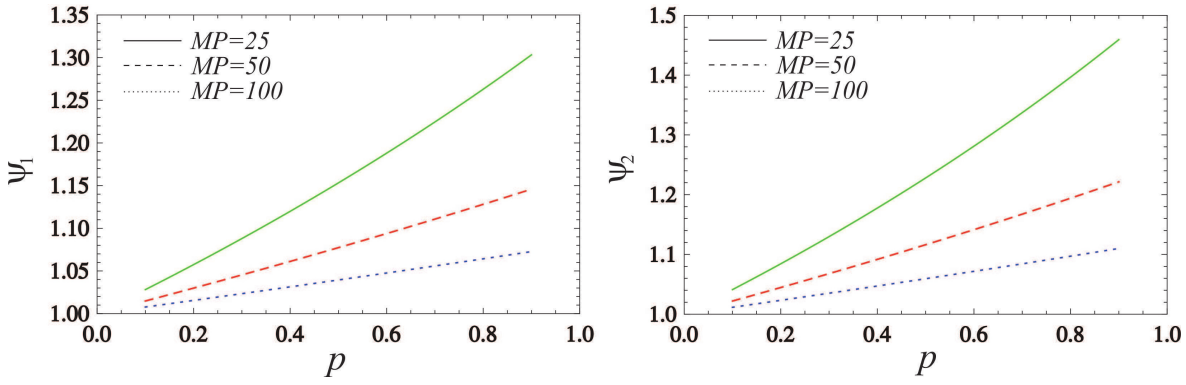

Figure 7. The relationship between the dimensionless parameter $p = \overline{F}/P_{\text{cr}}$ and (left) the ratio $\psi_1 = A_{n\text{I}}/A^0_{n\text{I}}$ and (right) the ratio $\psi_2 = A_{n\text{II}}/A^0_{n\text{II}}$ for different axial magnetic fields MP in the case of a moving concentrated harmonic force.

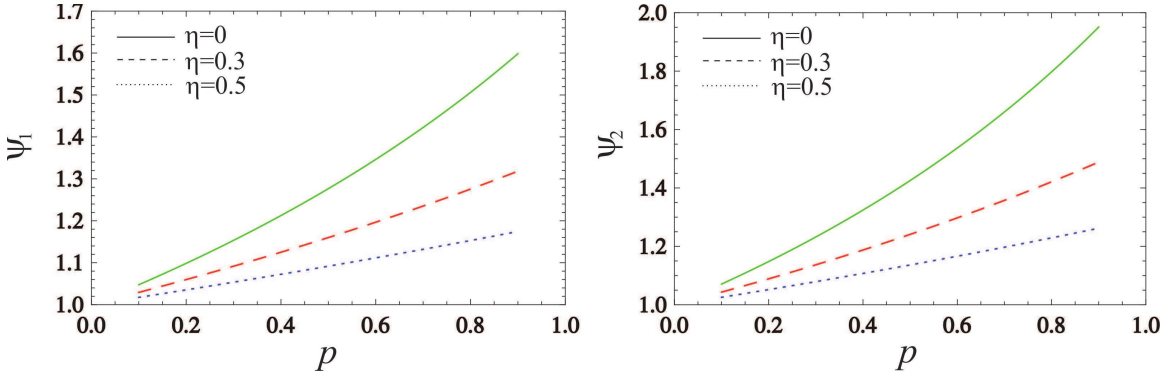

Figure 8. The relationship between the dimensionless parameter $p = \overline{F}/P_{\text{cr}}$ and (left) the ratio $\psi_1 = A_{n\text{I}}/A^0_{n\text{I}}$ and (right) the ratio $\psi_2 = A_{n\text{II}}/A^0_{n\text{II}}$ for different nonlocal parameters η in the case of a moving concentrated harmonic force.

and nonlocality η. This implies that the magnitudes of the steady-state vibration amplitudes $A_{n\text{I}}$ and $A_{n\text{II}}$ act in a similar manner to the case of the uniform harmonic excitation. It is interesting to note that values for the steady-state amplitude ratio are higher for the moving harmonic load than for the uniform harmonic loads. However, from the physical point of view, it can be noted that the speed of the moving load significantly affects the value of the steady-state vibration amplitudes $A_{n\text{I}}$ and $A_{n\text{II}}$ of the coupled nanobeams. The present results for the ratio of amplitudes are consistent with the results found in the literature [Zhang et al. 2008].

In order to compare the results of the presented study with those in the existing study by Zhang et al. [2008], the values of the steady-state vibration amplitude ratios ψ_1 and ψ_2 for the uniformly distributed harmonic load and the concentrated harmonic force are represented in Table 3. It is found that the ratios ψ_1 and ψ_2 in this case are totally the same. From the presented data we can conclude that the influence of the longitudinal magnetic field MP and the nonlocal parameter η on the relationship between ratio ψ_1 and ψ_2 causes a decrease in their values, as shown in the above figures.

[Zhang et al. 2008]			
MP	η	$\psi_1 = A_{n\mathrm{I}}/A^0_{n\mathrm{I}}$	$\psi_2 = A_{n\mathrm{II}}/A^0_{n\mathrm{II}}$
0	0	1.1965	1.3019
50	0.3	1.1499	1.2277
50	0.5	1.0872	1.1309
100	0.3	1.0779	1.1175
100	0.5	1.0436	1.0658

Table 3. Analytical validation of the steady-state vibration amplitude ratios ψ_1 and ψ_2. Here $\chi = 0.5$.

4.3. ***Forced vibration response.*** In this subsection, forced vibration responses at the nanobeams midpoints are analyzed for two cases of external excitation under the influence of the longitudinal magnetic field within the framework of the nonlocal elasticity theory. In the first case we consider that the uniform harmonic load acts on the first nanobeam in the DNBS (Figure 2) while in the second one we consider the moving harmonic concentrated force (Figure 4). Also, we assume that both nanobeams in the DNBS have the same geometric and material characteristics and are subjected to the axial compressive loads $\overline{F}_1$ and $\overline{F}_2$. By using the analytical solution for transversal displacements obtained for these two particular cases of external excitation, we plot $\overline{w}_1(\xi, \tau)$ and $\overline{w}_2(\xi, \tau)$ as functions of time for different nonlocal and magnetic field parameters, as shown in Figures 9–12.

To analyze forced vibrations, we use smaller values for the dimensionless stiffness modulus K and magnetic fields MP, because using larger values leads to obtaining very smaller values for the vibration amplitude of transversal displacements $\overline{w}_1(0.5, \tau)$ and $\overline{w}_2(0.5, \tau)$. The following dimensionless parameters of the coupled DNBS are used here in the numerical simulations: $K = 5$, $\chi = 0.5$, $\overline{F}_1 = 0.2$, $\xi = 0.5$, and $n = 1$, where the exciting frequency is $\Omega = 0.6\omega_{n\mathrm{II}}$. It can be observed that the axial magnetic field diminishes the amplitudes of transversal vibration $\overline{w}_1(\xi, \tau)$ and $\overline{w}_2(\xi, \tau)$ in both cases of external excitation. Moreover, this effect allows us to change the stiffness of the carbon nanotubes and therefore change the overall stiffness of the DNBS. However, changing the stiffness of the system leads to changes in the natural frequency of the system, so it is possible to avoid the resonance region for different cases of external excitation [Karličić et al. 2014c]. Furthermore, by carefully selecting the intensity of the magnetic field we can set the response vibration amplitude in a certain range without changing any other material and geometric characteristics of the DNBS. This fact has significance in practical applications for the control of vibration amplitude in the NEMS and nanocomposite structures based on the CNTs. Also, these figures show how the coupled DNBS responds to changes in the nonlocal parameter η for different cases of external excitation. It can be noticed that the nonlocal parameter has a dampening effect on both response vibration amplitudes of the DNBS, but in the case of the moving harmonic concentrated force we observe a larger effect on the vibration amplitude. This means that the effect of nonlocality causes a larger reduction of the vibration amplitude of transversal displacements $\overline{w}_1(0.5, \tau)$ and $\overline{w}_2(0.5, \tau)$ than in the first case of external excitation.

The presented work shows the possibility to control vibration amplitudes and natural frequencies in a certain range by changing only the external magnetic field parameter without changing any other physical parameter of the DNBS. Also, this ability provides us with a great practical application of such systems

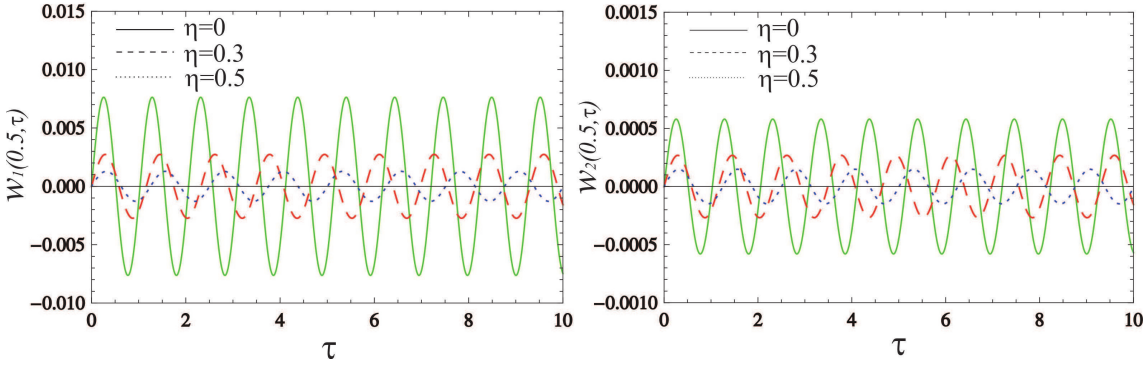

Figure 9. The relationship between forced vibrations $\overline{w}_1(0.5, \tau)$ (left) and $\overline{w}_2(0.5, \tau)$ (right) and dimensionless time for different nonlocal parameters η in the case of the uniformly distributed harmonic load.

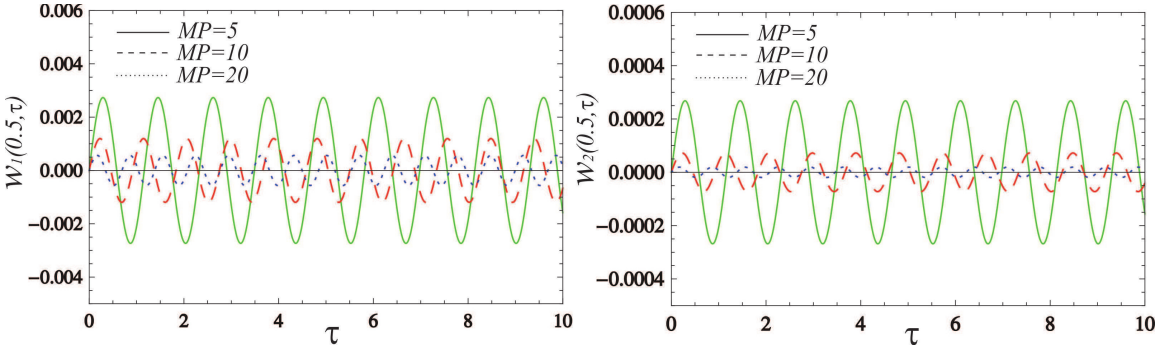

Figure 10. The relationship between forced vibrations $\overline{w}_1(0.5, \tau)$ (left) and $\overline{w}_2(0.5, \tau)$ (right) and dimensionless time for different axial magnetic fields MP in the case of the uniformly distributed harmonic load.

in dynamic absorbers, nanoresonators and nanoactuator devices. It should be noted that the longitudinal magnetic field can be considered analogous to a Pasternak-type foundation, where the Winkler medium represented by stiffness of the springs and magnetic field parameter represents shear coefficients of the Pasternak foundation, as shown in reference [Murmu et al. 2012a].

5. Conclusions

On the basis of the Euler–Bernoulli beam theory and Eringen nonlocal elasticity, this paper investigates a compressive nonlocal double single-walled carbon nanotube (SWCNT) system, under the influence of an axial magnetic field. The dynamic responses of the DSWCNT system for four different cases of external transversal load are considered. By using the nonlocal Euler–Bernoulli beam theory and classical Maxwell relation, the system of two nonhomogeneous partial differential equations of transversal motion is derived for the coupled DNBS. Closed form solutions for natural frequencies, amplitude ratio and forced vibration response under the influence of the magnetic field and the nonlocal parameter for four cases of external excitation are obtained by applying the method of separation of variables.

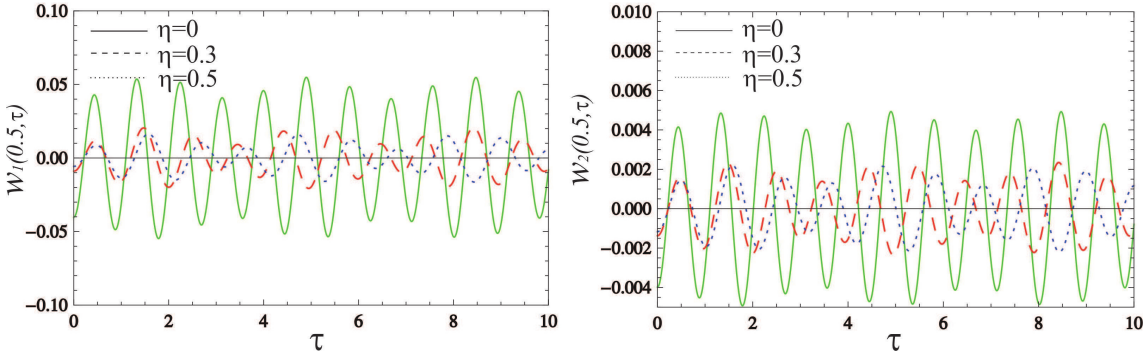

Figure 11. The relationship between forced vibrations $\overline{w}_1(0.5, \tau)$ (left) and $\overline{w}_2(0.5, \tau)$ (right) and dimensionless time for different nonlocal parameters η in the case of the moving concentrated harmonic force.

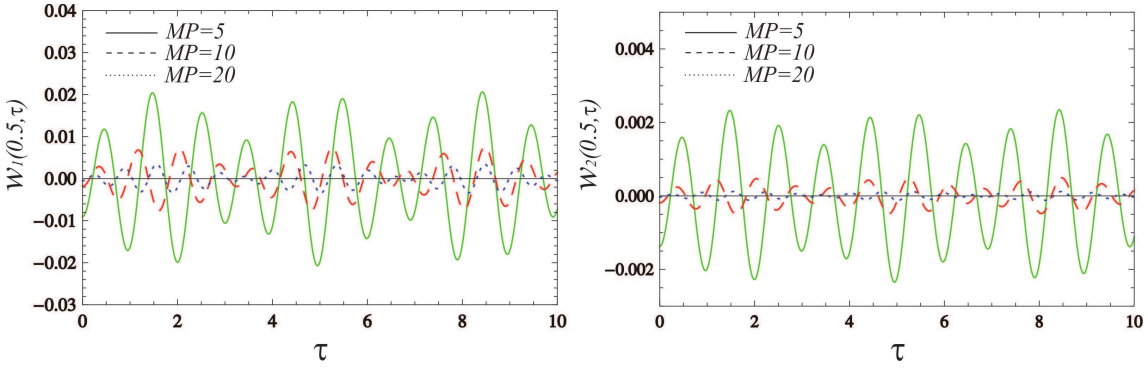

Figure 12. The relationship between forced vibrations $\overline{w}_1(0.5, \tau)$ (left) and $\overline{w}_2(0.5, \tau)$ (right) and dimensionless time for different axial magnetic fields MP in the case of the moving concentrated harmonic force.

Analytical expressions for the steady-state vibration amplitudes of the two nanobeams with the influence of the magnetic field and the nonlocal parameter are obtained, and numerical results based on them are presented. From the obtained results, we found that the nonlocal parameter and longitudinal magnetic field have a damping effect on the response vibration amplitude. In order to validate our results we compared the obtained results for the steady-state amplitude ratios with the results found in the literature and excellent agreement was achieved. It was found that the natural frequencies and response vibration amplitude of the system can change by varying the intensity of the axial magnetic field without the necessity to change any other material and geometric parameter of the DNBS. We analyzed amplitudes of transversal displacements for four cases of external excitation vibration and numerically presented the case of the uniformly distributed harmonic load and the case of the moving harmonic concentrated force with different nonlocal parameters and different axial magnetic fields. The obtained amplitudes of transversal vibration in both cases of external excitation are reduced due to the influence of the axial magnetic field. We noted that the effect of the magnetic field allows a change in the stiffness of carbon nanotubes and therefore a change in the overall stiffness of the DNBS. Changing the stiffness of the

system causes changes in the natural frequency of the system, thus avoiding the resonance region for different cases of external excitation. This possibility has great practical importance in the design of NEMS devices such as nanoactuators, nanoresonators, dynamic absorbers and nanocomposite structures based on the CNTs. Also, to validate the present analysis, MD simulations were conducted for an armchair SWCNT with different aspect ratios. The results predicted by the present model are found to be in agreement with the ones obtained from MD simulation, which indicates the capability of the present approach in accurately predicting frequencies of SWCNTs.

Acknowledgments

This research was supported by the research grant of the Serbian Ministry of Science and Environmental Protection under the number OI 174001 and OI 174011.

References

[Adhikari and Chowdhury 2010] S. Adhikari and R. Chowdhury, "The calibration of carbon nanotube based bionanosensors", *J. Appl. Phys.* **107**:12 (2010), Art. ID 124322.

[Ajayan et al. 2006] P. M. Ajayan, L. S. Schadler, and P. V. Braun (editors), *Nanocomposite science and technology*, Wiley, Weinheim, 2006.

[Aksencer and Aydogdu 2012] T. Aksencer and M. Aydogdu, "Forced transverse vibration of nanoplates using nonlocal elasticity", *Physica E* **44**:7–8 (2012), 1752–1759.

[Ansari and Sahmani 2012] R. Ansari and S. Sahmani, "Small scale effect on vibrational response of single-walled carbon nanotubes with different boundary conditions based on nonlocal beam models", *Commun. Nonlinear Sci. Numer. Simul.* **17**:4 (2012), 1965–1979.

[Ansari et al. 2012] R. Ansari, R. Gholami, and H. Rouhi, "Vibration analysis of single-walled carbon nanotubes using different gradient elasticity theories", *Compos. B Eng.* **43**:8 (2012), 2985–2989.

[Arani et al. 2013] A. H. G. Arani, M. J. Maboudi, A. G. Arani, and S. Amir, "2D-magnetic field and biaxiall in-plane pre-load effects on the vibration of double bonded orthotropic graphene sheets", *J. Solid Mech.* **5**:2 (2013), 193–205.

[Avouris et al. 2007] P. Avouris, Z. Chen, and V. Perebeinos, "Carbon-based electronics", *Nat. Nanotechnol.* **2**:10 (2007), 605–615.

[Barone and Peralta 2008] V. Barone and J. E. Peralta, "Magnetic boron nitride nanoribbons with tunable electronic properties", *Nano Lett.* **8**:8 (2008), 2210–2214.

[Bellucci et al. 2007] S. Bellucci, J. González, F. Guinea, P. Onorato, and E. Perfetto, "Magnetic field effects in carbon nanotubes", *J. Phys. Condens. Matter* **19**:39 (2007), 395017.

[Claeyssen et al. 2013] J. R. Claeyssen, T. Tsukazan, and R. D. Coppeti, "Nonlocal effects in modal analysis of forced responses with single carbon nanotubes", *Mech. Syst. Signal Process.* **38**:2 (2013), 299–311.

[Correa-Duarte et al. 2005] M. A. Correa-Duarte, M. Grzelczak, V. Salgueiriño-Maceira, M. Giersig, L. M. Liz-Marzán, M. Farle, K. Sierazdki, and R. Diaz, "Alignment of carbon nanotubes under low magnetic fields through attachment of magnetic nanoparticles", *J. Phys. Chem. B* **109**:41 (2005), 19060–19063.

[Şimşek 2010a] M. Şimşek, "Dynamic analysis of an embedded microbeam carrying a moving microparticle based on the modified couple stress theory", *Int. J. Eng. Sci.* **48**:12 (2010), 1721–1732.

[Şimşek 2010b] M. Şimşek, "Vibration analysis of a single-walled carbon nanotube under action of a moving harmonic load based on nonlocal elasticity theory", *Physica E* **43**:1 (2010), 182–191.

[Şimşek 2011] M. Şimşek, "Nonlocal effects in the forced vibration of an elastically connected double-carbon nanotube system under a moving nanoparticle", *Comput. Mater. Sci.* **50**:7 (2011), 2112–2123.

[Dresselhaus et al. 2005] M. S. Dresselhaus, G. Dresselhaus, R. Saito, and A. Jorio, "Raman spectroscopy of carbon nanotubes", *Phys. Rep.* **409**:2 (2005), 47–99.

[Duan et al. 2007] W. H. Duan, C. M. Wang, and Y. Y. Zhang, "Calibration of nonlocal scaling effect parameter for free vibration of carbon nanotubes by molecular dynamics", *J. Appl. Phys.* **101**:2 (2007), Art. ID 024305.

[Dubay and Kresse 2003] O. Dubay and G. Kresse, "Accurate density functional calculations for the phonon dispersion relations of graphite layer and carbon nanotubes", *Phys. Rev. B* **67**:3 (2003), 035401.

[Eringen 1972] A. C. Eringen, "Linear theory of nonlocal elasticity and dispersion of plane waves", *Int. J. Eng. Sci.* **10**:5 (1972), 425–435.

[Eringen 1983] A. C. Eringen, "On differential equations of nonlocal elasticity and solutions of screw dislocation and surface waves", *J. Appl. Phys.* **54**:9 (1983), 4703–4710.

[Eringen 2002] A. C. Eringen, *Nonlocal continuum field theories*, Springer, New York, 2002.

[Eringen and Edelen 1972] A. C. Eringen and D. G. B. Edelen, "On nonlocal elasticity", *Int. J. Eng. Sci.* **10**:3 (1972), 233–248.

[Ghorbanpour Arani and Shokravi 2014] A. Ghorbanpour Arani and M. Shokravi, "Vibration response of visco-elastically coupled double-layered visco-elastic graphene sheet systems subjected to magnetic field via strain gradient theory considering surface stress effects", *Proc. Inst. Mech. Eng. N J. Nanoeng. Nanosyst.* (online publication April 2014).

[Goerbig et al. 2006] M. O. Goerbig, R. Moessner, and B. Douçot, "Electron interactions in graphene in a strong magnetic field", *Phys. Rev. B* **74**:16 (2006), 161407.

[Hata et al. 2004] K. Hata, D. N. Futaba, K. Mizuno, T. Namai, M. Yumura, and S. Iijima, "Water-assisted highly efficient synthesis of impurity-free single-walled carbon nanotubes", *Science* **306**:5700 (2004), 1362–1364.

[Hu et al. 1999] J. Hu, T. W. Odom, and C. M. Lieber, "Chemistry and physics in one dimension: Synthesis and properties of nanowires and nanotubes", *Acc. Chem. Res.* **32**:5 (1999), 435–445.

[Iijima 1991] S. Iijima, "Helical microtubules of graphitic carbon", *Nature* **354**:6348 (1991), 56–58.

[Iijima et al. 1996] S. Iijima, C. Brabec, A. Maiti, and J. Bernholc, "Structural flexibility of carbon nanotubes", *J. Chem. Phys.* **104**:5 (1996), 2089–2092.

[Kacem et al. 2011] N. Kacem, S. Baguet, S. Hentz, and R. Dufour, "Computational and quasi-analytical models for non-linear vibrations of resonant MEMS and NEMS sensors", *Int. J. Non-Linear Mech.* **46**:3 (2011), 532–542.

[Karličić et al. 2014a] D. Karličić, S. Adhikari, T. Murmu, and M. Cajić, "Exact closed-form solution for non-local vibration and biaxial buckling of bonded multi-nanoplate system", *Compos. B Eng.* **66** (2014), 328–339.

[Karličić et al. 2014b] D. Karličić, P. Kozić, and R. Pavlović, "Free transverse vibration of nonlocal viscoelastic orthotropic multi-nanoplate system (MNPS) embedded in a viscoelastic medium", *Compos. Struct.* **115** (2014), 89–99.

[Karličić et al. 2014c] D. Karličić, T. Murmu, M. Cajić, P. Kozić, and S. Adhikari, "Dynamics of multiple viscoelastic carbon nanotube based nanocomposites with axial magnetic field", *J. Appl. Phys.* **115**:23 (2014), Art. ID 234303.

[Ke et al. 2009] L. L. Ke, Y. Xiang, J. Yang, and S. Kitipornchai, "Nonlinear free vibration of embedded double-walled carbon nanotubes based on nonlocal Timoshenko beam theory", *Comput. Mater. Sci.* **47**:2 (2009), 409–417.

[Kiani 2012] K. Kiani, "Transverse wave propagation in elastically confined single-walled carbon nanotubes subjected to longitudinal magnetic fields using nonlocal elasticity models", *Physica E* **45** (2012), 86–96.

[Kiani and Mehri 2010] K. Kiani and B. Mehri, "Assessment of nanotube structures under a moving nanoparticle using nonlocal beam theories", *J. Sound Vib.* **329**:11 (2010), 2241–2264.

[Kozić et al. 2014] P. Kozić, R. Pavlović, and D. Karličić, "The flexural vibration and buckling of the elastically connected parallel-beams with a Kerr-type layer in between", *Mech. Res. Commun.* **56** (2014), 83–89.

[Kraus 1984] J. Kraus, *Electromagnetics*, McGraw-Hill, New York, 1984.

[Krstić et al. 2004] V. Krstić, G. Wagnière, and G. L. J. A. Rikken, "Magneto-dynamics of chiral carbon nanotubes", *Chem. Phys. Lett.* **390**:1–3 (2004), 25–28.

[Kumar and Mohammad 2011] C. S. S. R. Kumar and F. Mohammad, "Magnetic nanomaterials for hyperthermia-based therapy and controlled drug delivery", *Adv. Drug Deliv. Rev.* **63**:9 (2011), 789–808.

[Lazarus et al. 2012] A. Lazarus, O. Thomas, and J.-F. Deü, "Finite element reduced order models for nonlinear vibrations of piezoelectric layered beams with applications to NEMS", *Finite Elem. Anal. Des.* **49**:1 (2012), 35–51.

[Li and Chou 2004] C. Li and T.-W. Chou, "Mass detection using carbon nanotube-based nanomechanical resonators", *Appl. Phys. Lett.* **84**:25 (2004), 5246–5248.

[Li et al. 2008] C. Li, E. T. Thostenson, and T.-W. Chou, "Sensors and actuators based on carbon nanotubes and their composites: A review", *Compos. Sci. Technol.* **68**:6 (2008), 1227–1249.

[Liu et al. 2003] Y. Liu, R. O. Jones, X. Zhao, and Y. Ando, "Carbon species confined inside carbon nanotubes: A density functional study", *Phys. Rev. B* **68**:12 (2003), 125413.

[Lu 1997] J. P. Lu, "Elastic properties of carbon nanotubes and nanoropes", *Phys. Rev. Lett.* **79**:7 (1997), 1297–1300.

[Moniruzzaman and Winey 2006] M. Moniruzzaman and K. I. Winey, "Polymer nanocomposites containing carbon nanotubes", *Macromolecules* **39**:16 (2006), 5194–5205.

[Murmu and Adhikari 2011] T. Murmu and S. Adhikari, "Nonlocal vibration of carbon nanotubes with attached buckyballs at tip", *Mech. Res. Commun.* **38**:1 (2011), 62–67.

[Murmu and Adhikari 2012] T. Murmu and S. Adhikari, "Nonlocal frequency analysis of nanoscale biosensors", *Sens. Actuators A Phys.* **173**:1 (2012), 41–48.

[Murmu et al. 2012a] T. Murmu, M. A. McCarthy, and S. Adhikari, "Nonlocal elasticity based magnetic field affected vibration response of double single-walled carbon nanotube systems", *J. Appl. Phys.* **111**:11 (2012), Art. ID 113511.

[Murmu et al. 2012b] T. Murmu, M. A. McCarthy, and S. Adhikari, "Vibration response of double-walled carbon nanotubes subjected to an externally applied longitudinal magnetic field: A nonlocal elasticity approach", *J. Sound Vib.* **331**:23 (2012), 5069–5086.

[Narendar et al. 2012] S. Narendar, S. S. Gupta, and S. Gopalakrishnan, "Wave propagation in single-walled carbon nanotube under longitudinal magnetic field using nonlocal Euler–Bernoulli beam theory", *Appl. Math. Model.* **36**:9 (2012), 4529–4538.

[Oniszczuk 2003] Z. Oniszczuk, "Forced transverse vibrations of an elastically connected complex simply supported double-beam system", *J. Sound Vib.* **264**:2 (2003), 273–286.

[Popov et al. 2014] A. M. Popov, I. V. Lebedeva, A. A. Knizhnik, Y. E. Lozovik, N. A. Poklonski, A. I. Siahlo, S. A. Vyrko, and S. V. Ratkevich, "Force and magnetic field sensor based on measurement of tunneling conductance between ends of coaxial carbon nanotubes", *Comput. Mater. Sci.* **92** (2014), 84–91.

[Reich et al. 2008] S. Reich, C. Thomsen, and J. Maultzsch, *Carbon nanotubes: Basic concepts and physical properties*, Wiley, Weinheim, 2008.

[Roth and Baughman 2002] S. Roth and R. H. Baughman, "Actuators of individual carbon nanotubes", *Curr. Appl. Phys.* **2**:4 (2002), 311–314.

[Ru 2001] C. Q. Ru, "Axially compressed buckling of a doublewalled carbon nanotube embedded in an elastic medium", *J. Mech. Phys. Solids* **49**:6 (2001), 1265–1279.

[Ruoff et al. 2003] R. S. Ruoff, D. Qian, and W. K. Liu, "Mechanical properties of carbon nanotubes: Theoretical predictions and experimental measurements", *C. R. Phys.* **4**:9 (2003), 993–1008.

[Saito 2003] Y. Saito, "Carbon nanotube field emitter", *J. Nanosci. Nanotechnol.* **3**:1–2 (2003), 39–50.

[Salvetat et al. 1999] J.-P. Salvetat, J.-M. Bonard, N. H. Thomson, A. J. Kulik, L. Forró, W. Benoit, and L. Zuppiroli, "Mechanical properties of carbon nanotubes", *Appl. Phys. A Mater. Sci. Process.* **69**:3 (1999), 255–260.

[Slavcheva and Roussignol 2011] G. Slavcheva and P. Roussignol, "Coherent magneto-optical polarisation dynamics in a single chiral carbon nanotube", *Superlattices Microstruct.* **49**:3 (2011), 325–330.

[Yang et al. 2010] J. Yang, L. L. Ke, and S. Kitipornchai, "Nonlinear free vibration of single-walled carbon nanotubes using nonlocal Timoshenko beam theory", *Physica E* **42**:5 (2010), 1727–1735.

[Zhang et al. 2008] Y. Q. Zhang, Y. Lu, and G. W. Ma, "Effect of compressive axial load on forced transverse vibrations of a double-beam system", *Int. J. Mech. Sci.* **50**:2 (2008), 299–305.

Received 25 May 2015. Revised 30 Sep 2015. Accepted 1 Jan 2016.

MARIJA B. STAMENKOVIĆ: s_marija86@yahoo.com
Mathematical Institute of the Serbian Academy of Science and Arts, Kneza Mihaila 36, 11001 Belgrade, Serbia

DANILO KARLIČIĆ: danilo.karlicic@masfak.ni.ac.rs
Faculty of Mechanical Engineering, University of Niš, A. Medvedeva 14, 18000 Niš, Serbia

GORAN JANEVSKI: gocky.jane@gmail.com
Department of Mechanical Engineering, University of Niš, A. Medvedeva 14, 18000 Niš, Serbia

PREDRAG KOZIĆ: kozicp@yahoo.com
Faculty of Mechanical Engineering, University of Niš, A. Medvedeva 14, 18000 Niš, Serbia

JOURNAL OF MECHANICS OF MATERIALS AND STRUCTURES
Vol. 11, No. 3, 2016
dx.doi.org/10.2140/jomms.2016.11.309

msp

A PHASE-FIELD MODEL OF QUASISTATIC AND DYNAMIC BRITTLE FRACTURE USING A STAGGERED ALGORITHM

HAMDI HENTATI, MARWA DHAHRI AND FAKHREDDINE DAMMAK

Fracture mechanisms in solids are governed by complex fracture phenomena such as crack initiation and multiple crack branching. Recently, the numerical modeling of dynamic fracture mechanisms has been based on the introduction of a crack phase field. Following our recent works on phase-field modeling of quasistatic brittle fracture, a numerical method is presented to investigate the dynamic failure mechanisms in brittle solids using the phase-field model and a staggered algorithm. For that, numerical experiments of a brittle piece under tensile loading are performed. Based on these numerical results, the importance of developing a numerical method to optimize the computation time is shown. The optimized method is presented in a linear (P1) finite elements case in elasticity. We then show the results of using the optimized method in the case of dynamic fracture mechanics in brittle materials, and we analyze when the dynamic solution converges to the quasistatic one. We also investigate the influence of the numerical parameters h (mesh size) and η (regularization parameter) on the evolution of energies, displacements and crack location. The influence of exerted loading δ and transverse wave speed C_T is also elaborated.

1. Introduction

Numerical and experimental studies of failure mechanisms under mechanical, thermal, quasistatic and dynamic loads have been investigated in [Kim and Paulino 2004; Bourdin et al. 2008; Jiang et al. 2012]. In these contexts, several phase-field approaches to brittle fracture have been elaborated. The developments related to the theory of brittle fracture are mainly based on the idea presented by Griffith [1921]. Despite his important contribution to this theory, it has some shortcomings as detailed in [Bourdin 1998; Francfort and Marigo 2002]. Recently, fracture mechanics have been revised by proposing different phase-field models for quasistatic brittle fracture cases, taking inspiration from Griffith's criterion. Significant contributions to the phase-field methods were made by Miehe et al. [2010a; 2010b], in the form of a thermodynamically consistent framework for brittle mode I fractures in the case of viscous material response. A staggered scheme was employed by Miehe et al. [2010a], in which a local energy history field was introduced as a state variable to ensure irreversible crack growth. Also, a variational theory was developed by Francfort and Marigo [1998], and was used to model brittle fracture in [Bourdin et al. 2000; 2008; Oleaga 2004; Amor et al. 2009; Pham and Marigo 2010a; 2010b; Buliga 1998; Hentati et al. 2015]. They proposed a new formulation for the brittle fracture problem, capable of predicting the creation of new cracks, their path and their interactions in two and three spacial dimensions. The functional proposed during the segmentation of images from Ambrosio and Tortorelli [1990; 1992] was

Keywords: brittle fracture, staggered algorithm, phase field.

adapted to the problem of brittle fracture by Bourdin [2000]. In the same context, a higher order phase-field model formulation adopting Bourdin's formalism was recently created by Borden et al. [2014], in order to gain more regular and faster converging solutions to the variational problem of brittle fracture.

Ambati et al. [2015] analyzed the efficiency of different numerical methods for phase-field modeling of brittle fracture and presented an overview of the existing quasistatic and dynamic phase-field fracture formulations.

Otherwise, the study of the fracture problem has been usually made in the quasistatic case [Bourdin et al. 2008; Amor et al. 2009; Pham and Marigo 2010a; Hentati et al. 2012a; 2012b; Msekh et al. 2015]. However, it was found that this simplification hypothesis is not valid in many cases, as shown in [Dumouchel et al. 2007; Kalthoff 2000]. There have been several attempts to adapt phase-field models to dynamic fracture problems [Bourdin et al. 2011; 2012; Hofacker and Miehe 2012; 2013; Hentati 2013; Schlüter et al. 2014].

Numerical procedures currently used for time integration in the analysis of dynamic problems are the central difference method, the Newmark [1959] scheme, the Houbolt [1950] method and the Bathe and Wilson [1972] method. Bert and Stricklin [1988] described and compared several different integration methods used to analyze dynamic responses for linear and nonlinear systems. They showed that the error increases as the time step increases in all of the above methods and concluded that the Houbolt and Bath and Wilson methods are the least efficient, and that the Newmark scheme gives very similar results compared to theoretical ones.

Due to the nonconvexity of the regularized energy functional, a robust solution scheme based on (staggered) algorithmic decoupling was used in [Bourdin et al. 2008; Miehe et al. 2010a; Hentati et al. 2012a]. Based on a monolithic scheme used in [Miehe et al. 2010b; Borden et al. 2012; Vignollet et al. 2014], a coupled method was proposed in order to compute the quasistatic fracture phase field. The robustness of the staggered algorithmic implementation was proven by Ambati et al. [2015].

In order to resolve the dynamic fracture problem, Borden et al. [2012] proposed another method by introducing an initial strain history field that induces a phase field at the initial crack location. The numerical solution of the dynamic problem requires spatial and temporal discretization. The spatial discretization was formulated by the Galerkin method and the monolithic time integration scheme is based on the generalized-α method introduced by Chung and Hulbert [1993].

Bourdin et al. [2011] also proposed a discrete time model for dynamic fracture. They approached the elastic dynamic problem by using a finite difference discretization on the partial differential equation. They deduced that the total energy is not conserved. Hentati et al. [2013] used the Newmark direct integration method to study the evolution of energies by supposing an elasticity problem. The quantitative agreement between numerical results using the finite element method with the Newmark scheme and the analytical ones using the characteristic method was shown. Furthermore, the efficiency of the numerical method using the finite element method with the Newmark scheme for simulating dynamic crack propagation in brittle materials was shown.

This paper is focused on modeling and computing the dynamic crack propagation using the phase-field model. This model was developed by Francfort and Marigo [1998] for the quasistatic brittle fracture problem. The first goal is to propose and test an optimized numerical method in order to simulate dynamic crack propagation. This finite element assembly code is without loops and also without any quadrature formula. It is entirely vectorized. This method, which is based on the staggered scheme

with the optimized algorithm, is validated. Quasistatic tests are elaborated and the numerical results are compared with the experimentation done in [Ambati et al. 2015] and are also validated with the numerical results obtained in [Ambati et al. 2015; Msekh et al. 2015]. The second goal is to analyze the computational results of dynamic crack propagation based on the numerical method detailed by Hentati et al. [2013]. The influence of numerical parameters (notably the ratio h/η) on energies and displacement evolution and crack location was also developed in this work.

2. Phase-field model of dynamic brittle fracture

A material is assumed to be elastic, isotropic and homogeneous with shear modulus μ and constant mass density ρ. The numerical model used for the antiplane case with constant toughness G_c is described below.

2A. ***Phase-field model.*** We introduce a discrete time model for dynamic brittle fracture which obeys the following principles:

- Elastic dynamic: away from the crack, the governing principle is the elastic dynamic equation. So, the dynamic problem consists in finding the displacement $u(x_1, x_2, t)$ satisfying

$$\rho \frac{\partial^2 u}{\partial t^2} = \mu \left(\frac{\partial^2 u}{\partial x_1^2} + \frac{\partial^2 u}{\partial x_2^2} \right). \tag{2-1}$$

- Energy balance: the evolution should satisfy an energy balance formula, similar to that found in the quasistatic setting, but now including kinetic energy.
- Maximal dissipation: if the crack can propagate while balancing energy, then it should propagate. Then, α minimizes the regularized energy $E(u, \alpha)$, given by

$$E(u, \alpha) = \frac{\mu}{2} \int ((1-\alpha)^2 + \epsilon(\eta)) \nabla u \cdot \nabla u \, dx + G_c \int \left(\frac{\alpha^2}{4\eta} + \eta \nabla \alpha \cdot \nabla \alpha \right) dx. \tag{2-2}$$

The time-discrete algorithm for dynamic fracture that was developed can be summarized as follows:

Staggered dynamic fracture algorithm.

- Choose numerical and material parameters.
- Find u using the Newmark direct integration algorithm for linear systems (Figure 1).
- Find α such that the regularized energy $E(u, \alpha)$ given by (2-2) is minimized with respect to the irreversibility condition $\alpha(\delta) \geq \alpha(\delta - d\delta)$.

Here u is the displacement, $x(x_1, x_2)$ is the spatial coordinate, η is a regularized numerical parameter, α is the damage variable and ϵ is a positive infinitesimal whose role is to render coercive the regularized functional. We choose the parameters $\beta = 0.25$, which ensures stability, and $\gamma = 0.5$, which ensures both stability and accuracy of the Newmark algorithm. Both problems will be computed iteratively by using the staggered solution scheme.

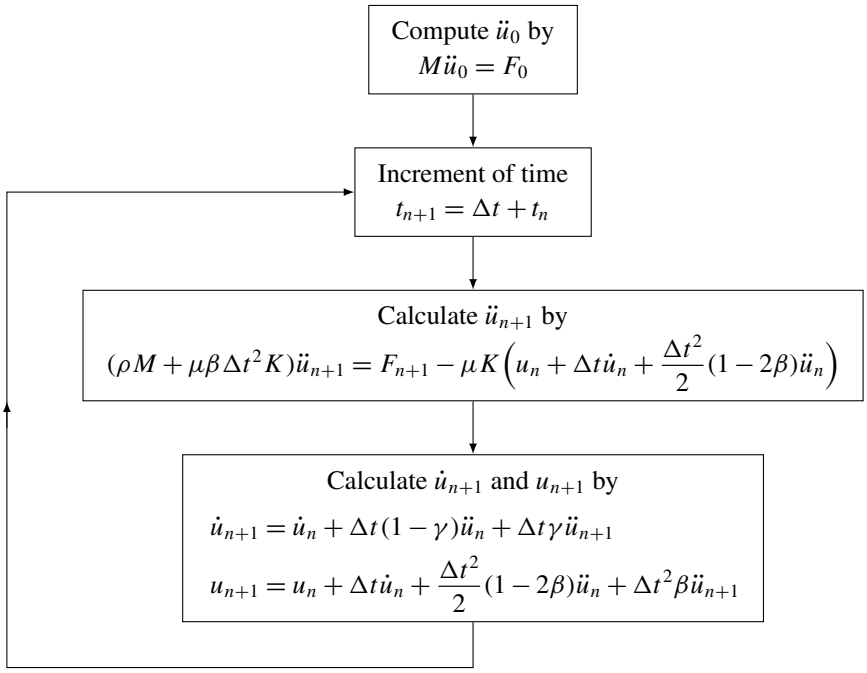

Figure 1. Direct Newmark integration algorithm for linear systems.

The elastic, surface and kinetic energies are given by

$$E_{\text{elast}}(t) = \frac{\mu}{2}\int_\Omega ((\alpha-1)^2+\epsilon)|\nabla u|^2\, dx_1\, dx_2, \tag{2-3}$$

$$E_{\text{surf}}(t) = G_c\int_\Omega \left(\frac{\alpha^2}{4\eta} + \eta|\nabla\alpha|^2\right) dx_1\, dx_2, \tag{2-4}$$

$$E_{\text{kine}}(t) = \frac{\rho}{2}\int_\Omega \left(\frac{\partial u(x_1, x_2, t)}{\partial t}\right)^2 dx_1\, dx_2. \tag{2-5}$$

We carry out some numerical computations in order to determine the evolution of these energies that depend on the time and the location of cracking.

2B. ***Problem description.*** A rectangular structure is considered, as shown in Figure 2, occupying the studied domain $\Omega \subset \mathbb{R}^2$, $\Omega = (0, L) \times (0, l)$, where L and l are the length and width of our structure.

The structure is fixed at the left edge and submitted to tensile loading at the right edge. A time-dependent Dirichlet boundary condition $\delta(t)$ is applied to the right edge, given by

$$\delta(t) = Kt^2. \tag{2-6}$$

Figure 2. Studied brittle structure with boundary conditions.

The boundary and initial conditions are

$$u(0, x_2, t) = 0, \qquad u(L, x_2, t) = \delta(t), \tag{2-7}$$

$$\frac{\partial u(x_1, 0, t)}{\partial n} = \frac{\partial u(x_1, l, t)}{\partial n} = 0, \tag{2-8}$$

$$u(x_1, x_2, 0) = 0, \quad \frac{\partial u}{\partial t}(x_1, x_2, 0) = 0, \tag{2-9}$$

$$\alpha(x_1, x_2, 0) = 0. \tag{2-10}$$

3. Validation of the optimized staggered algorithm

The regularization parameter η should be large enough as compared to the mesh size h ($\eta \gg h$). Moreover, we know that if the mesh is fine (h is small), the obtained solution using the finite element method will be accurate compared to the analytic one. Therefore, the choice of h is a compromise between the value of η and the capacity of the processor used to perform the calculation. However, if this condition is respected, the repetition of elements inserted in the matrices will be very expensive if the classical method is used. So, the optimized method will be used to simulate dynamic crack propagation, in order to improve the cost of the method.

In this section, we validate a new method of assembling matrices that is based on the sparse function. This method allows us to reduce the computation time and further refine the mesh. We remind the reader of the classical method. Recall that Ω_h is the triangular mesh of the studied domain $\Omega \subset \mathbb{R}^2$. The basis function φ_i satisfies $\{\varphi_i(q^j)\} = \delta_{i,j}$. Due to the support properties of P1 Lagrange basis functions, we have the classical algorithm. For each element, its element matrix is added to the global matrix. This operation is illustrated in Figure 3 for the 2D scalar fields case.

This proposed optimized assembling method is a standard one, used to assemble sparse matrices using triplet lists. The idea is to create three global 2D arrays, I_g, J_g and K_g, that allow the storage of the element matrices as well as the position of their elements in the global matrix. To create these three arrays, we first define three local arrays obtained from a generic element matrix $E(T_k)$:

- K_k^e contains the elements of the matrix $E(T_k)$ stored columnwise.
- I_k^e contains the global row indices associated with the elements stored in K_k^e.
- J_k^e contains the global column indices associated with the elements stored in K_k^e.

The three local arrays I_k^e, J_k^e and K_k^e are stored in the k-th column of the global arrays I_g, J_g and K_g, respectively.

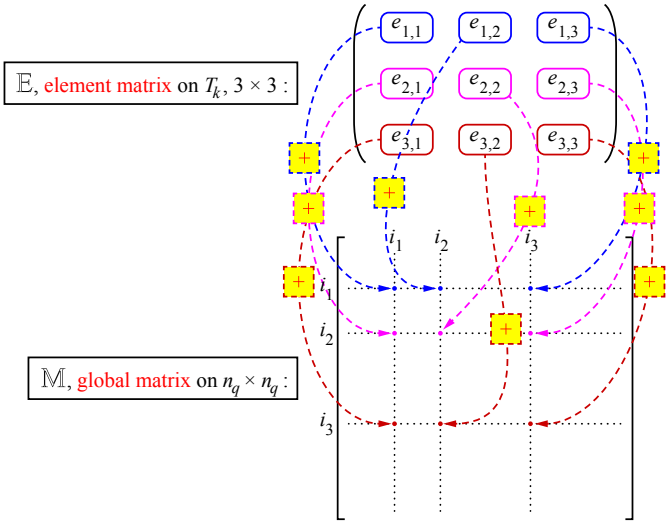

Figure 3. An element matrix added to the global matrix.

Function name	Calls per iteration	Total time of method (sec) classical	optimized
Mass assembling matrix	4	20	4
Stiffness assembling matrix	12	120	14
Find α that minimizes $E(u, \alpha)$	1	2	$\ll 1$
Find u as solution of dynamic equation	1	7	$\simeq 1$
Principal program (after 120 iterations)	1	18500	2700

Table 1. Computational cost of minimizer problem.

A natural way to build these three arrays consists of using a loop through the triangles T_k, in which we insert the local arrays columnwise.

We compared the performance of these two programming techniques (optimized and classical methods) for assembling finite element matrices in 2D. Some numerical computations were done to investigate the time difference between the two methods. Table 1 shows the computational cost of the mass and stiffness matrix assembly. The results show that the optimized method gives better results than the classical one.

In order to validate this optimized staggered algorithm, numerical tests of some quasistatic fracture cases were done and the results were compared to experimental and validated numerical tension tests. These tests were computed using the staggered scheme with the optimized algorithm used for assembling matrices. A standard linear (P1) Lagrange finite element method was used to discretize the problem on the displacement field and the damage variable α. The problem consists in finding the displacement $u(x_1, x_2, t)$ that satisfies $\Delta u = 0$, using u to find α and using the couple (u, α) to minimize the regularized energy $E(u, \alpha)$. So, the staggered quasistatic fracture algorithm was developed and can be summarized as follows:

Figure 4. Experimental test of a notched plate with hole: (left) geometry and boundary conditions, (center) experiment result and (right) experimental setup. All units are in mm.

Staggered quasistatic fracture algorithm.

- Choose numerical and material parameters.
- Find u that minimizes the regularized energy $E(u, \alpha)$, as given by (2-2).
- Find α such that the regularized energy $E(u, \alpha)$ is minimized with respect to the irreversibility condition $\alpha(\delta) \geq \alpha(\delta - d\delta)$.

3A. ***First test: notched plate with hole.*** For the first test, a sample consisting of a notched plate with a hole is presented. Figure 4 illustrates the experimental test of a notched plate with a hole as detailed by Ambati et al. [2015]. The geometry, boundary conditions and experimental setup are shown in Figure 4. The specimen is a notched plate with a hole offset from the center. The top pin is submitted to displacement loading and the lower pin is fixed.

The crack path is illustrated in Figure 5. A curved crack develops from the notch to the large hole. Later, a secondary straight crack appears from the hole to the sample edge.

3B. ***Second test: single edge notched.*** We apply the phase-field model to a square plate containing a straight horizontal notch located at mid-height on the left edge with a length of 0.5 mm. The geometric properties and boundary conditions of the specimen are shown in Figure 6. A vertical displacement is applied to the top edge.

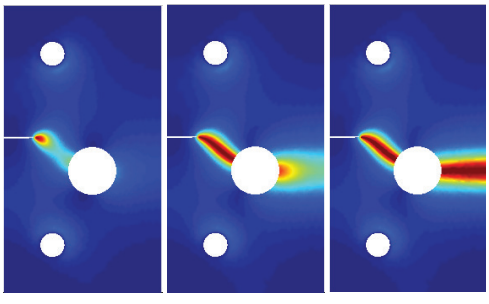

Figure 5. Notched plate with hole: quasistatic crack phase field.

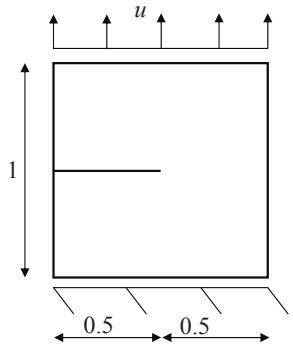

Figure 6. Geometry and boundary conditions for single edge notched specimen. All units are in mm.

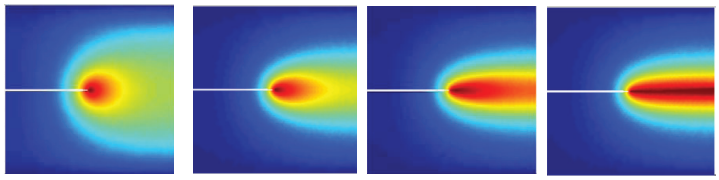

Figure 7. Single edge notched: quasistatic crack phase field.

Figure 7 shows the crack patterns at several stages of loading for the tested model. Here the red and blue colors indicate the damaged and undamaged material, respectively.

With this setup, the crack propagates towards the middle right edge of the specimen. The phase-field model using the optimized staggered algorithm yields very similar results, in terms of crack path, to [Ambati et al. 2015; Msekh et al. 2015].

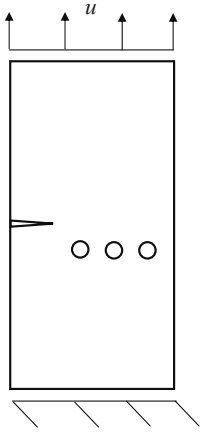

Figure 8. Notched rectangular specimen with three openings: geometry, loading and boundary conditions.

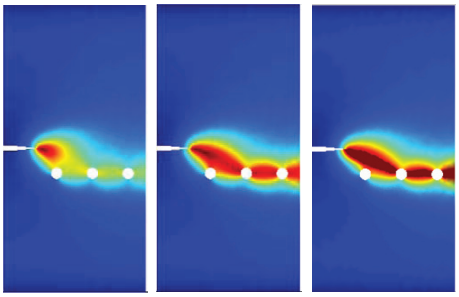

Figure 9. Notched rectangular specimen with three openings: quasistatic crack phase field.

3C. ***Third test: notched specimen with three openings.*** We simulate a sample consisting of a notched rectangular plate with three circular openings, in which the centers are aligned horizontally. The three circular openings are near the initial notch as shown in Figure 8. The applied loading and boundary conditions are also shown.

As shown in Figure 9, the presence of the opening nearest to the notch causes a kinking of the crack path just above it; however, the opening is not near enough to the notch line to arrest crack propagation. This occurs just above the second opening along with the initiation of a new crack segment, similar to what was observed in the first test. We compared the numerical result of this study with the numerical crack pattern from [Msekh et al. 2015], and the comparison shows that the present phase-field model is able to predict the correct trajectory of a curved crack. Msekh et al. studied the effect of varying the proximities of openings in altering the propagation of a crack path. They showed that for holes situated significantly far away from the notch line, crack propagation is virtually unaffected, whereas for sufficiently close openings the crack path is modified.

The current and preceding tests highlight an important strength of the phase-field method, specifically that the initiation of a crack does not require the introduction of a notch, and that a crack may initiate anywhere within the geometry of a given structure. So, we have shown that the phase-field model using the staggered scheme and the optimized algorithm of assembling matrices is in agreement with experimental and validated numerical results in terms of crack pattern. This numerical method is used in the next section for simulating dynamic crack propagation.

4. Numerical experiments of dynamic fracture mechanics

The following settings were chosen for all numerical computations. The material properties are $G_c = 1$, $\rho = 1$ and $\mu = 1$. The numerical parameter is $\epsilon = 10^{-5}$. The dimensions of the structure are $L = 2$ and $l = 1$. Table 2 shows the values of the selected parameters for the simulations.

A Dirichlet condition was applied on the right and left boundaries in the 1st test:

$$\alpha(x_1 = 0, x_2, t) = \alpha(x_1 = L, x_2, t) = 0. \tag{4-1}$$

In this section, the evolution of α and of different energies was studied while varying the exerted load. Also, the influence of numerical parameters on the critical load-causing fracture (δ_c), the evolution of energies and the location of crack was analyzed.

4A. ***Regularized damage field.*** Using the parameters from the 1st test, the coordinates of some nodes are shown in Table 3.

First, we studied the evolution of the damage field at these nodes as a function of time. The applied load is $\delta(t) = t^2$. The evolution of α changing with respect to time is illustrated in Figure 10. The nodes N01, N02, N03 and N04 have α greater than 0.7 while α reaches the value 1 in other nodes. Therefore, the fracture is not brutal because α does not reach the value 1 at the same time for all nodes in the cracked area.

We then investigated the evolution of the damage field in the cracked zone. The fracture occurs during the 1950th iteration ($t = 1.95$). During this time, few nodes have a damage value $\alpha = 1$. Table 4 shows the evolution of α in nodes N05 (x_1(N05) = 1.84) and N06 (x_1(N06) = 1.83). For both nodes, the value of α is less than 1, but it increases slowly until its value reaches 1 after some iterations. In the same context, the damage field in quasistatic hypothesis is unregularized in time. It jumps suddenly to the

Test	η	h	Time step dt (sec)	Boundary conditions (BC) on α
1st test	0.02	0.007	0.001	with BC
2nd test	0.02	0.007	0.001	without BC
[Hentati 2013]	0.03	0.01	0.0025	without BC

Table 2. Numerical parameters in different simulation tests.

Nodes	N01	N02	N03	N04	N05	N06
x_1 coordinate	1.84	1.83	1.7	1.65	1.84	1.83
x_2 coordinate	0.5	0.5	0.5	0.5	0.2	0.7

Table 3. Node coordinates.

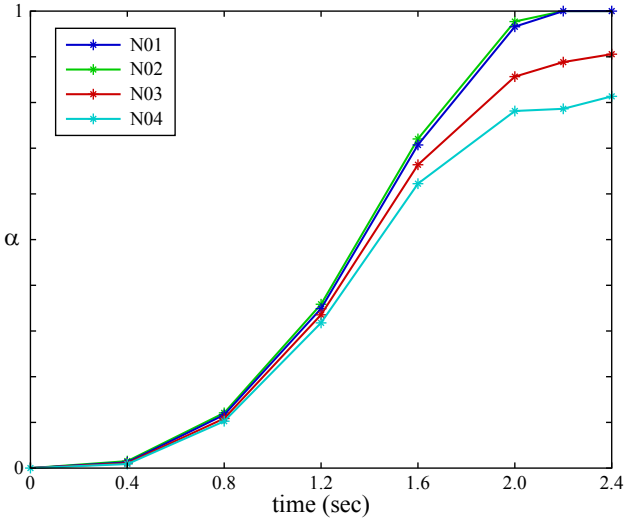

Figure 10. Evolution of α depending on time.

Time (sec)	α at N05	α at N06
1.60	0.69	0.70
1.80	0.80	0.80
1.85	0.84	0.83
1.90	0.85	0.84
1.92	0.85	0.84
1.95	0.86	0.85
1.97	0.86	0.85
1.98	0.87	0.86
2.00	0.88	0.86
2.30	0.97	0.93
2.50	1.00	0.98
2.60	1.00	1.00

Table 4. Evolution of α in different nodes.

value 1 and brutal cracking appears. But, in the dynamic crack propagation case, it is regularized in time and in space.

Next, the displacement before and after crack initiation in the 1st test case was studied. The displacement evolution at different times and their differences versus x_1-coordinates are presented in Figures 11, 12 and 13. We show that, after crack initiation at $t = 1.95$, the displacement is nonzero and is increasing in time. This is due to the rigidity of the structure. Some nodes have a value of $\alpha = 1$ and other nodes in the cracked area have a value of α less than 1. After the crack initiation, the difference between the displacements become smaller in time. This is due to the increase in the number of nodes in which $\alpha = 1$.

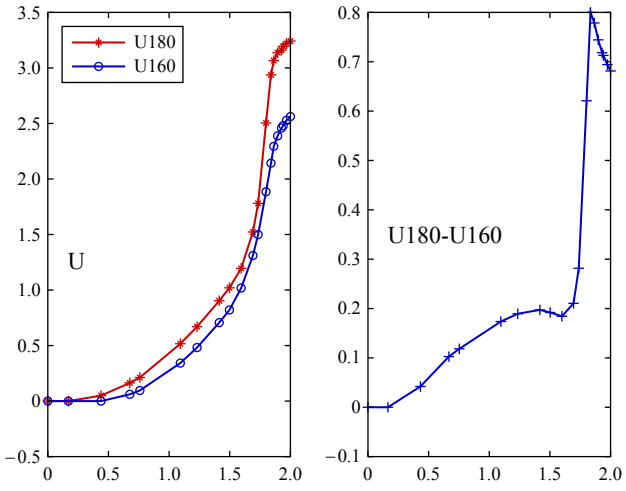

Figure 11. Left: displacement versus x_1 coordinate at $t = 1.60$ (U160) and at $t = 1.80$ (U180). Right: difference between U180 and U160.

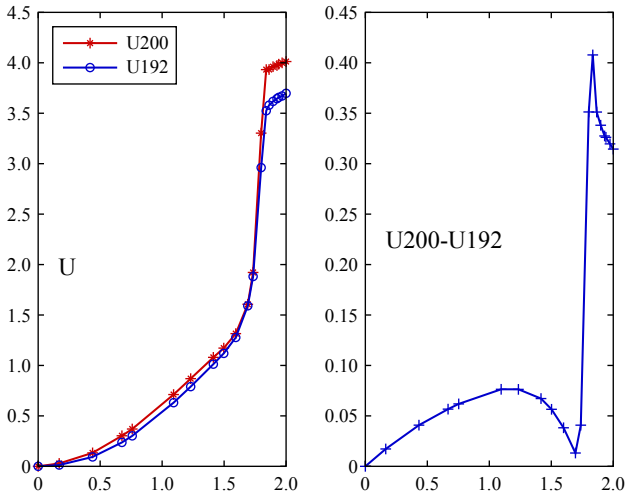

Figure 12. Left: displacement versus x_1 coordinate at $t = 1.92$ (U192) and at $t = 2.00$ (U200). Right: difference between U200 and U192.

4B. ***Evolution of computed energies.*** We refer the reader to the results found by Hentati et al. [2013]. For $t = t_c = 1.6$ ($\delta = \delta_c = 2.56$), the elastic energy E_{elast} reaches its maximum value and decreases. The kinetic energy E_{kine} reaches its minimum value ($dE_{\text{kine}}/dt = 0$) and then rises ($dE_{\text{kine}}/dt > 0$). At this time, crack propagation occurs. The surface and total energies become constant if $\delta > 2.56$, and the sum $(E_{\text{elast}} + E_{\text{kine}})$ is constant. Note that E_{surf} is nonzero before the critical load δ_c is reached. This is due to the insufficiently small value of the mesh parameter.

Figures 14 and 15 describe the evolution of computed energies versus time using the applied load $\delta(t) = t^2$.

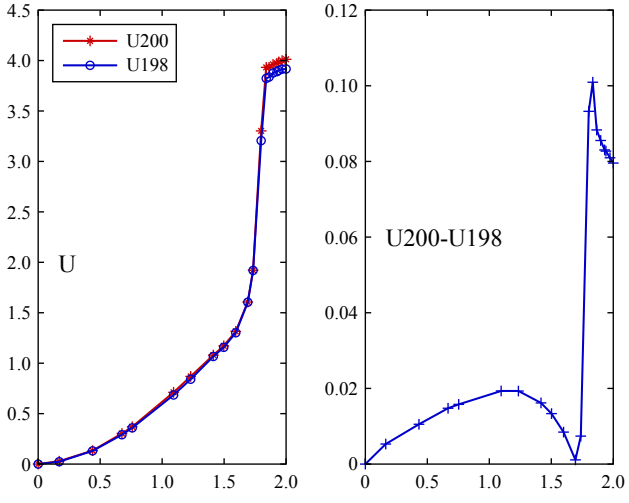

Figure 13. Left: displacement versus x_1 coordinate at $t = 1.98$ (U198) and at $t = 2.00$ (U200). Right: difference between U200 and U198.

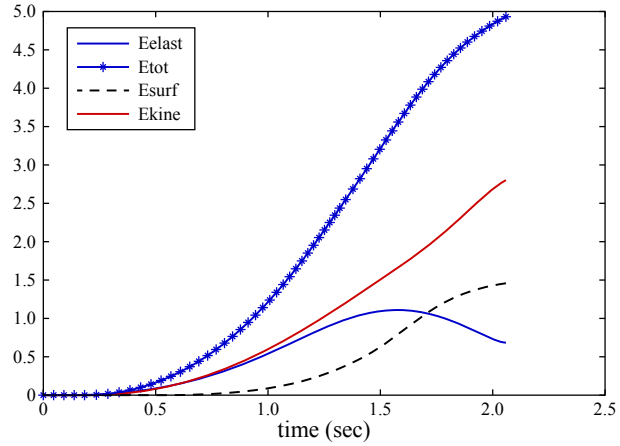

Figure 14. Evolution of computed energies in the 1st test.

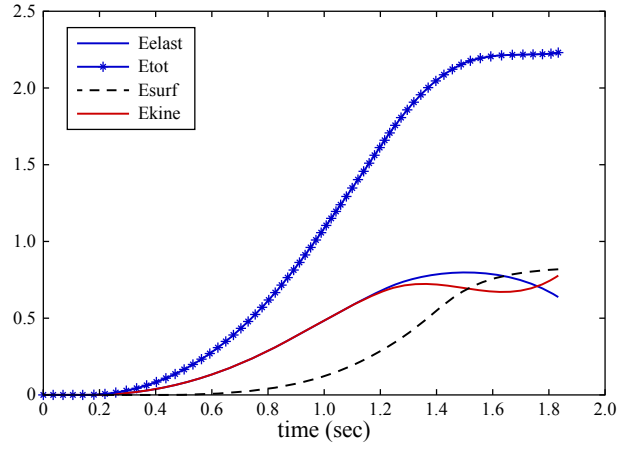

Figure 15. Evolution of computed energies in the 2nd test

In order to study the influence of numerical parameters and boundary conditions essentially on the energies' evolution as well as the critical time value, we illustrate in Table 5 the main results.

Using the numerical results obtained by Hentati [2013], the surface energy E_{surf} becomes nonzero at $t = 0.62$. But, in the 2nd test (Figure 15), the surface energy E_{surf} becomes nonzero at $t = 0.65$. Then, if the regularized parameter η is small, E_{surf} will remain zero almost all of the time. However, after the

Test	η	h/η	t_c	E_{surf} at $t = t_c$
1st test	0.02	0.35	1.95	1.4
2nd test	0.02	0.35	1.65	0.8
[Hentati 2013]	0.03	0.33	1.6	0.75

Table 5. Main results in different tests.

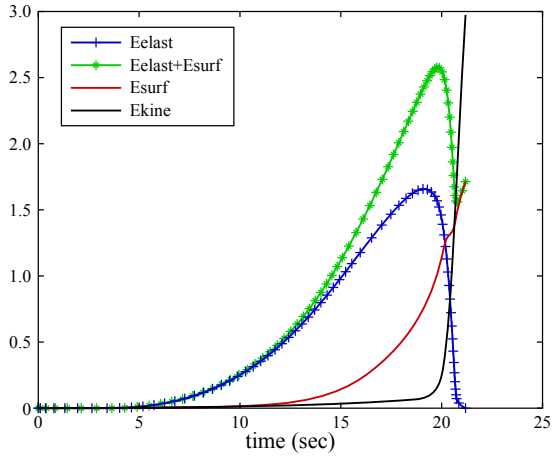

Figure 16. Influence of the applied load on the evolution of energies ($K = 0.01$).

initiation of crack (some nodes have a value of $\alpha = 1$), the value of the surface energy E_{surf} and the critical time lead to fracture t_c depending on the ratio h/η.

In fact, as shown in Table 5, the critical time t_c and the surface energy E_{surf} decrease when the ratio h/η decreases as revealed by the study of influence of numerical parameters and boundary conditions on the evolution of energies and the localization of crack. So, in the 1st test, the fracture will be at $t = t_c = 1.95$ (see Figure 14).

Although the ratio $h/\eta = 0.35$ is conserved, this critical time value t_c is not the same in the 2nd test (see Figure 15). Also, in the 1st test, the elastic energy E_{elast} reaches the maximum value and decreases before the fracture of structure. The kinetic energy E_{kine} increases in time ($dE_{\text{kine}} > 0$). At time $t = 1.65$,

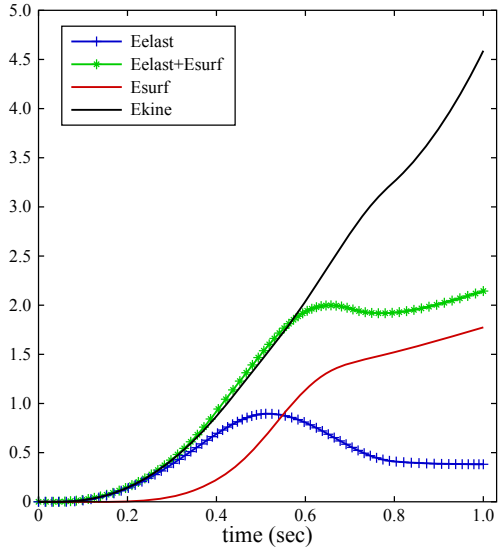

Figure 17. Influence of the applied load on the evolution of energies ($K = 5$).

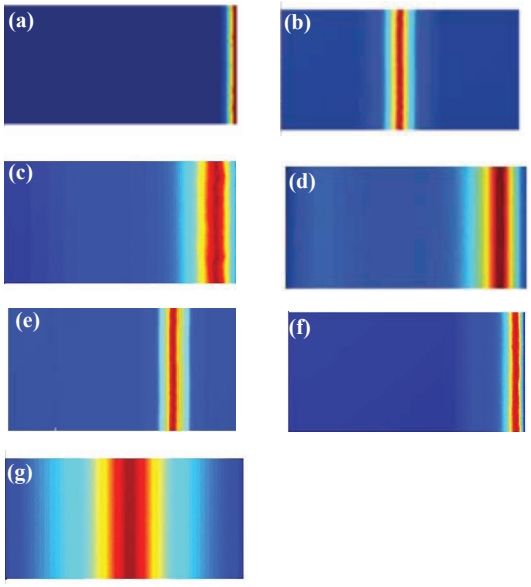

Figure 18. Location of cracks in quasistatic and dynamic fracture: (a) quasistatic fracture with Neumann boundary condition on α and $K = 1$ [Hentati 2013], (b) quasistatic fracture with Dirichlet boundary condition on α and $K = 1$ [Hentati et al. 2012a], (c) dynamic fracture in the 2nd test, (d) dynamic fracture in the 1st test, (e) dynamic fracture like the 1st test but with $C_T = 10$, (f) dynamic fracture like the 1st test but with $K = 5$ and (g) dynamic fracture like the 1st test but with $K = 0.01$.

$E_{\text{surf}} = E_{\text{elast}}$, the energy E_{surf} increases in time and E_{elast} decreases and if $t = 1.95$ a crack propagation occurs.

4C. ***Influence of applied load.*** In this section, the influence of the acceleration $a = \partial^2\delta(t)/\partial t^2$ on the evolution of the crack is investigated. So, we impose the Dirichlet boundary condition on damage variable α on the right and left edges of our structure (1st test). Based on (2-6), the acceleration is $a = 2K$. Two coefficients of the applied load were chosen in the following tests: $K = 0.01$ and $K = 5$. Figures 16 and 17 represent the evolution of energies as a function of time t.

In conclusion, for $K \ll 1$, α passes rapidly from the value 0.7 to 1 in a few iterations. Rupture occurs for loading $\delta = 3.76$ (i.e., at $t = 19.4$). E_{elast} reaches its maximum and then decreases at the time of rupture. This energy vanishes after cracking. E_{surf} increases until reaching E_{elast} after the break and is then set to 1. When the coefficient K is high, the evolution of energies is similar to the case $K = 1$, but different than the case of $K \ll 1$.

5. Comparison between quasistatic and dynamic fracture

Figure 18 summarizes the location of cracks in quasistatic and dynamic fracture cases and their dependence on the transverse wave speed C_T, the acceleration $a = 2K$ and the boundary condition on α.

In the quasistatic computations, and as shown in [Hentati et al. 2012a; 2012b], the Dirichlet boundary condition applied on α does not have a significant influence on the propagation condition of a crack. However, it does have an influence on the location of a crack. The elastic energy E_{elast} decreases from its maximum value and the surface energy of the computed solution is overestimated ($E_{\text{surf}} > 1$) as compared to a theoretical value of $E_{\text{surf}}^{\text{th}} = G_c l = 1$. Figure 18(a)–(b) show the locations of cracks in the quasistatic case with and without boundary conditions on α, respectively. Also, in quasistatic computations, there can be an instant decrease in E_{elast} when α increases (i.e., the crack grows), at which point brutal cracking appears in the brittle rectangular domain. The critical load is overestimated ($\delta_c > \delta_c^{\text{th}} = 2$) as compared to the theoretical critical load, given by

$$\delta_c^{\text{th}} = \sqrt{\frac{2LG_c}{\mu}}. \tag{5-1}$$

In dynamic crack propagation, we show that after the initiation of a crack during the 1950th iteration ($t = 1.95$), the displacement is nonzero and increasing in time. This is due to the rigidity of the structure. Some nodes have a value of $\alpha = 1$ while other nodes in the cracked area have a value of $\alpha < 1$. After the initiation of the crack, the differences between the displacements becomes smaller over time. This is due to the increase in the number of nodes that have a value of $\alpha = 1$. So, the damage field in the quasistatic problem is nonregularized in time and space. It jumps suddenly to the value 1 and brutal cracking appears. But in the dynamic case, the crack propagation is progressive and the phase field is regularized in time and space. Equally important, the location of crack depends on the value of the transverse wave speed C_T, given by

$$C_T = \sqrt{\frac{\mu}{\rho}}. \tag{5-2}$$

Also, the coefficient K has an influence on the location and thickness of crack, the evolution of the damage field and the evolution of energy, but has no effect on the critical load δ_c.

Quasistatic computations were also done in [Hentati 2013]. It was shown that the Dirichlet boundary condition on α does not have an effect on the evolution of energies, but it does affect the crack location. Brutal cracking appears in the brittle solid and there can be an instant decrease in the elastic energy when the crack grows. In the dynamic fracture case, crack growth takes place if $dE_{\text{kine}}/dt = 0$ instead of $G = G_c$ as in quasistatic fracture case, and the propagation condition of the crack is $dE_{\text{kine}}/dt > 0$ instead of $G > G_c$, as in the quasistatic fracture case. This condition only occurs if the Dirichlet boundary conditions on α are not applied to different edges than where the displacement field was applied, whereas if we apply a Dirichlet condition on the right and left boundaries ($\alpha(x_1 = 0, x_2, t) = \alpha(x_1 = L, x_2, t) = 0$), the dynamic crack will grow after $E_{\text{surf}} > E_{\text{elast}}$ and $dE_{\text{kine}}/dt > 0$.

We present the main results of this comparative study between quasistatic and dynamic crack propagation in rectangular structures below:

- In dynamic problems, crack location depends on the load coefficient K and the transverse wave speed C_T. If the term $\rho\partial^2 u/\partial t^2$ is not negligible compared with the term $\partial^2 u/\partial x^2$, we should consider the problem to be dynamic and the existence of waves alters the location of crack (see Figure 18(e)–(f)).

- If the load coefficient $K \ll 1$, the dynamic solution will converge to the quasistatic one (see Figure 18(g)).
- Crack propagation is progressive in the dynamic fracture case and brutal in the quasistatic one.

6. Conclusion

Phase-field modeling of brittle fracture shows promise as a computational tool for use in fracture problems that have geometries with complex crack surface topologies. We improved the performance of quasistatic and dynamic phase-field models of fracture by using staggered implementation schemes. Using formulations stemming from Griffith's theory, we focused on the quasistatic model featuring tension tests in which we use the phase-field model. We found agreement in terms of crack pattern with experimental and numerical results from literature. We also examined the staggered algorithm's implementation on dynamic problems, due to the algorithm's proven robustness. For that, an optimized method was proposed in order to simulate dynamic crack propagation in order to reduce the computation time and refine the mesh. This method consists of assembling matrices based on the sparse function. Furthermore, dynamic fracture mechanics were studied and the influence of numerical parameters on evolution of energies and crack location was investigated.

Acknowledgement

Thanks are due to F. Cuvelier (Laboratoire Analyse, Géométrie et Applications, Université Paris 13) for his critical help in the first parts of this paper.

References

[Ambati et al. 2015] M. Ambati, T. Gerasimov, and L. De Lorenzis, "A review on phase-field models of brittle fracture and a new fast hybrid formulation", *Comput. Mech.* **55**:2 (2015), 383–405.

[Ambrosio and Tortorelli 1990] L. Ambrosio and V. M. Tortorelli, "Approximation of functionals depending on jumps by elliptic functionals via Γ-convergence", *Comm. Pure. Appl. Math.* **43**:8 (1990), 999–1036.

[Ambrosio and Tortorelli 1992] L. Ambrosio and V. M. Tortorelli, "On the approximation of free discontinuity problems", *Boll. Un. Mat. Ital. B* (7) **6**:1 (1992), 105–123.

[Amor et al. 2009] H. Amor, J.-J. Marigo, and C. Maurini, "Regularized formulation of the variational brittle fracture with unilateral contact: numerical experiments", *J. Mech. Phys. Solids* **57**:8 (2009), 1209–1229.

[Bathe and Wilson 1972] K. J. Bathe and E. L. Wilson, "Stability and accuracy analysis of direct integration methods", *Earthq. Eng. Struct. Dyn.* **1**:3 (1972), 283–291.

[Bert and Stricklin 1988] C. W. Bert and J. D. Stricklin, "Comparative evaluation of six different numerical integration methods for nonlinear dynamic systems", *J. Sound Vib.* **127**:2 (1988), 221–229.

[Borden et al. 2012] M. J. Borden, C. V. Verhoosel, M. A. Scott, T. J. R. Hughes, and C. M. Landis, "A phase-field description of dynamic brittle fracture", *Comput. Methods Appl. Mech. Eng.* **217–220** (2012), 77–95.

[Borden et al. 2014] M. J. Borden, T. J. R. Hughes, C. M. Landis, and C. V. Verhoosel, "A higher-order phase-field model for brittle fracture: formulation and analysis within the isogeometric analysis framework", *Comput. Methods Appl. Mech. Eng.* **273** (2014), 100–118.

[Bourdin 1998] B. Bourdin, *Une méthode variationnelle en mécanique de la rupture, théorie et applications numériques*, thesis, Université Paris-Nord, 1998, Available at https://www.math.lsu.edu/∼bourdin/downloads/Bourdin-1998a.pdf.

[Bourdin et al. 2000] B. Bourdin, G. A. Francfort, and J.-J. Marigo, "Numerical experiments in revisited brittle fracture", *J. Mech. Phys. Solids* **48**:4 (2000), 797–826.

[Bourdin et al. 2008] B. Bourdin, G. A. Francfort, and J.-J. Marigo, "The variational approach to fracture", *J. Elasticity* **91**:1-3 (2008), 5–148.

[Bourdin et al. 2011] B. Bourdin, C. J. Larsen, and C. L. Richardson, "A time-discrete model for dynamic fracture based on crack regularization", *Int. J. Fract.* **168**:2 (2011), 133–143.

[Buliga 1998] M. Buliga, "Energy minimizing brittle crack propagation", *J. Elasticity* **52**:3 (1998), 201–238.

[Chung and Hulbert 1993] J. Chung and G. M. Hulbert, "A time integration algorithm for structural dynamics with improved numerical dissipation: the generalized-α method", *J. Appl. Mech.* (*ASME*) **60**:2 (1993), 371–375.

[Dumouchel et al. 2007] P. E. Dumouchel, J.-J. Marigo, and M. Charlotte, "Rupture dynamique et fissuration quasi-statique instable", *C. R. Mécanique* **335**:11 (2007), 708–713.

[Francfort and Marigo 1998] G. A. Francfort and J.-J. Marigo, "Revisiting brittle fracture as an energy minimization problem", *J. Mech. Phys. Solids* **46**:8 (1998), 1319–1342.

[Francfort and Marigo 2002] G. A. Francfort and J.-J. Marigo, "Vers une théorie énergétique de la rupture fragile", *C. R. Mécanique* **330**:4 (2002), 225–233.

[Griffith 1921] A. Griffith, "The phenomena of rupture and flow in solids", *Phil. Trans. R. Soc. A* **221**:582–593 (1921), 163–198.

[Hentati 2013] H. Hentati, *Numerical method to simulate the dynamic crack propagation based on the variational approach*, thesis, University of Sfax, Tunisia, 2013.

[Hentati et al. 2012a] H. Hentati, R. Abdelmoula, A. Maalej, and K. Maalej, "Quasi static analysis of anti-plane shear crack", *Appl. Mech. Mater.* **232** (2012), 92–96.

[Hentati et al. 2012b] H. Hentati, R. Abdelmoula, A. Maalej, and K. Maalej, "Quasi static fracture: global minimizer of the regularized energy", *Appl. Mech. Mater.* **232** (2012), 97–101.

[Hentati et al. 2013] H. Hentati, R. Abdelmoula, A. Maalej, and K. Maalej, "Numerical analysis solving the elastic dynamic problem", *Int. J. Model. Identif. Control.* **19**:3 (2013), 299–305.

[Hentati et al. 2015] H. Hentati, I. Ben Naceur, W. Bouzid, and A. Maalej, "Numerical analysis of damage thermo-mechanical models", *Adv. Appl. Math. Mech.* **7**:5 (2015), 625–643.

[Hofacker and Miehe 2012] M. Hofacker and C. Miehe, "Continuum phase field modeling of dynamic fracture: variational principles and staggered FE implementation", *Int. J. Fract.* **178** (2012), 113–129.

[Hofacker and Miehe 2013] M. Hofacker and C. Miehe, "A phase field model of dynamic fracture: robust field updates for the analysis of complex crack patterns", *Int. J. Numer. Methods Eng.* **93**:3 (2013), 276–301.

[Houbolt 1950] J. C. Houbolt, "A recurrence matrix solution for the dynamic response of elastic aircraft", *J. Aeronaut. Sci.* **17** (1950), 540–550.

[Jiang et al. 2012] C. P. Jiang, X. F. Wua, J. Li, F. Song, Y. F. Shao, X. H. Xu, and P. Yan, "A study of the mechanism of formation and numerical simulations of crack patterns in ceramics subjected to thermal shock", *Acta Mater.* **60** (2012), 4540–4550.

[Kalthoff 2000] J. F. Kalthoff, "Models of dynamic shear failure in solids", *Int. J. Fract.* **101** (2000), 1–31.

[Kim and Paulino 2004] J. H. Kim and G. H. Paulino, "Simulation of crack propagation in functionally graded materials under mixed-mode and non-proportional loading", *Int. J. Mech. Mater. Des.* **1**:1 (2004), 63–94.

[Miehe et al. 2010a] C. Miehe, M. Hofacker, and F. Welschinger, "A phase field model for rate-independent crack propagation: robust algorithmic implementation based on operator splits", *Comput. Methods Appl. Mech. Eng.* **199**:45-48 (2010), 2765–2778.

[Miehe et al. 2010b] C. Miehe, F. Welschinger, and M. Hofacker, "Thermodynamically consistent phase-field models of fracture: variational principles and multi-field FE implementations", *Int. J. Numer. Methods Eng.* **83**:10 (2010), 1273–1311.

[Msekh et al. 2015] M. A. Msekh, J. M. Sargado, M. Jamshidian, P. M. Areias, and T. Rabczuk, "Abaqus implementation of phase-field model for brittle fracture", *Comput. Mater. Sci.* **96**:B (2015), 472–484.

[Newmark 1959] N. M. Newmark, "A method of computation for structural dynamics", *J. Eng. Mech. Div.* (*ASCE*) **85** (1959), 67–94.

[Oleaga 2004] G. E. Oleaga, "On the path of a quasi-static crack in mode III", *J. Elasticity* **76**:2 (2004), 163–189.

[Pham and Marigo 2010a] K. Pham and J.-J. Marigo, "Approche variationnelle de l'endommagement, I: Les concepts fondamentaux", *C. R. Mécanique* **338** (2010), 191–198.

[Pham and Marigo 2010b] K. Pham and J.-J. Marigo, "Approche variationnelle de l'endommagement, II: Les modèles à gradient", *C. R. Mécanique* **338** (2010), 199–206.

[Schlüter et al. 2014] A. Schlüter, A. Willenbücher, C. Kuhn, and R. Müller, "Phase field approximation of dynamic brittle fracture", *Comput. Mech.* **54**:5 (2014), 1141–1161.

[Vignollet et al. 2014] J. Vignollet, S. May, R. de Borst, and C. V. Verhoosel, "Phase-field models for brittle and cohesive fracture", *Meccanica* (*Milano*) **49**:11 (2014), 2587–2601.

Received 12 Jan 2016. Revised 27 Feb 2016. Accepted 3 Mar 2016.

HAMDI HENTATI: hamdi.hentati@yahoo.fr
LA2MP Laboratory, National School of Engineers of Sfax, University of Sfax, 3038 Sfax, Tunisia

MARWA DHAHRI: marwadhahri70@yahoo.com
LA2MP Laboratory, National School of Engineers of Sfax, University of Sfax, 3038 Sfax, Tunisia

FAKHREDDINE DAMMAK: fakhreddine.dammak@enis.rnu.tn
LA2MP Laboratory, National School of Engineers of Sfax, University of Sfax, 3038 Sfax, Tunisia

SUBMISSION GUIDELINES

ORIGINALITY

Authors may submit manuscripts in PDF format online at the Submissions page. Submission of a manuscript acknowledges that the manuscript is original and has neither previously, nor simultaneously, in whole or in part, been submitted elsewhere. Information regarding the preparation of manuscripts is provided below. Correspondence by email is requested for convenience and speed. For further information, write to contact@msp.org.

LANGUAGE

Manuscripts must be in English. A brief abstract of about 150 words or less must be included. The abstract should be self-contained and not make any reference to the bibliography. Also required are keywords and subject classification for the article, and, for each author, postal address, affiliation (if appropriate), and email address if available. A home-page URL is optional.

FORMAT

Authors can use their preferred manuscript-preparation software, including for example Microsoft Word or any variant of TEX. The journal itself is produced in LATEX, so accepted articles prepared using other software will be converted to LATEX at production time. Authors wishing to prepare their document in LATEX can follow the example file at www.jomms.net (but the use of other class files is acceptable). At submission time only a PDF file is required. After acceptance, authors must submit all source material (see especially Figures below).

REFERENCES

Bibliographical references should be complete, including article titles and page ranges. All references in the bibliography should be cited in the text. The use of BibTEX is preferred but not required. Tags will be converted to the house format (see a current issue for examples); however, for submission you may use the format of your choice. Links will be provided to all literature with known web locations; authors can supply their own links in addition to those provided by the editorial process.

FIGURES

Figures must be of publication quality. After acceptance, you will need to submit the original source files in vector format for all diagrams and graphs in your manuscript: vector EPS or vector PDF files are the most useful. (EPS stands for Encapsulated PostScript.)

Most drawing and graphing packages—Mathematica, Adobe Illustrator, Corel Draw, MATLAB, etc.—allow the user to save files in one of these formats. Make sure that what you're saving is vector graphics and not a bitmap. If you need help, please write to graphics@msp.org with as many details as you can about how your graphics were generated.

Please also include the original data for any plots. This is particularly important if you are unable to save Excel-generated plots in vector format. Saving them as bitmaps is not useful; please send the Excel (.xls) spreadsheets instead. Bundle your figure files into a single archive (using zip, tar, rar or other format of your choice) and upload on the link you been given at acceptance time.

Each figure should be captioned and numbered so that it can float. Small figures occupying no more than three lines of vertical space can be kept in the text ("the curve looks like this:"). It is acceptable to submit a manuscript with all figures at the end, if their placement is specified in the text by means of comments such as "Place Figure 1 here". The same considerations apply to tables.

WHITE SPACE

Forced line breaks or page breaks should not be inserted in the document. There is no point in your trying to optimize line and page breaks in the original manuscript. The manuscript will be reformatted to use the journal's preferred fonts and layout.

PROOFS

Page proofs will be made available to authors (or to the designated corresponding author) at a Web site in PDF format. Failure to acknowledge the receipt of proofs or to return corrections within the requested deadline may cause publication to be postponed.

Journal of Mechanics of Materials and Structures

Volume 11, No. 3 May 2016

An Eulerian formulation for large deformations of elastically isotropic elastic-viscoplastic membranes M. B. Rubin and Ben Nadler 197

Physical meaning of elastic constants in Cosserat, void, and microstretch elasticity Roderic S. Lakes 217

On low-frequency vibrations of a composite string with contrast properties for energy scavenging fabric devices Askar Kudaibergenov, Andrea Nobili and Ludmilla Prikazchikova 231

Wave propagation in layered piezoelectric rings with rectangular cross sections JianGong Yu, XiaoDong Yang and Jean-Etienne Lefebvre 245

Effective boundary condition method and approximate secular equations of Rayleigh waves in orthotropic half-spaces coated by a thin layer Pham Chi Vinh and Vu Thi Ngoc Anh 259

Nonlocal forced vibration of a double single-walled carbon nanotube system under the influence of an axial magnetic field Marija B. Stamenković, Danilo Karličić, Goran Janevski and Predrag Kozić 279

A phase-field model of quasistatic and dynamic brittle fracture using a staggered algorithm Hamdi Hentati, Marwa Dhahri and Fakhreddine Dammak 309

1559-3959(2016)11:3;1-6